RADC-TR-86-240
Final Technical Report
February 1987

RESEARCH IN TRAVELING WAVE CHARGE TRANSPORT TECHNOLOGY

University of Illinois

Sponsored by
Defense Advanced Research Projects Agency (DOD)
ARPA Order No. 5015

APPROVED FOR PUBLIC RELEASE; DISTRIBUTION UNLIMITED

The views and conclusions contained in this document are those of the authors and should not be interpreted as necessarily representing the official policies, either expressed or implied, of the Defense Advanced Research Projects Agency or the U.S. Government.

ROME AIR DEVELOPMENT CENTER
Air Force Systems Command
Griffiss Air Force Base, NY 13441-5700

RESEARCH IN TRAVELING WAVE CHARGE TRANSPORT TECHNOLOGY

B. J. Hunsinger
M. J. Hoskins
E. G. Bogus
C. E. Warren
B. C. Schmukler
J. Dallesasse
J. W. Peterson
J. Pryst
R. L. Miller
W. D. Hunt

Contractor: University of Illinois
Contract Number: F30602-84-C-0132
Effective Date of Contract: Jun 84
Contract Expiration Date: Jun 86
Short Title of Work: Research In Traveling Wave Charge Transport Technology
Program Code Number: 4G10
Period of Work Covered: Jun 84 - Jun 86

Principal Investigator: Dr. Bill Hunsinger
Phone: (217) 367-2600

Project Engineer: Richard D. Hinman
Phone: (315) 330-3224

This research was supported by the Defense Advanced Research Projects Agency of the Department of Defense and was monitored by Richard D. Hinman (DCCD), Griffiss AFB NY 13441-5700, under Contract F30602-84-C-0132.

UNCLASSIFIED
SECURITY CLASSIFICATION OF THIS PAGE

AD-A182 767

REPORT DOCUMENTATION PAGE

Form Approved
OMB No. 0704-0188

1a. REPORT SECURITY CLASSIFICATION UNCLASSIFIED	1b. RESTRICTIVE MARKINGS N/A
2a. SECURITY CLASSIFICATION AUTHORITY N/A	3. DISTRIBUTION/AVAILABILITY OF REPORT Approved for public release; distribution unlimited.
2b. DECLASSIFICATION/DOWNGRADING SCHEDULE N/A	
4. PERFORMING ORGANIZATION REPORT NUMBER(S) N/A	5. MONITORING ORGANIZATION REPORT NUMBER(S) RADC-TR-86-240
6a. NAME OF PERFORMING ORGANIZATION University of Illinois 6b. OFFICE SYMBOL (If applicable)	7a. NAME OF MONITORING ORGANIZATION Rome Air Development Center (DCCD)
6c. ADDRESS (City, State, and ZIP Code) 1101 W. Springfield Avenue Urbana IL 61801	7b. ADDRESS (City, State, and ZIP Code) Griffiss AFB NY 13441-5700
8a. NAME OF FUNDING/SPONSORING ORGANIZATION Defense Advanced Research Projects Agency 8b. OFFICE SYMBOL (If applicable) TTO	9. PROCUREMENT INSTRUMENT IDENTIFICATION NUMBER F30602-84-C-0132
8c. ADDRESS (City, State, and ZIP Code) 1400 Wilson Blvd Arlington VA 22209	10. SOURCE OF FUNDING NUMBERS PROGRAM ELEMENT NO. 62702E 62702F PROJECT NO. 4519 TASK NO 42 WORK UNIT ACCESSION NO. 44

11. TITLE (Include Security Classification)
RESEARCH IN TRAVELINC WAVE CHARCE TRANSPORT TECHNOLOGY

12. PERSONAL AUTHOR(S) B. J. Hunsinger, M. J. Hoskins, E. C. Bogus, C. E. Warren, B. C. Schmukler, J. Dallesasse, J. W. Peterson, J. Pryst, R. L. Miller, W. D. Hunt

13a. TYPE OF REPORT	13b. TIME COVERED	14. DATE OF REPORT (Year, Month, Day)	15. PAGE COUNT
Final	FROM Jun 84 TO Jun 86	February 1987	260

16. SUPPLEMENTARY NOTATION
N/A

17. COSATI CODES		
FIELD	GROUP	SUB-GROUP
17	02	
20	12	

18. SUBJECT TERMS (Continue on reverse if necessary and identify by block number)
GaAs, Surface Acoustic Wave, Ion Implantation, SAW, Gallium Arsenide, SAW Waveguides, ACT, Acoustic Charge Transport, SAW Propagation

19. ABSTRACT (Continue on reverse if necessary and identify by block number)
This final report describes progress in fundamental tasks directed toward the development of traveling wave charge transport technology. Research projects addressing the tasks fall into three basic areas:

(1) Device Physics and Modeling, including theory of charge injection into a traveling wave, study of nondestructive sensing or charge, and study of potential distributions in traveling wave devices.

(2) Fabrication Technology Research, including study of dielectric for low temperature processing, development of photolithographic methods for ion-implanted thick active layers, and study of leakage current in CaAs Schottky barriers.

20. DISTRIBUTION/AVAILABILITY OF ABSTRACT	21. ABSTRACT SECURITY CLASSIFICATION
☒ UNCLASSIFIED/UNLIMITED ☐ SAME AS RPT. ☐ DTIC USERS	UNCLASSIFIED
22a. NAME OF RESPONSIBLE INDIVIDUAL Richard D. Hinman	22b. TELEPHONE (Include Area Code) (315) 330-3226 22c. OFFICE SYMBOL RADC (DCCD)

DD Form 1473, JUN 86 *Previous editions are obsolete.*

SECURITY CLASSIFICATION OF THIS PAGE
UNCLASSIFIED

(3) GaAs Surface Acoustic Wave Research, including development of waveguide structures for high intensity surface acoustic waves (SAW), and study of SAW propagation in GaAs.

Individual reports on each project are presented. Research in each basic area is summarized and directions for future work are indicated.

TABLE OF CONTENTS

Introduction

This report is composed of a series of individual technical summaries which span several fundamental research projects associated with traveling wave charge transport technology development. A detailed description of the GaAs traveling wave charge transport device and its potential capabilities may be found in Reference 4. This device is of interest for transversal filtering and other signal processing applications due to the precise, high speed charge transfer and distributed charge sensing functions which can be accomplished in the device over a very broad bandwidth.

The projects described in this report fall into three basic areas: device physics and modeling, fabrication technology research, and GaAs surface acoustic wave (SAW) research. An overview of the fundamental technology development tasks is presented via a brief description of the individual projects.

Device Physics and Modeling

1) Traveling Wave Charge Injection Research

The complicated theoretical problem of charge injection into a buried channel traveling wave charge transfer device is addressed. The problem is analyzed by formulating an adequate physical model for the injection process and solving this model to obtain theoretical predictions and performance trends for injection parameters. This research involves extremely intensive numerical computation.

2) Non-Destructive Sensing Research

A theoretical model is formulated to describe charge detection by capacitively coupled sense electrodes on the surface of the traveling wave charge transport device. The detection characteristics peculiar to this mode of signal detection are studied.

3) Transport Research

Various field problems are studied and analyzed to assess the impact of non-uniform surface structures in the charge transport device. The result of this work may also be applied to the analysis of the conventional charge coupled device.

Fabrication Technology Research

4) Low Process Temperature Dielectric Research

This project involves a study of the polyimide dielectric for GaAs IC applications where low process temperature schedules are required to preserve the structural and electronic quality of circuit features. This is particularly useful in applications where Schottky barrier diode leakage degradation due to heat treatment must be minimized.

5) Deep Implantation Research

The present architectures for the traveling wave charge transfer device utilize relatively thick active layers for electronic channel definition. This project involves the development of photolithographically definable masks for high energy ion implantation processing of thick active layers and a study of the material properties resulting from high energy implantation.

6) Schottky Barrier Leakage Research

Charge transfer devices require low values of channel leakage current for optimum operation. This project involves a study of primary factors which influence reverse bias leakage current in GaAs Schottky barriers.

GaAs Surface Acoustic Wave Research

7a) GaAs SAW Waveguide Research

Acoustic waveguides provide an elegant means for achieving controlled propagation of high power acoustic fields. SAW generation and propagation in GaAs waveguide structures is investigated and the application of these structures in the traveling wave charge transfer device is explored.

7b) GaAs SAW Propagation Research

The achievement of transversal filter functions in the traveling wave charge transfer device requires SAW propagation through large arrays of surface electrodes. This project involves a study of the fundamental properties of SAW propagation and diffraction in both bare GaAs and GaAs with surface electrode structures.

In some cases, project research has resulted in the completion of advanced degree thesis. These cases are noted, where applicable, in the individual technical summaries. In these instances a more detailed description of the research and its results may be found in these references.

1. Traveling Wave Charge Injection Research

Objective

The objective of this research is to study the charge injection mechanism of a GaAs buried channel traveling wave charge transport device. This task is accomplished by developing a model which describes the injection process and reveals how its performance is influenced by substrate parameters, electrode geometry and acoustic wave potential amplitude.

Theoretical Work

The injection phenomenon occurs at the input section of the traveling wave charge transport device and encompasses the entire process of converting a voltage signal into discrete packets containing continuously variable amounts of charge. Figure 1 provides a conceptual view of how a charge packet forms during a period of 3 time units. The basic parameters necessary for modeling the injection are extracted from this figure. The doping profile, bias voltages and electrode placement set the transport location and control the quantity of injected charge. The injection is also influenced by the acoustic wave potential amplitude and phase. Experiments have shown that injection is inhibited by the presence of a SAW potential minimum in the vicinity of the input contact.

The model is developed to include these parameters along with some simplifying approximations. A complete description involves three space dimensions and time. The time variable is immediately suppressed by considering a steady state condition at each instant of time. This is a good approximation because the potential environment established by the SAW changes insignificantly during the relaxation time of the mobile charge. By assuming a uniform distribution of charge in the z-direction (axis orientation is indicated in Fig. 1) the problem requires only a two-dimensional analysis.

The channel current resulting from a voltage signal is an important measurable quantity for assessing device performance. The current amplitude is related to the individual charge packet size

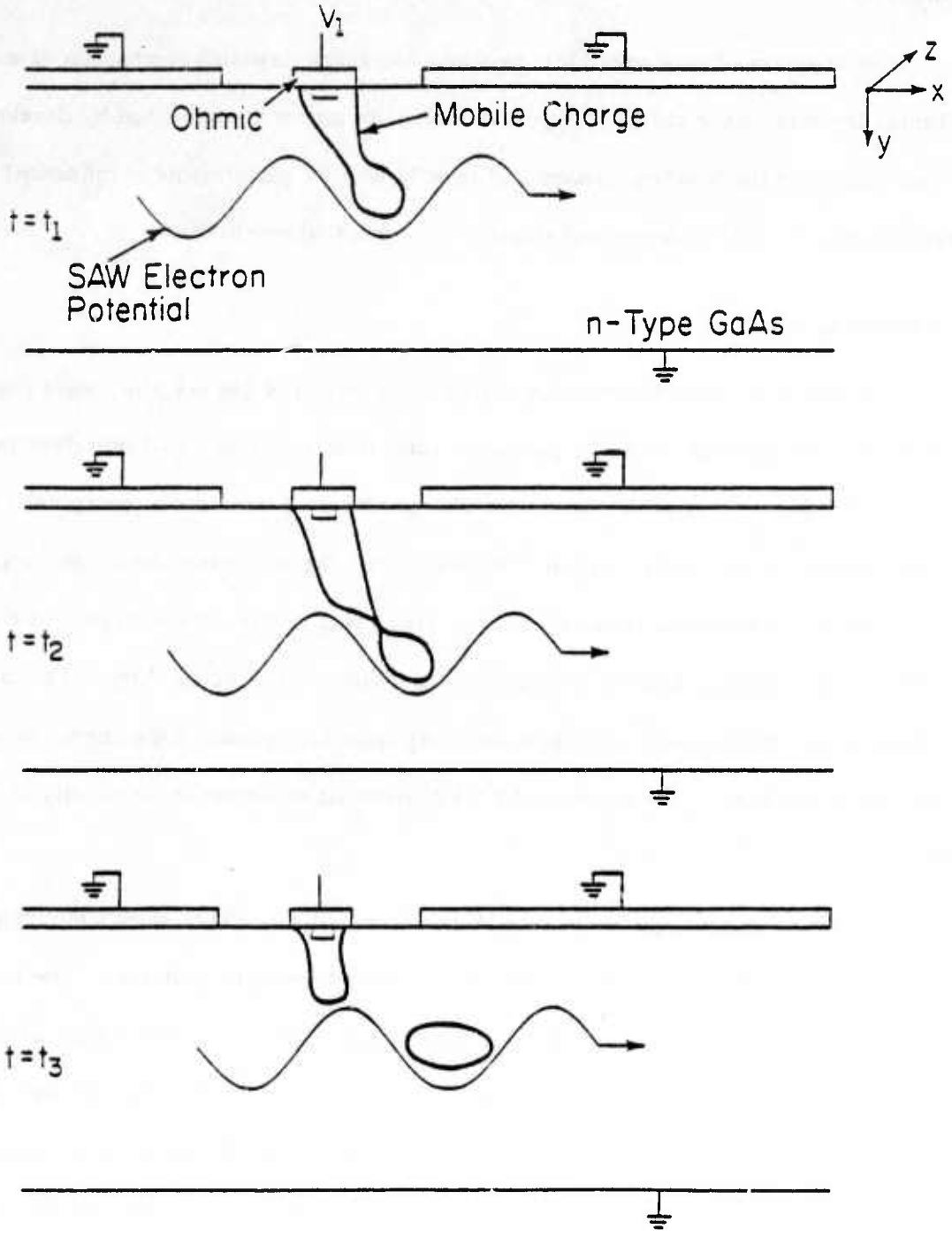

Figure 1. The charge injection process in a traveling wave charge transport device.

through the SAW velocity since by definition current is charge transported per unit time. Therefore the size of the charge packet which is injected into the transport channel for a specified device bias, signal voltage, doping profile and SAW potential amplitude is the essential quantity which the model will provide. To calculate this quantity, it is necessary to solve for the mobile carrier distribution of the injected charge using the coupled set of nonlinear differential semiconductor equations. See appendix A for details of the solution method.

Due to the nonlinearity of this two-dimensional problem, it is necessary to utilize a numerical algorithm to solve the system of coupled equations. The specific algorithm that is employed for the present problem was developed by Herbert Stone.[1] It was chosen since it has been used successfully by other authors in applications involving high voltages and large areas,[2,3] which are typical conditions found in the traveling wave device.

Theoretical Results

By separating the injection problem, as posed in Fig. 1, into several simpler cases, basic processes which contribute to the total solution are made evident. This also allows for a verification of the correctness of the numerical algorithm without the complexities of the complete problem. The algorithm is tested with two cases:

1) An input section with no SAW potential.

2) A transport channel far removed from the input section with a SAW potential impressed on it.

Figure 2(a) shows an input section and transport channel of the traveling wave device. Bias voltages are applied to the various contacts but the SAW is absent. In this steady state condition, mobile charge surrounds the ohmic input contact while the transport channel is devoid of carriers. This is illustrated in Fig. 2(b) which is a calculated contour plot of the charge distribution. The region of high charge density surrounds the ohmic contact because it is a point of maximum potential and a source of electrons. Moving away from the contact, the carrier density decreases and

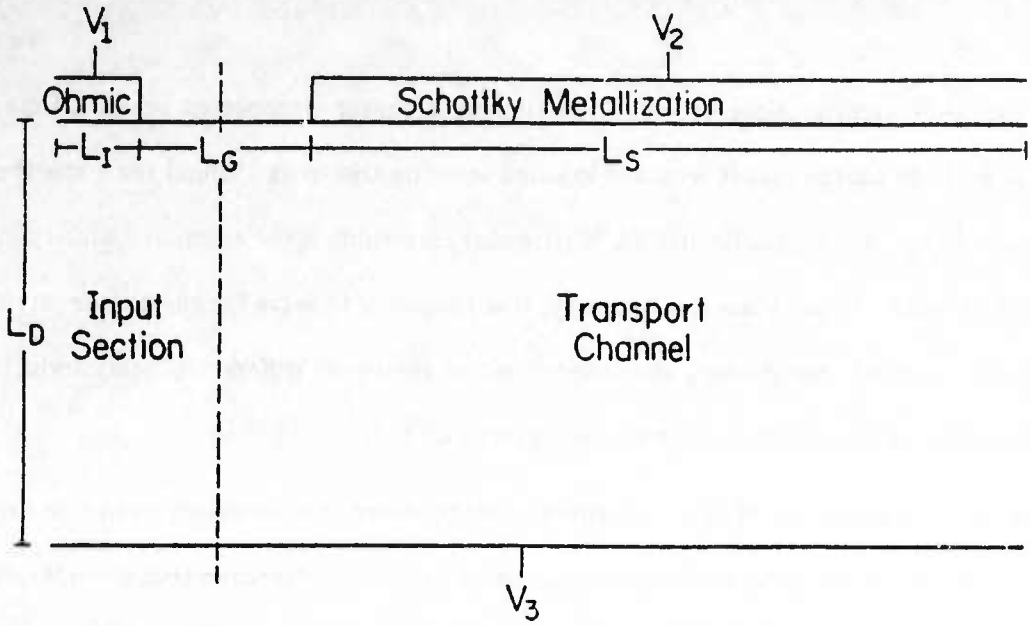

Figure 2(a). The input section and transport channel of a charge transport device.

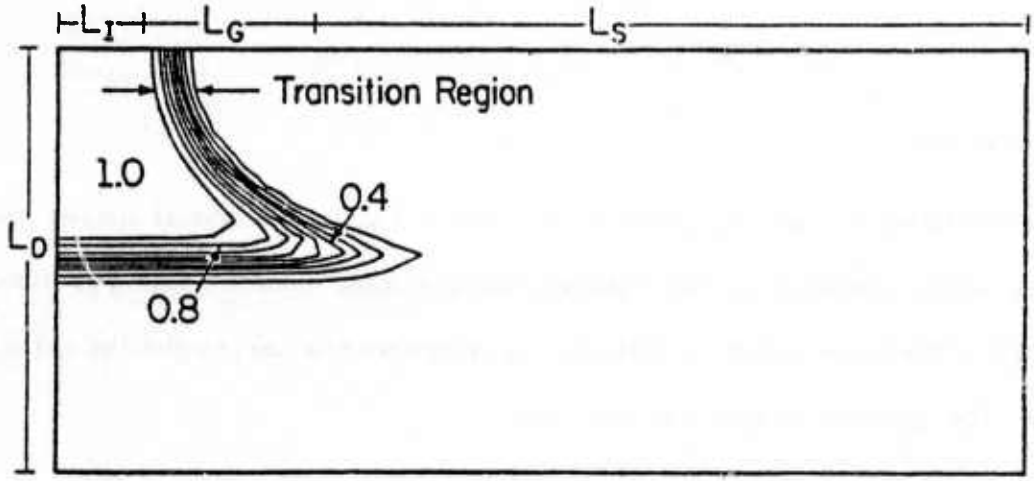

Figure 2(b). The mobile carrier distribution at the input section when the SAW potential is absent.

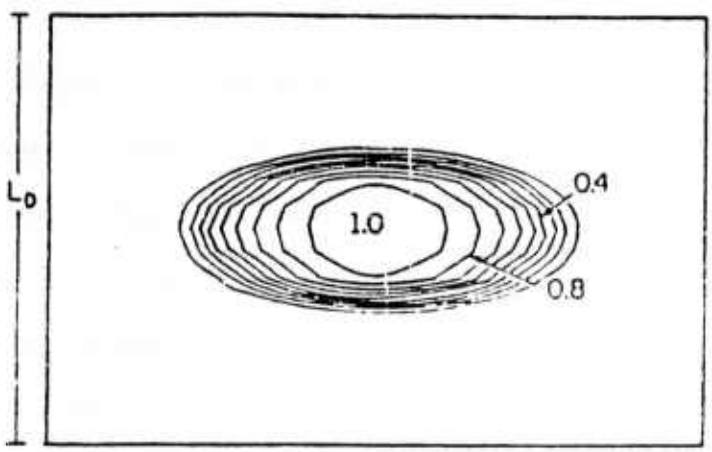

Figure 2(c). The distribution of mobile carriers confined by a two-dimensional potential well.

eventually approaches zero in the transport channel. The transition region which separates the high carrier density region from the low density region is approximately 5 Debye lengths wide and is exhibited on the plot by the series of closely spaced equi-charge density curves. They are labeled as fractions of the maximum density which exists at the ohmic contact. The transition region produces a boundary around the mobile carriers which lacks sharpness due to carrier diffusion.

The effect of a SAW potential is introduced into the model by adding a sinusoidal variation to the doping density profile which is an approximate representation of the true SAW induced polarization charge density. The confinement of mobile charge in the resulting two-dimensional potential well is clearly exhibited in Fig 2(c). This carrier density plot is drawn from data that was calculated at a location far removed from the input contact. Again, the smeared packet boundary is evident. The problem of charge bunching in a SAW induced potential well has been previously solved.[4] The solution method and the approximations employed differ from the present technique. However, the results shown here agree qualitatively with that work. Further analysis is required to correlate the two solutions.

The analysis of the injection problem involves solving for the carrier distribution which exists at the input section when the SAW potential is present. This is essentially a joining of the two previous cases. In this situation, charge is trapped in the SAW potential well and the packet breaks away from the input source of electrons as the wave progresses into the transport channel. The distance which the SAW travels before a packet splits from the electron source, depends on the contact voltage, V_{IC}. It is convenient to measure this distance from the center of the input contact where the SAW is assigned a phase of 0 degrees. Since the location of split off is not known beforehand, an iterative procedure is performed which involves solving for the carrier distribution in a series of steady state problems of increasing SAW phase. The phase is increased, simulating wave motion, until it is determined that a charge packet has split off. At this point, the amount of charge in the injected packet is obtained by integrating the carrier density distribution over the packet boundaries.

This analysis is performed on the device structure shown in Fig. 1 for an 8 μm wavelength SAW in a 4 μm thick n-layer that is uniformly doped with a donor concentration of $N_D = 10^{15}/cm^3$. A bias voltage of 0V is applied to the Schottky electrodes with the bottom of the n-layer also held at 0V. The input contact is biased with 3V. The SAW, now with its true y directed variation, is specified to have a 1/2 V zero to peak potential at a depth where the channel electron potential resulting from the depletion charge, the bias voltages and the SAW is a minimum.

The computed results are presented in Fig. 3. Each frame shows the carrier distribution at instants in time specified by fractions of T, where T is the time for the SAW to travel one wavelength. The equi-charge density contour lines differ by $1.4 \times 10^{14}/cm^3$ with the outer most line representing a concentration of $7 \times 10^{13}/cm^3$. At t=0, the SAW electron potential minimum is located at the center of the input contact. The resulting carrier distribution is shown in frame 1. In frame 2, the SAW has propagated 1 μm to the right and pulls the mobile carriers with it. As one potential well of the SAW propagates away from the input, a preceding well is advancing towards the input. The fields of this well attract mobile electrons from the input contact and consequently it will fill with charge. Each of these two wells will hold the same amount of charge when they are symmetrically located about the input contact as shown in frame 3. The last frame depicts the split off of a packet from the electron source. For this bias condition, split off occurred after a time of .71T = 1.98 ns.

Since V_{IC} varies the charge load of the injected packet and consequently the channel current, a transconductance curve can be generated by repeating the above analysis for different values of V_{IC}. This was performed and the result is shown in Fig. 4 for a 400 μm wide channel. The parameter ϕ_m is the minimum electron potential due to ionized donors in a layer depleted of mobile carriers as calculated using a 1 dimensional analysis. If V_{IC} is less than ϕ_m, a conducting channel would exist between the input contact and output contact of the transport device in the absence of a SAW field. Therefore ϕ_m represents the minimum input contact voltage required to deplete the

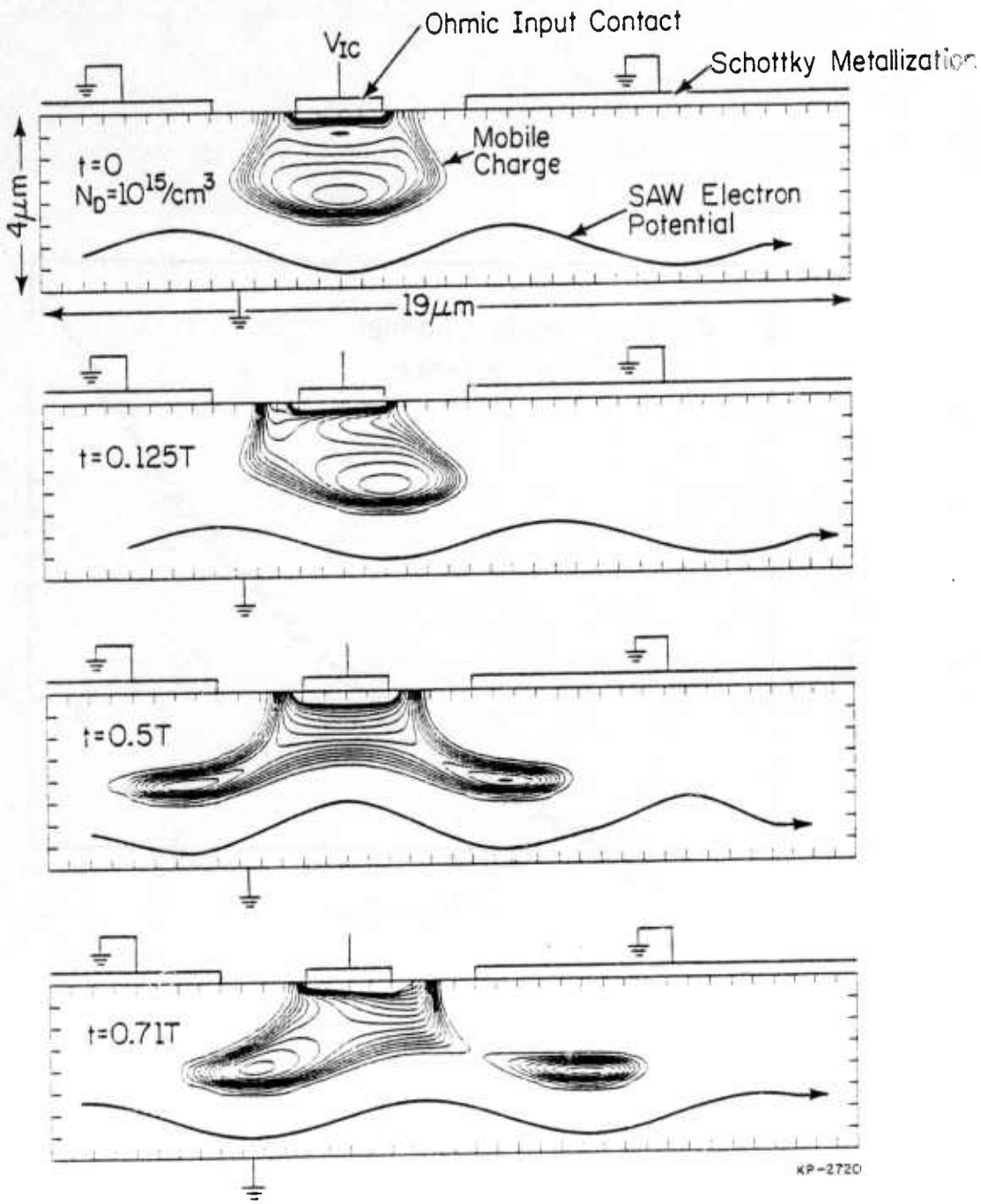

Figure 3. The mobile charge density distribution at four time instants during the charge injection process in an ACT device.

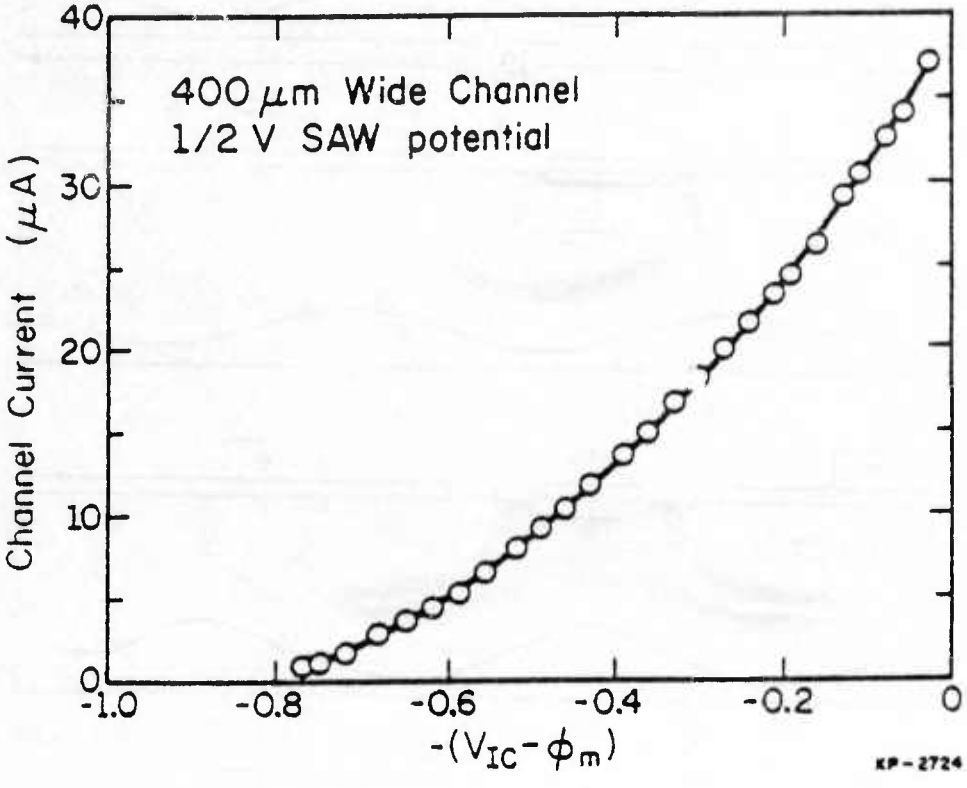

Figure 4. Theoretical input transconductance curve of an ACT device.

n-layer. By subtracting this value from the applied contact voltage as done in Fig. 4, it enables the transconductance of devices with different bias and doping parameters to be conveniently compared.

Conclusion

A model of the charge injection mechanism in a GaAs buried channel traveling wave charge transport device is developed. It includes the effects of substrate parameters and electrode geometry. Results are generated for two special cases which are used to test the numerical algorithm. The potential and mobile carrier density distributions in a biased transport channel are obtained in the vicinity of the injecting contact when the SAW is absent and at a location removed from the injector when the SAW is present. The process by which a charge packet is injected into the transport channel is demonstrated and a characteristic transconductance curve for the traveling wave charge transport device is calculated.

2. Non-Destructive Sensing Research

Objective

The objective of this research is to study the fundamental properties of non-destructive sensing of charge in a traveling wave charge transport device by providing a theoretical model for the small signal time and frequency domain responses of the non-destructive sense structure in terms of the physical parameters of the transport channel and the sense structure.

Theoretical Work

Time and frequency domain responses for a line charge traveling in a single tap current sensing electrode structure (Fig. 5(a)) are determined by computing the charge induced upon the sense electrodes by the line charge.[5] Analytical results for the frequency response are obtained for arbitrary charge depth when the gaps between electrodes are negligible, while numerical results are obtained for non-zero gaps. Normalized time and frequency response data for the structure of Fig. 5(a) for several values of charge depth and gap size are generated. Figure 6 shows the time domain response for the structure of Fig. 5(a) with a vanishingly small gap between the surface plates. The spreading of the response about the center is greater for larger charge depth due to the greater spreading of lines of flux emanating from the charge packet. Hence, the rolloff in the frequency response is greater for larger depths of transport. The presence of gaps between current sense electrodes introduces additional rolloff in the frequency response. A small signal equivalent circuit for current sensing consists of a single current source shunted by the structure capacitance.

The frequency response for the single tap voltage sensing structure of Fig. 5(b) has been computed analytically in terms of a superposition of current sense responses.[5] Voltage sensing introduces a multiplicative factor into the frequency response, which is dependent upon the length of the sense electrode. It is found that a null in the frequency response may be introduced by proper choice of sense electrode length. An equivalent circuit for the single tap voltage sensing structure consists of a voltage source in series with the structural capacitance of adjacent electrodes. It is

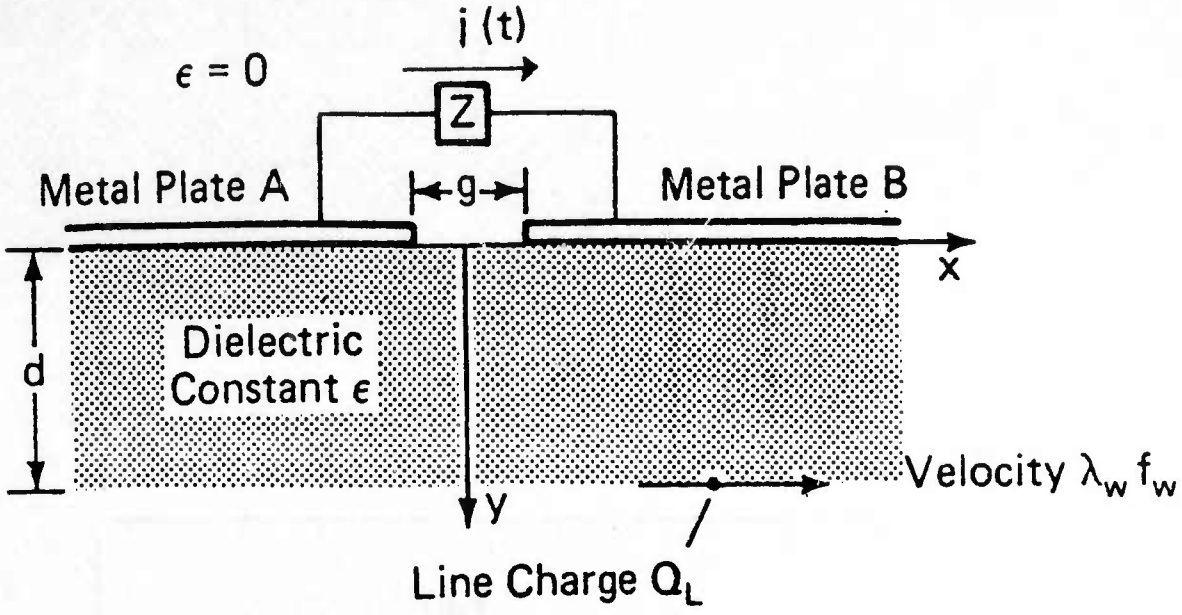

Figure 5(a). AC model of simple current sensing structure.

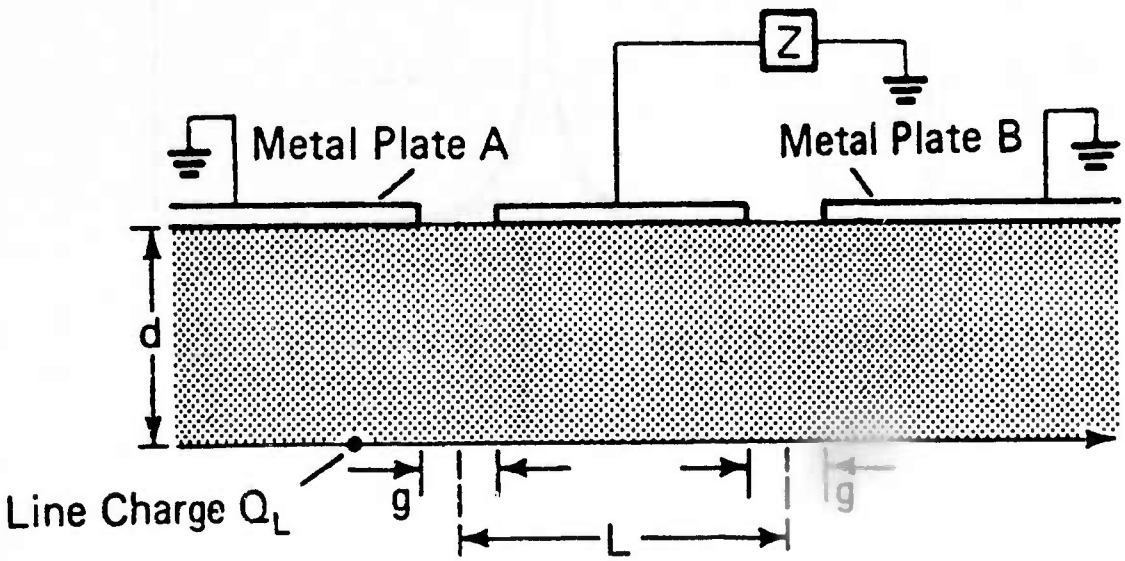

Figure 5(b). AC model of single electrode voltage sensing structure.

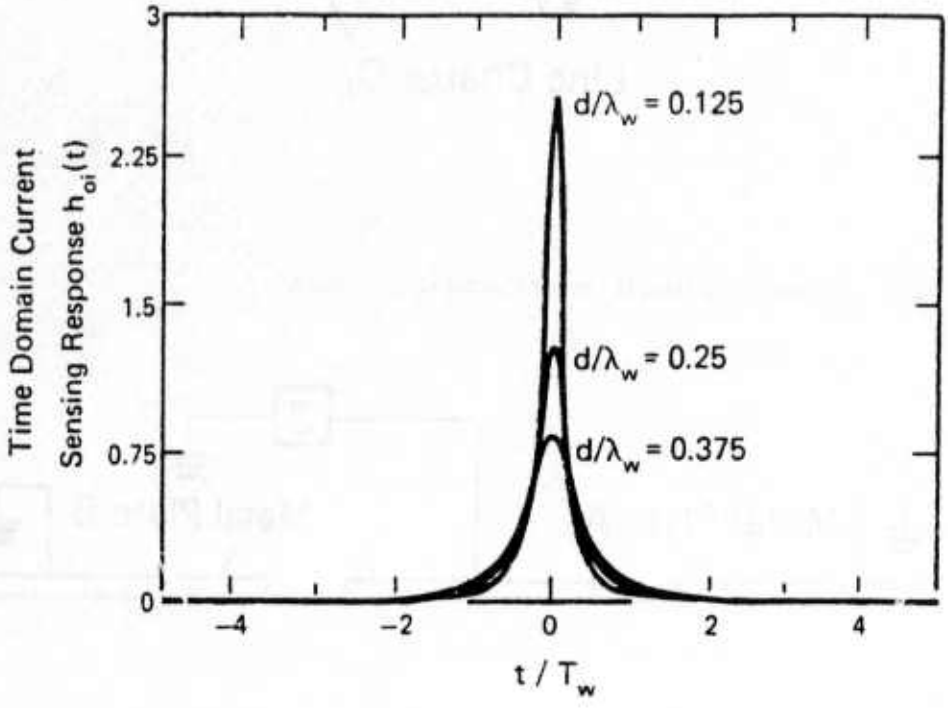

Figure 6. Normalized time domain current sensing responses for infinitesimal gap structure.

found that frequency response rolloff is lessened for shorter electrode length.

The effect of the distribution of charge in the packet upon current and voltage sensing frequency responses is determined numerically,[5] using previous results for the packet charge distribution.[4] For small charge loads, the rolloff introduced by the packet shape at low frequencies is much smaller than the more fundamental current and voltage sensing frequency response rolloffs.

Theoretical work has also focused upon nonlinearities introduced into the frequency response of the ACT device due to the finite, non-point nature of the surface acoustic wave (SAW) as a sampler of charge. Figure 7 illustrates the dependence of the normalized charge density in a single charge packet as a function of time for 50% normalized charge load as it flows in the ACT channel.[5] It is found that the size and shape of the packet is a function of the amount of charge contained in the packet. Therefore, the spectrum (Fourier transform) of the charge packet is also a function of charge load. This gives rise to the introduction of new frequencies (harmonics) in the frequency response of the ACT device to sinusoidal steady state input.

For a single tone input, a theoretical method has been devised for the computation of the level of the harmonic components present in the output signal as a function of the magnitude and frequency of the input tone. Initial computations with this method were limited to cases for which the signal frequency is an integer fraction of the SAW frequency, but recently a method has been found to treat the general case. Shown in Fig. 8 is a plot of the magnitude of the second harmonic versus the magnitude of the fundamental signal, for f_{signal}/f_{saw} = 1/7 and 0 to 50% signal charge load with a 50% quiescent charge load. The curve shows the expected quadratic behavior, since this is a second order effect. For a signal charge load of 40%, the curve indicates that second harmonic supression of 55dB below the fundamental component. Computation of the third harmonic for this case has also been carried out.

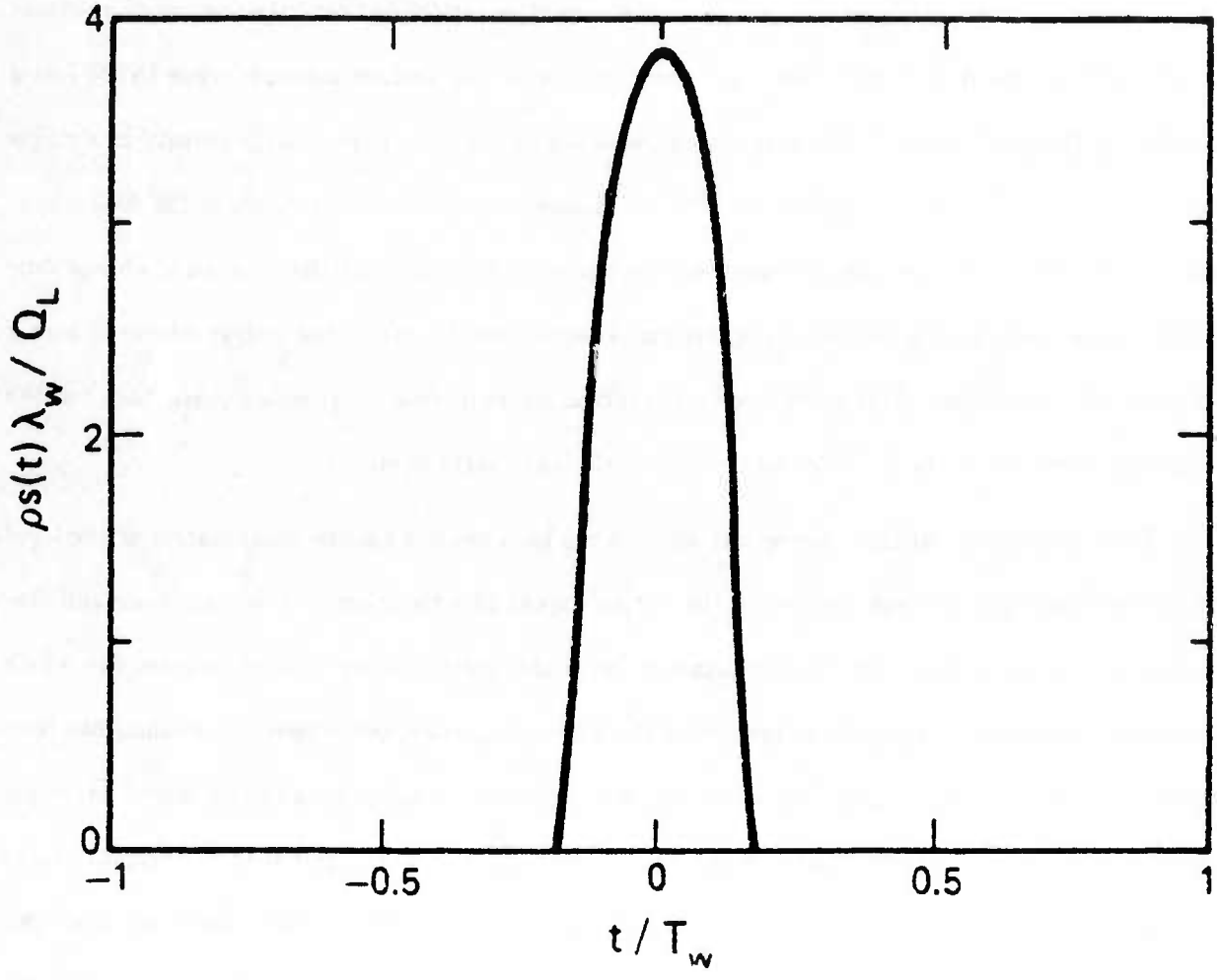

Figure 7. Time variation of one-dimensional packet charge density for 50% charge load.

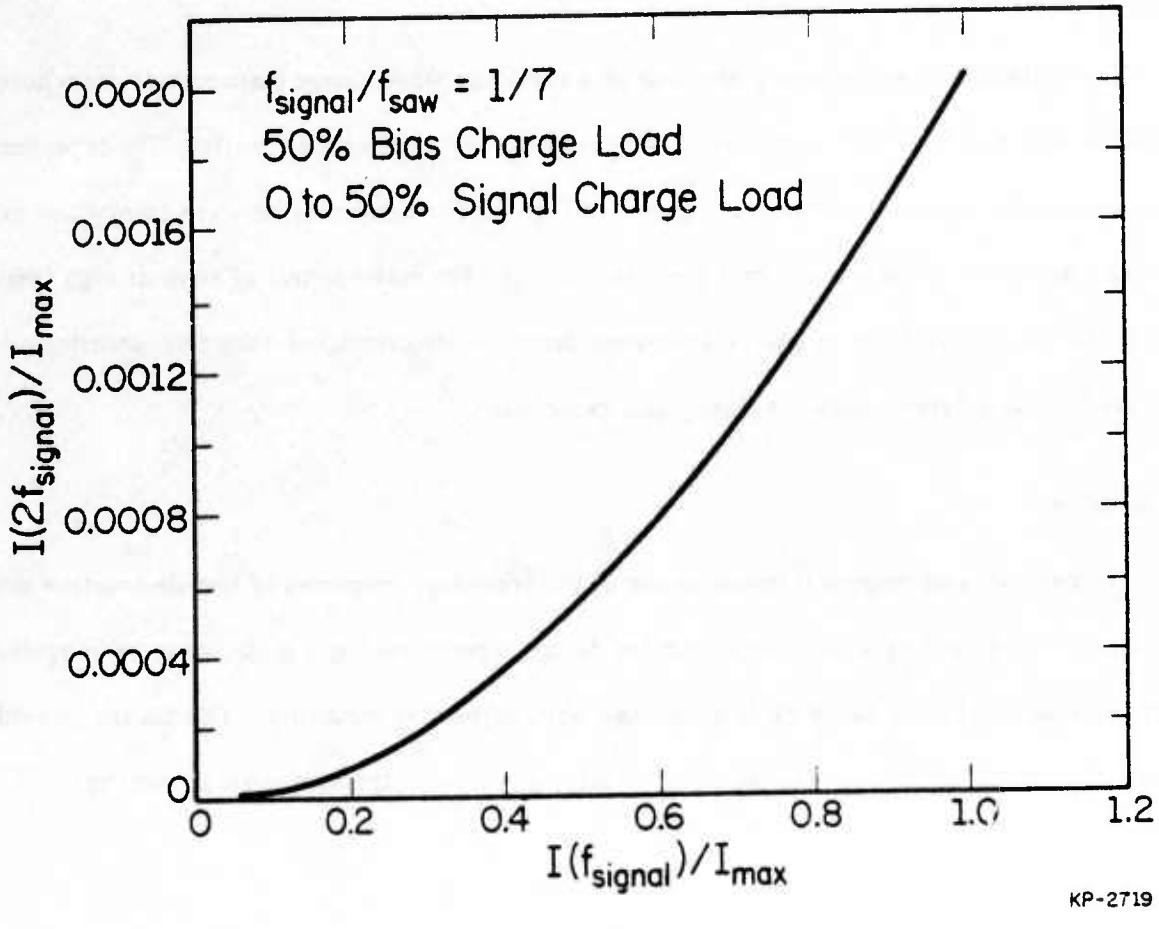

Figure 8. Magnitude of 2nd harmonic vs fundamental for 50% quiescent charge load and f_{sig}/f_{saw} = 1/7.

Future Work

Computation of harmonic components for cases with arbitrary relation between SAW and signal frequency will be carried out, as will simulation of the two-tone input signal. Experiments will be designed to verify the theory. Additionally, theory of large signal detection in NDS structures will be treated.

Experimental Work

The voltage sensing frequency response of a traveling wave charge transport device whose AC model is shown in Fig. 5(b) is measured and compared with theoretical results. The experimental and theoretical frequency responses are shown in Fig. 9. The agreement between theory and experiment is very good in the low and mid-frequency range. The major source of error at high frequencies is due to uncertainity in charge transport depth. It is calculated that this uncertainty can account for the difference between theory and experiment.

Conclusion

An analytic and numerical investigation of the frequency responses of non-destructive sensing structures in a traveling wave charge transfer device is performed and is shown to be in agreement with experimental data taken on a single tap voltage sensing structure. The theory provides a foundation for accurate electrical modeling of arbitrary non-destructive sense structures.

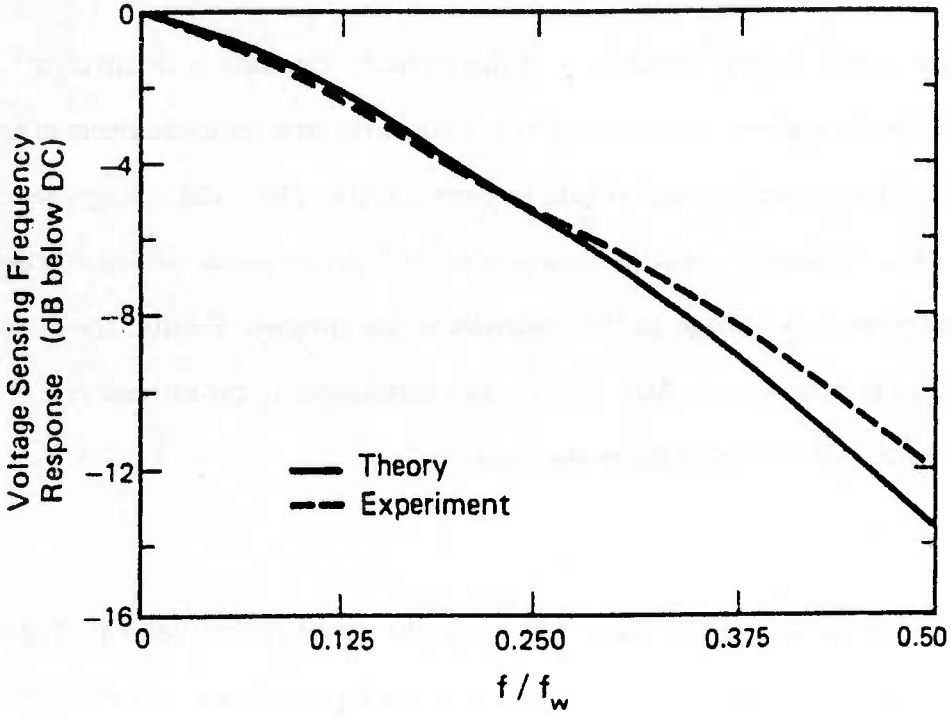

Figure 9. Theoretical and measured frequency responses for the structure of Figure 5(b).

3. Transport Research

Objective

The objective of this work is to develop the theory and computer programs to calculate the two-dimensional potentials in the transport channel of an acoustic charge transport (ACT) device for various device architectures and to ascertain the effects of these potentials on the basic transport properties of an ACT device.

Overview

There are several tasks of significance in this research. One task is to calculate the electrostatic potentials in the channel. Another task is to analyze the transfer inefficiencies in an ACT device caused by surface structures such as gaps between Schottky plates and voltages on electrodes in the channel. Also of interest is charge storage in an ACT device which corresponds to the case of applying a large negative voltage to the electrodes in the channel. Finally, there is the task of analyzing charge extraction in an ACT device which corresponds to the extreme case of applying a large positive voltage to the electrodes in the channel.

Potentials

Figure 10 shows typical structures for which the potentials are desired. Typically, these structures consist of an n-type active layer on top of a p-type substrate, or a semi-insulating substrate that is modeled as p-type due to trapping effects, with Schottky plates on the surface of the n-type active layer. The size of the gaps are not small enough to be neglected and must be included in the analysis.

The key to solving for the desired potentials in a simple fashion is to separate the problem into two parts and to utilize superposition to obtain the total solution. Figure 11 illustrates the separation of the problem. All of the potential variation due to space charge is separated into a one-dimensional problem. The solution to this problem can be found analytically and is added to the solution of a two-dimensional Laplace problem. This two-dimensional problem is picked such

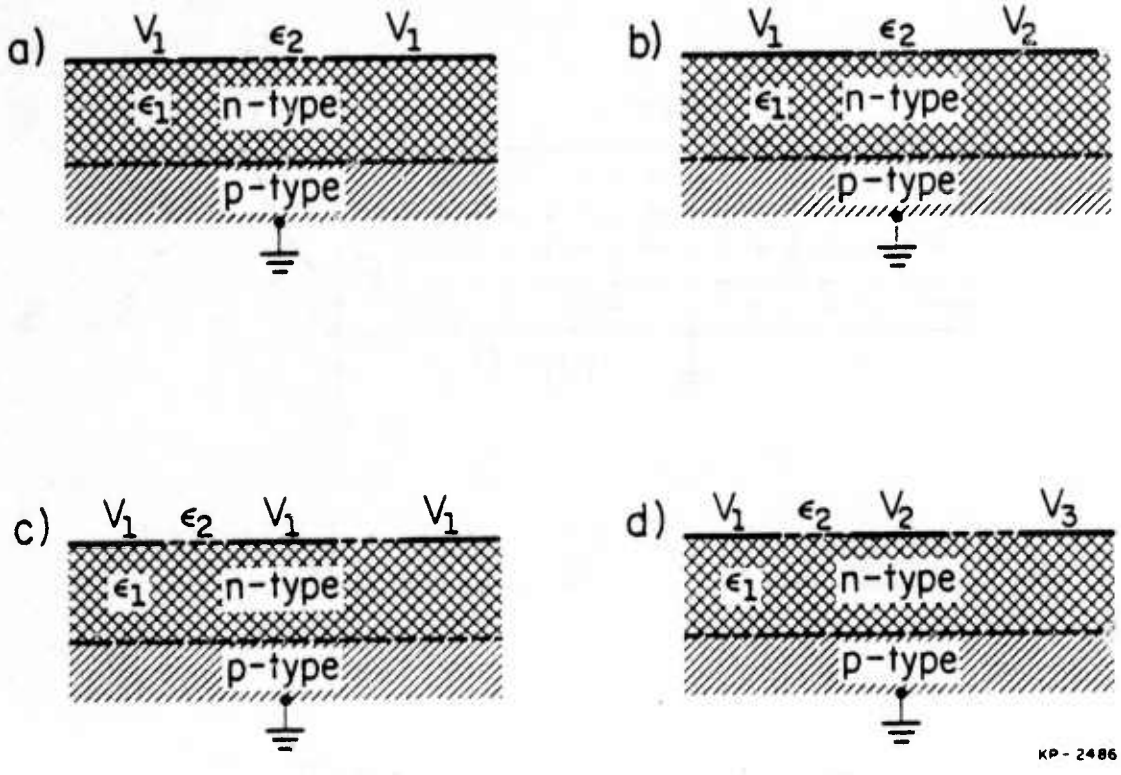

Figure 10. Typical structures encountered in buried channel charge transfer devices.
(a) Isolated gap with symmetrical biasing.
(b) Isolated gap with unsymmetrical biasing.
(c) Isolated sense electrode.
(d) Arbitrary periodic structure.

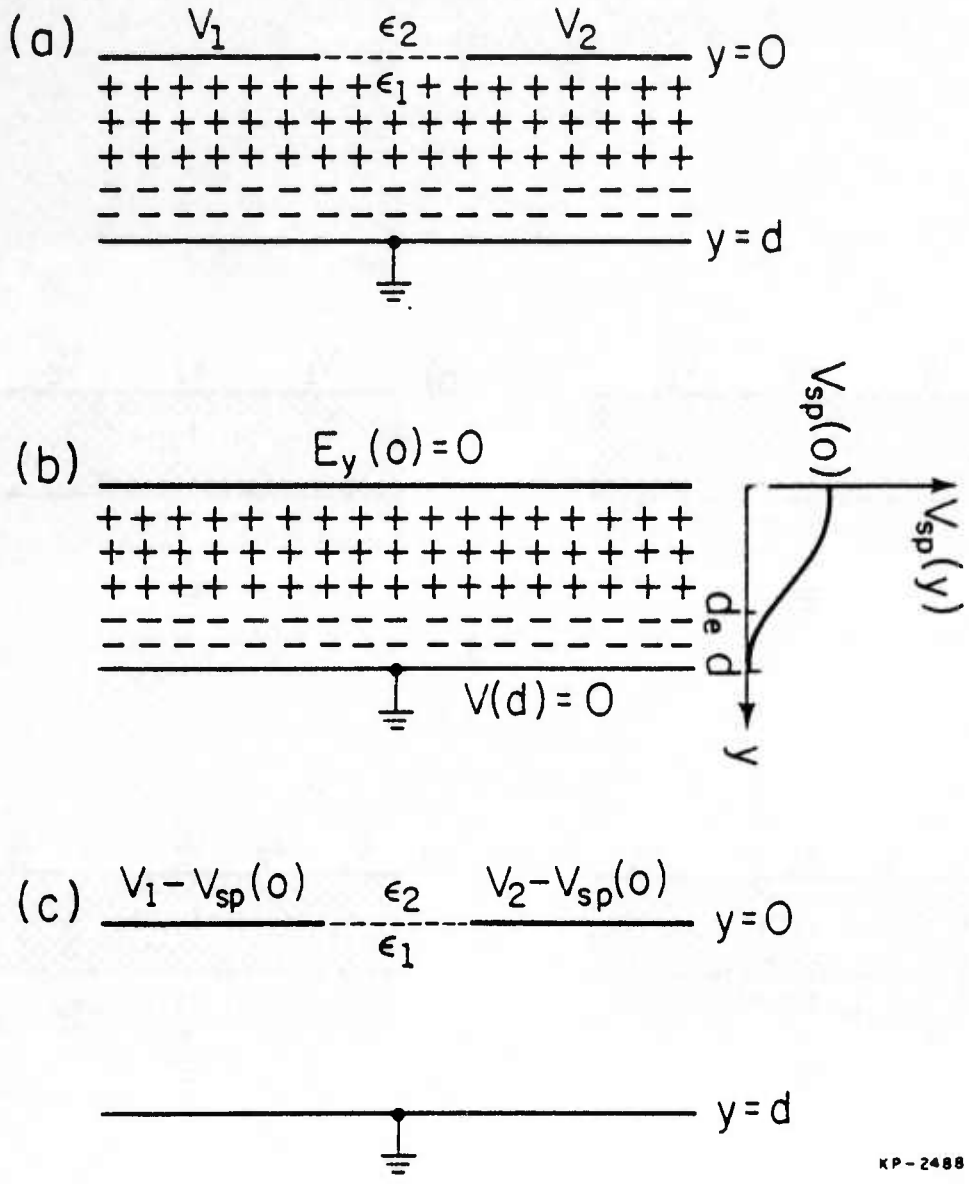

Figure 11. Separation of a potential problem into two problems.
(a) Two-dimensional potential problem with space charge.
(b) One-dimensional potential problem containing all space charge.
(c) Two-dimensional potential problem without space charge.

that subsequent superposition with the one-dimensional potential satisfies all differential equations and boundary conditions. This two-dimensional Laplace problem is then solved using Fourier analysis or conformal mapping. Full details of these calculations are in reference [6].

By using these techniques one can obtain the empty channel potentials for any arbitrary structure and doping profile. Figure 12 shows the normalized potential deviation from the regular one-dimensional potential caused by a single gap with gap width to active layer ratio of 2:3. To obtain the actual potential deviation for a given doping profile and channel minimum point one must multiply the normalized potential deviation by the scaling factor.

$$SF_1 = \frac{d}{\epsilon_1 + \epsilon_2} \int_0^{y_m} \rho(y)dy$$

where d is the active layer depth, y_m is the transport depth, $\rho(y)$ is the charge density of the channel, ϵ_1 is the permittivity of the substrate, and ϵ_2 is the permittivity of the dielectric above the substrate. Plots for other gap dimensions are in reference [1].

The above analysis doesn't include mobile charge in the channel however, it is still useful in analyzing charge storage, charge extraction, and transfer inefficiency. A way has been theoretically derived to include mobile charge packets in the channel and to also find the equilibrium boundaries associated with these charge packs. This method avoids the necessity of evaluating the two-dimensional convolution integral previously used in evaluating charge packet potentials and also avoids a finite difference approach. It has the promise of greatly reducing the computation time required to model mobile charge in the channel. At present the programming required is not fully completed and, hence, no results are currently available.

Transfer Inefficiency

The desired quantities of interest in this area are the transfer inefficiencies as a function of gap size, transport depth, SAW power and induced or applied electrode voltage. The first step in calculating the transfer efficiency is to calculate the reduction in charge capacity as a function of various

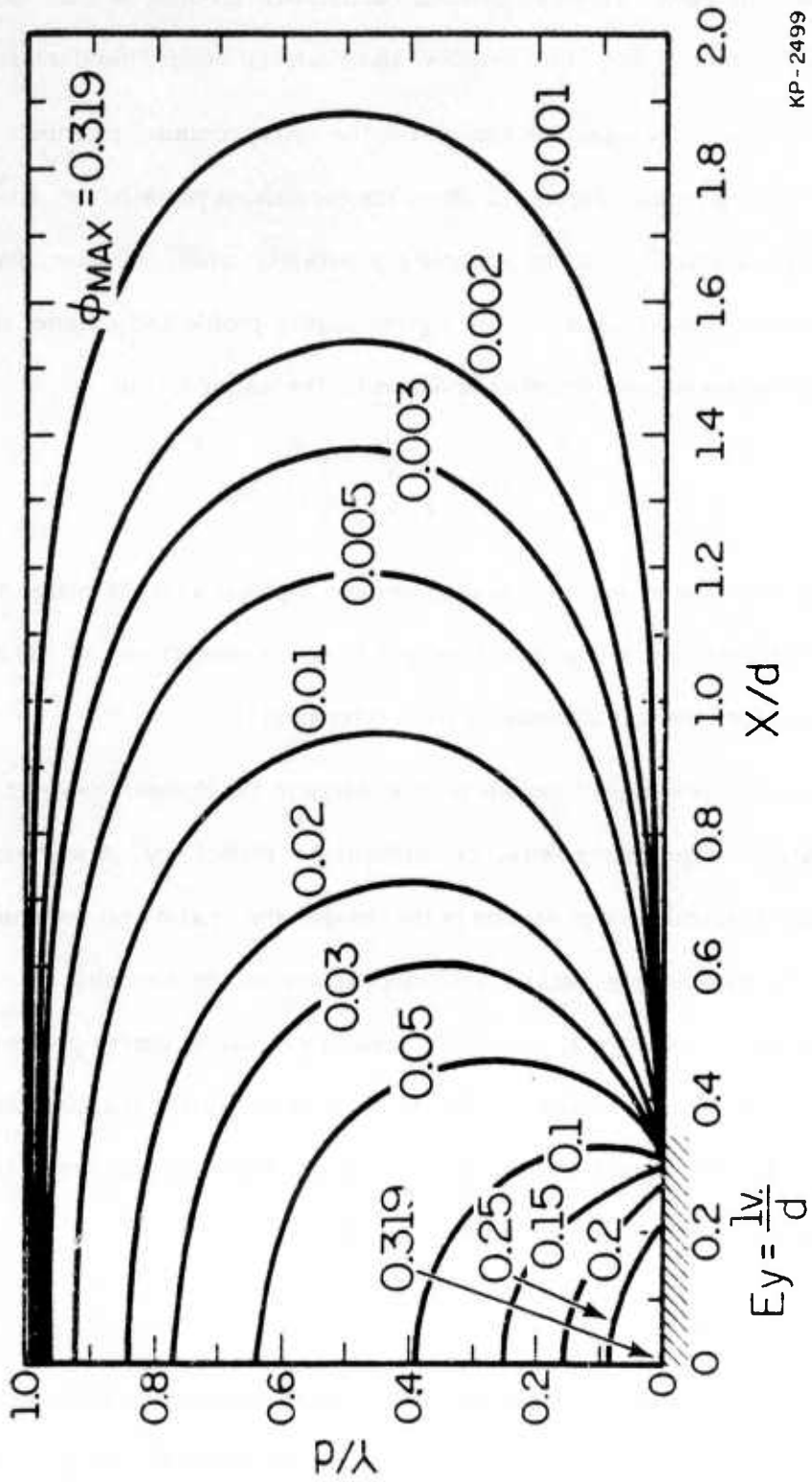

Figure 12. Normalized potential deviation, for an isolated gap, $\left(\frac{a}{d} = 1/3\right)$.

parameters. A one-dimensional charge packet model predicts that the charge capacity reduction factor (ccrf) as a function of E_x, which is the x-component of the perturbing field, is

$$ccrf = \frac{E_x}{kV_{saw}}$$

where k is the wave vector of the SAW.

The effect of gaps in the channel on charge transport is a problem of great concern. Figure 13 shows the normalized peak perturbing, E_x, as a function of normalized gap size for various normalized transport depths. The parameter g is the gap size and the parameter d is the total depletion depth of the device. To unnormalize the result one multiplies by the scaling factor $SF_2 = \frac{1}{\epsilon_1 + \epsilon_2} \int_0^{y_m} \rho(y)dy$. The ccrf is then easily found for various SAW frequencies and potentials. If the maximum operating charge capacity of an ACT device exceeds the adjusted charge capacity given by the maximum SAW capacity less the percentage given by the ccrf, then significant transfer inefficiency can be expected; otherwise, the transport will be minimally perturbed. A similar analysis can be done to find the ccrf due to small voltages on electrodes in the channel.

Charge Storage

In analyzing charge storage the desired quantities of interest are the threshold voltage of storage and the cutoff voltage of transport. Given a few assumptions and approximations it is possible to generate estimates of these quantities.

The first assumption is that a pulse will be used to store the charge. The ramification of this is that the deep traps in the semi-insulating layer will not react with the barrier pulse due to the long time constants of the traps. Also, if the length of the barrier electrode is long enough such that it can be assumed to be semi-infinite, then the fields due to two coplanar, semi-infinite, surface plates separated by a gap are sufficient to describe the barrier fields. The maximum E_x of the structure for a given transport depth provides the stopping force to charge transport. A good estimate

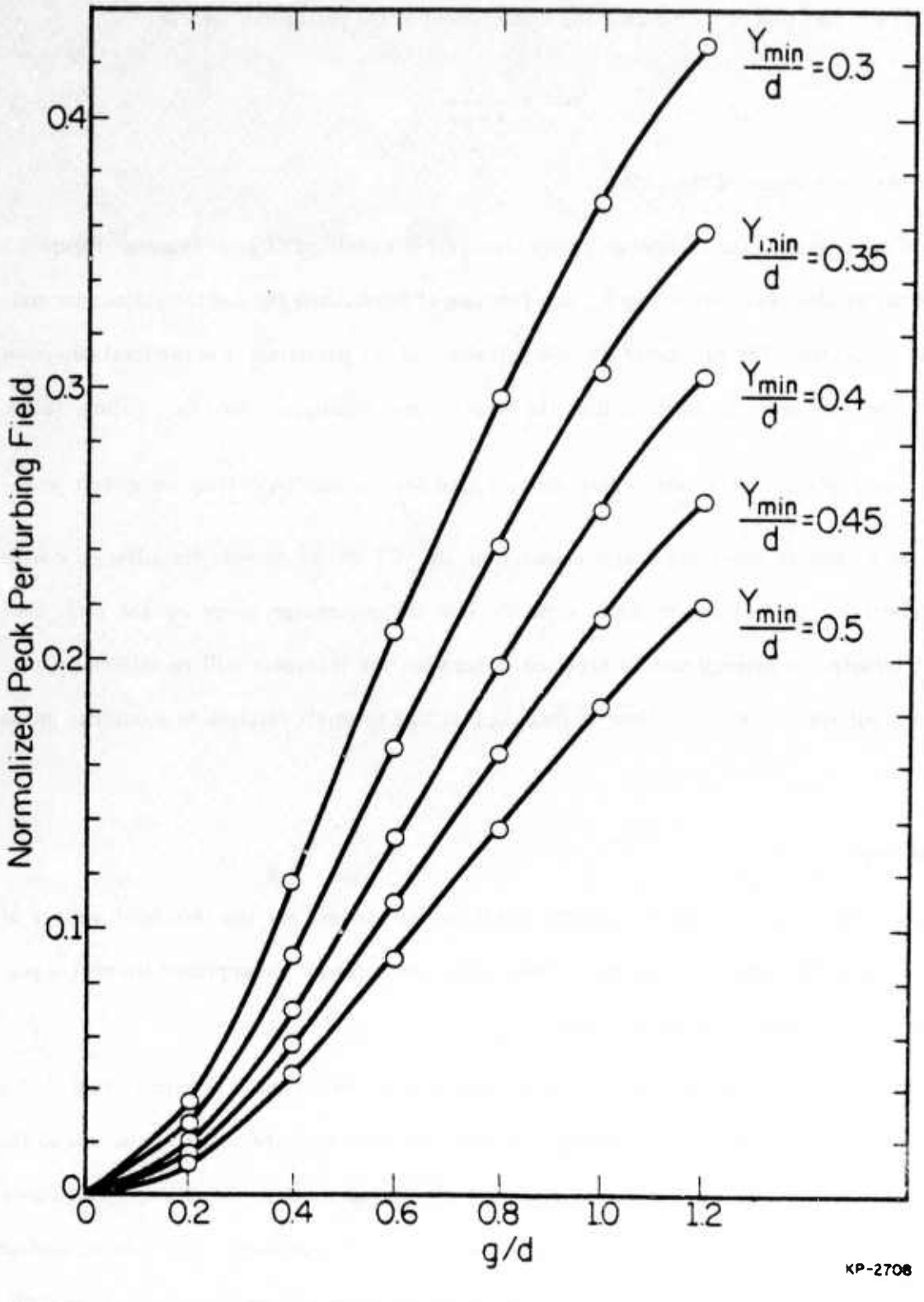

Figure 13. Perturbing E-field vs gap size.

of the maximum E_x is E_x down the center of the gap. For large transport depths, this is the maximum E_x. Since the fields in the described problem scale linearly with the barrier voltage V_b and the gap width g, a normalized plot of E_x can be made and is depicted in Fig. 14. Fig. 14 shows E_{norm}, normalized E_x, versus y_{norm}, the normalized y_{min}. The following relations are used to find E_x for a given y_{min}:

$$E_x = E_{xnorm} V_b/g$$

$$y_{min} = y_{norm}g$$

The threshold voltage of storage is achieved when E_x equals the product of V_{saw} and k. The cutoff voltage of transport is somewhat higher, for to guarantee that no charge leaks past the barrier the E_x of the barrier must overcome the peak SAW E-field, the induced E-field of the stored charge, E_{in}, and the barrier must also supply a sufficient potential height on top of this to prevent diffusion over the barrier. E_{in} can be approximated by an infinite train of line charges simulating the packets stored behind the barrier. Table 1 gives estimates of maximum E_{in} for various ratios of y_{min} to SAW wavelength. Thus, V_b can be determined for the total required E_x from Fig. 14. In addition, to ensure a barrier against diffusion, twice the desired diffusion barrier should be added to the result to predict the cutoff voltage of transport. This is because the first half goes to raising the potential of the stored charge and the second half goes towards stopping the diffusion.

Charge Extraction

This phenomenon is by far the most difficult to analyze. The extract voltage and pulse shape of the extracted packet depend on the doping profile as well as the structure. To extract charge from the channel it is necessary to have a clear trajectory to the extract electrode. In general, the shallower transport depths require less extraction voltage. Table 2 yields the predicted extract voltages with reference to the Schottky plates for various y_{min} for a 2 micron Schottky electrode between 2 micron gaps on a 5 micron active layer of doping 10^{15} cm^{-3}.

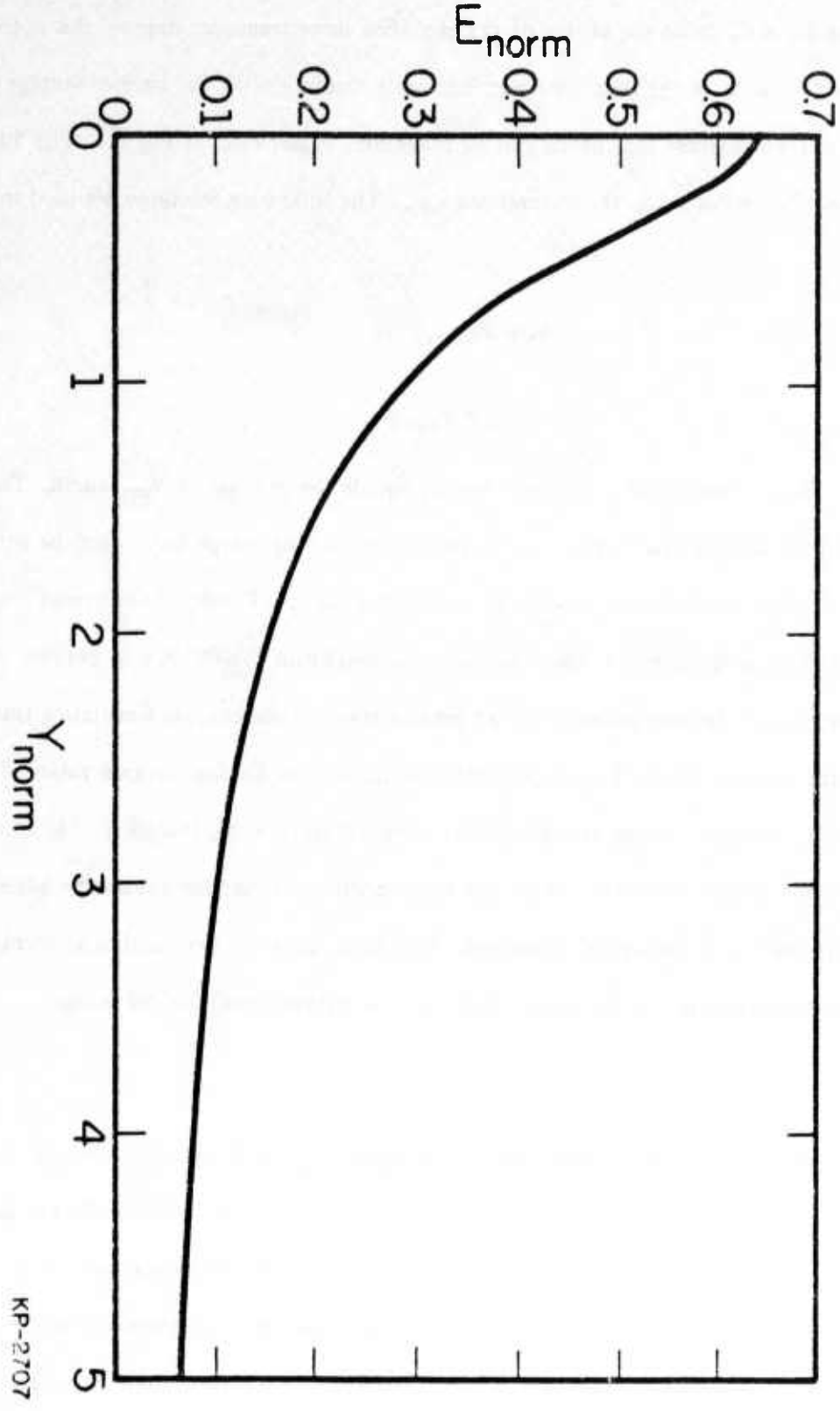

Figure 14. Stopping E-field per barrier volt vs transport depth.

Table 1. Normalized Induced E-field

$\frac{y_{min}}{\lambda_{SAW}}$	E_{in}
.1	.0996
.2	.338
.3	.613
.4	.865
.5	1.079

$$E_\xi = \frac{Q_{max}}{2\pi\epsilon\,\lambda_{SAW} W} E_{in}$$

W == width of channel
Q_{max} == maximum charge capacity of a well
E_ξ == induced E-field

$$E_x(\text{total}) = V_{SAW} * k + E_\xi$$

Table 2. Extract Voltages

y_{min}	$V_{extract}$
2.5	9.395
2.0	8.456
2.25	7.516
1.75	6.577
1.5	5.637

4. Low Process Temperature Dielectric Research

Objective

The objective of this research is to develop a low temperature fabrication process for multilevel interconnections using a polyimide dielectric. Material properties of the dielectric processed with the above low temperature fabrication procedure are also studied.

Experimental Work

Development of the wet chemical fabrication process includes polyimide dielectric selection, polyimide etchant evaluation, and comprehensive parametric optimization of basic processing parameters. Figure 15a and 15b outline the basic steps in the fabrication process.

Unique qualities of the interlayer dielectric and fabrication process are:

a. Low dielectric constant to reduce capacitive coupling between adjacent metalizations.

b. Application of two polyimide layers to achieve low pinhole density, reducing interlevel shorts.

c. Etchant selection which achieves minimal degradation of the GaAs substrate and first-level metal surface morphology during processing.

d. Low temperature polyimide cure to eliminate alloying of the first-level Schottky barrier features into the GaAs substrate.

e. Favorable edge profile for uninterrupted metalizations while providing small geometry capability. See Figs. 15c through 15f.

The electrical and mechanical properties of polyimide films are evaluated using three test vehicles: capacitor, via, and crossover arrays. The following polyimide film characteristics are evaluated and corresponding values listed in Table 3: dissipation factor, dielectric constant, dielectric breakdown strength, pinhole density, and via resistance.

The completeness of the low temperature polyimide cure can be determined from dissipation factor measurements. The average dissipation factor of capacitors with plate areas (809 μm)^2, (572 μm)^2, and (404 μm)^2 is similar. This similarity of dissipation factors suggests a bulk limited loss mechanism.

The relative dielectric constant is calculated from capacitance data taken during dissipation factor measurements.

Dielectric breakdown strength is measured using a capacitor test structure. Voltage across the capacitor plates is slowly increased until the dielectric fails.

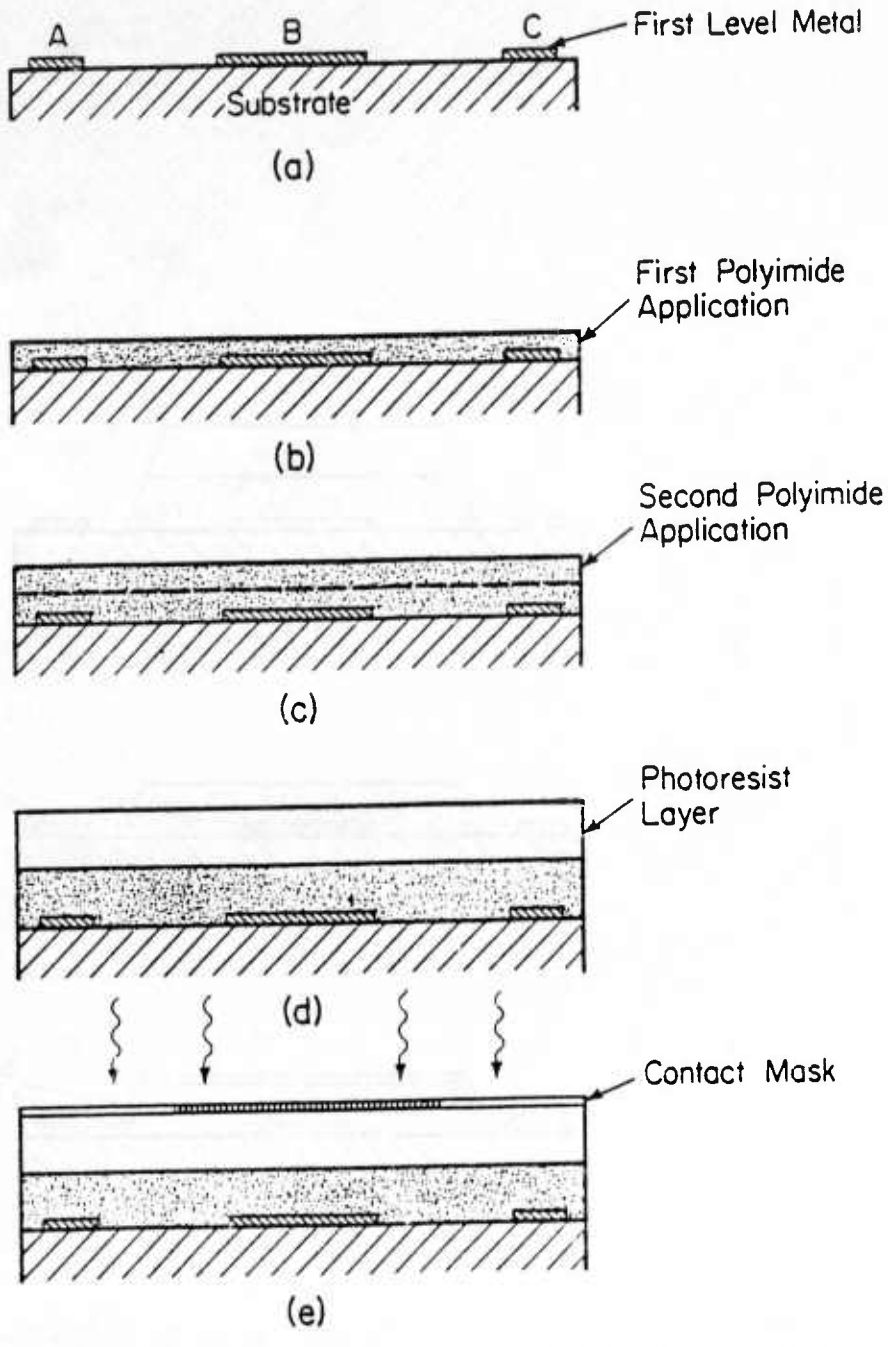

Figure 15a. Process sequence for electrical connection between points A and C without connection to point B.
a. Substrate with first-level metalization present.
b. Apply first polyimide coating and soft-bake.
c. Apply second polyimide coating and soft-bake.
d. Apply photoresist and soft-bake.
e. Align and expose.

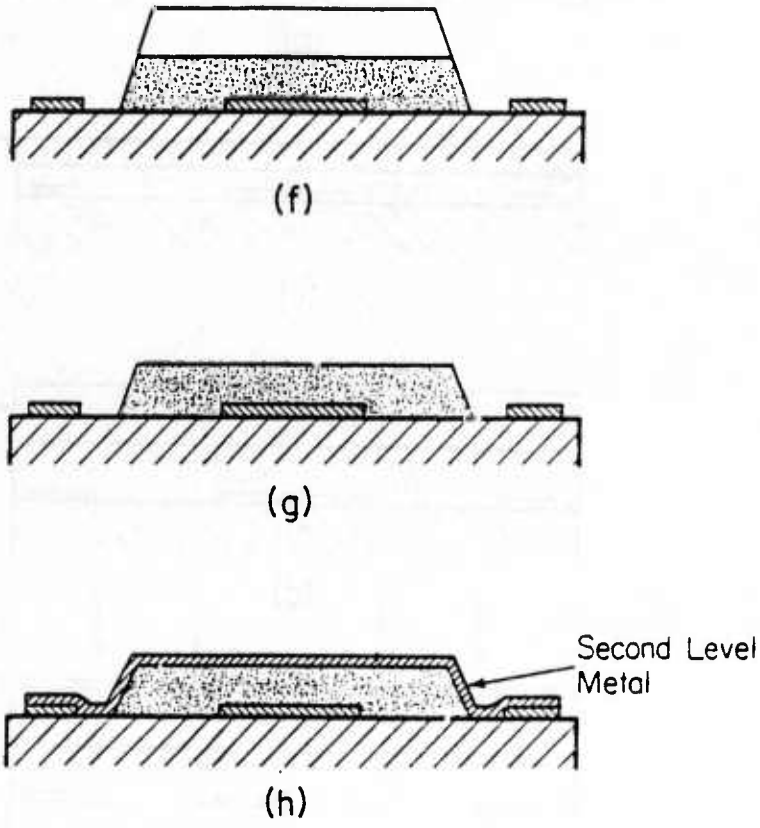

Figure 15b. f. Develop photoresist and pattern underlying polyimide coating.
g. Strip photoresist and cure polyimide coating.
h. Deposit second-level metalization.

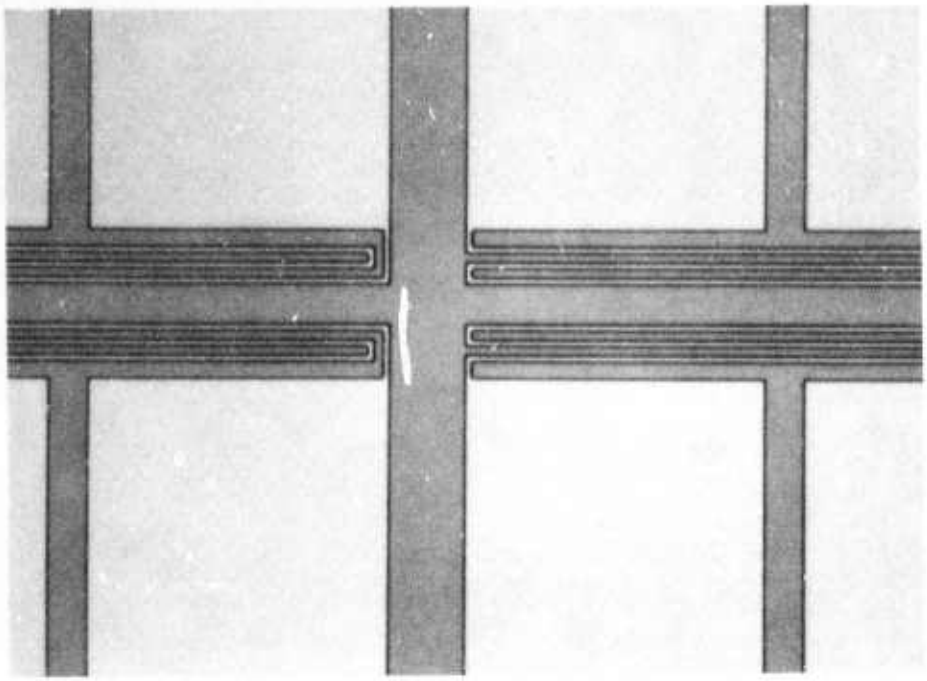

Figure 15c. Pattern resolution obtainable. Dark regions are polyimide.

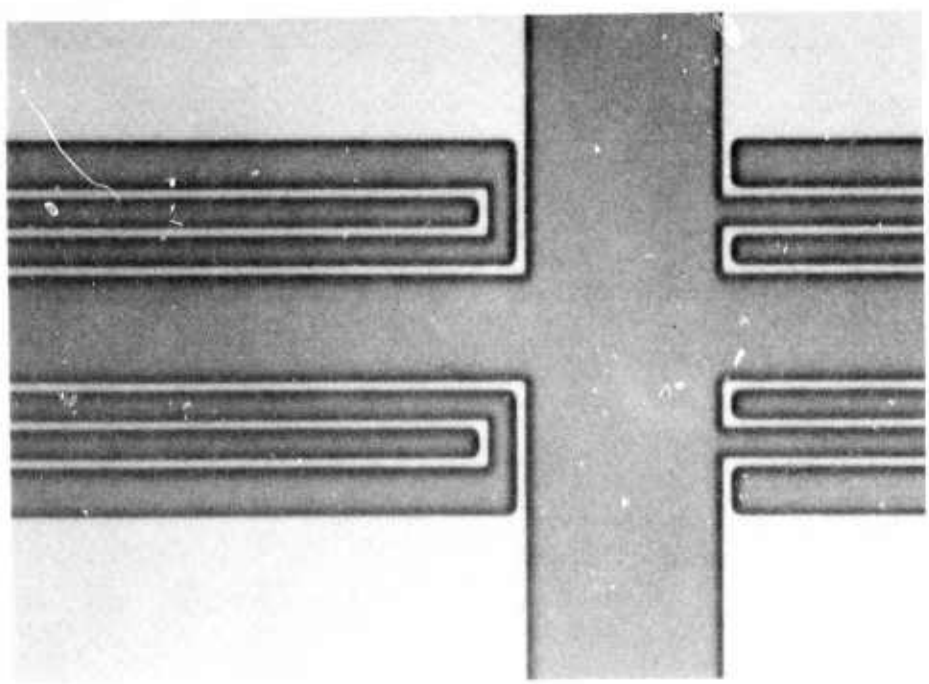

Figure 15d. Pattern resolution obtainable. Dark regions are polyimide.

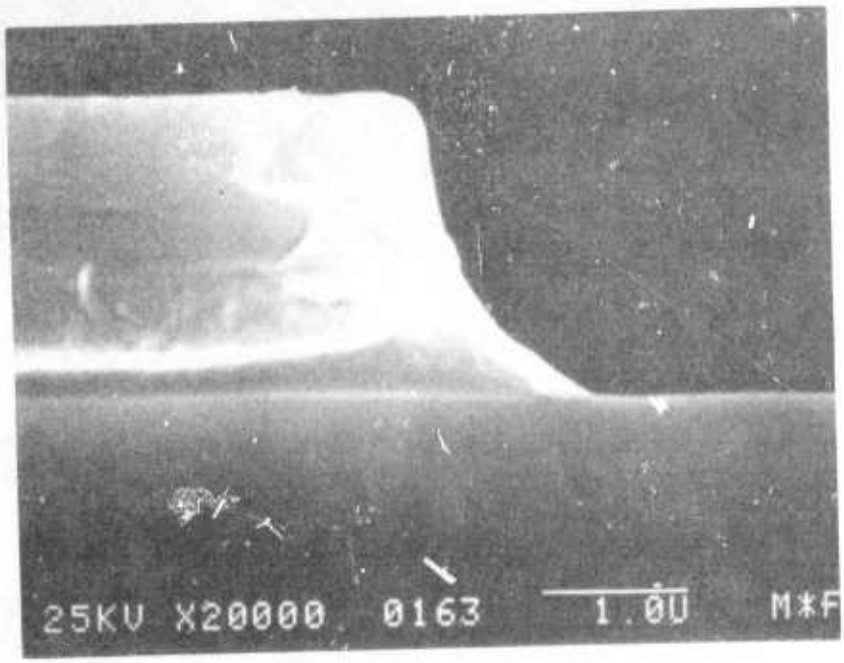

Figure 15e. Cleaved edge profile after pattern definition with photoresist layer unstripped.

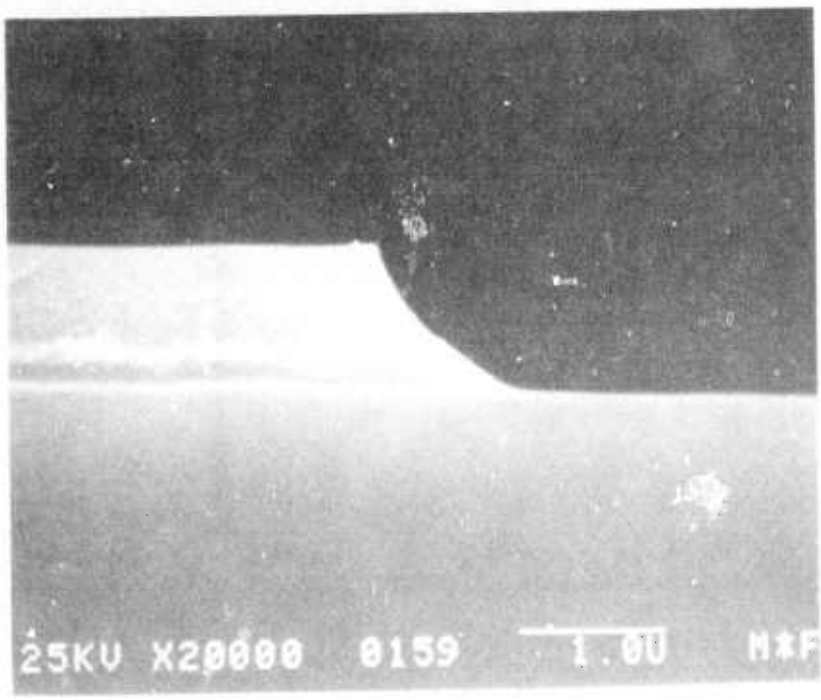

Figure 15f. Cleaved edge profile after pattern definition with photoresist layer stripped.

Table 3

Dissipation factor	0.0143 ± 0.0004 at 1 MHz
Dielectric constant	between 3.9 and 4.2 at 1 MHz
Dielectric breakdown strength	193 ± 60 V/u m DC
Pinhole density	less than 1.17/cm^2
Via resistance	between 2 and 6 ohms

The total area tested for interlevel shorts from pinholes measured 85 mm^2. Crossover arrays are used for this measurement. No shorts were found.

Resistance of vias with contact areas of (100 μm)^2, (50 μm)^2, and (10 μm)^2 is measured. No correlation between via contact area and via resistance is noted. It is believed that only point contact between adjacent metalizations is achieved due to the oxide of the first-level metal. Lower resistance could probably be obtained if the oxide of the first-level metal could be more effectively removed, or if vias are sintered. However, sintering would alloy Schottky barrier features into the GaAs substrate.

A more thorough discussion of the dielectric processing can be found in reference [7].

Conclusion

A low temperature process to pattern polyimide dielectric is achieved. Polyimide has adequate electrical and mechanical properties for interlayer isolation. The fabrication procedure developed is compatible with both photolithographic and process parameter constraints. Improvements in reducing via contact resistance need to be addressed.

5. Deep Implantation Research

Objective

The overall objective of this research is to study the fundamental properties of deep implants into GaAs and explore the basic processing techniques necessary to apply deep implants to GaAs ICs. Work to date has concentrated on one specific form of deep implant into GaAs: the isolation implant. The purpose of this form of implant is to create a disordered layer in the crystal structure, thereby greatly increasing the resistivity of the material. This technique is very useful for providing electrical isolation between active regions on a GaAs substrate.

Studies thus far have been in two areas. The first of t. ese is the development of GaAs compatible processing techniques. In this area, the primary goal has been the development of a photolithographically definable deep implant mask capable of completely stopping the light high energy particles used in isolation implants. The second area of study has been research into the fundamental aspects of deep implants. Here, work is being done on examining the general characteristics of isolation implants both into bare GaAs and through thin films on GaAs. A comparison of these general characteristics will hopefully lead to more effective masking strategies and better device isolation. Since studies in this area will be done using both proton and deuteron implant isolation, comparisons of the basic properties of each of these will also be obtained.

Deep Implant Mask

Several criterion exist which the deep implant mask must meet in order to fulfill both the requirement of complete masking and the needs of specific applications. The mask must be photolithograp'.ically definable, have high resolution and high aspect ratios, be thick enough to completely stop light, high energy particles, and be easily removable. These criterion can not be met using conventional implant masking processes due to the low mass and high energy of the incident ions.

One masking technique capable of achieving these goals which appears particularly promising has been the focus of this investigation. A cross sectional view of this mask appears in Fig. 16. The purpose of each of the layers is as follows:

*** Dielectric Layer: The primary function of this layer is to allow easy removal of the mask after the high energy implant has been performed.

*** Thin Metal: This layer functions as an electrode during the plating of the thick metal layer.

*** Thick Photoresist: This layer confines the plating to specific areas and prevents lateral spreading of the plated metal. It is removed prior to implantation.

*** Thick Metal: This metal stops incident high energy particles, masking the substrate in areas where it is plated.

This mask has been effectively used for protecting areas of thick epitaxial layers on GaAs during proton isolation. Preliminary results are very promising, indicating that masked areas were well protected from the implant.

Isolation Implant Research

Although this work is in the early stages, some preliminary investigations have been performed. Most noteworthy of these has been the investigation of epitaxial layer resistivity change with implant isolation dose for 295 KeV protons. Using a substrate prepared as in Fig. 17, the resistance of the epitaxial layer was measured as the proton dose was incrementally increased. Using measured length and width values for the substrate, these resistance measurements were then used to calculate the sheet resistance of the epitaxial material. The resultant graph of sheet resistance versus proton dose appears in Fig. 18. The inset graph shows the doping profile of the substrate used in this experiment. From this graph, some general conclusions about the properties of proton isolation implants may be drawn. First, the shape of the graph indicates that carrier removal per incident ion drops near zero above a certain value of sheet resistance. In these experiments, this value was found to be approximately 400 megaohms per square. Assuming an epitaxial

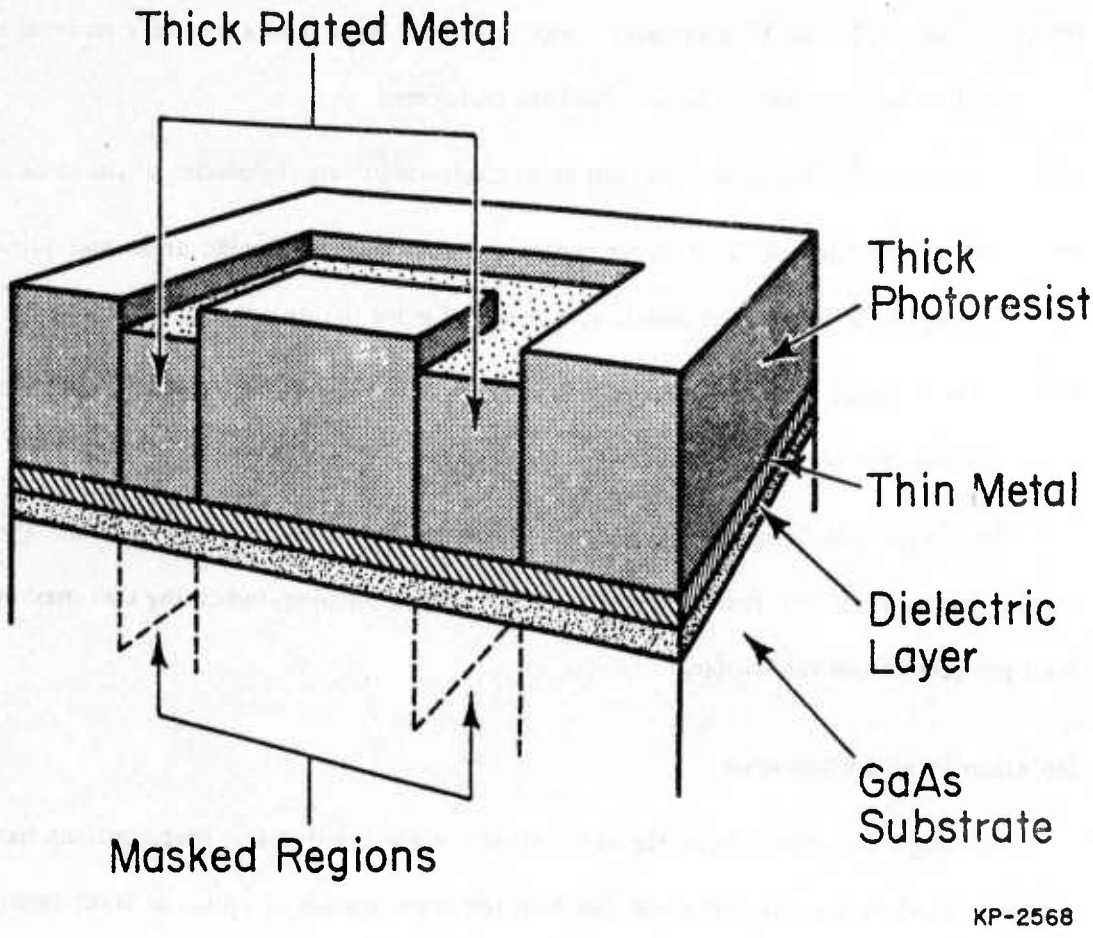

Figure 16. Cross sectional view of high energy implant mask.

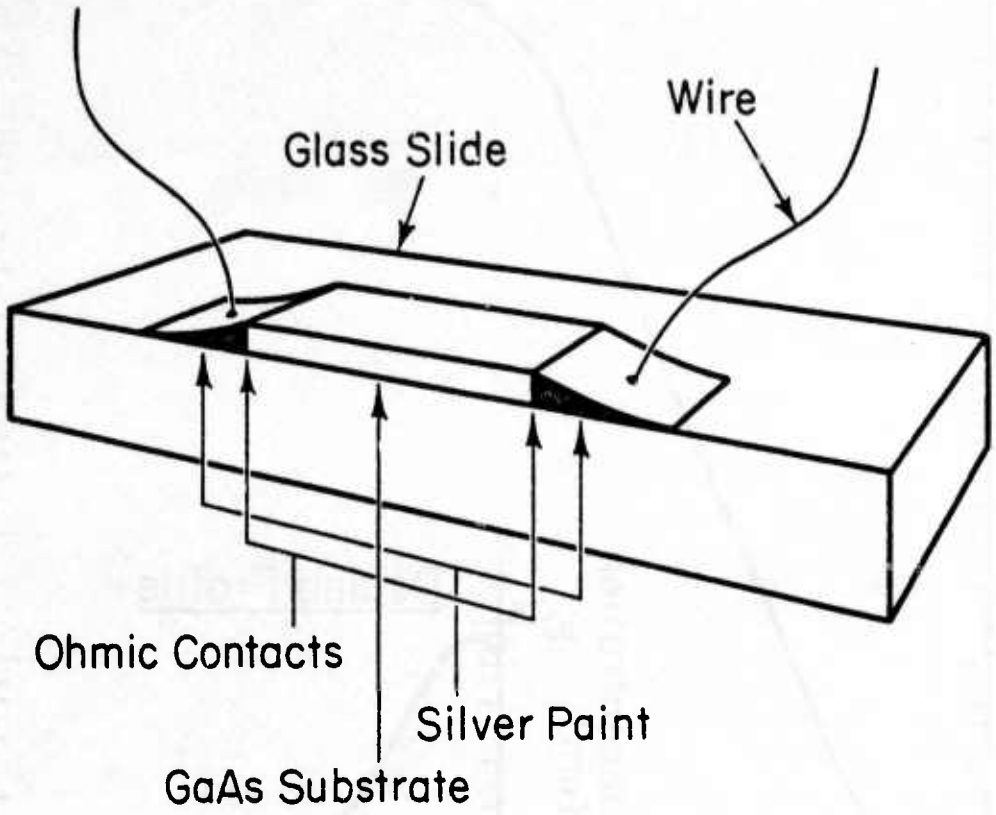

Figure 17. Cross sectional view of substrate prepared for *in-situ* resistivity measurement.

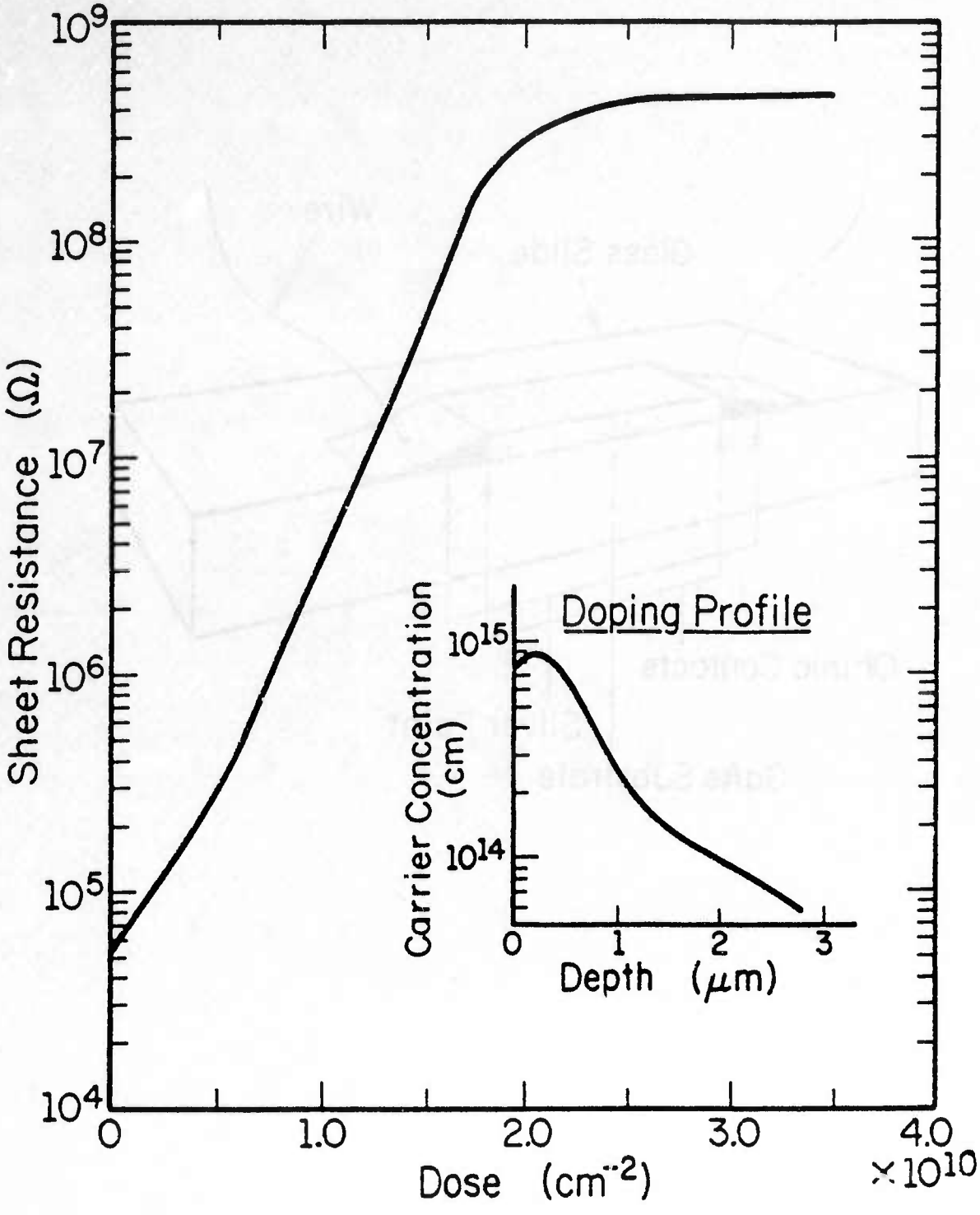

Figure 18. Sheet resistance variation with increasing dose for 295 KeV protons.

layer thickness of 2.75 microns, this corresponds to a material resistivity of 110 kilo-ohm-cm. This value is somewhat lower than values previously reported in the literature. Two effects may be responsible for this. The first effect is bulk conduction through the substrate. This effect becomes important as the material resistivity of the proton bombarded epitaxial layer approaches the resistivity of the semi-insulating substrate. the second effect, surface leakage, also produces a shunt path across the epitaxial layer. Once again, this will place an upper limit on measurable material resistivity.

Another useful result which may be extracted from this data set is the average carrier removal per incident proton. This number is not intended to serve as a tool whereby exact dosages tc isolate epitaxial layers can be calculated, since carrier removal has been found by previous researchers to vary with depth. Rather, it allows one to get a macroscopic view of the carrier removal process. To do the calculation, sheet resistance is first converted into n_s, the average free carrier concentration per cm^2, using the relationship $n_s = (q\mu R_s)^{-1}$. As increasing doses are applied to the substrate, n_s decreases. The change in free carrier concentration divided by the change in dose, $\Delta n_s/\Delta dose$, yields the approximate average carrier removal per proton. In the calculation, mobility is assumed to be constant. This assumption should be fairly valid since mobility is determined by impurity concentration, and this does not change significantly for the proton doses used in the experiment. If mobility does change to a non-trivial degree, the numbers calculated for carrier removal will be somewhat higher. For the data set presented in Fig. 18, the initial value of carrier removal at low doses was found to be 4.3 carriers/proton. At higher doses, this value declined significantly. This value is very likely to be low since the range of protons in GaAs is greater than the thickness of the epitaxial layer used in this experiment. Hence, not all of the protons take place in the carrier removal process. In a similar experiment performed on epitaxial layers having a thickness greater than the range of protons in GaAs, average carrier removal rate was found to vary from 10.4 at low doses to 0.14 carriers/proton at higher doses. This data is presented in Table 4.

Table 4
Carrier Removal per Proton for 295 KeV Isolation Implant
of a Thick Epitaxial Layer on GaAs

Sheet Resistance (ohms/square)	n_s (cm^{-2})	Proton Dose cm^{-2}	$\Delta n_s/\Delta$dose
2.75 k	3.79 E 11	0	0
3.21 k	3.25 E 11	5.2 E 9	10.38
3.66 k	2.85 E 11	10.4 E 9	7.69
4.28 k	2.43 E 11	15.6 E 9	8.08
5.49 k	1.90 E 11	2.60 E 10	5.1
8.31 k	1.25 E 11	7.60 E 10	1.3
9.38 k	1.11 E 11	12.8 E 10	0.27
10.69 k	9 74 E 10	23.0 E 10	0.14

A final conclusion which may be drawn from the evidence to date is that isolation also occurs near the surface of the epitaxial layer. This conclusion is based on the observation that fairly high isolation sheet resistances are obtained in spite of doping near the surface. If isolation were not occuring near the surface, much lower sheet resistances would be anticipated. Because isolation is theorized to result from protons inducing disorder in the crystal lattice, and because this disorder is usually induced near the end of an individual proton's range, isolation near the surface appears at first to be an anomaly if one assumes a simple gaussian model for the distribution of protons on GaAs. The work to be described next offers one explanation of this.

Future work in this area will study deuterium isolation and will involve in situ monitoring of the change in doping profile. This work should provide sufficient data to more accurately calculate the carrier removal per ion and analyze the carrier removal versus depth. Previous research[15] indicates that resistivity for deuterium may increase to a plateau and then actually decrease somewhat as the mechanism of hopping conduction begins to manifest itself.

A second investigation which has yielded valuable data studies the physical distribution of implanted protons and deuterons in GaAs. In this study, bare GaAs is bombarded with one of the above ions at an energy of 100, 200, or 295 KeV and a dose of 2×10^{15} ions/cm^2. Next, using secondary ion mass spectrometry (SIMS), the density distribution of the implanted species is observed. This is easily done for deuterium, but cannot be as easily accomplished for hydrogen due

to a high background level present in the SIMS unit used for these analyses. Hence, the exact shape of the hydrogen profile has not been determined, but a peak was observable to give a rough estimate of the range. Experimental range data obtained from these measurements appears in Table 5. Note that the range of 295 KeV deuterium is very close to that of 295 KeV hydrogen. An example of the distribution for a 295 KeV deuterium implant is shown in Fig. 19. (Distributions for implants at 100 and 200 KeV are very similar to this in shape, but shallower in depth.) Given the assumption that the shape of the hydrogen profile is similar to that of deuterium, an insight is gained into the ability of a single energy implant to isolate near the surface. In examining the profile, it is revealed that the portion of the implant near the substrate surface deviates from the simple gaussian predicted by first order theory. It is believed that the presence of this 'tail' accounts for isolation in the surface region. This will be verified in future studies.

In a related experiment, implants are done through thin surface layers on GaAs. This allows prediction of the effectiveness of these materials as components of isolation masks. By discovering the degree to which these materials attenuate incident ion energy, implant parameters may be optimized for a given mask design. To date, the range of penetration of 295 KeV deuterons into GaAs through thin layers of polyimide has been studied. Here, it has been found that polyimide attenuates deuteron energy by roughly 120 KeV per micron of polyimide thickness. A summary of currently available range data is given in Table 5.

Conclusion

One procedure for masking selected areas of a GaAs substrate during high energy implants has been developed and shown to be effective.

Using ohmic contacts made on the cleaved edge of an epitaxial layer substrate, sheet resistance changes with 295 KeV proton dose variation have been measured. The approximate value of material resistivity obtained with proton bombardment was found to be 110 kilo-ohm-cm. Because this value is fairly high, it is reasonable to assume that the entire epitaxial layer has been isolated.

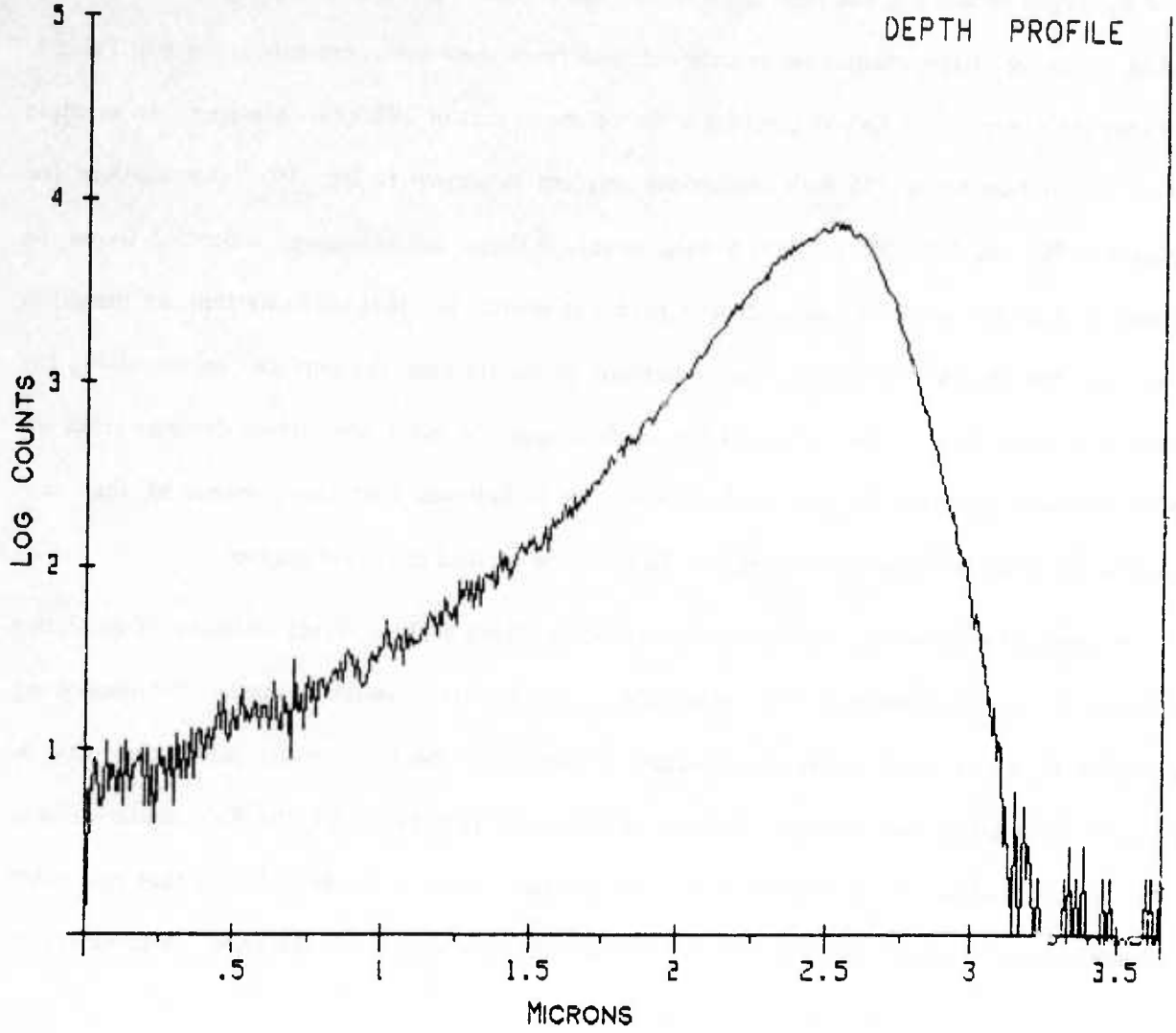

Figure 19. Distribution of 295 KeV deuterium in bare [100] cut GaAs.

Table 5

Range of Protons and Deuterons in Bare GaAs
and Through Thin Surface Films on GaAs

	100 KeV	200 KeV	295 KeV
Proton Range in Bare GaAs	---	---	2.51
Deuteron Range in Bare GaAs	0.99	1.75	2.50
Deuteron Range in GaAs Through 1/2 micron of Polyimide	---	---	2.0
Deuteron Range in GaAs Through 1 micron of Polyimide	---	---	1.45

* All Values in table are in microns *

An approximate value for average carrier removal per proton at low doses was found to be 7-10 carriers/proton for a thick epitaxial layer doped at 10^{15} cm^{-3}

Initial studies of proton and deuteron distribution in GaAs as a result of ion implantation at energies of 100, 200, and 295 KeV have been performed. These studies have suggested an explanation for the observed surface region isolation in spite of large ion range.

Studies of deuterium bombardment through surface films have demonstrated that a 295 KeV deuteron implant is attenuated by approximately 120 KeV per micron of PI-2555 polyimide.

6. Schottky Barrier Leakage Research

Objective

The objective of this research is to investigate the factors which influence reverse bias leakage current in GaAs Schottky barrier junctions. This work is accomplished by studying the effect of diode edge guarding, barrier metal type, and process temperature on leakage current behavior.

Experimental Work

A Schottky barrier diode array photomask is designed to permit the fabrication of diodes with several sizes of active area. The mask is designed so that half of the diodes are constructed with a polyimide guard ring to reduce edge leakage, while the other half are unguarded.

Diode arrays are fabricated with different barrier metal types using standard GaAs compatible lift off processes for both the ohmic contact and Schottky level pattern steps. The photoresist developer used in this process automatically strips the surface oxide in the diode active area before metallization occurs so that the undesirable effects of surface oxide are minimized. After all photolithography is completed, the diode arrays are diced into small groups, subjected to well controlled heat treatment (annealing) using a nitrogen ambient in the range of 25°C - 275°C, and DC probed to obtain Schottky barrier height and reverse leakage current data.

Experimental Results

The effect of polyimide guard rings which reduce edge leakage is shown in Fig. 20 where the reverse leakage current as a function of diode area is plotted for constant reverse bias voltage. The theoretical leakage current obtained using thermionic emission theory with the measured Schottky barrier height is also shown for comparison. This data shows the relative contributions of bulk and edge leakage encountered in typical GaAs Schottky barrier diodes of this size since the leakage current difference between the guarded and unguarded diodes may be presumed to be due to edge leakage. Although the barrier in this experiment is a multi-layer combination of Cr (100 Angstroms) and Cu/Al (1500 Angstroms), the Cr metal determines the diode characteristics

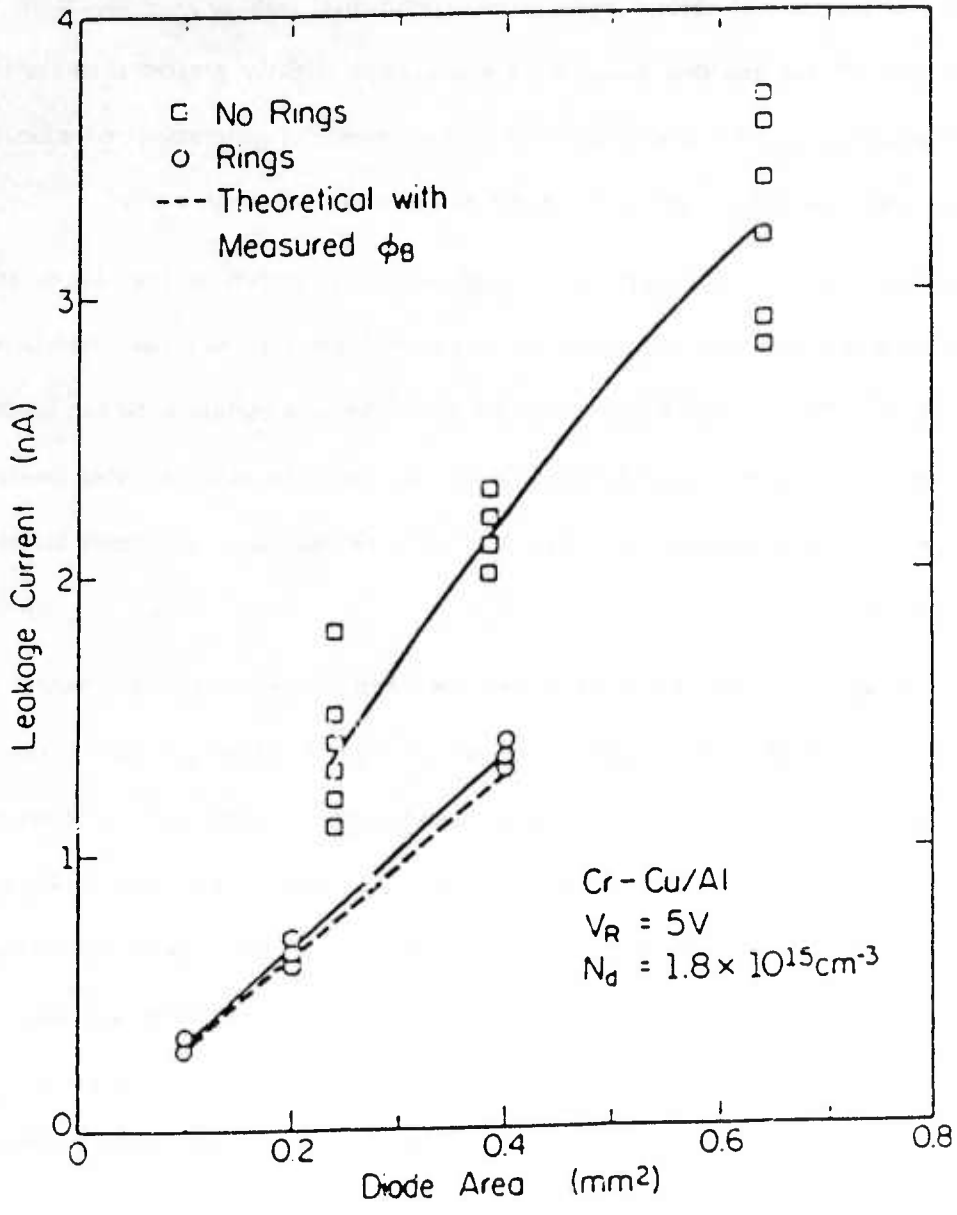

Figure 20. Leakage current versus diode area.

because it is the metal layer which contacts the GaAs surface. The edge leakage component derived from tests like these can vary significantly from one batch of diodes to the next and in some cases it can be an order of magnitude higher than the corresponding bulk value. This variation is believed to be due to varying surface contamination levels which are very process dependent. Although variations in measured Schottky barrier heights are obtained, once the barrier height is experimentally determined, the theory predicts the experimental leakage very accurately as shown in Fig. 20. In general, the guarded diode leakage is always slightly greater than the theoretical prediction. Experiments indicate that this is due to the presense of generation-recombination leakage components which are not accounted for in the barrier leakage theory.

The impact of barrier metal type on leakage current is shown in Fig. 21, where leakage current is plotted as a function of diode area for unguarded, unannealed diodes with barrier metal type as a parameter. Barrier height measurements show that the metals with the lowest leakage currents also have the largest barrier height. Hence, the variation in unannealed leakage current with metal type is directly attributable to the varying work functions (and hence barrier heights) which the metals possess.

Schottky diodes which are subjected to heat treatment can exhibit large changes in leakage current. An example of this phenomenon is shown in Fig. 22 where the leakage current in Al diodes is plotted as a function of reverse bias with annealing temperature as a parameter, for an anneal time of 60 minutes. A leakage current reduction of roughly two orders of magnitude is obtained by annealing the Al diodes at 275°C for one hour. This effect has been observed by other workers[3] and is due to the formation of a thin AlGaAs layer at the metal semiconductor interface which raises the effective barrier height of the junction. The precise effect of annealing is dependent on the particular metal and the temperature. Both leakage current increases and reductions have been observed for various metals.

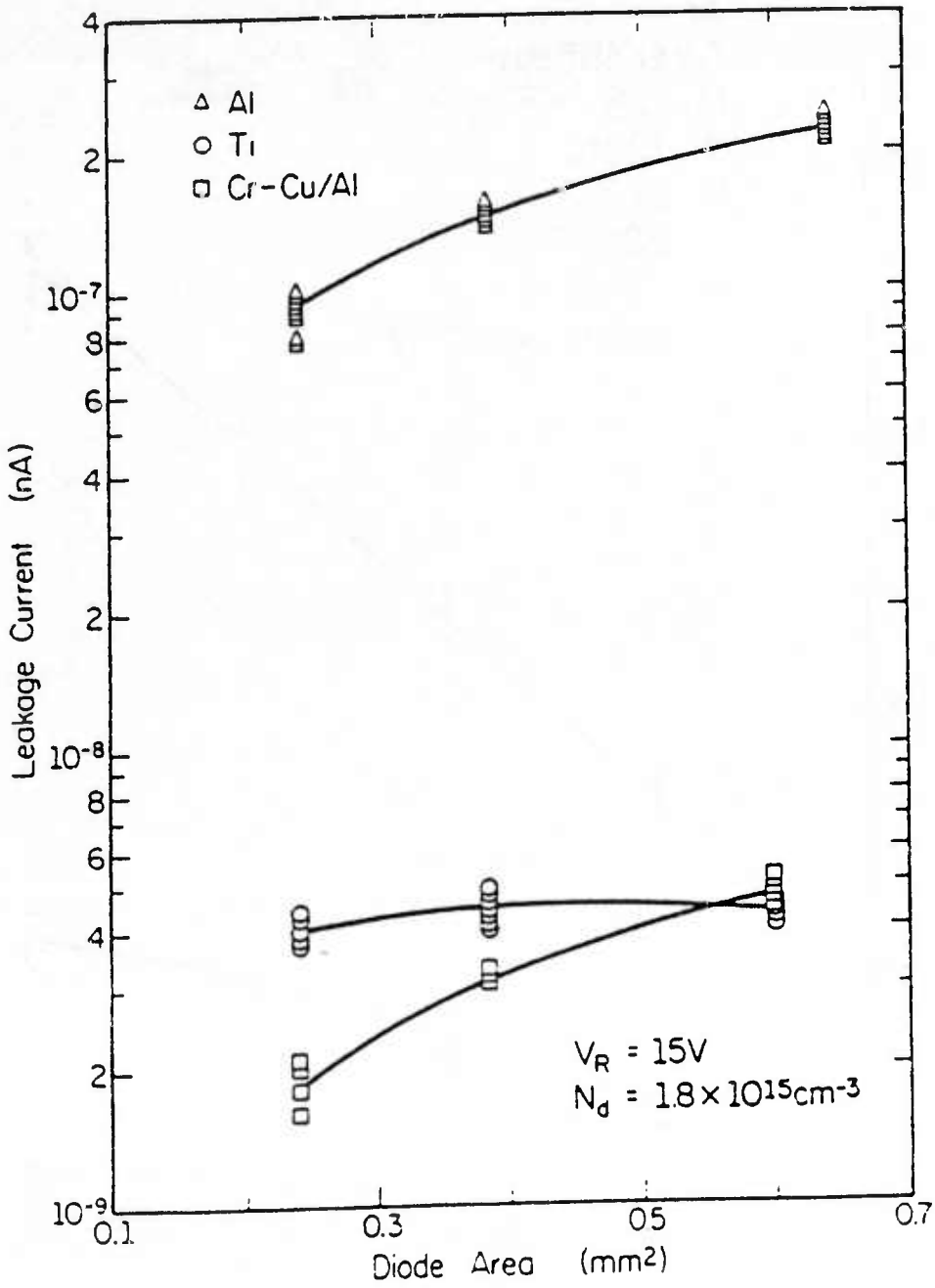

Figure 21. Leakage current versus diode area for three different Schottky metallizations.

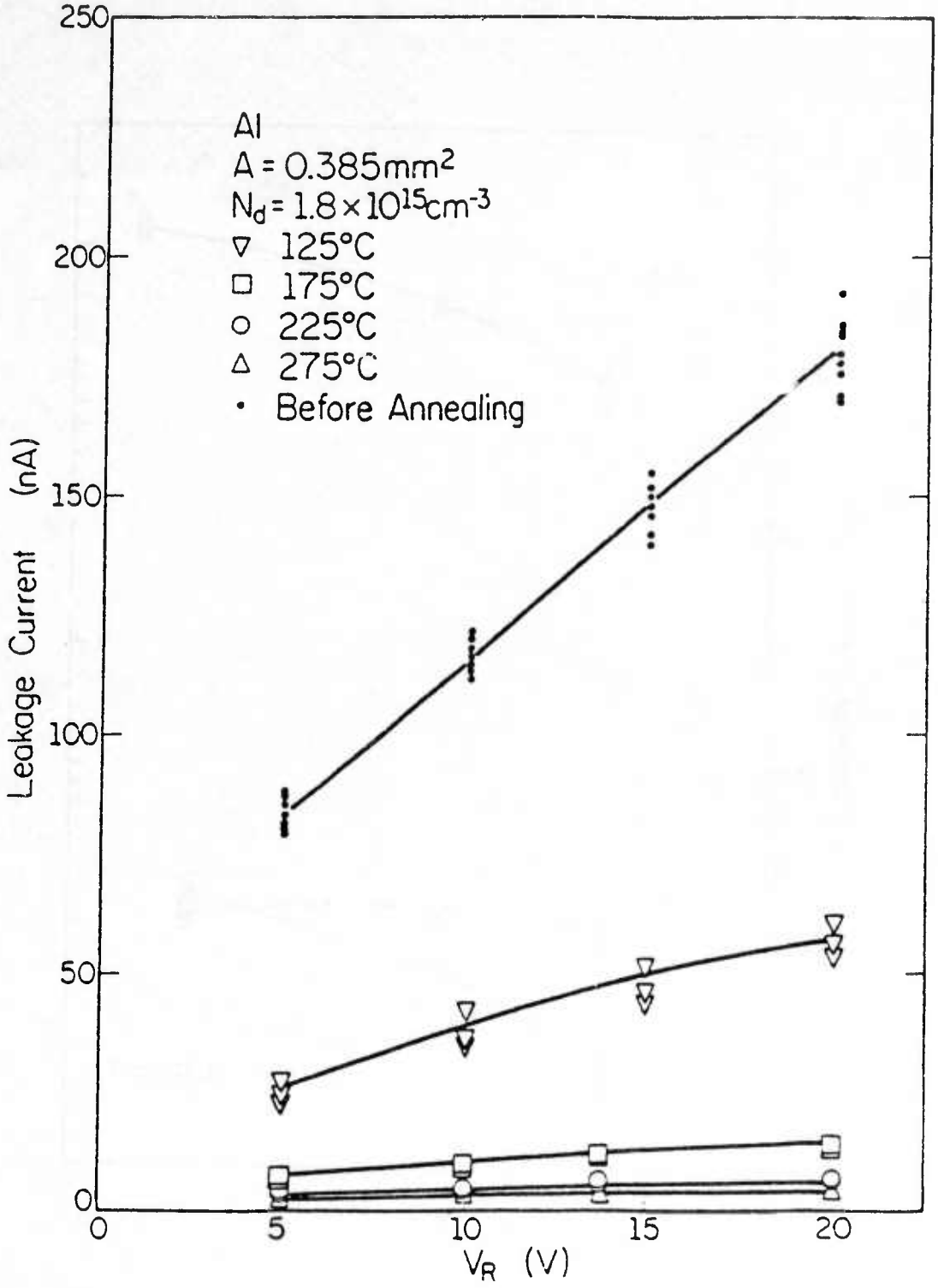

Figure 22. Leakage current versus applied reverse bias voltage for aluminum diodes.

Conclusion

Several important conclusions may be drawn from this leakage current investigation:

* GaAs Schottky barrier junction leakage may be reduced significantly by eliminating the edge leakage component with a polyimide dielectric guard ring.
* Near theoretical leakage current levels can be obtained in properly fabricated guarded diodes.
* Unannealed diode leakage currents can be correlated with Schottky barrier heights and hence metal work functions.
* Leakage current behavior can be significantly altered by relatively low temperature heat treatments.

More extensive details of this study are provided in reference 18.

7a. GaAs SAW Waveguide Research

Objective

The objective of this work is to study SAW generation and propagation in GaAs acoustic waveguides. Part of the work involves gaining more detailed knowledge of losses in basic SAW propagation on GaAs, and energy loss mechanisms in the surface wave transducers. The remainder involves investigation of the use of beam compressors and waveguides to focus and confine modest amounts of total SAW power to achieve large amplitudes in narrow channel acoustic systems. One embodiment to be studied involves an acoustic resonant ring: a waveguide "racetrack" which reuses the acoustic energy for as long as possible.

Theoretical Work

A mathematical model has been derived in order to study losses in SAW transducers having internal reflections. Loss terms dealing with finger resistance and SAW propagation losses have been derived and added to the differential equations of an existing coupled-mode model by Hartmann et al.[9] The solutions to the new differential equations have been used in a computer modeling program.

The program calculates SAW amplitude and electrical drive current as a function of either position in the transducer or frequency. Outputs from this program agree well with experimental data on reflective transducers on ST quartz, YZ $LiNbO_3$, and GaAs.

Our model predicts that finger resistance losses are more serious than propagation loss, even though the internal reflections cause the SAW energy to bounce around inside the transducer longer. This would imply that the metal thickness of transducer fingers should be increased.

Other theoretical work involving waveguide calculations such as mode shapes and velocities uncovers an important detail. The pseudo-SAW has propagation loss which depends strongly on the direction in which the wave is launched[10] (Fig. 23) The loss is minimum exactly along a [110] direction, and increases sharply at small angles up to about 6 degrees away. A waveguide

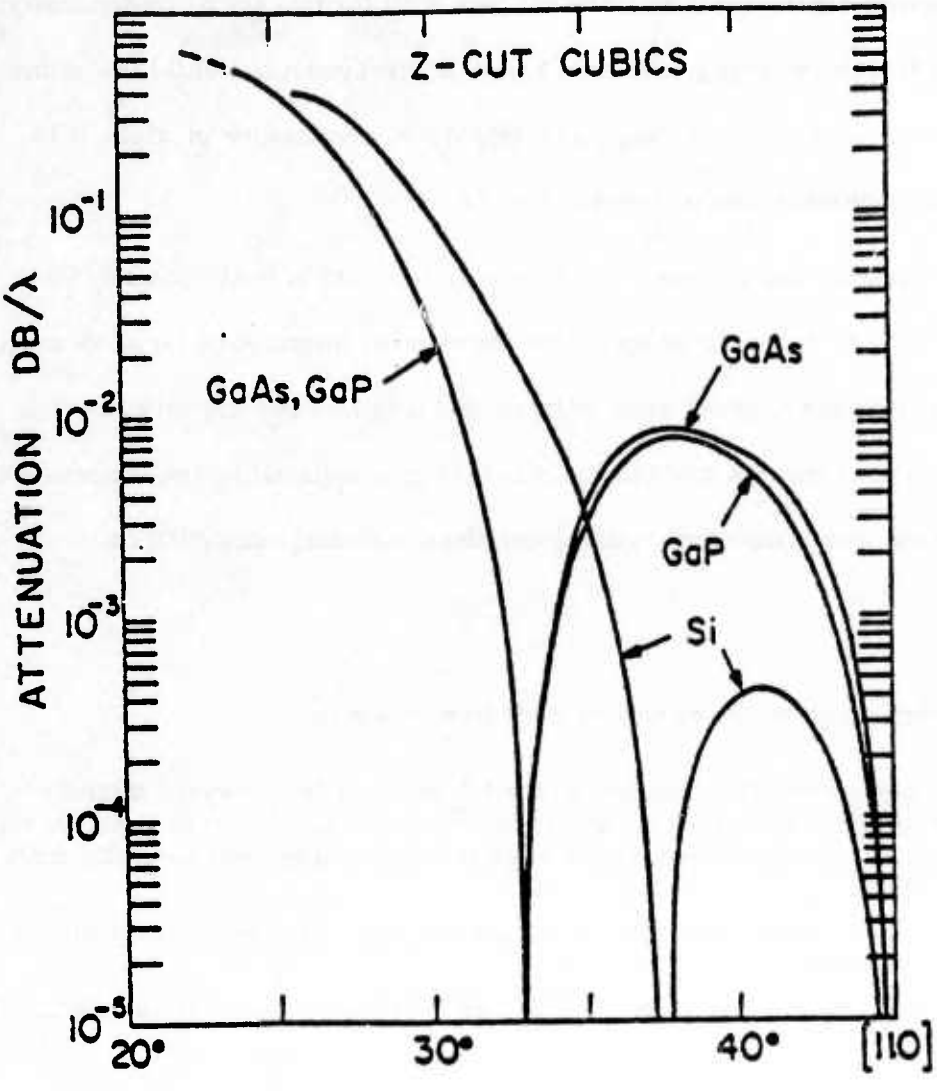

Figure 23. Attenuation of the leaky surface wave for Z-cut Si, GaAs, and GaP, after reference.[10]

mode is equivalent to a set of rays which zigzag along the guide at some angle to the guide axis, and this angle decreases with increasing guide width. Thus, propagation loss should vary inversely with guide width. We have recently verified this experimentally.

Experimental Work

A high-precision automated laser probe has been built for this work. Its demonstrated capabilities include a frequency range greater than 1 GHz, position resolution of 0.1 μm, minimum laser spot size of 2 μm, large dynamic range, and amplitude repeatability of about 0.3%. A block diagram of the laser probe system is shown in Fig. 24.

The probe has been used to measure SAW propagation data in semi-insulating GaAs, which is summarized in Table 6. It should be noted that the material measured so far is not exactly {100} cut, but the more common material whose plate normal is rotated two degrees away from the [100] direction. Some crystal growers need this for growth of good epitaxial layers. These measurements will be repeated for several different crystal orientations, including exact {100} cut.

Conclusion

Several important observations may be made from this data:

1) Unguided propagation loss rises as the 1.5 power of frequency, as observed by Melloch & Wagers.[11] We cannot explain at this time why our observed losses are higher than theirs, but feel our measurement method is more direct and hopefully more accurate than theirs.
2) The velocity dispersion under an aluminum layer is stronger than predicted by Datta and Hunsinger.[12]
3) Guided propagation loss does increase with decreasing guide width, as predicted.

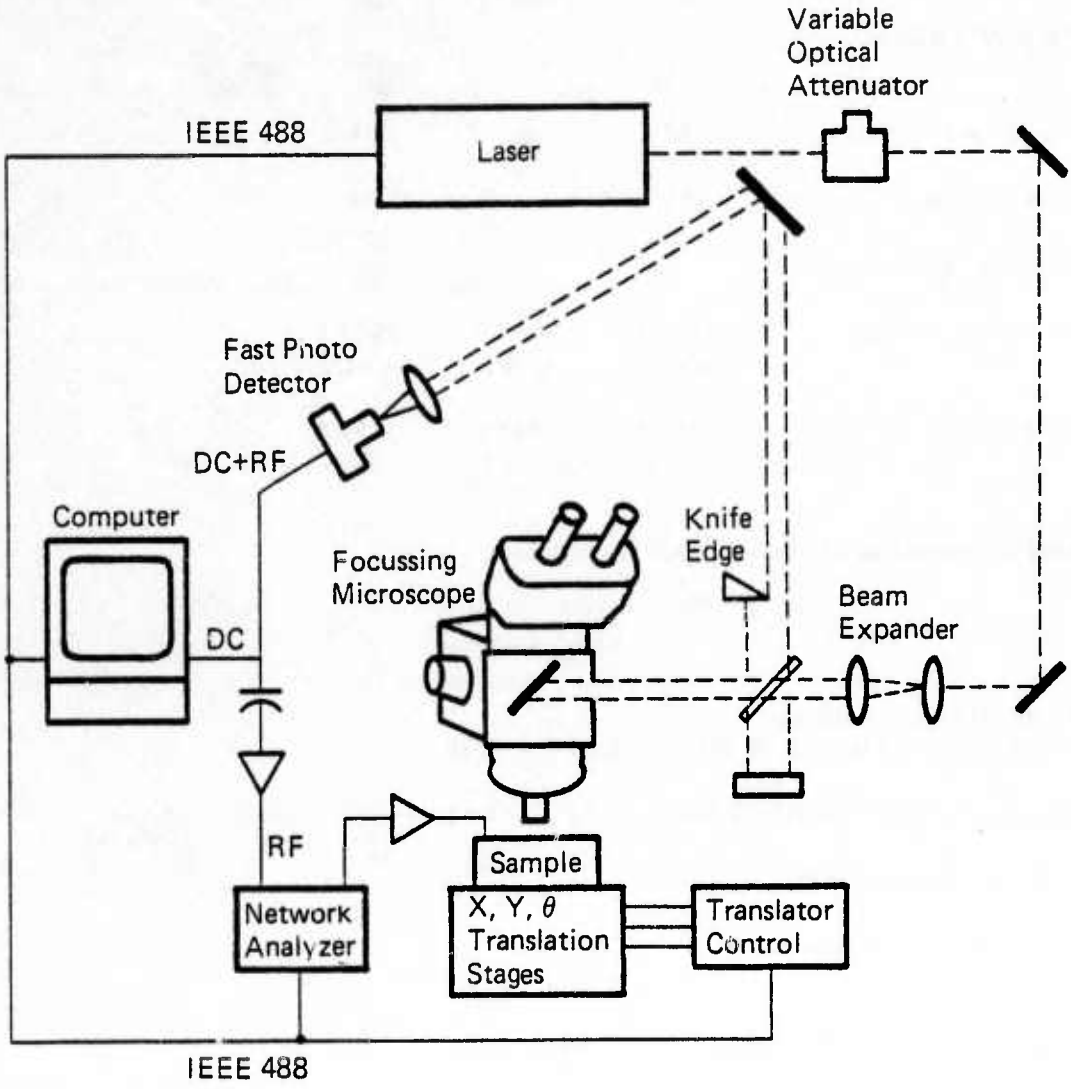

Figure 24. Block diagram of laser probe system.

Table 6.

Measurements of Guided & Unguided SAW Propagation Constants on {100} Cut, [110] Propagating GaAs

I. Unguided Propagation

	360 MHz	720 MHz	1070 MHz
A. Propagation loss, dB/usec			
Metallized surface	.971	3.4	5.28
Free surface	.985	---	5.58
B. Velocity, meters/sec [*]			
Metallized surface	2873.1 +/-0.1	2885.9 +/-0.1	2904.3 +/-4.9
Free surface	2861.5 +/-0.2	2862.9 +/-3.5	2859.8 +/-0.8

II. Guided Propagation (delta-V/V slot waveguide)

	360 MHz	1070 MHz
A. Propagation Loss, dB/usec		
Wide Guide (10 lambda @ 360)	1.59	7.38
Narrow Guide (3 lambda @ 360)	3.04	8.61
B. Velocity, meters/sec [*]		
Wide guide, fundamental symmetric mode	2871.4 +/-0.2	
Narrow guide, fundamental symmetric mode	2884.9 +/-0.4	
Narrow guide, first anti-symmetric mode	2917.0 +/-0.4	

[*] **Note:** The velocity tolerances stated above are preliminary, and are only meant to give some idea of the relative uncertainties of the measurements.

7b. GaAs SAW Propagation Research

Objective

The objective of this research is to investigate the details of SAW propagation in GaAs. This includes the development of models which can be used to predict the propagation of beam profiles through bare GaAs and through metal grating structures. The work will also include the verification of these models by laser probe experiments.

Theoretical Work

A computer program has been developed which uses standard diffraction theory[12] to predict the beam profile propagated a distance specified by the user. This program allows one to use either an experimentally determined slowness surface or one which is theoretically derived. To illustrate, the user enters into the program a laser probe scan taken at position (a) shown in Fig. 25, and this scan is propagated the distance specified by the user according to the selected slowness surface. A comparison between the beam profile measured with the laser probe at position (b) and the profile predicted for position (b) by the diffraction theory program is presented in Fig. 26. For this calculation an isotropic slowness surface was assumed and it is clear from the inaccuracies in the fine structure of the beam profile that the isotropic slowness surface does not closely approximate the GaAs slowness surface. Because no experimental data is available in the literature on the slowness surface of GaAs a method of computing it from laser probe scans was developed. The details of this method are described in a recently completed publication.[13]

Experimental Work

Laser probe measurements were made of a beam propagating away from a bidirectional transducer on a [100]-cut Horizontal Bridgman Cr-doped GaAs substrate and the slowness surface obtained is shown in Figure 27. The velocity and attenuation data obtained, compares favorably with theoretical predictions made by Penunuri[9] and the measured data of Deacon and Heighway which are also presented in Figure 27.

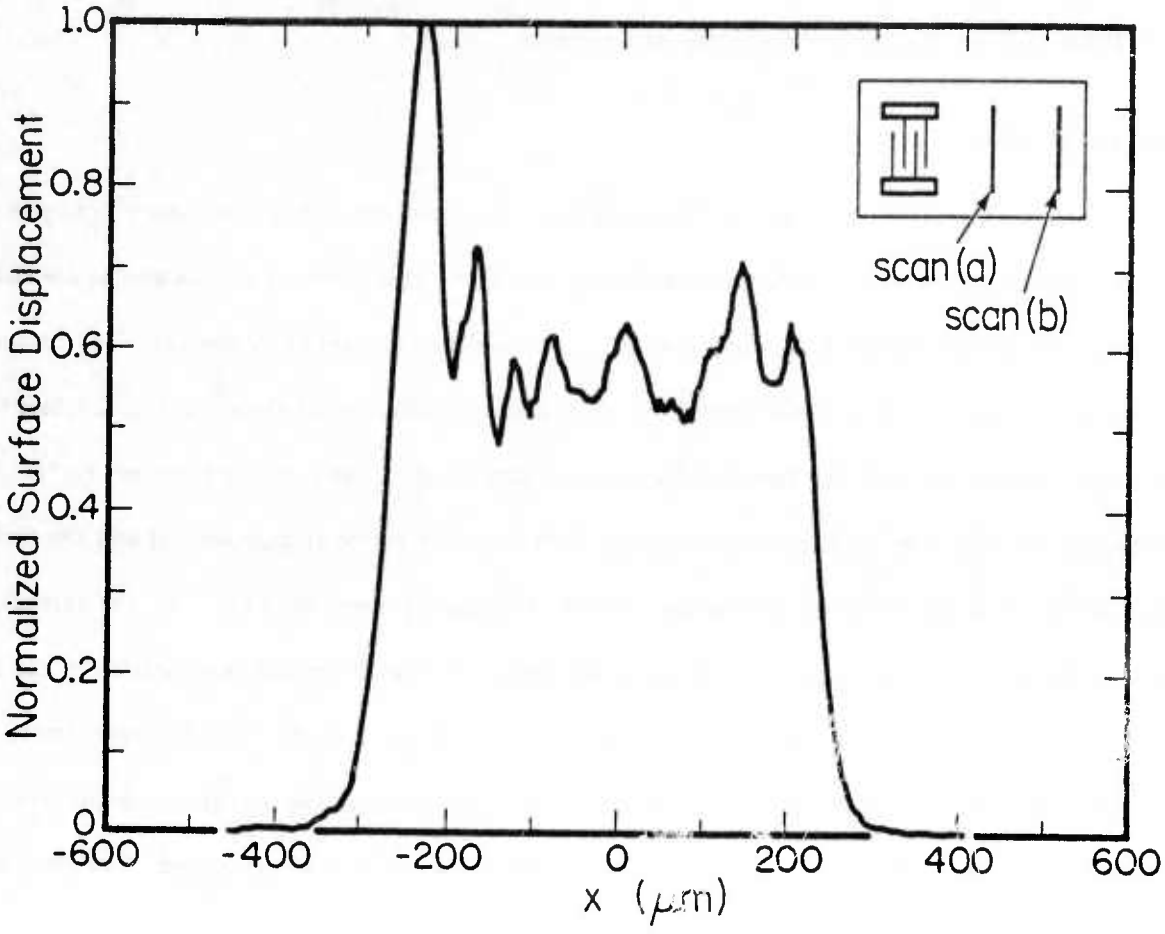

Figure 25. Measured beam profile at position (a).

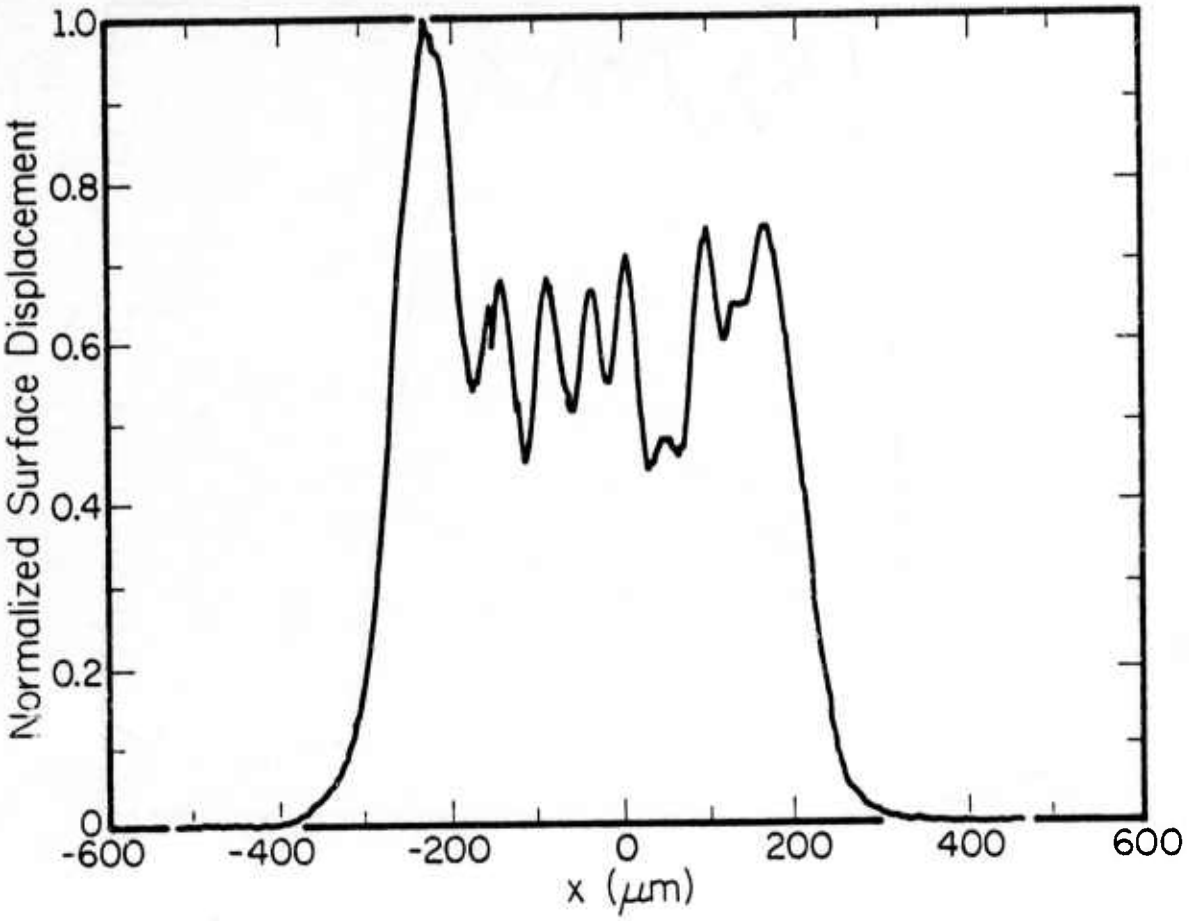

Figure 26(a). Measured beam profile at position (b).

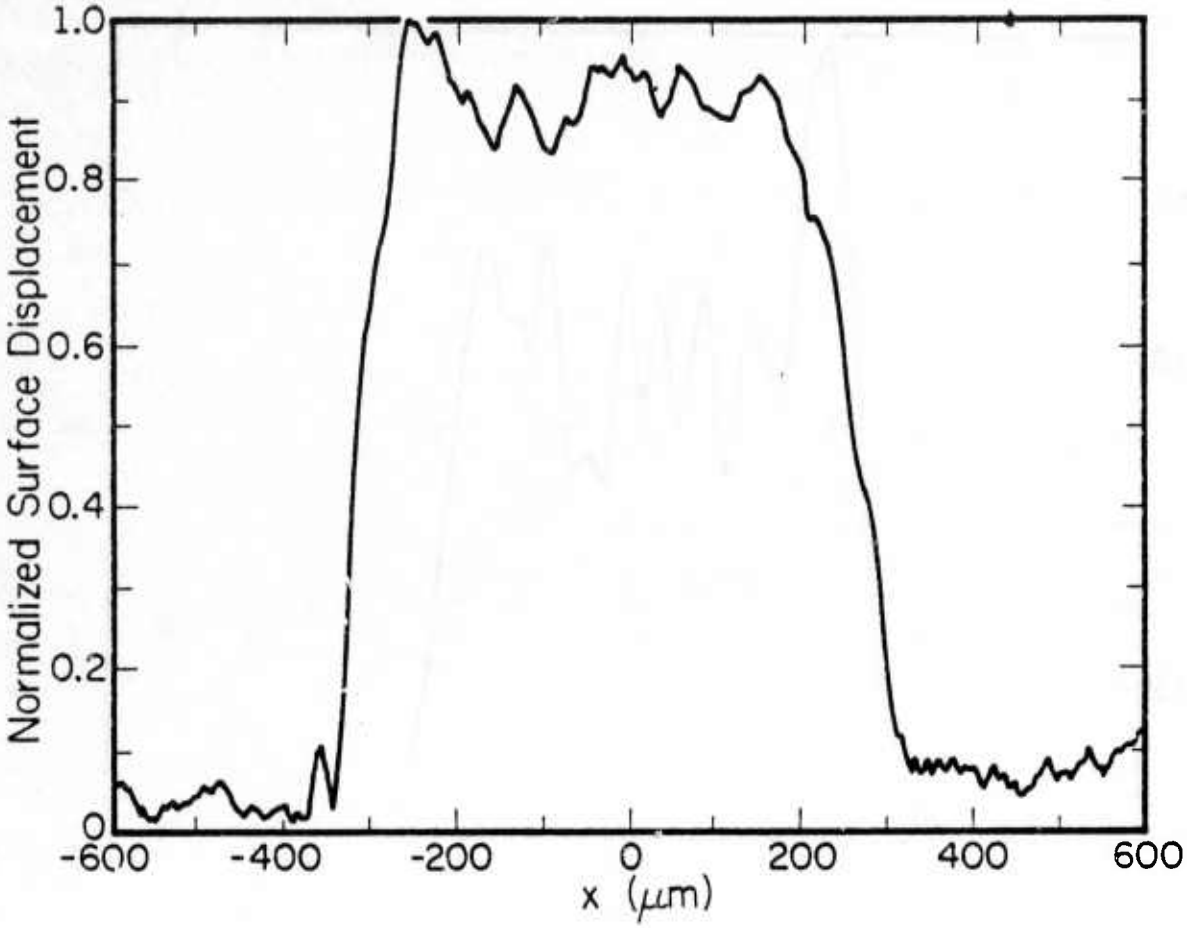

Figure 26(b). Beam profile predicted by computer program at position (b).

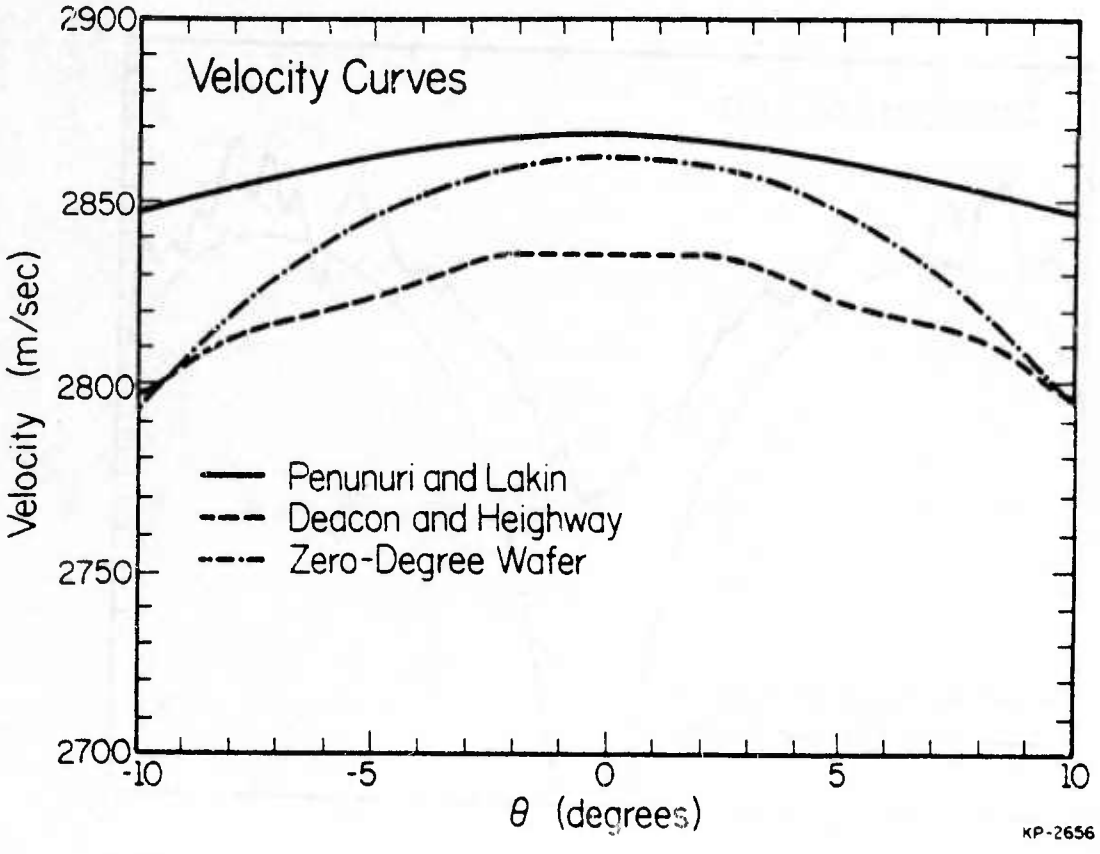

Figure 27. a) Slowness surface - velocity.

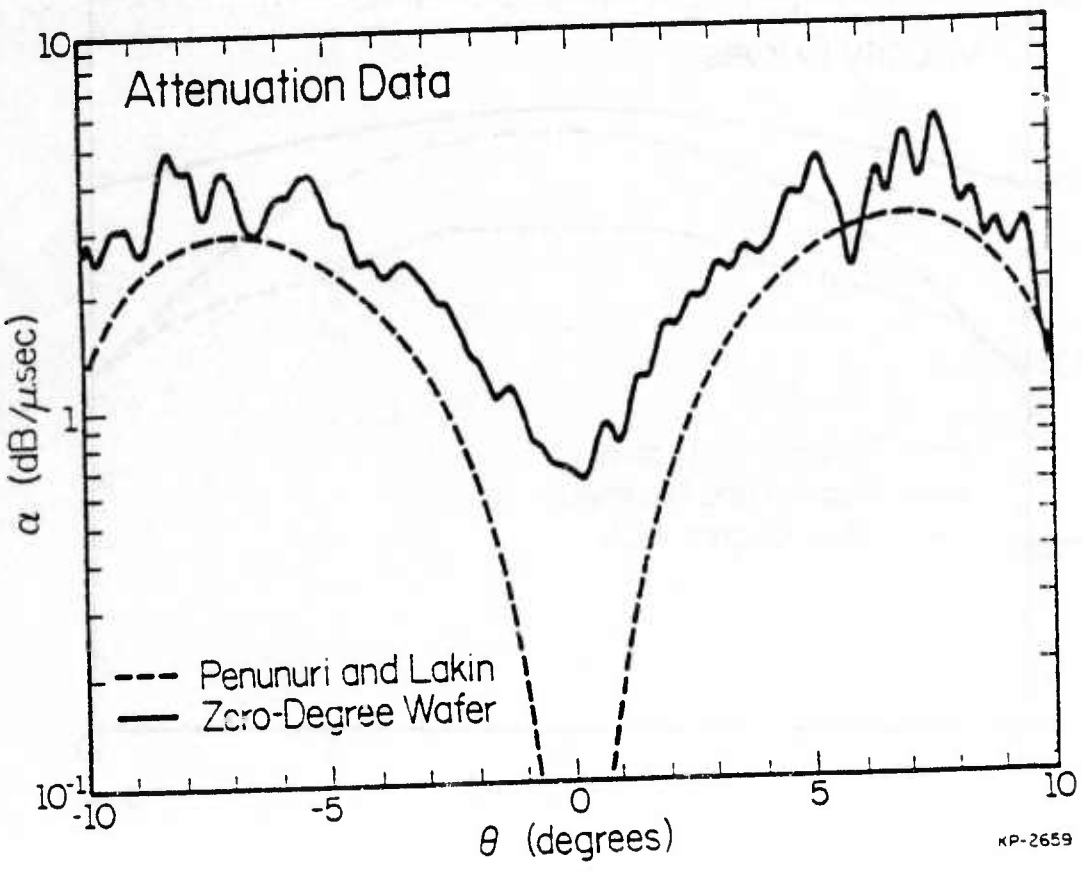

Figure 27. b) Slowness surface - attenuation

This experimentally derived slowness surface has been used in the diffraction theory program and very accurate predictions of both the magnitude and phase of the beam profile have been obtained as can be seen in Figure 28. The preciseness of the beam profile predictions validates the theoretical basis of the diffraction program as well as the accuracy of the slowness surface so calculated. In addition to these measurements, laser probe scans were made for a range of kF drive powers and no appreciable change in beam profile shape was observed. This preliminary work indicates that the diffraction of a beam propagating in unmetallized GaAs does not vary with acoustic power.

Conclusion

A technique for computing the slowness surface of GaAs has been developed and the results compare favorably with the theoretical predictions of Penunuri.[9] The true test of the slowness surface measurement is in its ability to predict the details of beam profile propagation and the slowness surface presented herein yielded very good agreement between the predicted profile and the actual profile. In addition, laser probe scans have been made at a succession of transducer RF drive powers and no appreciable change in beam diffraction is observed.

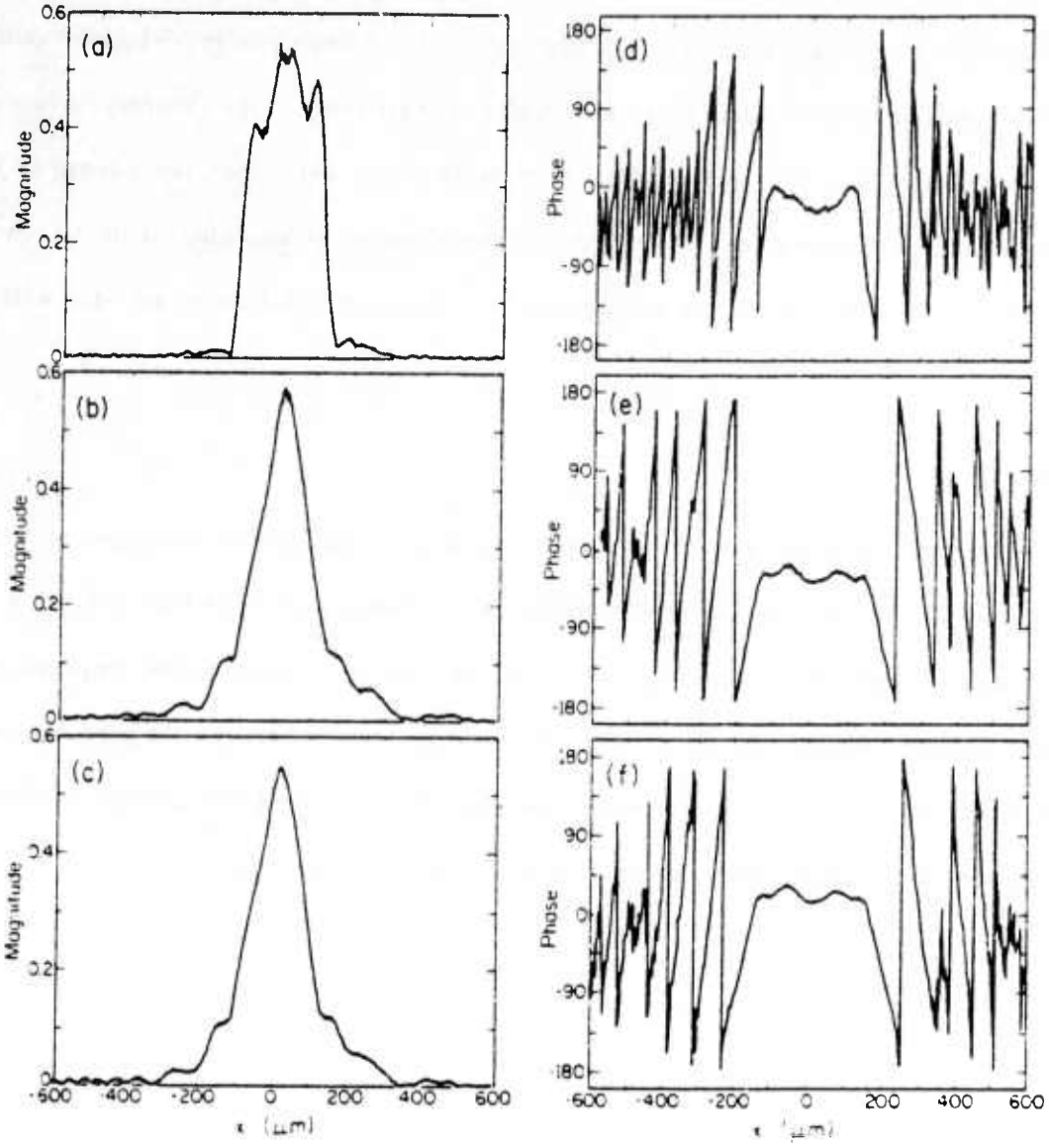

Figure 28. Beam profiles predicted from slowness surface
a) magnitude scan at position (a)
b) magnitude scan at position (b)
c) predicted magnitude scan at position (b)
d) phase scan at position (a)
e) phase scan at position (b)
f) predicted phase scan at position (b)

8. Research Summary

Device Physics and Modeling

A physical model for traveling wave charge injection and a numerical technique for solving this model have been established. Preliminary results are given.

A comprehensive small signal theory describing the frequency response and sensitivity of non-destructive charge sensing electrodes has been developed. The agreement with experimental data is excellent. Future work in this area will focus on a theoretical description of large signal operation.

A general technique for determining the impact of arbitrary static surface boundary conditions on the channel potential in an acoustic charge transport (ACT) device has been developed. Simple one-dimensional models are given for charge storage and transfer inefficiency due to gaps. Charge extraction voltages can be calculated from the empty-channel potentials and examples are given.

Fabrication Technology Research

A fabrication process has been developed for defining polyimide dielectric features using low process temperatures. The electrical characteristics of the resulting dielectric have been evaluated and found to give adequate DC and RF characteristics for GaAs integrated circuit and crossover applications.

An initial investigation of the impact of diode edge guarding. barrier metal type and process temperature on the reverse biased leakage current of Schottky barrier GaAs diodes has been performed. The work indicates that drastic reductions in leakage current may be obtained through proper choice of barrier metal type and process temperature.

A fabrication process for achieving a photolithographically definable high resolution mask which is capable of withstanding high energy particle bombardment has been developed. This basic process has served as the foundation for constructing traveling wave charge transfer device

architectures based on high energy proton isolation. Initial studies of device isolation effectiveness have been completed.

GaAs Surface Acoustic Wave Research

GaAs SAW propagation losses in unguided and guided structures have been accurately measured. The operation of GaAs SAW waveguide structure has been demonstrated. A methodology for determining the slowness surface of GaAs was developed and demonstrated. A computer program was developed to predict the beam profile magnitude and phase as the beam propagates and very accurate results were obtained. Future work in this area will focus on SAW propagation through large electrode arrays and the continued development of GaAs SAW waveguide structures.

9. References

[1] H.L. Stone, "Iterative Solution of Implicit Approximations of Multidimensional Partial Differential Equations," SIAM J. Numer. Anal., Vol. 5, pp. 530-558, Sept. 1968.

[2] S.P. Gaur, "Two-Dimensional Analysis of High-Voltage Power Transistors," IBM J. Res. Develop, p. 306-314, July 1977.

[3] K. Yokoyama, M. Tomizawa, A. Yoshii and T. Sudo, "Semiconductor Device Simulation at NTT," to be published.

[4] M.J. Hoskins, "Acoustic Charge Transport in GaAs," Ph.D. Thesis, University of Illinois, 1983.

[5] C.E. Warren, "Nondestructive Sensing in Buried Channel Traveling Wave Charge Transfer Devices," M.S. Thesis, University of Illinois, 1985.

[6] B.C. Schmukler, "Two-Dimensional Potentials for Buried Channel Charge Transfer Devices including Plate Separation," M.S. Thesis, University of Illinois, 1985.

[7] A.K. Srivastava and B.M. Arora, "Effect of Annealing on the Richardson Constant of Al-GaAs Schottky Diodes," Solid State Electronics, Vol. 24, No. 11, p. 1049, 1981.

[8] C.S. Hartmann, P.V. Wright, R.J. Kansy, E.M. Garber, "An analysis of SAW Interdigitated Transducers with Internal Reflections and the Application to the Design of Single-Phase Unidirectional Transducers," 1982 IEEE Ultrasonics Symposium Proc., IEEE Cat.#82CH1823-4, p. 40.

[9] D. Penunuri, "Some Theoretical Aspects of Surface Acoustic Wave Propagation," Ph.D. Thesis, University of Southern California, 1976.

[10] M.R. Melloch, R.S. Wagers, "Propagation Loss of the Acoustic Pseudosurface Wave on (ZXt) 45-degree GaAs," Appl. Phys. Lett., Vol. 43, No. 11, 1 Dec. 1983, p. 1008.

[11] B.J. Hunsinger, "Research to Provide a Theoretical Determination of Surface Acoustic Wave Velocity and Impedance Differences Between Metal Strips and Free Surface Regions of Metallic Gratings," Final Report RADC-TR-81-173, July 1981.

[12] J.W. Goodman, *Introduction to Fourier Optics*, McGraw-Hill, New York, 1968.

[13] W.D. Hunt, R.L. Miller and B.J. Hunsinger, "Slowness Surface Measurements for Zero and Five Degree [100]-cut GaAs," submitted to *Journal of Applied Physics*.

[14] J.M. Deacon and J. Heighway, "Acoustic-Surface Wave Propagation on Gallium Arsenide," Electronics Letters, Vol. 8, NO. 1, p. 6, 1972.

[15] I.J. Saunders and K. Steeples, "Hydrogen Ion Bombardment of GaAs for Device Isolation," Proc. First International Conf. on Semi-Insulating III-V Materials, Nottingham 1980, ed. by G.J. Rees, Shiva Publishing, Nottingham.

[16] D.. Scharfetter and H.K. Gummel, "Large-Signal Analysis of a Silicon Read Diode Oscillator," IEEE Trans. Electron Devices, Vol. ED-16, no. 1, pp. 64-77, Jan. 1969.

[17] M. Kurata, Numerical Analysis for Semiconductor Devices, D.C. Heath and Co., Lexington, 1982.

[18] J.M. Pryst, "Gallium Arsenide Schottky Barrier Leakage Currents," M.S. Thesis, University of Illinois, 1986.

Appendix A
Solution Method for the Nonlinear Differential Semiconductor Equations

The mathematical description of the injection process is given by equations (A1)-(A3). These three relations are Poisson's equation, the current equation and the continuity for electrons, respectively.

$$\nabla^2\phi = \frac{-q}{\epsilon}\left[N_D^+ - n + N_{SAW}\right] \tag{A1}$$

$$J_n = q\mu_n nE + qD_n\nabla n \tag{A2}$$

$$\frac{\partial n}{\partial t} = \frac{1}{q}\nabla \cdot J_n + G_n - R_n \tag{A3}$$

where
ϕ = electrostatic potential
n = mobile electron density
N_D^+ = ionized donor impurity density
qN_{SAW} = acoustic wave polarization charge density
J_n = electron current density
G_n = electron generation rate
R_n = electron recombination rate
D_n = electron diffusion coefficient
μ_n = electron mobility

All equations and terms involving holes have been excluded from this formulation since the ACT device is a buried channel transport device and minority carriers can be neglected. A further simplification results by dropping the generation-recombination terms which are not considered as fundamental factor in the injection process. Hot electron effects will also not be considered because the fields which act on the carriers are much less than the velocity saturation field for GaAs. For channels which are much wider than one acoustic wavelength a uniform distribution for the potential and carrier concentration can be assumed in the transverse direction. This allows for a two dimensional analysis instead of a three dimensional analysis. the final simplification involves the time variable. Although injection is a time dependent process, its duration is much longer than the relaxation time of the mobile electrons. Therefore with $\partial n/\partial t$ set equal to zero, (A1)-(A3) can be solved at a series of time instants with the assumption that at each time instant a steady state condition prevails. These simplifications allow equations (A1)-(A3) to be written in a reduced form as given in (A4)-(A6)

$$\nabla^2\phi = \frac{-q}{\epsilon}\left[N_D^+ - n + N_{SAW}\right] \tag{A4}$$

$$J_n = q\mu nE + qD_n\nabla n \tag{A5}$$

$$\nabla \cdot J_n = 0 \tag{A6}$$

where $\nabla = \frac{\partial}{\partial x}\hat{x} + \frac{\partial}{\partial y}\hat{y}$

Equations (A4)-(A6) along with appropriate boundary conditions provide the mathematical description of charge injection. The solution is obtained numerically by the finite difference method.

Additional manipulations of these equations are performed prior to discretization in order to insure numerical stability. By assuming $\phi = \psi + \delta$, where ψ is an initial potential and δ is a correction term, (A4) is written as a linear differential equation for δ. This is obtained by replacing n in (A4) by $n_i e^{(q(\psi+\delta-\phi_n)/kT}$ and then expanding the exponential function in a Taylor series with all terms of second and higher order in δ being neglected. n_i and ϕ_n are the intrinsic carrier concentration and the electron quasi fermi level, respectively. A procedure developed by Scharfetter and Gummel[15] is used to rewrite (A5) before substituting it into (A6). This has been shown to be necessary for stability.[17] Lastly, the equations for δ and n are normalized into a dimensionless form. These normalized equations are discretized with finite differences to obtain two systems of equations which together will approximate the potential, ϕ, and the carrier concentration, $\bar{n}$, at a discrete number of grid points throughout the device. These two systems are given in matrix form in (A7) and (A8). The potential ϕ is calculated from δ as shown in (A9).

$$\bar{A}_1\delta = \bar{b}_1 \tag{A7}$$

$$\bar{A}_2\bar{n} = \bar{b}_2 \tag{A8}$$

$$\phi = \psi + \delta \tag{A9}$$

The strongly implicit numerical method of Herber Stone[1] isused to solve (A7) and (A8).

APPENDIX B

NONDESTRUCTIVE SENSING IN BURIED CHANNEL TRAVELLING WAVE CHARGE TRANSFER DEVICES

BY

CHARLES EDWARD WARREN

B. S., University of Illinois, 1984

THESIS

Submitted in partial fulfillment of the requirements
for the degree of Master of Science in Electrical Engineering
in the Graduate College of the
University of Illinois at Urbana-Champaign, 1985

ABSTRACT

A theory is presented for the determination of time and frequency domain responses of sense electrode structures in buried channel travelling wave charge transfer devices for real time analog and digital signal processing. Two fundamental nondestructive sense techniques are described, current sensing and voltage sensing. Analytical and numerical results are derived for the responses of several sense electrode structures. The results obtained are shown to be in agreement with experimental data obtained from a simple voltage sensing structure.

ACKNOWLEDGEMENTS

I wish to thank my advisors Dr. Michael J. Hoskins and Professor Bill J. Hunsinger for their guidance and support throughout the course of my research. The experimental data provided by Dr. Hoskins and Electronics Decisions Incorporated are highly appreciated.

I express thanks to Julie Overholt for her assistance in the preparation of this manuscript. Finally, appreciation is expressed to my parents for their constant interest and support in my education and research.

This work was supported by the United States Air Force under contract number F30602-84-C-0132, and by the Joint Services Electronics Program under contract number N00014-84-C-0149.

1. Introduction

The need for wideband, real time analog and digital signal processing functions has given rise to a variety of semiconductor processors which may be integrated monolithically with passive and active semiconductor devices. A wide variety of signal processing functions may be obtained via the realization of linear and nonlinear operations, including gain, summation, multiplication, and delay. The charge transfer device (CTD) was developed to allow the achievement of analog delay, the most difficult of these functions.

The CTD employs a travelling electrical potential well for the transport of charged carriers through the device. The carrier transport mechanism may be realized in a number of ways, including clocked electrical potential barriers and wells (employed in the charge coupled device (CCD),[1]) or the propagation of a sinusoidal surface acoustic wave (SAW) in a piezoelectric semiconductor (employed in the buried channel travelling wave CTD[2]).

In a surface channel CTD, specifically the surface channel CCD,[3] carriers flow near a material interface formed by a semiconductor and an insulating layer. Metal electrodes placed above the insulator form a metal-insulator-semiconductor (MIS) capacitor. Carriers are transferred via the coupling of the potential wells formed by adjacent capacitors held at time varying potentials. The surface channel CCD suffers from bandwidth limitation due to interaction of the signal charge with traps at the semiconductor insulator interface and because diffusion rather than drift is the charge transport mechanism. Buried channel CTD's[4] overcome this limitation by transporting the carriers not at an interface, but rather by establishing a potential maximum (for electron transport) within the semiconductor so that carriers may be transported in the bulk material. Such devices do not suffer the limitations due to surface effects, and drift fields play a role in charge transport in buried channel CCD's, enabling higher speed operation. However, buried channel devices utilizing non-destructive sensing (NDS) suffer a bandwidth limitation due to the finite spreading of flux lines emanating from the signal charge. In the buried channel travelling wave CTD, the charge is carried in synchronism with a travelling electric field, and diffusion plays no role in the charge transport.

The general problem of non-destructive sensing consists of computing the time and frequency domain responses of a set of sense electrodes to a known charge distribution in the channel. The knowledge of these responses is necessary for the successful design of sense electrode structures in buried channel travelling wave CTD's for the realization of signal processing functions. This thesis presents an analytical method for the computation of these responses. Several NDS electrode structures are analyzed. Analytical expressions for the responses in the simple cases are developed, and numerical computation is employed in the more complex structures. Results of the developed theory are compared with experimental data taken on an NDS electrode structure in a simple charge transfer device.

II. Theory

A. Current Sensing

The structure in Figure 1a depicts a line charge of linear density Q_L carried at a depth d by a travelling wave of wavelength λ_w and frequency f_w beneath infinitely long, perfectly conducting plates A and B separated by a distance g, and connected together by a load of impedance Z. The magnitude of the travelling wave is assumed to be large enough so that the line charge is rigidly carried a constant depth below the surface. The dielectric constant of the infinitely thick material is assumed to be much larger than that of the medium above the surface. For simplicity, the dielectric constant of the upper medium will be taken to be zero. The assumption of zero dielectric constant is equivalent to requiring that no electric flux lines leave the channel, or that no charge can be induced in the surface gap. The zero dielectric constant assumption is valid when the dielectric constant of the channel material is much larger than that of the medium above the gap. The approximation is valid for real travelling wave CTD's since the channel material in those devices is a semiconductor having a high dielectric constant. This assumption permits an analytical computation of the induced charge density on the electrodes for arbitrary gap size g. The electrical center of the induced charge density perfectly tracks the line charge, which flows in the x direction at a constant velocity given by

$$v_w = \lambda_w f_w \tag{1}$$

The line charge velocity v_w is assumed to be much less than the speed of light so that electromagnetic effects may be ignored. As the line charge reaches the region beneath the gap, more and more flux lines terminate on plate B and fewer on plate A. Thereby an image current is established in the surface electrodes, which must be carried by the load Z. The impedance of the load is assumed to be small, so that the channel potential is unperturbed by the voltage drop across the load while the current flows through it. For simplicity, Z is taken to be zero so that plates A and B may be assumed to be at the same potential. The time dependent current per unit channel width $i_o(t)$ and its Fourier transform $I_o(f)$ are the fundamental building blocks for the calculation

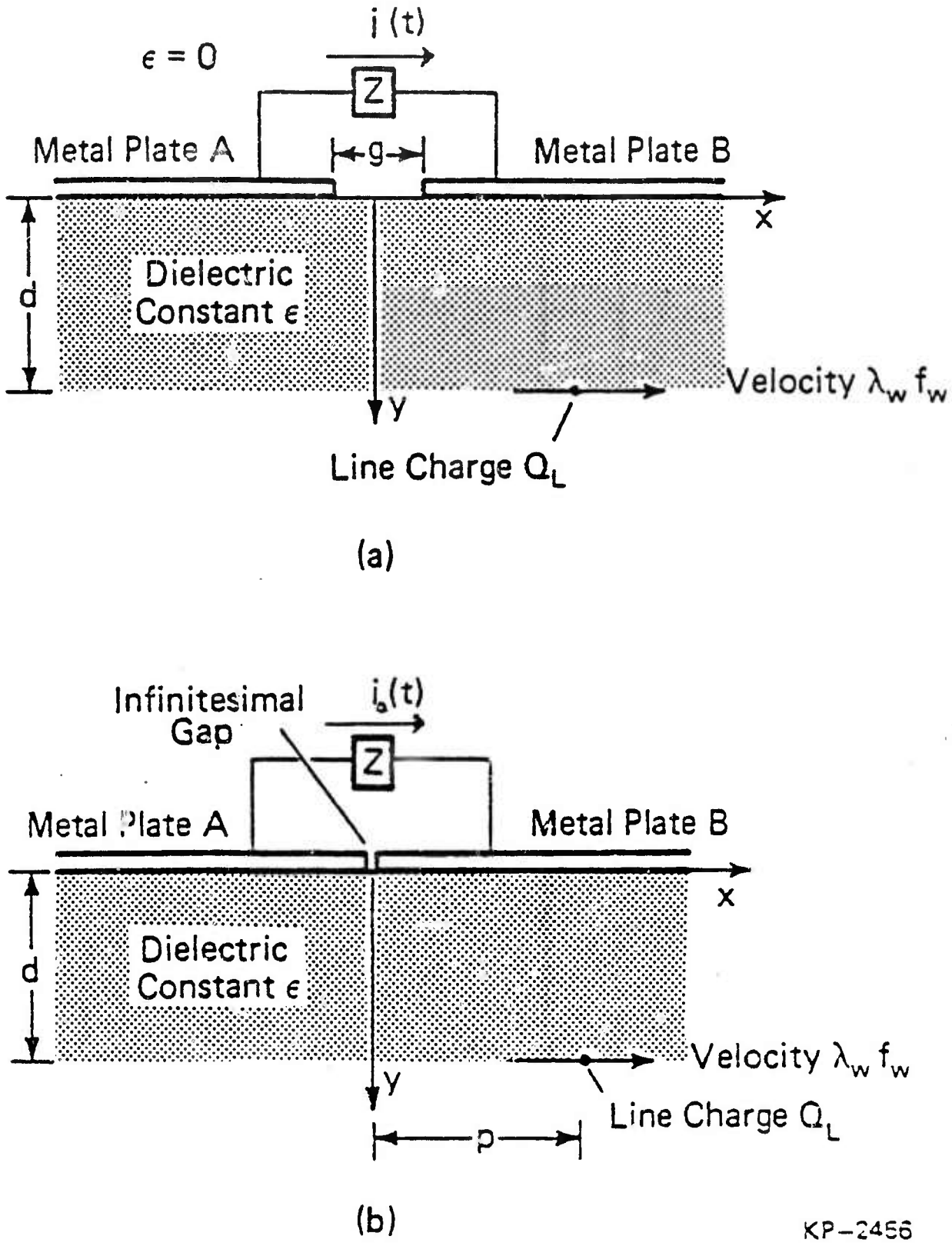

Fig. 1. AC models of simple current sensing structures

(a) Structure with arbitrary size gap between surface plates

(b) Structure with infinitesimal gap.

of non-destructive sense responses.

The solution for finding i(t) begins by solving Poisson's equation

$$\nabla^2\phi = \frac{-\rho(x,y)}{\epsilon} \tag{2}$$

in the channel subject to the boundary conditions

$$\phi = 0 \quad |x| > g/2 \tag{3a}$$

$$\frac{d\phi}{dy} = 0 \quad |x| \leq g/2 \tag{3b}$$

Since the potential is known from the solution of Eq. (2), the normal electric field and the induced charge distribution on the metal electrodes may be calculated. The normal electrical displacement D_y at the surface may be found by taking the normal derivative of the potential evaluated at the surface

$$D_y = -\epsilon \left.\frac{d\phi}{dy}\right|_{y=0} \tag{4}$$

Since the plates are assumed to be perfectly conducting, the induced surface charge density is simply equal to the displacement

$$\rho_{IND}(x,p,d) = -\epsilon \left.\frac{d\phi}{dy}\right|_{y=0} \tag{5}$$

where p is the x coordinate of the line charge.

The total charge per unit channel width on plate B may be found by integrating ρ_s along the entire plate

$$Q(p,d) = \int_{PlateB} \rho_{IND}(x,p,d)dx \tag{6}$$

The current per unit channel width may be found by taking the time derivative of Q(p,d)

$$i_o(t) = \frac{dQ(p,d)}{dt} \tag{7}$$

Since the charge is moving at constant depth, only the lateral position p is a function of time, and $i_o(t)$ may be found by application of the chain rule

$$i_o(t) = \frac{dQ(p,d)}{dp}\,\frac{dp}{dt} \tag{8}$$

The time derivative of position p is the constant velocity of the line charge. Eqs. (1) and (8) may be combined

$$i_o(t) = \lambda_w f_w \left.\frac{dQ(p,d)}{dp}\right|_{p=\lambda_w f_w t} \tag{9}$$

where the origin of time is taken to be when the line charge is directly beneath the center of the gap.

First, consider the special case of the current sensing structure having an infinitesimally small gap, shown in Figure 1b. The problem consists of finding the fields induced by the line charge Q_L a distance d below an infinite continuous conducting plane. Assume the origin to be the point where plates A and B meet. The potential may be found by applying the method of images. The potential below the metal is the same for the structure shown in Figure 2, equal and opposite line charges of magnitude Q_L placed symmetrically a distance d about the plane occupied by the conducting plate, which is taken to be at zero potential. The potential at any point in the channel is given by[5]

$$\phi = \frac{-Q_L}{2\pi\epsilon}\,\ln\,\frac{\left[(y-d)^2 + (x-p)^2\right]^{1/2}}{\left[(y+d)^2 + (x-p)^2\right]^{1/2}} \tag{10}$$

The induced charge density from Eq. (5) is then

$$\rho_{IND}(x,p,d) = \frac{-Q_L d/\pi}{(x-p)^2 + d^2} \tag{11}$$

The total charge on plate B is found by integrating $\rho_{IND}(x,p,d)$ from x=0 to x=∞

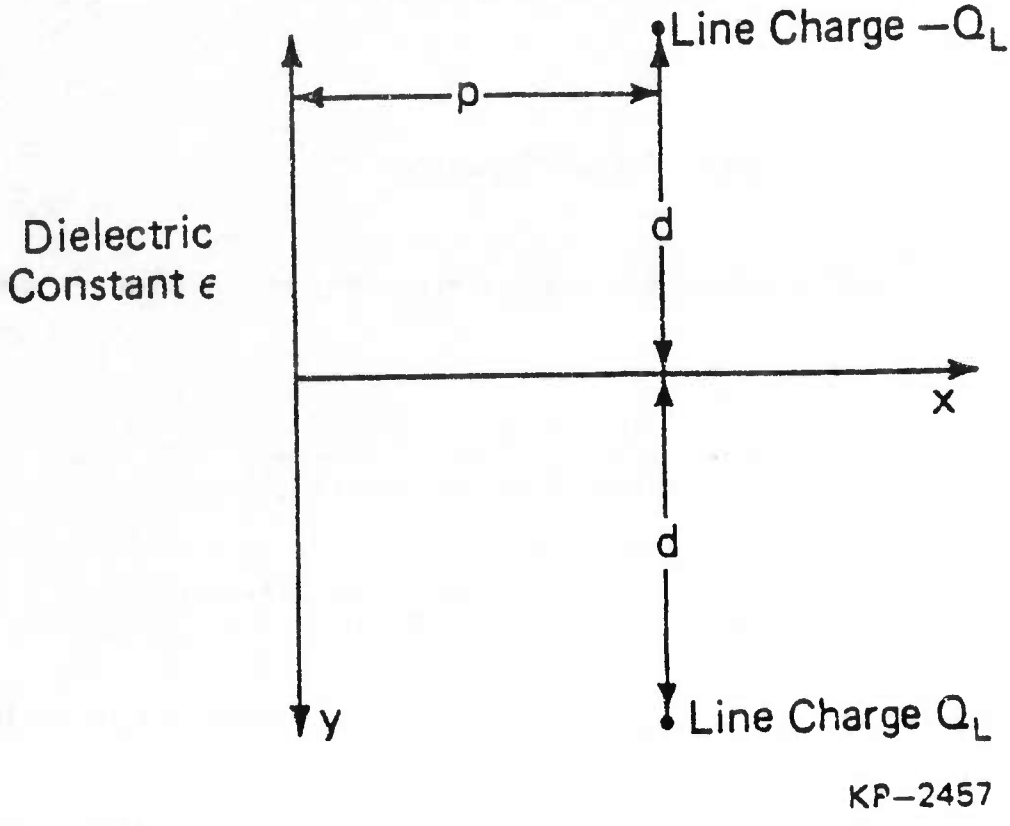

Fig. 2. Set of line charges for calculation of potential in infinitesimal gap structure.

$$Q(p,d) = \frac{-Q_L d}{\pi} \int_0^\infty \frac{1}{(x-p)^2+d^2}\,dx = \frac{Q_L}{\pi}\tan^{-1}(p/d) \tag{12}$$

The current per unit channel width flowing through the load connecting the plates is

$$i_o(t) = \lambda_w f_w \left.\frac{dQ(p,d)}{dp}\right|_{p=\lambda_w f_w t} = \frac{Q_L f_w}{\pi}\,\frac{d}{\lambda_w}\,\frac{1}{\left(\frac{d}{\lambda_w}\right)^2 + \left(\frac{t}{T_w}\right)^2}, \tag{13}$$

where T_w is the period of the travelling wave ($T_w = 1/f_w$). The Fourier transform $I_o(f)$ of the current $i_o(t)$ is

$$I_o(f) = \int_{-\infty}^{\infty} i(t)e^{-j2\pi ft}dt = Q_L\, e^{-2\pi\frac{d}{\lambda_w}\left|\frac{f}{f_w}\right|} \tag{14}$$

The time and frequency domain current sensing responses may be normalized to dimensionless expressions

$$h_{oi}(t) = \frac{i_o(t)}{Q_L f_w} = \frac{1}{\pi}\,\frac{d}{\lambda_w}\,\frac{1}{(t/T_w)^2 + (d/\lambda_w)^2} \tag{15}$$

$$H_{oi}(f) = \frac{I_o(f)}{Q_L} = e^{-2\pi\frac{d}{\lambda_w}\left|\frac{f}{f_w}\right|} = 54.6\,\frac{d}{\lambda_w}\,\frac{f}{f_w}\ \text{dB below DC} \tag{16}$$

$h_{oi}(t)$ is normalized such that its integral over all $\frac{t}{T_w}$ is unity. Graphs of $h_{oi}(t)$ and $H_{oi}(f)$ are shown in Figures 3 and 4, respectively, for $\frac{d}{\lambda_w} = 0.125$, 0.25, and 0.375. The width of the current pulse in the time domain increases with increasing depth of the line charge below the surface, due to the greater spreading of electric flux lines emanating from the line charge and terminating on the surface plates. Similarly, the rolloff in the frequency domain is a linear function of depth.

For the general case of a current sensing structure with a gap of arbitrary size between conducting plates (Figure 1a), the fields may be computed analytically, under the assumption that $\epsilon = 0$ above the channel. The conducting plates A and B are again assumed to be at zero potential.

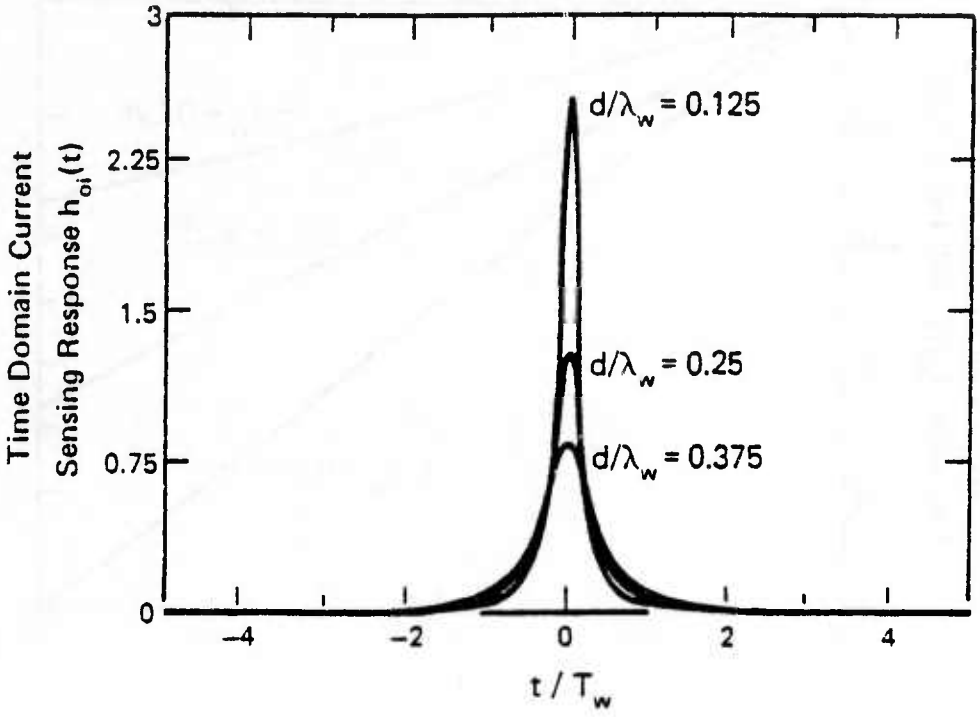

Fig. 3. Normalized time domain current sensing responses for infinitesimal gap structure.

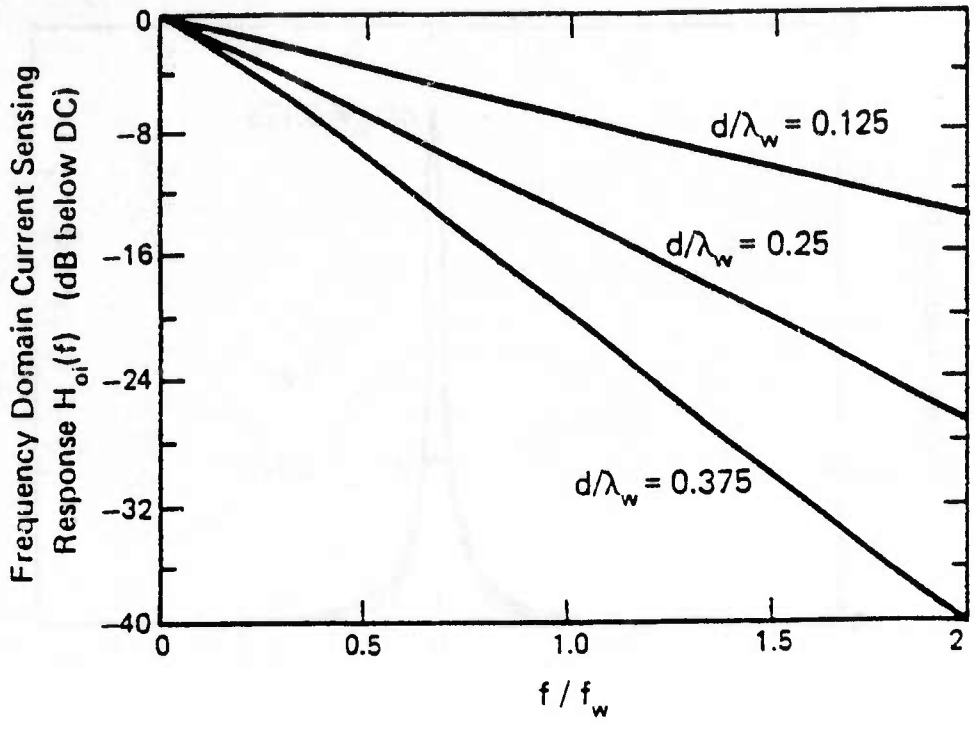

Fig. 4. Normalized frequency domain current sensing responses for infinitesimal gap structure.

To simplify the solution of the problem, the transformation

$$w = u + jv = \ln \frac{z - g/2}{z + g/2} \tag{17}$$

is employed which maps the upper half of the z-plane ($z = x + jy$) onto a horizontal strip of width π in the w-plane, as shown in Figure 5. If the conducting planes A and B are taken to lie on the $x \leq -g/2$, $y=0$ and $x \geq g/2$, $y=0$ axes, respectively, in the w-plane there is a continuous conducting plane at zero potential at $v=0$ and a continuous interface at $v=\pi$ where the boundary condition on the potential is

$$\frac{d\phi}{dv} = 0 \tag{18}$$

If a line charge Q_L is present in the z-plane at $x=p$ and $y=d$ the location of the charge in the w-plane is given by

$$w_o = \ln \frac{p - \frac{g}{2} + jd}{p + \frac{g}{2} + jd} \tag{19}$$

Now, the potential due to the line charge located at w_o in the w-plane is found, and transformed back to the z-plane to obtain the potential in the channel. Due to the electrostatic shielding provided by the conducting plane at $v=0$, the fields in the region $0 < v < \pi$ induced by the line charge located at w_o are unchanged by any charge distribution or material structure which may be present below $v=0$. Therefore, we are free to introduce a line charge $-Q_L$ symmetrically below the conducting plane. This new line charge is located at w_o^*. Also, let an additional boundary condition of zero normal potential gradient exist at $v = -\pi$. We now have a structure, shown in Figure 6, which is entirely symmetric about the v axis, except for the signs of the line charges. Since the line charges are of equal magnitude and opposite sign, the $v=0$ plane remains an equipotential surface of value zero, even in the absence of the conducting plane. Therefore, the problem is reduced to finding the fields due to two line charges placed symmetrically between

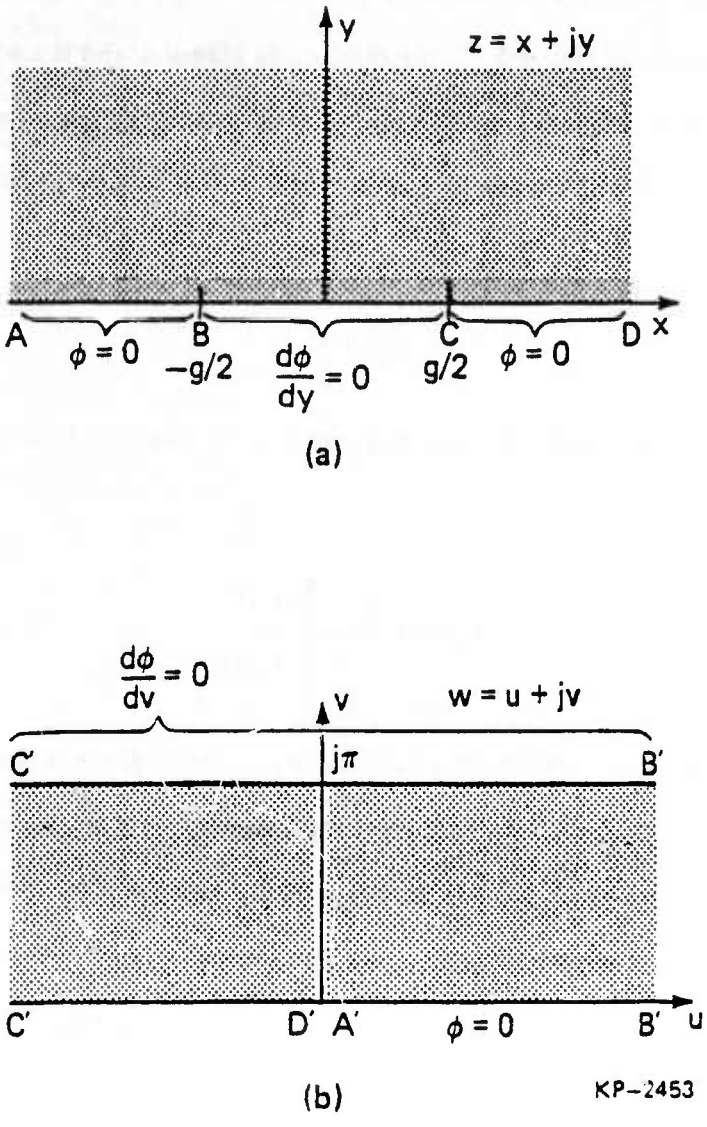

Fig. 5. The mapping $w=u+jv=\ln \frac{z-g/2}{z+g/2}$

(a) z-plane.

(b) w-plane.

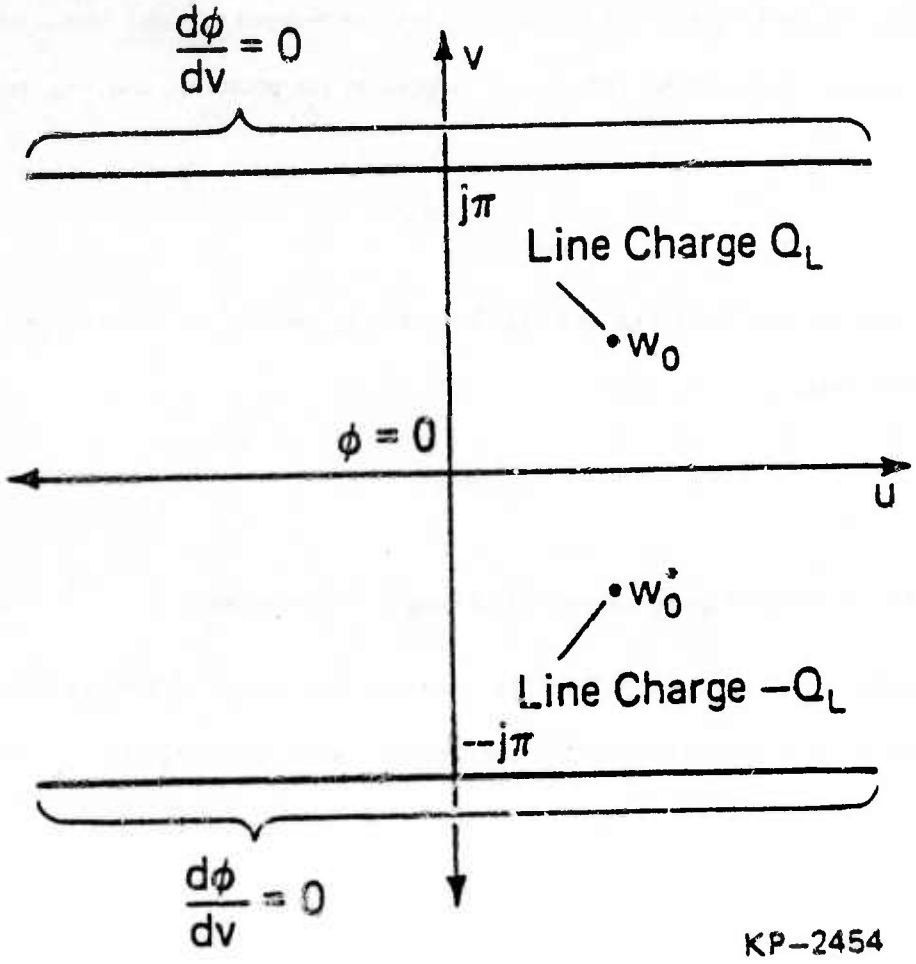

Fig. 6. Set of line charges in the w-plane for calculation of potential in arbitrary gap structure.

planes at which the boundary condition is that the normal potential gradient be zero. This new problem may be solved with the transformation

$$s = r + jq = e^{(w+j\pi)/2} \tag{20}$$

which maps a horizontal strip of width 2π centered about the u-axis into the upper half of the s-plane, as shown in Figure 7. The boundaries at $v = \pm \pi$ are mapped to a continuous boundary at q=0. The line charges located at w_o and w_o^* are mapped to the points s_{01} and $-s_{01}^*$ respectively, where

$$s_{01} = e^{(w_o + j\pi)/2} \tag{21}$$

In the s-plane, there are line charges Q_L and $-Q_L$ located at s_{01} and $-s_{01}^*$ respectively, and a surface at q=o where the boundary condition is

$$\frac{d\phi}{dq} = 0 \tag{22}$$

Again, the solution is obtained using the method of images. In the absence of the $\frac{d\phi}{dq} = 0$ boundary surface the boundary condition there will still be satisfied if line charges of like sign and magnitude are placed symmetrically opposite the q=0 plane, and the fields in the region will be unchanged. The following set of line charges in the s-plane determine the potential in the channel:

Line Charge	**Location in s-plane**
Q_L	$s = s_{01}$
$-Q_L$	$s = -s_{01}^*$
Q_L	$s = s_{01}$
$-Q_L$	$s = -s_{01}^*$

The complex potential function W in the s-plane due to this set of line charges is given by

$$W = \phi + j\psi = \frac{-Q_L}{2\pi\epsilon} \ln \frac{(s-s_{01})(s-s_{01}^*)}{(s+s_{01}^*)(s+s_{01})} \tag{23}$$

The induced charge density on the conducting plates is given by

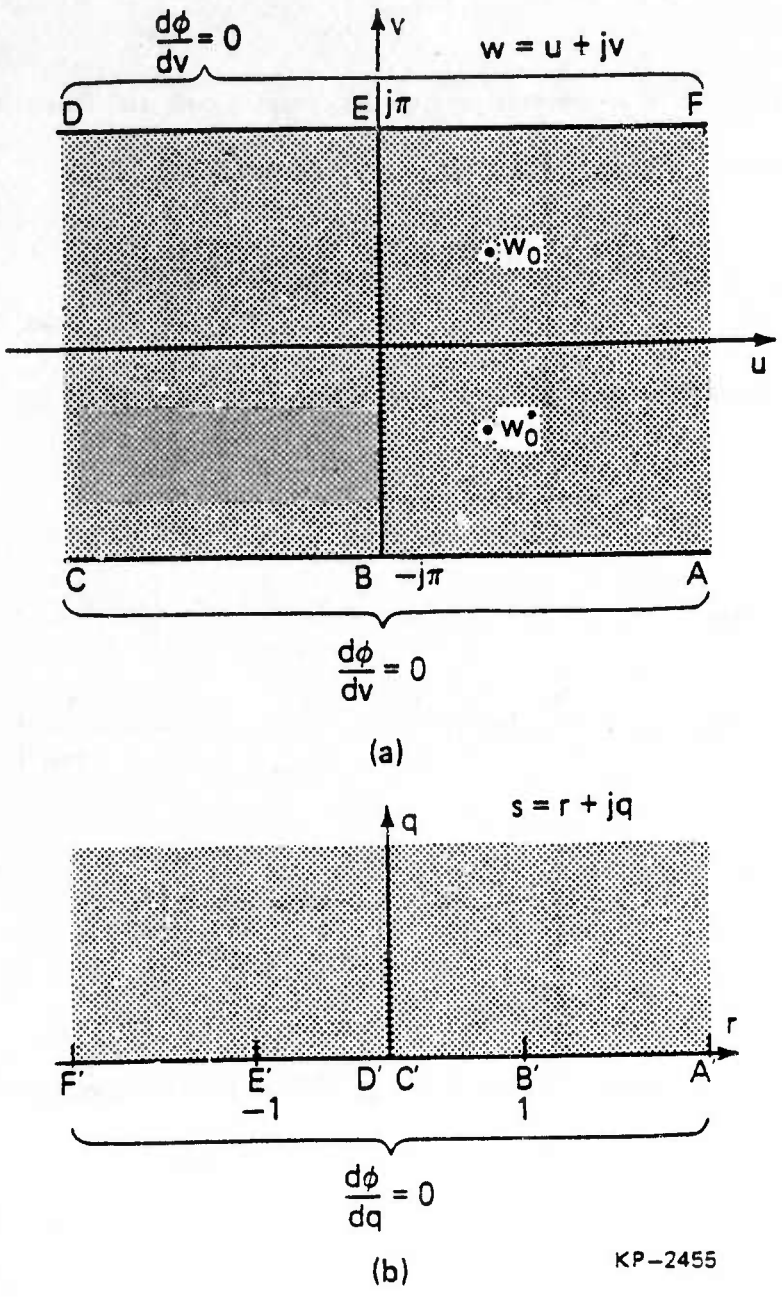

Fig. 7. The mapping $s = r + jq = e^{(w+j\pi)/2}$

(a) w-plane.

(b) s-plane.

$$\rho_{IND}(x,p,d,g) = \epsilon \, \mathrm{Im} \left[\frac{dW}{dz} \right]_{y=0} = -\epsilon \left. \frac{d\phi}{dy} \right|_{y=0} \tag{24}$$

where the electric potential ϕ is the real part of the complex potential function W. The charge density ρ_{IND} may be found by repeated application of the chain rule

$$\rho_{IND}(x,p,d,g) = \epsilon \, \mathrm{Im} \left[\frac{dW}{dz} \right]_{y=0} = \epsilon \, \mathrm{Im} \left[\frac{dW}{ds} \frac{ds}{dw} \frac{dw}{dz} \right]_{y=0} \tag{25}$$

The derivative of the complex potential function with respect to s is given by

$$\frac{dW}{ds} = \frac{-Q_L}{2\pi\epsilon} \left[\frac{1}{s-s_{01}} + \frac{1}{s-s_{01}^*} - \frac{1}{s+s_{01}^*} - \frac{1}{s+s_{01}} \right] \tag{26}$$

The charge density is then

$$\rho_{IND}(x,p,d,g) = \frac{-Q_L}{2\pi} \, \mathrm{Im} \left\{ \left[\frac{1}{s-s_{01}} + \frac{1}{s-s_{01}^*} - \frac{1}{s+s_{01}^*} - \frac{1}{s+s_{01}} \right] \cdot \frac{e^{(w+j\pi)/2}}{2} \left[\frac{1}{z-\frac{g}{2}} - \frac{1}{z+\frac{g}{2}} \right] \right\}_{y=0} \tag{27}$$

where w and s are given in terms of z,g and d in Eqs. (17) and (20), respectively. s_{01} is related to p, d, and g through Eqs. (19) and (21). It may be shown that $\rho_{IND}(x)$ is zero for $|x| < g/2$. This is as expected since no charge can lie in the gap region due to the imposed zero flux boundary condition there. As in the gapless structure, the total charge Q(p,d,g) is found by integrating ρ_{IND} on plate B

$$Q(p,d,g) = \int_{x=g/2}^{\infty} \rho_{IND}(x,p,d,g) \, dx \tag{28}$$

The current per unit beamwidth as a function of time through the load connecting plates A and B is again given by

$$i_o(t) = i(t,d,g) = \lambda_w f_w \left. \frac{dQ(p,d,g)}{dp} \right|_{p=\lambda_w f_w t} \tag{29}$$

The integration and differentiation in Eqs. (28) and (29) have been performed numerically for various values of d/λ_w and g/λ_w. As in the gapless case, $h_{oi}(t) = \dfrac{i_o(t)}{Q_L f_w}$ is a dimensionless quantity dependent on t/T_w, d/λ_w and g/λ_w.

The normalized Fourier transform $H_{oi}(f) = \dfrac{I_o(f)}{Q_L}$ is computed numerically with a fast Fourier transform (FFT) routine from the calculation of $h_{oi}(t)$. Graphs of $H_{oi}(f)$ for charge depths d = 0.125 λ_w, 0.25 λ_w, and 0.375 λ_w are shown in Figures 8, 9, and 10, respectively. Each graph shows the frequency response for gap size g = 0.125 λ_w, 0.25 λ_w, and 0.5 λ_w. For the cases of small gap size (g/λ_w = 0.125) the frequency response differs negligibly from the zero gap case (Figure 4) over the range of f/f_w shown. As the gap gets larger (g/λ_w = 0.25, 0.5) the rolloff due to the longer transit time under the gap becomes significant.

B. Voltage Sensing

Introduction of isolated electrodes between grounded conducting planes as shown in the AC model of Figure 11 permits the charge to be sensed with single ended detector circuits. This is in contrast to the current sensing structure, which would require a differential amplifier to achieve a multi-tap impulse response. The simplest voltage sensing structure consists of a single sense electrode placed symmetrically between infinite conducting planes A and B, as shown in Figure 12. Let g be the size of the gaps separating the electrode from plates A and B and let L be the separation between the gap centers. Therefore, the length of the sense electrode is L-g. As in the current sensing structure, assume a line charge of density Q_L to be flowing a distance d below the surface features. The electrode is terminated in an arbitrary load of impedance Z. Assume the coupling between the electrode and the ground plates to be purely capacitive. Let C_S denote the total effective structural capacitance (per unit beamwidth) between the electrode and ground.

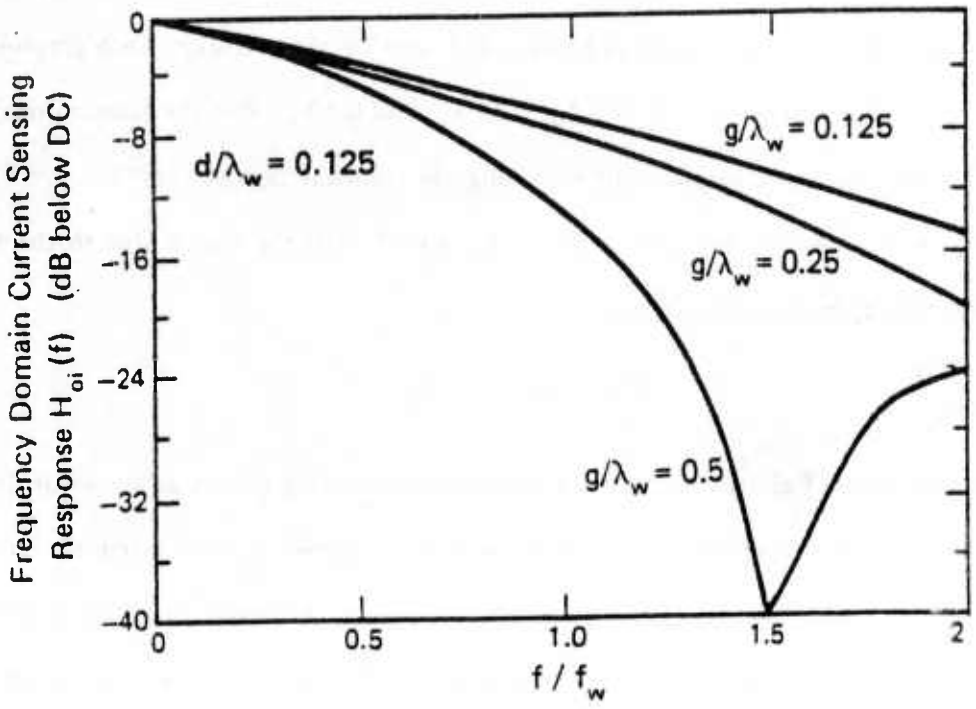

Fig. 8 Normalized frequency domain current sensing responses for structure with d/λ_w = 0.125 and nonzero gap sizes.

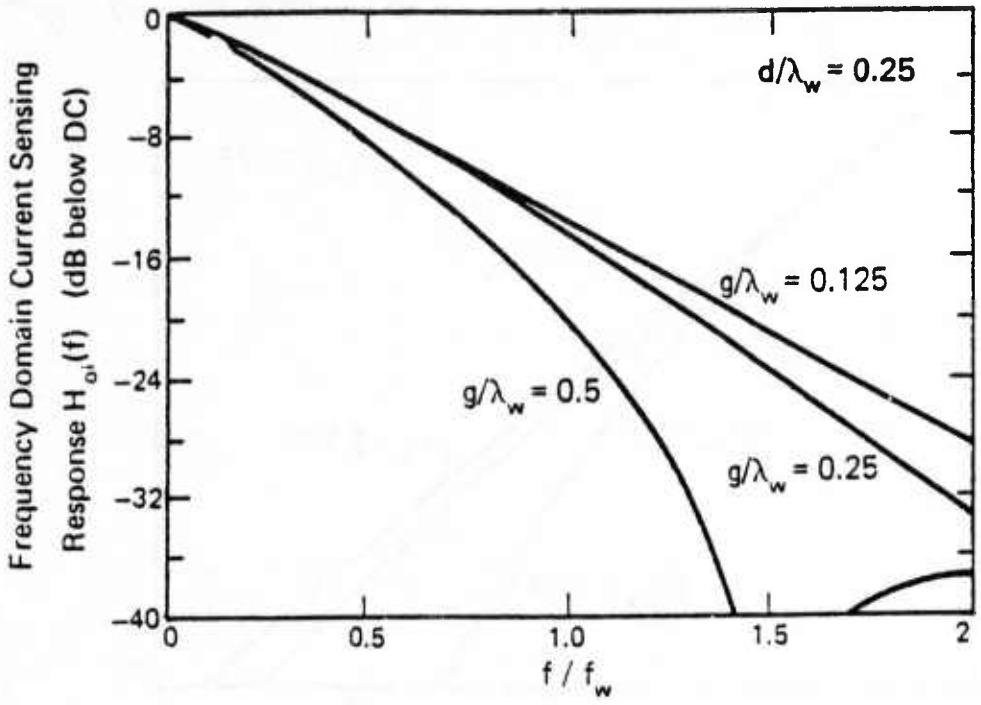

Fig. 9 Normalized frequency domain current sensing responses for structure with $d/\lambda_w = 0.25$ and nonzero gap sizes.

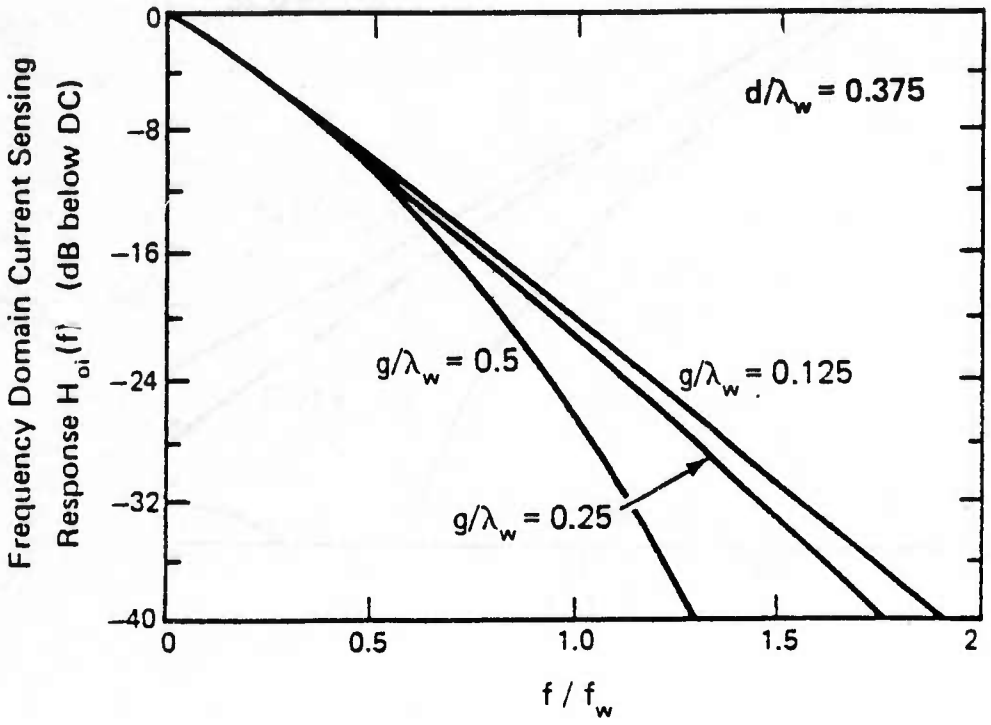

Fig. 10 Normalized frequency domain current sensing responses for structure with d/λ_w = 0.375 and nonzero gap sizes.

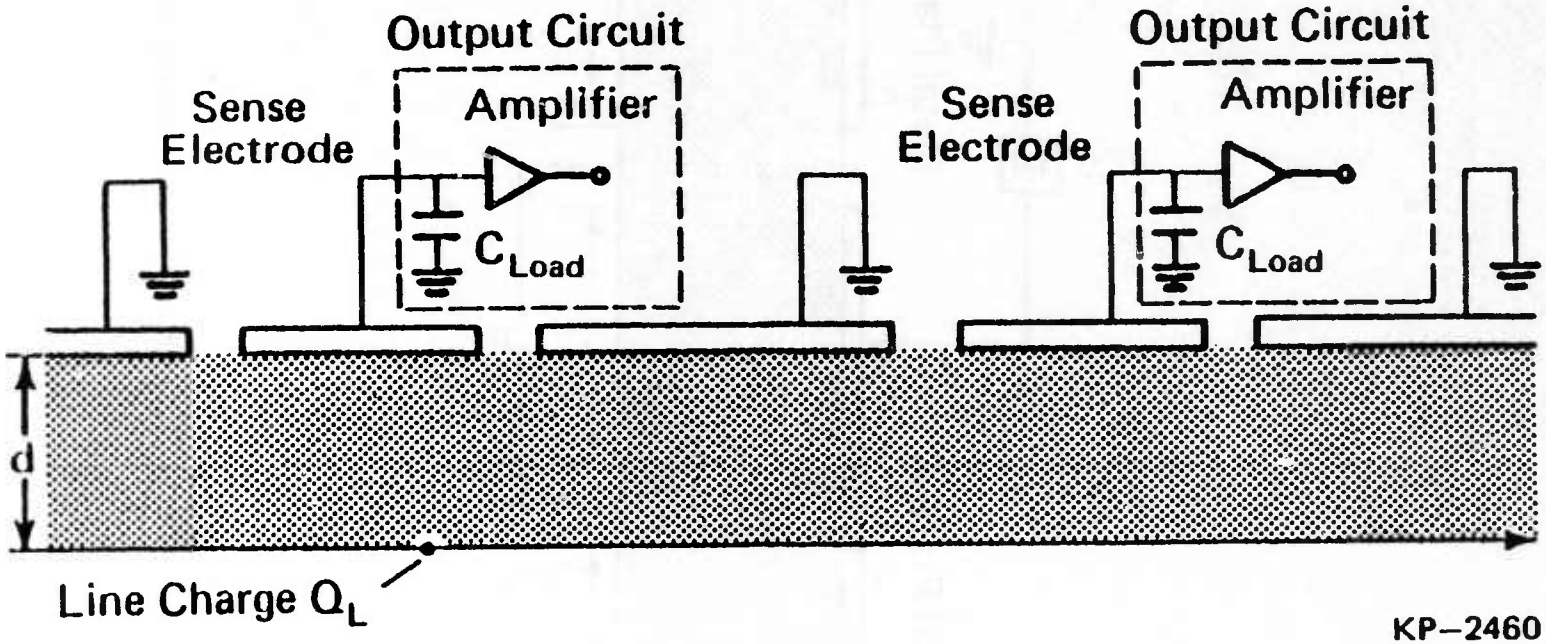

Fig. 11. AC model of voltage sensing structure with isolated sense electrodes.

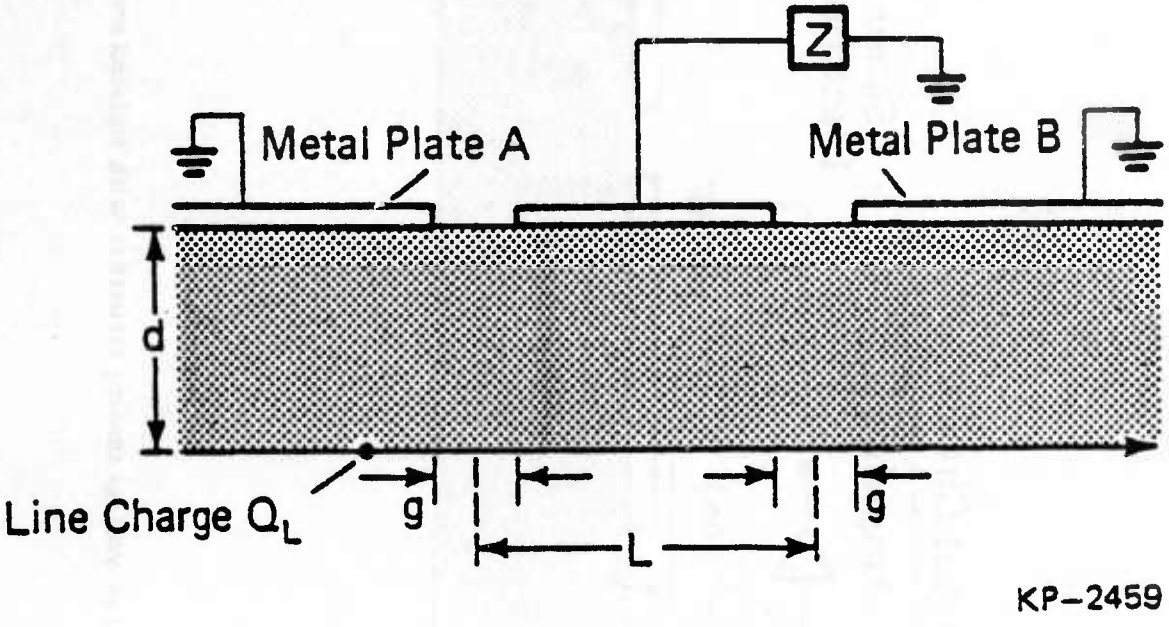

Fig. 12. AC model of single electrode voltage sensing structure.

Additionally, assume that any voltage drop across surface features is small so that the travelling wave potential is unperturbed, and hence the position of charge transport through the channel is constant. The problem of voltage sensing consists of finding the voltage induced on the sense electrode by the line charge as a function of time, and its Fourier transform, the frequency response of the voltage sensing structure. It is expected that there will be a rolloff in the frequency domain response due to voltage sensing because the sense electrode is not a point sampler. Rather, it has a finite width, which will introduce a bandwidth reduction.

The voltage sensing structure of Figure 12 may be modeled as two parallel current sources driving a load consisting of the structural capacitance $C_S l$ and the external load of impedance Z, where l is the channel width. The structural capacitance per unit beamwidth C_S has been analytically calculated for the structure of Figure 12.[6] The current sources are physically separated by the spacing between gap centers, since each source is taken to lie at the center of its gap, as assumed in the current sensing derivation. The sources are of equal magnitude, and differ in phase by an amount proportional to the constant transit time of the line charge between gap centers. In the frequency domain, the total current $I_v(f)$ flowing into the load is thus given by the superposition of the current sources

$$I_v(f) = I_i(f)e^{j2\pi f\frac{\Delta T}{2}} - I_i(f)\, e^{-j2\pi f\frac{\Delta T}{2}} \tag{30}$$

where $I_i(f)$ is the current sensing frequency response of the gap between either grounded plate and the voltage sense electrode, and ΔT is the transit time between gap centers, given by $\Delta T = L/v_w = L/\lambda_w f_w$. The equivalent circuit is shown in Figure 13a. Since the line charge flows at a constant velocity given by Eq. (1), Eq. (30) may be written

$$I_v(f) = I_i(f)2j \sin \frac{\pi f L}{f_w \lambda_w} \tag{31}$$

Therefore, the voltage across the load is

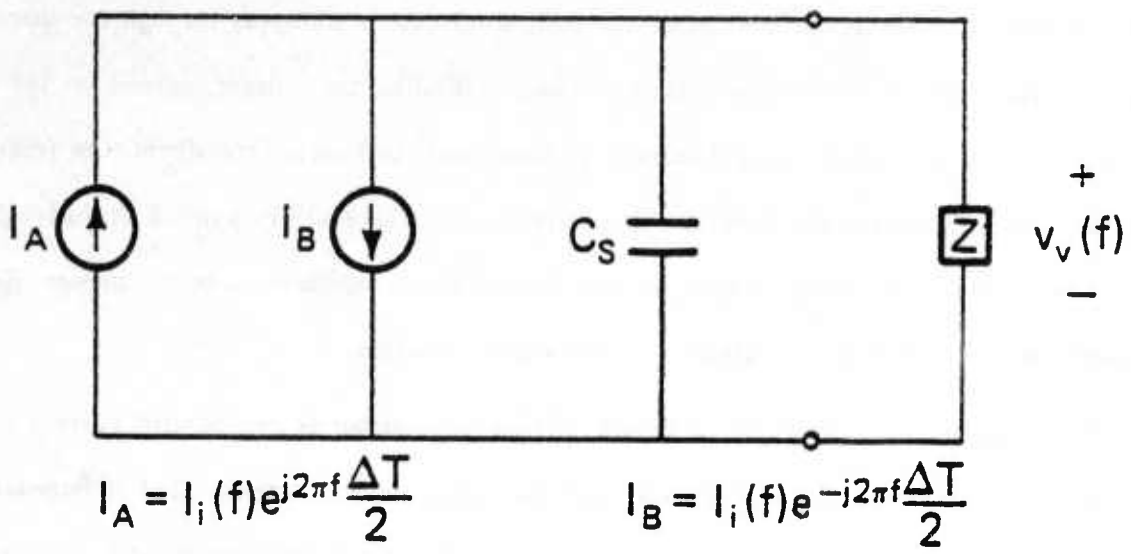

(a)

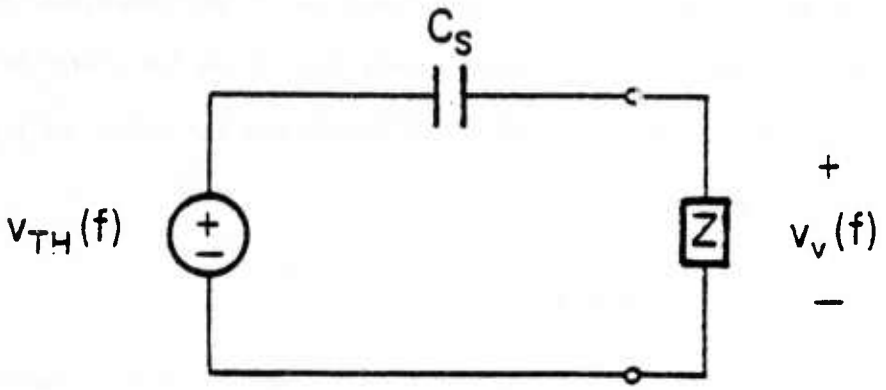

(b)

KP-2458

Fig. 13. Equivalent circuits for single tap voltage sense structure.

(a) Representation by parallel current sources.

(b) Thevenin equivalent circuit.

$$V_v(f) = \frac{Zl \cdot \frac{1}{j2\pi f C_S}}{Zl + \frac{1}{j2\pi f C_S}} \, 2j \sin\left(\frac{\pi f L}{f_w \lambda_w}\right) I_i(f) \tag{32}$$

A more convenient model for the voltage sensing structure is the Thevenin equivalent circuit of the circuit of Figure 13a, consisting of a voltage source $V_{TH}(f)$ in series with the structural capacitance C_s driving the external load of impedance Z. The Thevenin equivalent is shown in Figure 13b. The voltage $V_v(f)$ across the external load is found by the voltage divider equation

$$V_v(f) = \frac{Zl}{Zl + \frac{1}{j2\pi f C_s}} V_{TH}(f) \tag{33}$$

thus the Thevenin voltage source has strength

$$V_{TH}(f) = \frac{Zl + \frac{1}{j2\pi f C_s}}{Zl} V_v(f) \tag{34}$$

Eq. (34) may be combined with Eq. (32) to yield

$$V_{TH}(f) = \frac{L}{f_w \lambda_w} \frac{I_i(f)}{C_S} \frac{\sin \frac{\pi f L}{f_w \lambda_w}}{\frac{\pi f L}{f_w \lambda_w}} \tag{35}$$

which may be written as a product of terms

$$V_{TH}(f) = \frac{I_i(f) L_v(f)}{C_S f_w} \frac{L}{\lambda_w} \tag{36}$$

where $L_v(f)$ is a dimensionless factor accounting for the response to voltage sensing. This factor may be written

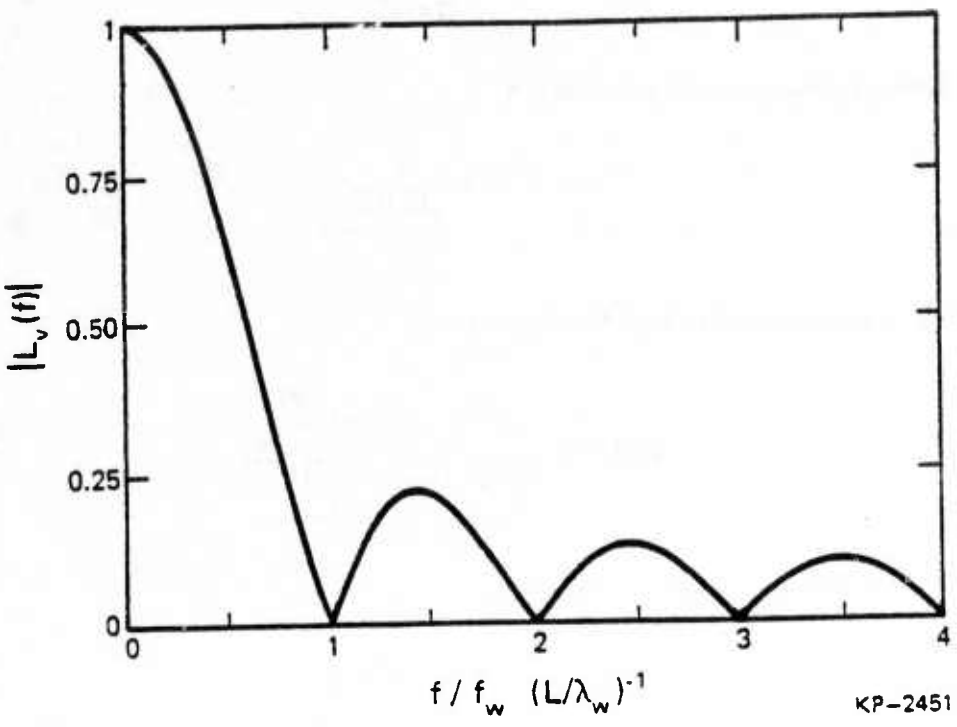

Fig. 14. Normalized frequency domain response due to voltage sensing.

$$L_v(f) = \frac{\sin \pi \dfrac{f}{f_w} \dfrac{L}{\lambda_w}}{\pi \dfrac{f}{f_w} \dfrac{L}{\lambda_w}} \tag{37}$$

$L_v(f)$, graphed in Figure 14, has nulls at frequencies which are multiples of $f_w \dfrac{\lambda_w}{L}$. The inverse Fourier transform of Eq. (37) is given by

$$L_v(t) = \int_{-\infty}^{\infty} L_v(f) e^{j2\pi ft}\, df = \frac{f_w}{L/\lambda_w} P_{\Delta T}(t) \tag{38}$$

where $P_{\Delta T}(t)$ is a unit pulse of duration ΔT centered about t=0. The inverse Fourier transform of Eq. (35) may be written as a convolution of $L_v(t)$ and the current sensing response in the time domain

$$v_{TH}(t) = \frac{1}{C_s} i_o(t) * P_{\Delta T}(t) = \frac{1}{C_s} i_o(t) * \frac{L/\lambda_w}{f_w} L_v(t) \tag{39}$$

where * denotes convolution.

$V_{TH}(f)$ and $v_{TH}(t)$ may be expressed in terms of the normalized responses $h_{oi}(t)$ and $H_{oi}(f)$ derived in the analysis of the current sensing structure. The Thevenin time domain voltage may be written

$$v_{TH}(t) = \frac{Q_L f_w}{C_s} h_{oi}(t) * P_{\Delta T}(t) = \frac{Q_L}{C_s} \frac{L}{\lambda_w} h_{oi}(t) * L_v(t) \tag{40}$$

and in the frequency domain,

$$V_{TH}(f) = \frac{Q_L}{C_S f_w} H_{oi}(f)\, L_v(f) \frac{L}{\lambda_w} \tag{41}$$

Equations (40) and (41) make physical sense because for an infinite sequence of line charges Q_L spaced by a distance λ_w in the channel, the average charge per unit channel width is $Q_L \cdot \dfrac{L}{\lambda_w}$ and thus the induced DC voltage is $\dfrac{Q_L L}{C_s \lambda_w}$. As in the current sensing case, responses for voltage sensing

may be normalized to dimensionless quantities

$$h_{ov}(t) = \frac{v_{TH}(t)}{Q_L/C_S} = f_w h_{oi}(t) * P_{\Delta T}(t) \tag{42}$$

$$H_{ov}(f) = \frac{V_{TH}(f)}{Q_L/C_S f_w} = \frac{L}{\lambda_w} H_{oi}(f) L_v(f) \tag{43}$$

Therefore, the rolloff in the frequency domain due to the finite size of the voltage sensing electrode is found by evaluating $L_v(f)$ at the desired frequency.

Closed form expressions for the voltage in the time and frequency domains are possible in the special case of very small gaps between ground planes and the sense electrode. Combining Eqs. (43) and (16) yields

$$H_{ov}(f) = e^{-2\pi \frac{d}{\lambda_w} \left| \frac{f}{f_w} \right|} \frac{\sin \pi \dfrac{fL}{f_w \lambda_w}}{\pi \dfrac{f}{f_w} \dfrac{L}{\lambda_w}} \tag{44}$$

The inverse Fourier transform of Eq. (44) may be computed analytically[7]

$$\frac{h_{ov}(t)}{f_w} = \int_{-\infty}^{\infty} H_{ov}(f) e^{j2\pi ft} \frac{df}{f_w} = 2 \int_0^{\infty} e^{-2\pi \frac{d}{\lambda_w} \frac{f}{f_w}} \frac{\sin \pi \dfrac{f}{f_w} \dfrac{L}{\lambda_w}}{\pi \dfrac{f}{f_w} \dfrac{L}{\lambda_w}} \cos 2\pi ft \frac{df}{f_w} \tag{45}$$

$$\frac{h_{ov}(t)}{f_w} = \frac{\pi}{L/\lambda_w} \left\{ \tan^{-1} \frac{4 \dfrac{d}{\lambda_w} \dfrac{L}{\lambda_w}}{4 \left(\dfrac{d}{\lambda_w} \right)^2 - \left(\dfrac{L}{\lambda_w} \right)^2 + \left(\dfrac{t}{T_w} \right)^2} + \pi P_r(t) \right\} \tag{46a}$$

where

$$\tau = \frac{T_w}{2}\left[\left|\left(\frac{L}{\lambda_w}\right)^2 - 4\left(\frac{d}{\lambda_w}\right)^2\right|\right]^{1/2} \tag{46b}$$

where $P_\tau(t)$ is the unit pulse function previously defined.

As in the case of current sensing, numerical results are available for the responses for structures with arbitrary gaps. Since the frequency dependence due to voltage sensing is a closed form multiplicative factor in the frequency response, numerical data for the current sensing frequency response need only be multiplied by the appropriate factor (as in Eq. (43)) to obtain normalized voltage sensing frequency responses. The inverse Fourier transform of the frequency response may be numerically computed to obtain the normalized voltage sensing time domain response.

C. Distributed Charge Density in the Packet

An actual packet of charge in the channel of a buried channel travelling wave charge transfer device occupies a finite space due to the fact that the confining potential is spatially continuous rather than abrupt. A rolloff in NDS frequency responses is expected due to the finite size of the charge packet.

The charge packet density and shape are found by the solution of Laplace's equation

$$\nabla^2 \phi_{tot}(x,y) = 0 \tag{47}$$

where $\phi_{tot}(x,y)$ is the sum of the empty well channel potential ϕ_e and the potential due to the mobile charge, ϕ_c. The mobile charge density $\rho(x,y)$ is thus given by

$$\rho(x,y) = \epsilon \nabla^2 \phi_e(x,y) \tag{48}$$

An approximate solution for the mobile charge density has been found[8]

$$\rho(x,y) = \begin{cases} \rho_w \cos\dfrac{2\pi(x-x_o)}{\lambda_w} + \rho_d, & |x - x_o| \leq x_b, \\ & 2\pi \left| \dfrac{y-d}{\lambda_w} \right| \leq \left| \dfrac{2\phi_{CL}\rho_w}{\phi_o \rho_d} C \right|^{1/2} \\ 0, & \text{elsewhere} \end{cases} \tag{49}$$

where ρ_w is the polarization charge density of the sinusoidal travelling wave and ρ_d is the depletion charge density in the material, and x_b is given by

$$x_b = \frac{\lambda_w}{2\pi} \cos^{-1}\left[1 - \frac{\phi_{CL}}{\phi_o}\right] \tag{50}$$

ϕ_{CL} is the mobile charge potential difference between the center of the charge packet and its edge in the x-direction. ϕ_o is the amplitude of the travelling wave. The center of the symmetric packet is taken to lie at the coordinate ($x=x_o$, $y=d$). C is the so-called boundary parameter and it is a constant chosen so that the equipotential surfaces still have the functional form of the empty well potential. In the case where the depletion charge density is large, the two-dimensional mobile charge density may be taken to lie along the y=d plane, having variation only in the x-direction. In this case the one-dimensional (sheet) charge density has the form[9]

$$\rho_s(x) = \begin{cases} \rho_o \left[\cos\dfrac{2\pi(x-x_o)}{\lambda_w} - \left[1 - \dfrac{\phi_{CL}}{\phi_o}\right]\right]^{1/2}, & \dfrac{|2\pi(x-x_o)|}{\lambda_w} \leq \cos^{-1}\left[1 - \dfrac{\phi_{CL}}{\phi_o}\right] \\ 0, & \text{elsewhere} \end{cases} \tag{51}$$

The constant ρ_o is chosen that the total linear charge density is equal to that of the line charge used previously, Q_L. Therefore, $\rho_s(x)$ is such that

$$\int_{\text{packet}} \rho_s(x)dx = Q_L \tag{52}$$

or

$$\rho_o = \frac{Q_L}{\int_{x_o - x_b}^{x_o + x_b} \left| \cos 2\pi \frac{x - x_o}{\lambda_w} - \left| 1 - \frac{\phi_{CL}}{\phi_o} \right| \right|^{1/2} dx} \tag{53}$$

The integral in Eq. (52) is given by an elliptic function. It can also be integrated numerically, which is preferable since the result cannot be expressed in closed form.

Since the fundamental NDS responses derived thus far assume a line charge, the time domain response due to an arbitrary one-dimensional charge distribution is given by the convolution of the fundamental time domain NDS response with the packet charge distribution in the time domain. Equivalently, the NDS frequency response due to the arbitrary charge distribution is given by the product of the fundamental frequency domain NDS response with the Fourier transform of the time dependent charge distribution. The spatial charge distribution is converted to a time domain distribution with the substitution

$$x - x_o = v_w t = \lambda_w f_w t \tag{54}$$

so that the one-dimensional charge distribution of Eq. (51) becomes

$$\rho_s(t) = \begin{cases} \rho_o \left| \cos 2\pi \frac{t}{T_w} - \left| 1 - \frac{\phi_{CL}}{\phi_o} \right| \right|^{1/2}, & \left| \frac{t}{T_w} \right| \leq \frac{1}{2\pi} \cos^{-1} \left| 1 - \frac{\phi_{CL}}{\phi_o} \right| \\ 0, & \text{elsewhere} \end{cases} \tag{55}$$

For current sensing responses, the time domain current is

$$i(t) = i_o(t) * \frac{\lambda_w f_w}{Q_L} \rho_s(t) \tag{56}$$

where $i_o(t)$ is the fundamental current sensing time domain response due to a line charge. In the frequency domain,

$$I(f) = I_o(f) \frac{\lambda_w f_w}{Q_L} \rho_s(f) \tag{57}$$

where $I_o(f)$ and $\rho_s(f)$ are the Fourier transforms of $i_o(t)$ and $\rho_s(t)$, respectively. Similarly, voltage sensing responses are given by

$$v(t) = v_o(t) * \frac{\lambda_w f_w}{Q_L} \rho_s(t) \tag{58}$$

$$V(f) = V_o(f) \frac{\lambda_w f_w}{Q_L} \rho_s(f) \tag{59}$$

where $v_o(t)$ and $V_o(f)$ are the time and frequency domain voltage sense responses for a line charge. As in the line charge case, normalized, dimensionless responses for current sensing ($h_i(t)$ and $H_i(f)$) and voltage sensing ($h_v(t)$ and $H_v(f)$) in the time and frequency domains may be written

$$h_i(t) = \frac{i(t)}{Q_L f_w} = \frac{\lambda_w f_w}{Q_L} h_{oi}(t) * \rho_s(t) \tag{60}$$

$$H_i(f) = \frac{I(f)}{Q_L} = \frac{\lambda_w f_w}{Q_L} H_{oi}(f) \rho_s(f) \tag{61}$$

$$h_v(t) = h_i(t) * P_{\Delta T}(t) f_w \tag{62}$$

$$= f_w^2 \left[h_{oi}(t) * \frac{\rho_s(t)}{Q_L/\lambda_w} * P_{\Delta T}(t) \right]$$

$$H_v(f) = H_i(f) L_v(f) = \frac{\lambda_w f_w}{Q_L} H_{oi}(f) \rho_s(f) L_v(f) \tag{63}$$

where $h_{oi}(t)$ and $H_{oi}(f)$ are the normalized dimensionless NDS responses due to a line charge.

The Fourier transform of Eq. (55) cannot be expressed in closed form, even for specific values of ϕ_{CL}/ϕ_o. The transform can be obtained using an FFT routine. For the special case of ϕ_{CL}/ϕ_o = 1/2, the time dependent normalized charge density and its Fourier transform are shown in Figures 15 and 16, respectively. Since the charge packet is localized to a region only 1/3 wavelength long for ϕ_{CL}/ϕ_o = 1/2, the rolloff added by the packet is not large (less than 1.5 dB for frequencies below the travelling wave frequency). The rolloff in the frequency response will be dominated by

other effects, namely the current and voltage sensing losses.

However, larger values of charge load will contribute greater rolloff, since the packet will be of greater spatial extent. Since the signal level directly determines the charge load of any given packet, nonlinearities in NDS frequency responses with respect to input signal level are to be expected. Further research into the nonlinearities associated with the signal level is likely to be motivated by the interest in knowing NDS responses to transient, time varying signals, where the charge load of packets varies due to the time varying input signal.

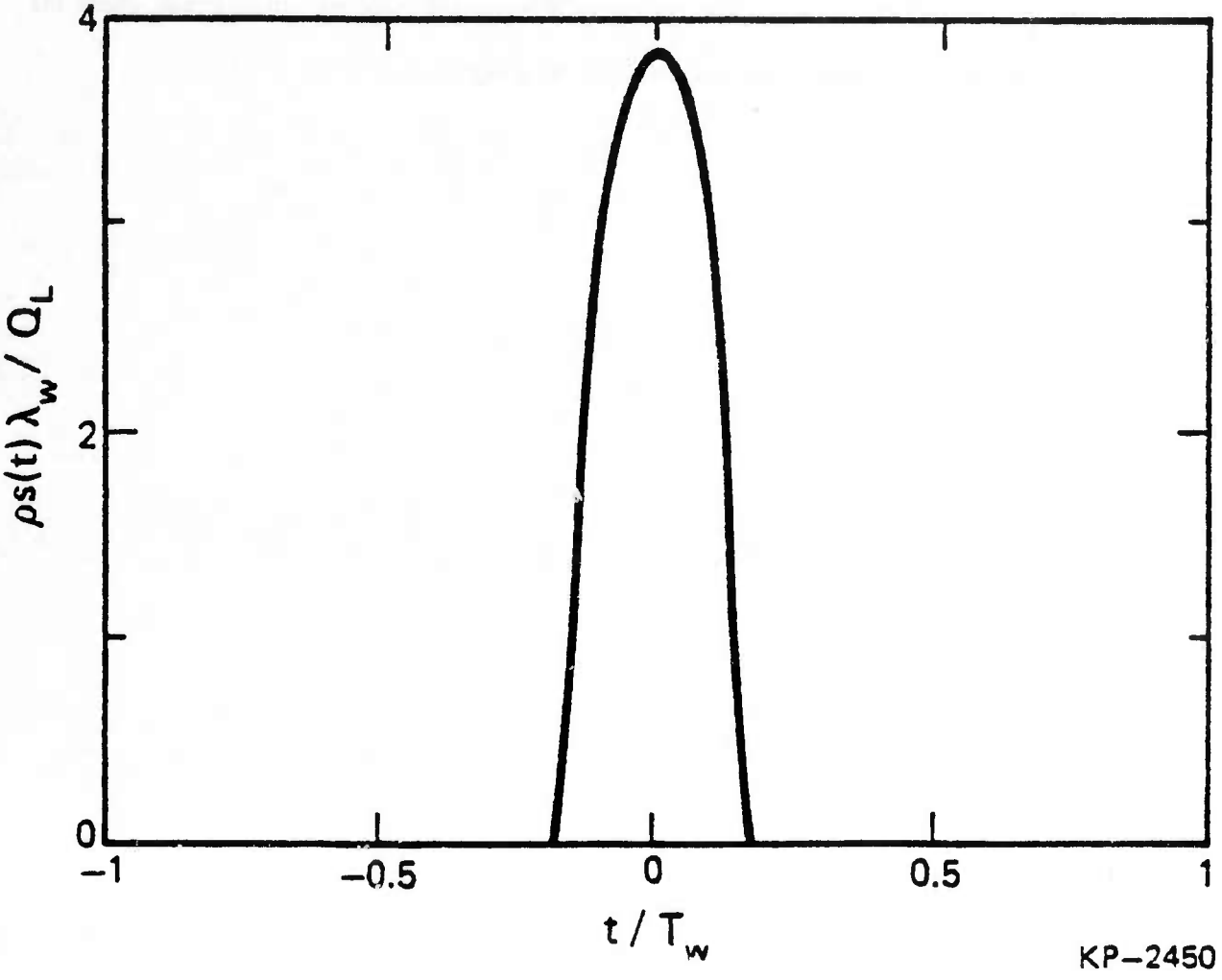

Fig. 15. Time variation of one-dimensional packet charge density for $\phi_{CL}/\phi_o = 1/2$.

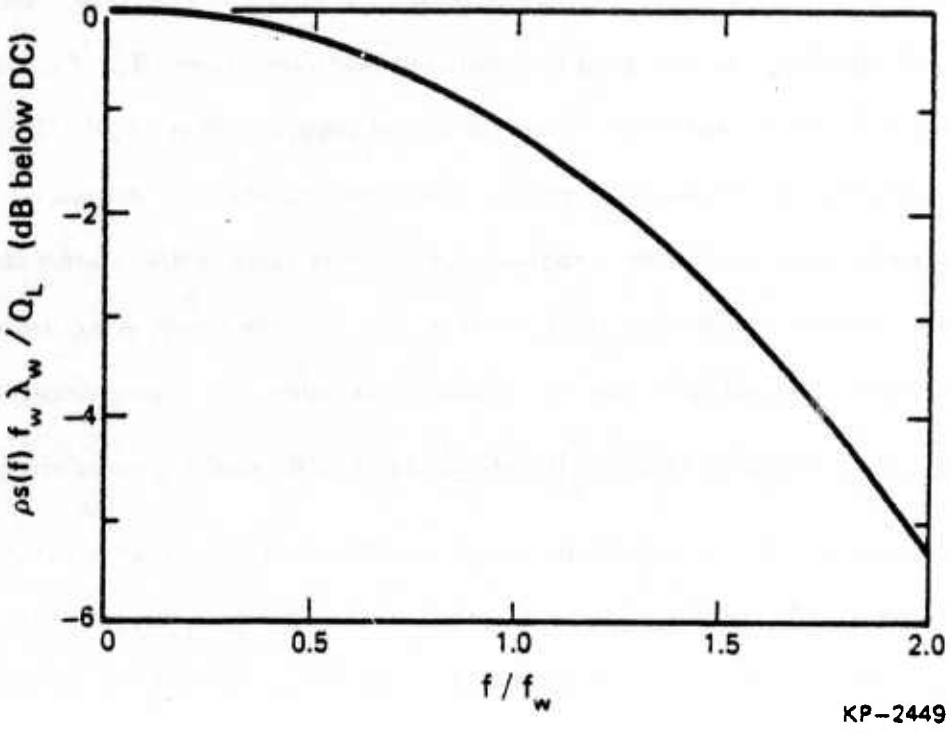

Fig. 16. Frequency dependence of one-dimensional packet charge density for $\phi_{CL}/\phi_o = 1/2$.

III. Experimental Verification of NDS Frequency Response

The voltage sensing frequency response was measured for a single tap structure on a buried channel travelling wave charge transfer device, whose a.c. model is shown in Figure 17. The structure has $d/\lambda_w \approx 0.34$, $g/\lambda_w = 1/4$ and $L/\lambda_w = 1$. The charge load of the mobile packet was assumed to be 50%. The voltage on the sense electrode was detected by a high-input impedance amplifier which drove a network analyzer configured to measure insertion loss.

The experimental and theoretical frequency responses are shown in Figure 18. Agreement between theory and experiment is very good for small and moderate values f/f_w. The difference between the theory and experimental result reaches an error of about 1.5 dB at $f/f_w = 1/2$, at which point the theory predicts the frequency response to be approximately 13.5 dB below the d.c. response. The major source of error is the uncertainty in the exact value of d/λ_w, which cannot be directly measured. Instead, it is derived from the level at which the device is d.c. biased, and depends on the physical properties of the semiconductor, including the doping density of the channel material. An uncertainty in the value of $\frac{d}{\lambda_w}$ of $\pm$ 20% would give an error in the frequency response at $f/f_w = 1/2$ of $\pm$ 1.88 dB, which would account for the difference in theory and experiment seen at $f/f_w = 1/2$. Additional error in the agreement between theory and experiment would result from error in the estimation of normalized charge load, due to uncertainty in the wave potential ϕ_o.

The theory successfully predicts the salient features observed in measured NDS responses:

- Approximately linear decibel rolloff due to the spreading of flux lines of the charge in the channel.
- $\frac{\sin x}{x}$ dependence due to the finite size of the voltage sense electrode.

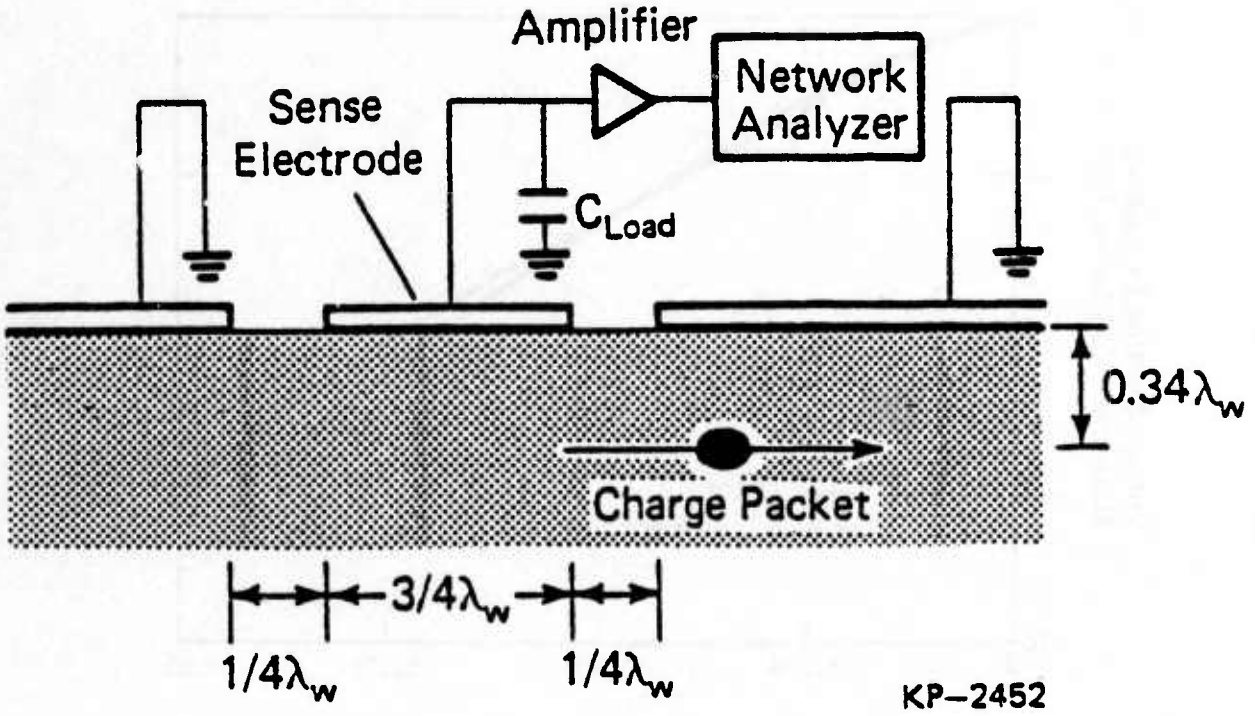

Fig.17. AC model of voltage sense structure used for experimental verification of frequency response.

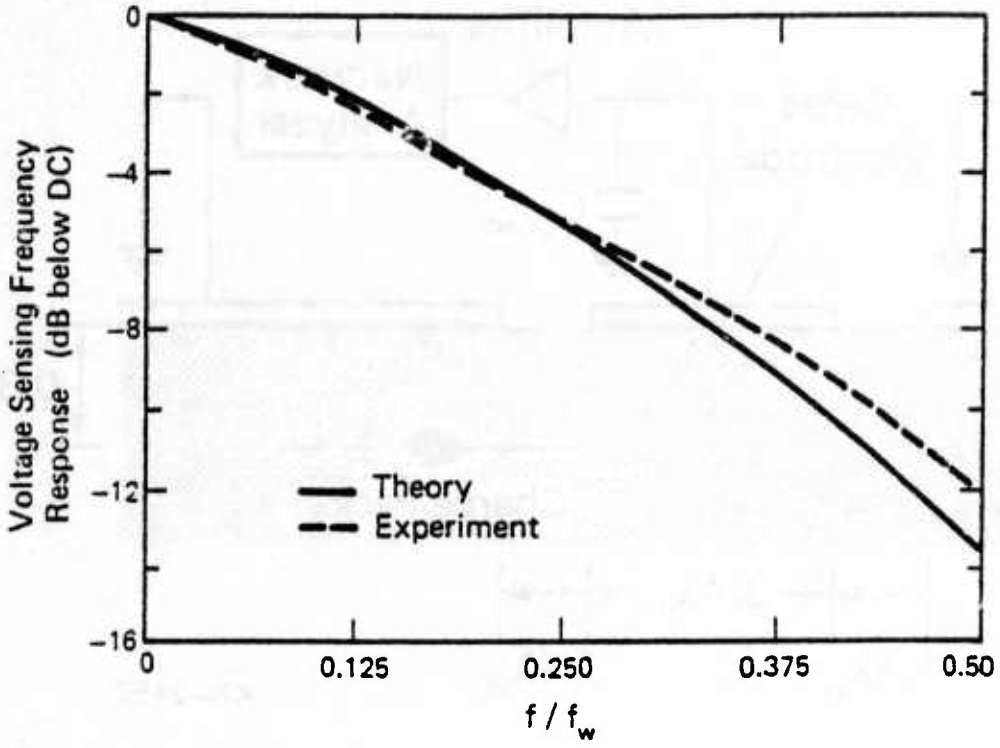

Fig. 18. Theoretical and measured frequency responses for the structure of Figure 17.

IV. Conclusion

A theory is presented for the computation of the time and frequency domain responses of simple non-destructive sensing electrode structures in buried channel travelling wave charge transfer devices. Two fundamental sensing methods are analyzed: current sensing and voltage sensing. Current sensing is the detection of the current consisting of the image of the travelling charge packet flowing in the buried channel. Voltage sensing is the detection of voltage induced by the image charge on an isolated sense electrode. Current sensing responses are computed analytically in the zero gap case, and numerical solutions are presented for the case of arbitrary gap. It is shown that the voltage sensing response may be expressed as the superposition of the fundamental current sensing responses in the frequency domain. A numerical analysis of the dependence of the NDS frequency response on the shape of the charge packet is presented, in the case of a one-dimensional charge distribution in the channel.

Experimental results for the voltage sensing frequency response are presented for a simple one tap voltage sense structure, and good agreement between theory and experiment is observed.

The theory presented in this thesis has been shown to correctly predict the nondestructive sensing response for a simple buried channel travelling wave charge transfer device. It is expected to be a useful tool in the analysis and design of signal processors employing the buried channel travelling wave CTD concept.

List of References

[1] W.F. Kosonocky, "Charge Coupled Devices - An Overview," *1974 Western Electron. Show and Conv. Techn. Papers*, vol. 18, pp. 2/1-2/20, Sept. 10-13, 1974.

[2] M.J. Hoskins, H. Morkoc and B.J. Hunsinger, "Charge Transport by Surface Acoustic Waves in GaAs," *Appl. Phys. Lett.*, 41(4), p. 332, Aug. 15, 1982.

[3] W.S. Boyle and G.E. Smith, "Charge Coupled Semiconductor Devices," *Bell System Tech. Journal*, vol. 49, pp. 587-593, April, 1970.

[4] I. Deyhimy, R.C. Eden and J.S. Harris, Jr., "GaAs Charge Coupled Devices," *Appl. Phys. Lett.* 32(6), p. 383, March 15, 1978.

[5] William R. Smythe. *Static and Dynamic Electricity*. New York: McGraw-Hill, p. 63, 1968.

[6] C.P. Wen, "Coplanar Waveguide: A Surface Strip Transmission Line Suitable for Nonreciprocal Gyromagnetic Application," *IEEE Trans. on Microwave Theory and Techniques*, vol. MTT-17, No. 12, Dec. 1969, p. 1087.

[7] I.S. Gradshteyn and I.M. Ryzhik, *Table of Integrals, Series, and Products*. New York: Academic Press, p. 492, 1980.

[8] M.J. Hoskins and B.J. Hunsinger, "Simple Theory of Buried Channel Acoustic Charge Transport in GaAs," *J. Appl. Phys.*, 55(2) p. 419, January 15, 1984.

[9] M.J. Hoskins and B.J. Hunsinger, "Simple Theory of Buried Channel Acoustic Charge Transport in GaAs," p. 423.

APPENDIX C

TWO-DIMENSIONAL POTENTIALS FOR BURIED CHANNEL CHARGE TRANSFER DEVICES INCLUDING PLATE SEPARATION

BY

BRUCE C. SCHMUKLER

B. S., University of Illinois, 1984

THESIS

Submitted in partial fulfillment of the requirements
for the degree of Master of Science in Electrical Engineering
in the Graduate College of the
University of Illinois at Urbana-Champaign, 1985

Urbana, Illinois

ABSTRACT

Two theoretical methods for calculating the electrostatic potential in a buried channel charge transfer device are presented with the emphasis on the effects of plate separation. The methods utilize the superposition principle and either conformal mapping or Fourier analysis. The conformal mapping method yields quick and accurate results for structures that have one plate separation (i.e., an isolated gap), while the Fourier analysis method yields results with low overshoot and ripple for arbitrary surface structures but requires more computing time. In addition, normalized data is presented using the conformal mapping method for the case of an isolated gap in a uniformly biased device.

ACKNOWLEDGEMENTS

I would like to thank Professor Bill J. Hunsinger and Dr. Michael J. Hoskins for their guidance and support. The assistance of Alex Crosman is greatly appreciated for collecting most of the data used in this thesis and helping with the required programming. In addition, the patience and typing skills of Julie Overholt are greatly appreciated.

This work was jointly supported by the United States Air Force under Contract No. F30602-84-C-0132 and by the Joint Service Electronics Program under Contract No. N00014-84-C-0149.

1. INTRODUCTION

Buried channel charge transfer devices have been around for many years. Ever since the conception of these devices, many studies have been performed on the potential distribution created by the device geometries [1-10]. Most of these studies assume zero plate separation, although some studies which include the analysis of gaps between plates have been done. Most of those studies are based on the finite-element technique. Other approaches include a resistive carbon paper technique and a Fourier series solution [3,7]. All of these techniques are good for analyzing potential distributions in the absence of signal charge. However, analytic solutions are best when one wants to include the analysis of signal charge. The Fourier series method presented by McKenna and Schryer [3] is a suitable base model for the analysis of signal charge in the buried transport channel; however, it is quite complicated.

The purpose of this thesis is to present simpler analytical expressions for the potential distribution in a buried channel charge transfer device with the effects of gap separation between plates taken into account. One technique to be presented uses conformal mapping to analyze the effects of a single isolated gap. Another technique to be presented uses a simplified Fourier series model to analyze arbitrary surface geometries.

One problem with calculating potential distributions in buried channel charge transfer devices is that often a large amount of work must be done to obtain a reasonably accurate potential distribution. Thus, it is also the purpose of this paper to present equations and graphs that can be used to obtain an estimate of the potential distribution for a variety of structures. This data shall be presented for an isolated single gap in the surface structure of a buried channel charge transfer device.

2. THE PROBLEM AND ITS SEPARATION

The basic problem addressed by this thesis is the determination of the potential distribution for a buried channel charge transfer device built with reverse biased Schottky plates. This type of structure is in common use in GaAs charge transfer devices. In particular, various types of structures for a buried channel traveling wave charge transfer device were analyzed. Of course, it is virtually impossible to solve any real physical problem exactly; thus, approximations had to be made. The approximations used, however, are consistent with those in previous published literature.

Figure 1 shows typical structures which occur in buried channel charge transfer devices. To solve for these potentials without use of an approximation would be a difficult task. To simplify the analysis, two approximations are made throughout this thesis. One is the depletion approximation and the other is the uniform depletion depth approximation. Both of these approximations are consistently used in previously published literature. It is possible to incorporate a non-uniform depletion depth into the potential models, but the calculation of the potential would become a cumbersome, iterative procedure. The first step of this iterative procedure is the analysis given in this thesis. Future works may contain models that include non-uniform depletion depths.

Included in Fig. 1 are periodic structures and non-periodic structures. Most of the non-periodic structures must be solved with a periodic algorithm using a long period. For the isolated gap case, shown in Figs. 1a and 1b, if one can assume $\epsilon_2=0$, then a periodic algorithm need not be used. In this case, a conformal mapping solution can be used instead of a Fourier series solution. The conformal mapping solution is also used to select the period required in the periodic algorithm to approximate a non-periodic structure. One might ask why one should even bother with a conformal mapping solution when a Fourier series solution can be used to solve virtually any arbitrary structure. The answer is simple. A conformal mapping solution is quicker, more accurate, and easier to use than a Fourier series solution. Thus, a conformal mapping solution should be done whenever possible.

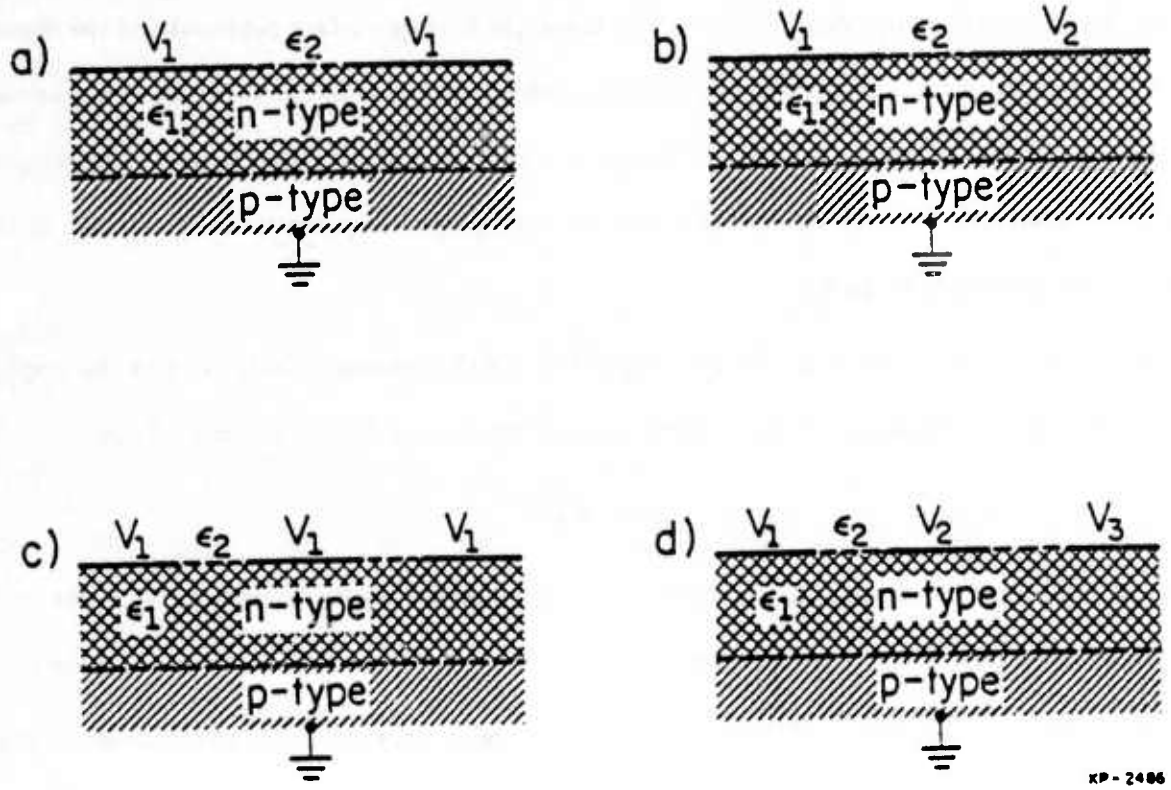

Fig. 1. Typical structures encountered in buried channel charge transfer devices.
(a) Isolated gap with symmetrical biasing.
(b) Isolated gap with unsymmetrical biasing.
(c) Isolated sense electrode.
(d) Arbitrary periodic structure.

The first step in the solution for the potentials of the structures given in Fig. 1 is to separate the problem into two parts and use the superposition principle to obtain the entire answer. After separation, the two problems that need to be solved are a one-dimensional problem that contains all the space charge and a two-dimensional problem that contains no space charge but which has a mixed boundary condition at the surface of the device.

The first step in defining the one-dimensional problem is to find the average depletion depth. To find the average depletion depth, one needs to know the average surface potential and the doping profile. The average surface potential may not be readily known, since the potential is not known between the plates. A good guess can be made, however, and several iterations can be used to obtain a good answer. For the isolated gap case, the average surface potential is the average of the potentials on either side of the gap.

The solution of the potential for the structure of Fig. 2 is needed in order to find the average depletion depth. Here d_e is the epi-layer depth and d is the average depletion depth. Thus,

$$d=d_e + d_p$$

where d_p represents the distance that the depletion region penetrates the substrate. V_a is the average surface potential, and $p(y)$ is the charge density. To solve this problem one must find the solution to the Poisson's equation, $\nabla^2 V = -\frac{p(y)}{\epsilon}$, for the region $0<y<d$ under the boundary conditions $V(0)=V_a$, $V(d)=0$ and $E(d)=0$. E(d) is the electric field at d. The potential is found by integrating Poisson's equation twice, applying the boundary conditions as necessary and using integration by parts to eliminate the double integral. The potential solution to Fig. 2 is

$$V(y)=-\int_d^y \frac{p(y')dy'}{\epsilon} + \int_d^y \frac{y'p(y')dy'}{\epsilon} \qquad (2.1)$$

From this we see

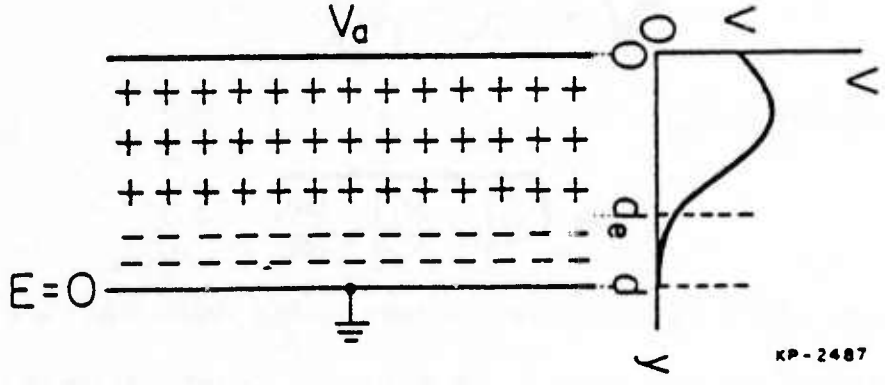

Fig. 2. One-dimensional potential containing space charge. Boundary conditions are V(0)=V E(d)=0 and V(d)=0 where d is an unknown.

$$V_a = V(0) = \int_d^0 \frac{y' p(y') dy'}{\epsilon}. \tag{2.2}$$

Thus, Eq. (2.2) is the general equation that must be satisfied to obtain d and hence d_p. Most of the time the substrate can be modeled as having constant doping. That is $p(y) = -qN_a$ for $d_e < y < d$. Under this condition Eq. (2.1) reduces to

$$V_a = \int_{d_e}^0 \frac{y\, p(y) dy}{\epsilon} + \frac{qN_a}{2\epsilon}\left(d_p^2 + 2d_e \cdot d_p\right).$$

Solving for d,

$$d = \sqrt{d_e^2 + \frac{2\epsilon V_a}{qN_a} - \frac{2}{qN_a}\int_{d_e}^0 y\, p(y) dy}\,. \tag{2.3}$$

For the case of an abrupt junction,

$$d = \sqrt{d_e^2\left(1 + \frac{N_d}{N_a}\right) + \frac{2\epsilon V_a}{qN_a}}\,.$$

With the knowledge of the average depletion depth, one can proceed with the solution of the potential for structures like those in Fig. 1. The solution for the potential can be facilitated by dividing the problem into two problems and using superposition to obtain the final result. The necessary conditions for the proper use of the superposition principle are that the total potential must satisfy the Poisson equation and the appropriate boundary conditions. It should be noted that there are many ways to use superposition to separate a problem, and they all yield the unique solution provided that the necessary conditions are satisfied. It is desirable to separate the space charge from the mixed boundary condition at the surface of the device, for solving the Poisson equation with the mixed boundary condition at the surface is, indeed, a difficult task. This task is simplified by letting the total potential be the sum of a potential that satisfies Laplace's equation. Let the former be called V_{sp} and the latter, V_{lap}. In addition, let the potential that satisfies the Poisson equation have the boundary condition that the normal electric field at the surface vanishes. Since the charge density for the structure under study only varies with y, this potential only depends on

y and can be denoted as $V_{sp}(0)$. $V_{sp}(y)$ at the surface, is not zero; therefore, the voltage boundary conditions at y=0 for V_{lap} must be offset from the original voltage boundary conditions by $V_{sp}(0)$ so that the total potential, V_{sp} plus V_{lap}, satisfies the original boundary conditions. For regions of plate separation the boundary condition for V_{lap} is that the electric flux must be continuous. This ensures that the total electric flux is continuous in regions of plate separation as V_{sp} contributes zero electric flux at the surface. Figure 3 illustrates the separation of a particular problem.

To obtain $V_{sp}(y)$, the Poisson equation, $\nabla^2 V_{sp} = \frac{-\rho(y)}{\epsilon}$, must be solved under the boundary conditions $V_{sp}(d) = 0$ and $\frac{\partial V_{sp}(0)}{\partial y} = 0$. The result is

$$V_{sp}(y) = -y \int_0^y \frac{p(y')dy'}{\epsilon} + \int_0^y \frac{y'p(y')dy'}{\epsilon} + V_{sp}(0) \tag{2.4}$$

where

$$V_{sp}(0) = d\int_0^d \frac{p(y)}{\epsilon}dy - \int_0^d \frac{yp(y)}{\epsilon}dy \,. \tag{2.5}$$

The task is now to evaluate V_{lap} which is the solution of the Laplace equation for the structure with the plate voltages offset by the factor $V_{sp}(0)$. The remainder of this thesis discusses two methods that can be used to solve the two-dimensional Laplace equation under mixed boundary value conditions. The first method presented uses conformal mapping for isolated gaps, and the second method presented uses Fourier series for arbitrary-periodic surface structures.

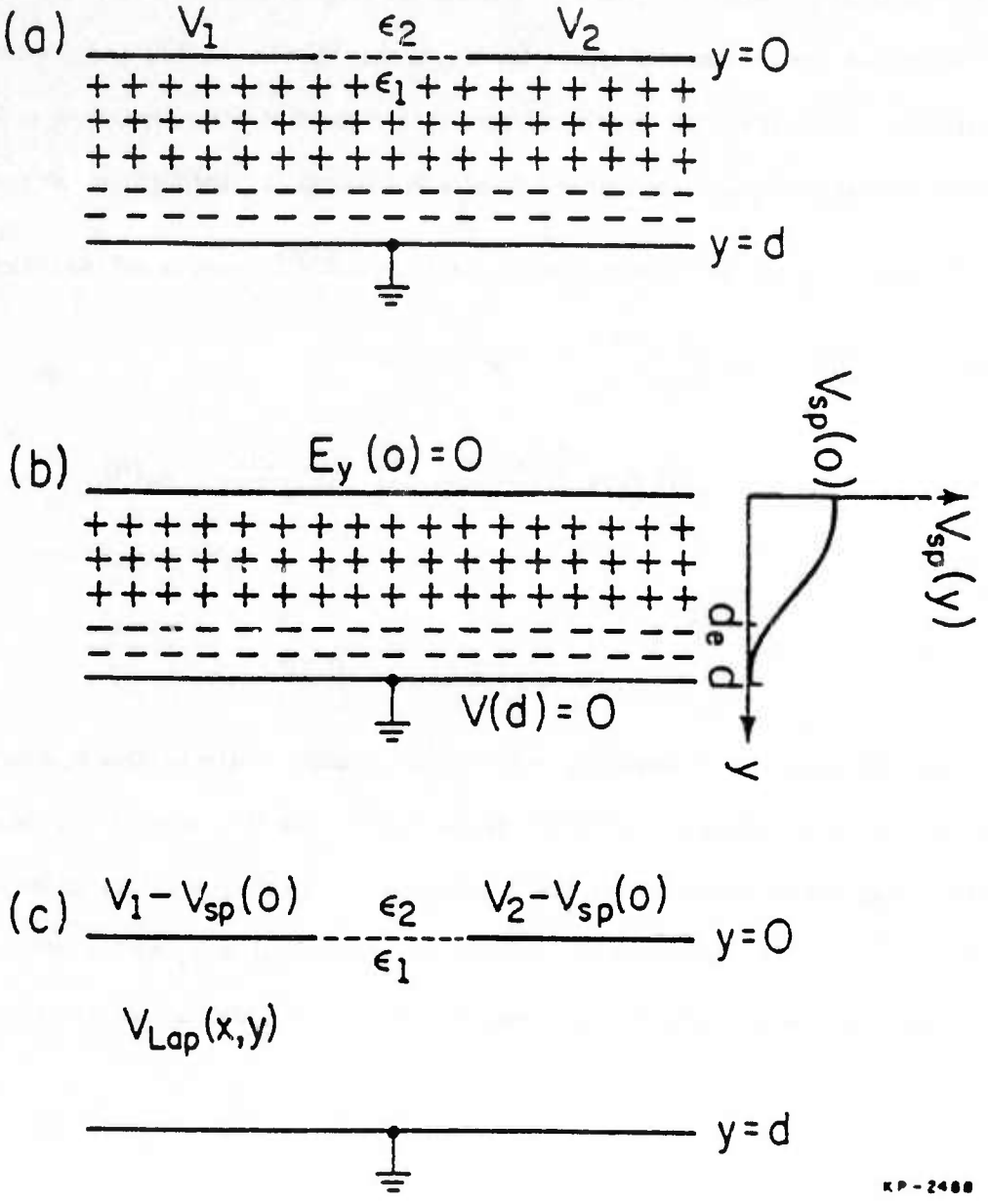

Fig. 3. Separation of a potential problem into two problems.
(a) Two-dimensional potential problem with space charge.
(b) One-dimensional potential problem containing all space charge.
(c) Two-dimensional potential problem without space charge.

3. CONFORMAL MAPPING SOLUTIONS

In general, solving boundary value problems that have mixed boundary conditions is not an easy task. For the case of a single isolated gap, Fig. 4a, an accurate approximation to the potential can be found using conformal mapping. The accuracy of the approximation depends on the parameters ϵ_1, ϵ_2, a, d, V_1 and V_2. For $\epsilon_2 = 0$, Fig. 4b, the solution is exact.

The potentials, $V_I(x,y)$ and $V_{II}(x,y)$, in the two regions illustrated in Fig. 4a must satisfy the following equations.

$$\nabla^2 V_I = 0 \tag{3.1}$$

$$\nabla^2 V_{II} = 0 \tag{3.2}$$

$$V_I(x,d) = 0 \tag{3.3}$$

$$V_I(x,0) = V_{II}(x,0) = V_1 \, , \; x < -a \tag{3.4}$$

$$V_I(x,0) = V_{II}(x,0) = V_2 \, , \; x < a \tag{3.5}$$

$$\epsilon_1 \frac{\partial V_I(x,0)}{\partial y} = \epsilon_2 \frac{\partial V_{II}(x,0)}{\partial y} \quad , \; -a < x < a \; . \tag{3.6}$$

We see that the potential is specified on the plates and that the electric flux must be continuous in the gap, $-a < x < a$. If $\epsilon_2 << \epsilon_1$, then Eq. (3.6) becomes

$$\epsilon_1 \frac{\partial V_I(x,0)}{\partial y} \approx 0 \, , \; -a < x < a \; . \tag{3.7}$$

Thus, all the boundary conditions of Region I are specified. The two region problem of Fig. 4a has been reduced to the one region problem of Fig. 4b. The necessary equations to solve for V(x,y) are

$$\nabla^2 V = 0 \tag{3.8}$$

$$V(x,d) = 0 \tag{3.9}$$

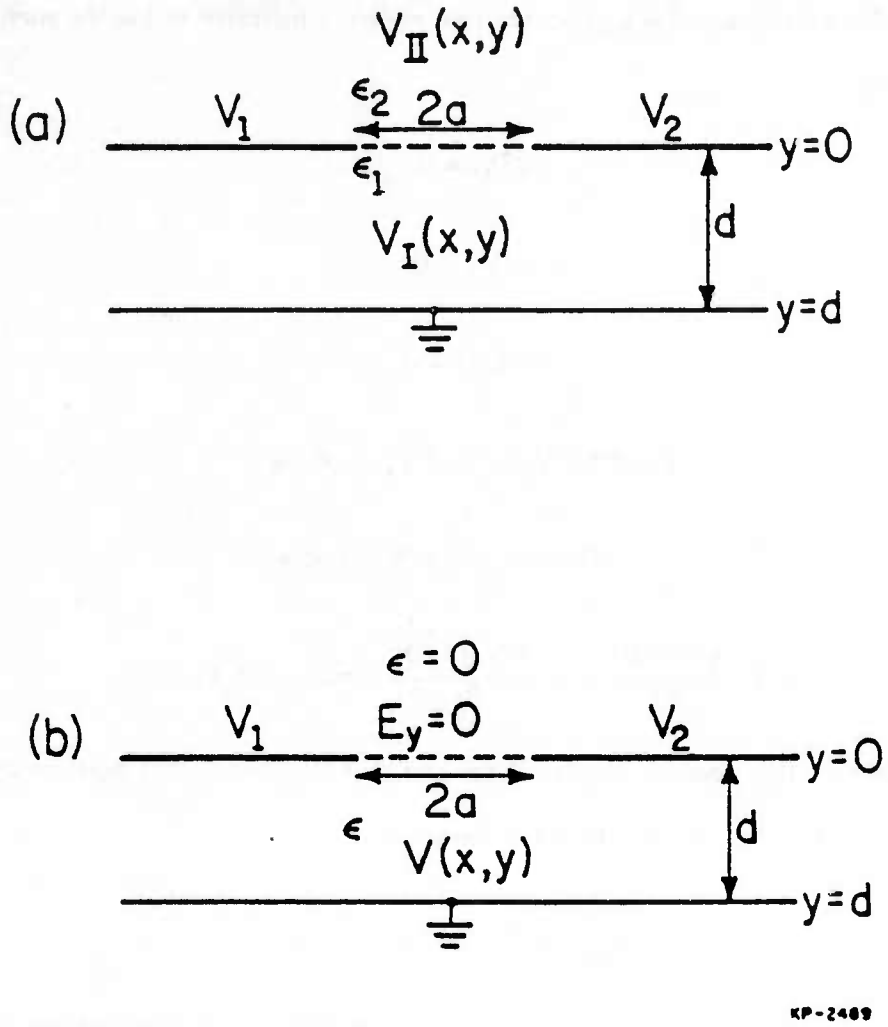

Fig. 4. Structure of an isolated gap.
(a) General case (two region problem).
(b) $\epsilon_2 << \epsilon_1$ such that $E_y(x.0) \approx 0$ for $-a < x < a$ (one region problem).

$$V(x,0) = V_1 \,, \quad x < -a \tag{3.10}$$

$$V(x,0) = V_2 \,, \quad a < x \tag{3.11}$$

$$\frac{\partial V}{\partial y}(x,0) = 0 \,, \quad -a < x < a \,. \tag{3.12}$$

To solve for V(x,y) under the constraints of Eqs. (3.8) to (3.12), one must use superposition and further break down the problem. Thus,

$$V(x,y) = V_A(x,y) + V_B(x,y) \tag{3.13}$$

where $V_A(x,y)$ and $V_B(x,y)$ must satisfy the Laplace equation and the following boundary conditions:

$$V_A(x,d) = V_B(x,d) = 0 \tag{3.14}$$

$$\frac{\partial V_A(x,0)}{\partial y} = \frac{\partial V_B(x,0)}{\partial y} = 0 \,, \quad -a < x < a \tag{3.15}$$

$$V_A(x,0) = V_1 \,, \quad x < -a \tag{3.16}$$

$$V_A(x,0) = 0 \,, \quad a < x \tag{3.17}$$

$$V_B(x,0) = 0 \,, \quad x < -a \tag{3.18}$$

$$V_B(x,0) = V_2 \,, \quad a < x \tag{3.19}$$

These boundary conditions are illustrated in Fig. 5a and Fig. 6a.

$V_A(x,y)$ can be found using three successive conformal mappings. The three successive mappings, ω_1, ω_2 and ω_2, are shown in Figs. 5b-5d. The transformations are

$$\omega_1 = -\exp\left[-\frac{\pi}{d}\, z\right] \quad (z = x + jy) \tag{3.20}$$

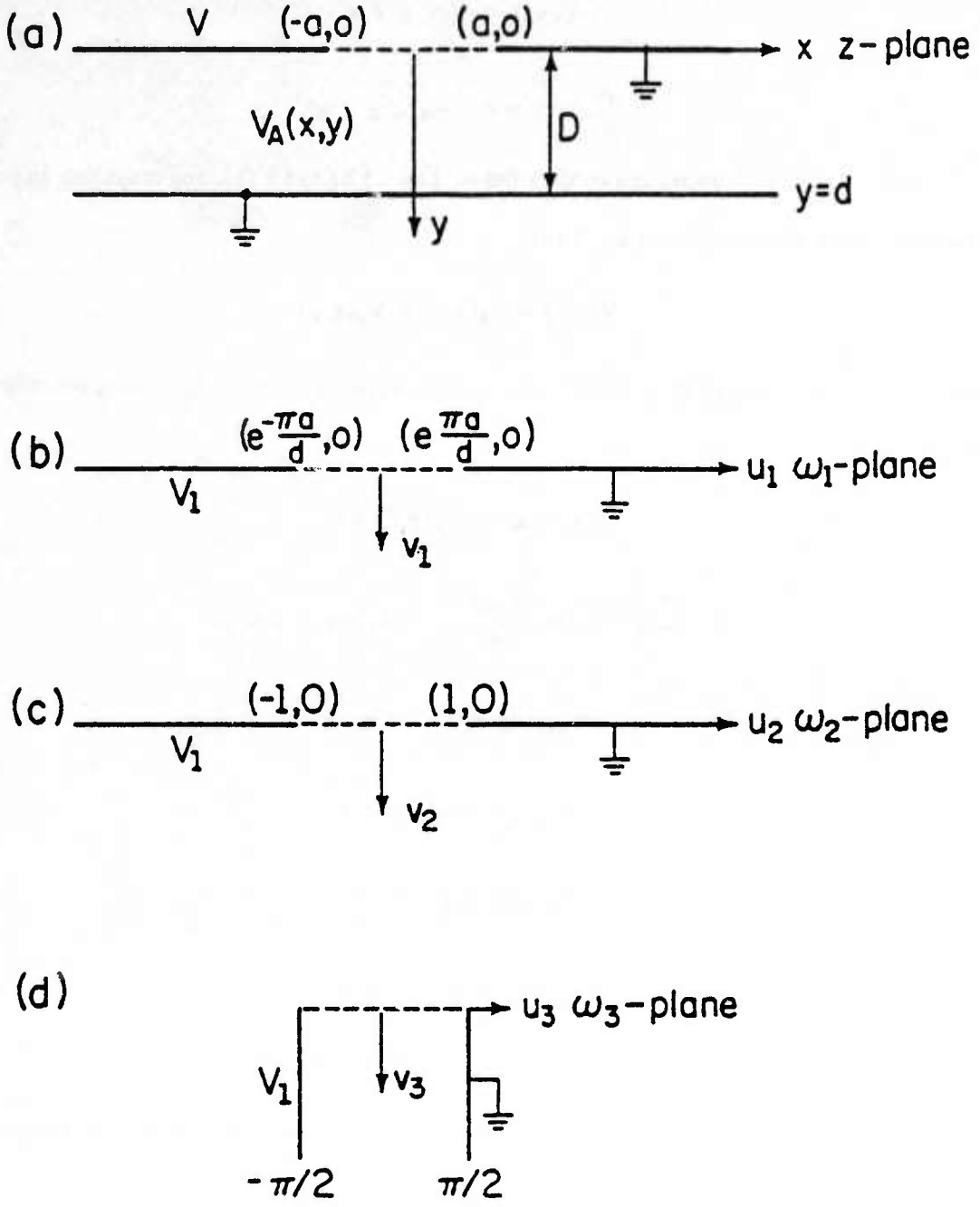

Fig. 5. Conformal mappings used to solve for $V_A(x,y)$.
(a) z-plane
(b) ω_1-plane
(c) ω_2-plane
(d) ω_3-plane

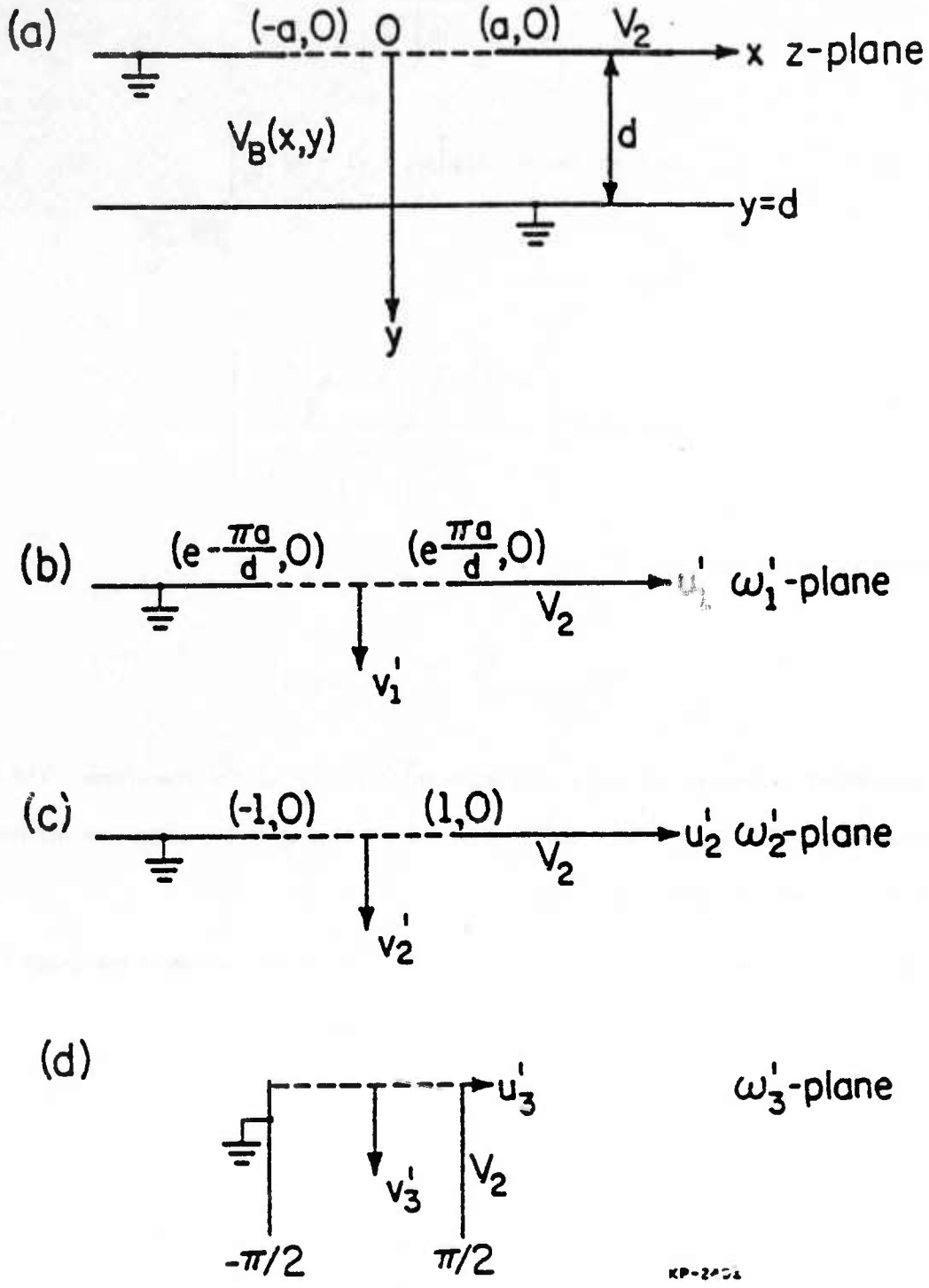

Fig. 6. Conformal mappings used to solve for $V_B(x,y)$.
(a) z-plane
(b) ω_1'-plane
(c) ω_2'-plane
(d) ω_3'-plane

$$\omega_2 = \frac{\omega_1 + \cosh\left(\frac{\pi a}{d}\right)}{\sinh\left(\frac{\pi a}{d}\right)} \tag{3.21}$$

$$\omega_3 = \sin^{-1}\omega_2 = -j\log\left(j\omega_2 + \left(1 - \omega_2^2\right)^{1/2}\right) \tag{3.22}$$

Thus,

$$\omega_3 = \sin^{-1}\left(\frac{-\exp\left(-\frac{\pi}{d}z\right) + \cosh\left(\frac{\pi a}{d}\right)}{\sinh\left(\frac{\pi a}{d}\right)}\right) \tag{3.23}$$

This yields, as seen in Fig. 5d,

$$V_A(x,y) = \frac{V_1}{\pi}\left(\frac{\pi}{2} - \text{real}\,(\omega_3)\right) \tag{3.24}$$

Three successive mappings are used to ensure invertibility of the transform. The Schwartz-Christoffel method could have been used to obtain the mapping, but it doesn't ensure invertibility, and a non-invertible mapping is of little use.

$V_B(x,y)$ can be solved for, in a similar manner. The three successive mappings for $V_B(x,y)$ ω_1', ω_2' and ω_3', are shown in Figs. 6b-6d. The transformations are

$$\omega_1' = \exp\left(\frac{\pi}{d}z\right) \tag{3.25}$$

$$\omega_2' = \frac{\omega_1' - \cosh\left(\frac{\pi a}{d}\right)}{\sinh\left(\frac{\pi a}{d}\right)} \tag{3.26}$$

$$\omega_3' = \sin^{-1}\omega_2' = -j\log\left[j\omega_2' + \left|1 - (\omega_2)^2\right|^{1/2}\right] \tag{3.27}$$

Thus,

$$\omega_3' = \sin^{-1}\left[\frac{\exp\left(\frac{\pi}{d}\,z\right) - \cosh\left(\frac{\pi a}{d}\right)}{\sinh\left(\frac{\pi a}{d}\right)}\right] \tag{3.28}$$

From Fig. 6d one can easily find the potential to be

$$V_B(x,y) = \frac{V_2}{\pi}\left[\text{real}\,(\omega_3') + \frac{\pi}{2}\right] \tag{3.29}$$

Hence, the potential V(x,y), under the constraints of Eqs. (3.8) to (3.12), has been found.

$$V(x,y) = \frac{V_1}{\pi}(\text{real}\,(w_3)+\frac{\pi}{2})+\frac{V_2}{\pi}(\text{real}\,(w_3')+\frac{\pi}{2})\,. \tag{3.29a}$$

An auxiliary problem to that posed by Eqs. (3.8) to (3.12) is that of constant field in the gap and grounded Schottky plates as shown in Fig. 7. The equations that must be satisfied are

$$\nabla^2 V_c(x,y) = 0 \tag{3.30}$$

$$V_c(x,d) = 0 \tag{3.31}$$

$$V_c(x,0) = 0,\ |x| > a \tag{3.32}$$

$$E_y(x,0) = \frac{-\partial V_c(x,0)}{\partial y} = E_s,\quad -a < x < a\,. \tag{3.33}$$

$V_c(x,y)$ can be found by using a superposition of V(x,y) with $V_1 = V_2 = V_o$, where $V_o = E_s d$, and a linear potential $V = \frac{-V_o}{d}(d-y)$. Letting $V_1 = V_2 = V_0$ in Eqs. (3.10) and (3.11), Eq. (3.29a) becomes

$$V(x,y) = \frac{V_o}{\pi}\left[\pi - \text{real}(\omega_3) + \text{real}(\omega_3')\right]. \tag{3.34}$$

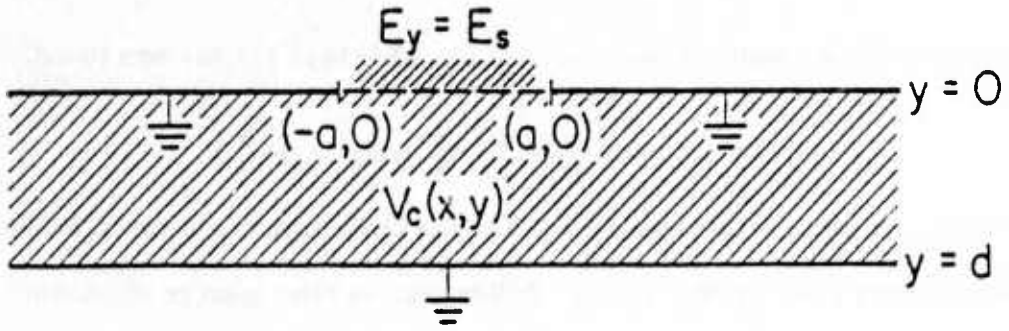

Fig. 7. Structure used to solve for $V_c(x,y)$.

$V(x,y)$ has a vanishing normal electric field between $-a < x < a$, that is, $E_y(x,0) = 0$ for $-a < x < a$, while the linear potential $V = \frac{-V_o}{d}(d-y)$ has an electric field of $E_y(x,0) = \frac{V_o}{d}$, which equals E_s. In addition $V(x,y)=V_o$ at $y=0$ and the linear potential equals $-V_o$ at $y=0$; hence, their sum is zero at $y=0$. Adding the two potentials together satisfies the boundary conditions and yields

$$V_c(x,y) = \frac{E_s d}{\pi}\left[\pi - \text{real}(\omega_3) + \text{real}(\omega_3)\right] - E_s(d-y) \tag{3.35}$$

$V_c(x,y)$ is zero for $x < -a$ and $x > a$, and $E_{cy}(x,0) = E_s$ for $-a < x < a$. Figure 8 illustrates the superposition used to find $V_c(x,y)$ for the structure of Fig. 7.

There is a simple relation between E_s and the sheet charge between $-a < x < a$ in Fig. 7. That is, the sheet charge, ρ_s, equals ϵE_s.

$$\rho_s = \epsilon E_s. \tag{3.36}$$

Thus, the problem of a uniform sheet charge ρ_s between -a and a at the surface is equivalent to that specified by Eqs. (3.30) to (3.33), which is shown in Fig. 7.

The potential of the structure of Fig. 7 can also be used to obtain the potential in Region I of Fig. 9 if the ratio $\frac{a}{d}$ is small. The potential in Fig. 9 must satisfy Laplace's equation and the following boundary conditions:

$$V_I(x,0) = V_{II}(x,0) = 0, \quad |x| > a$$

$$V_I(x,d) = 0$$

$$\epsilon_2 \frac{\partial V_{II}(x,0)}{\partial y} - \frac{\epsilon_1 \partial V_I(x,0)}{\partial y} = \rho_s, \quad -a < x < a.$$

$V_I(x,y)$ of Fig. 9 shall be solved for using $V_c(x,y)$. $V_{II}(x,y)$ is left unknown and is usually not required to be known.

Let the surface potential in the gap of Fig. 7 be called $V(x)$. That is, $V_c(x,0) = V(x)$ for $-a < x < a$. Let the potential in the gap of Fig. 9 be called $V'(x)$. That is, $V_I(x,0) = V'(x)$ for $-a < x < a$. $V(x)$ could have been calculated in Fig. 7 using a capacitance argument. One can view the gap as being broken up into many infinitesimally small plates each with a small charge, $\rho_s(x)$, on them.

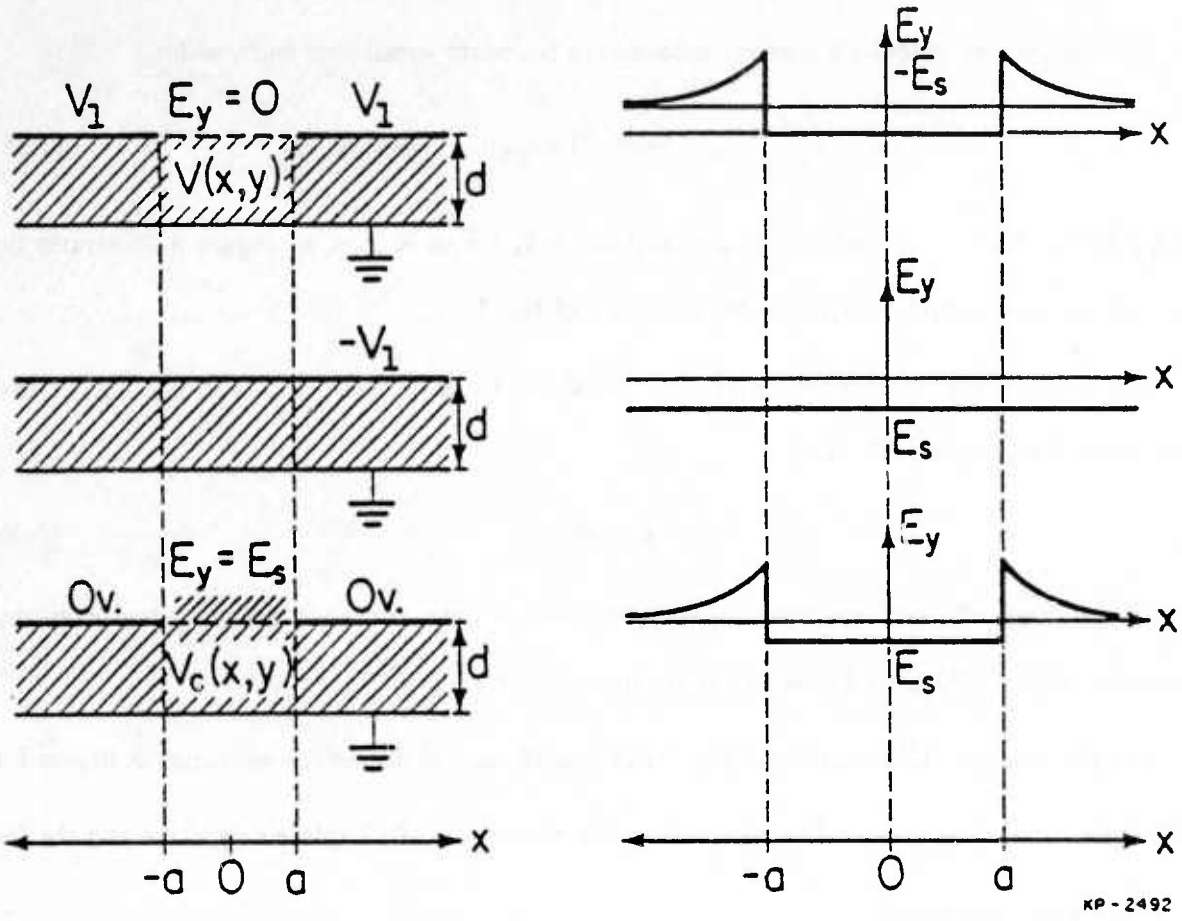

Fig. 8. Superposition of an isolated gap with symmetrical biasing and linear potential to form $V_c(x,y)$.

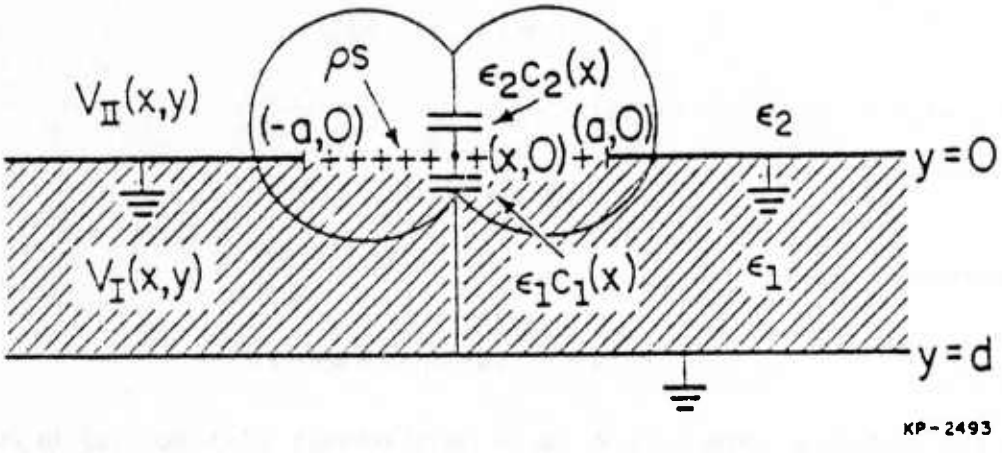

Fig. 9 Capacitive components from a point (x,0), where -a < x < a, to the grounded planes. The total capacitance is a sum of two components, $\epsilon_1 C_1(x)$ and $\epsilon_2 C_2(x)$.

The charge on these capacitors will be $\epsilon_1 E_s(x)$ where $E_s(x)$ represents the normal electric field at y=0. Each of the small plates will have a capacitance to the Schottky plates. This capacitance will depend on position. If the capacitance at every point were known at every point in the gap, then the potential could be calculated at every point. Let $C_T(x)$ represent the capacitance at point x. Then,

$$V(x) = \rho_s(x)/C_T(x).$$

Figure 9 shows that there are two contributions to $C_T(x)$. Let $C_1(x)$ and $C_2(x)$ represent free space capacitances, and ϵ_1 and ϵ_2 represent relative permittivities. Then, $\epsilon_2 C_2(x)$ is the capacitance through the dielectric above the substrate, and $\epsilon_1 C_1(x)$ is the capacitance through the substrate. Hence,

$$C_T(x) = \epsilon_1 C_1(x) + \epsilon_2 C_2(x).$$

For the case of $\epsilon_2 = 0$, $C_T(x) = \epsilon_1 C_1(x)$. Thus,

$$\rho_s(x) = V(x)\epsilon_1 C_1(x).$$

For $\epsilon_2 \neq 0$ one obtains

$$\rho_s(x) = V'(x)[\epsilon_1 C_1(x) + \epsilon_2 C_2(x)].$$

If the gap is small, a simple relation can be found between V'(x) and V(x). In small gap cases, $C_1(x) \approx C_2(x)$ as the ground plane at y=d will have negligible effect on the capacitance $C_1(x)$ if the gap is small compared to d. Then,

$$q(x) = V(x)\epsilon_1 C_1(x) \approx V'(x)(\epsilon_1 C_1(x) + \epsilon_2 C_1(x))$$

$$V'(x) = \frac{\epsilon_1}{\epsilon_1 + \epsilon_2} V(x) .$$

Thus, the relationship between V'(x) and V(x) is linear with the linear factor being $\epsilon_1/(\epsilon_1 + \epsilon_2)$. It should be noted that V(x) and V'(x) are only the potentials on the boundary. However, if the potentials on the boundary scaled by $\epsilon_1/(\epsilon_1 + \epsilon_2)$ then all of the potentials in the interior will also be scaled by the same factor. The potential for Fig. 9 is hence the potential $V_c(x,y)$, given in Eq. (3.35), scaled by $\epsilon_1/(\epsilon_1 + \epsilon_2)$.

$$V_1(x,y) = \frac{p_s}{\epsilon_1 + \epsilon_2} \left| \frac{d}{\pi} \left[\pi - \text{real}(\omega_3) + \text{real}(\omega_3) \right] - (d-y) \right| \tag{3.37}$$

where the substitution $E_s = \rho_s/\epsilon_1$ has been made.

This solution is compared with the Fourier series solution, which will be discussed in the next section, and the results are presented in Table 1. Table 1 shows that Eq. (3.37) is valid for ratios of a/d less than or equal to 1/3.

The potential of Fig. 4a for the case $V_1 = V_2$ and $\frac{a}{d} \leqslant 1/3$ can now be expressed. It is the sum of a linear potential $\frac{V_1}{d}(d-y)$ and Eq. (3.37) with $\rho_S = -\epsilon_1 V_1/d$.

$$V_1(x,y) = \frac{2\epsilon_1 + \epsilon_2}{\epsilon_1 + \epsilon_2} \frac{V_1}{d}(d-y) - \frac{\epsilon_1}{\epsilon_1 + \epsilon_2} \frac{V_1}{\pi}(\pi - \text{real}(w_3) + \text{real}(w_3')) \tag{3.38}$$

Thus, the potential due to an isolated gap has been solved for using the solution to Fig. 7, i.e., Eq. (3.35). Equation (3.35) turns out to be quite useful for analyzing the effects of gaps in an

TABLE 1

Table 1. Verification of ϵ_2 approximation for d=1 and E_s=1. Only maximum potentials are specified.

a/d	ϵ_2/ϵ_1	Fourier Series	ϵ_2 Approx.	% Error
1/2	1/13	.432V.	.423V.	2.13%
1/2	8/13	.297	.282	5.32%
1/2	1	.243	.228	6.58%
1/3	1/13	.302	.296	2.03%
1/3	8/13	.205	.197	4.06%
1/3	1	.166	.160	3.75%
1/4	1/13	.231	.226	2.21%
1/4	8/13	.155	.151	2.65%
1/4	1	.126	.122	3.28%
1/5	1/13	.186	.183	1.64%
1/5	8/13	.125	.122	2.46%
1/5	1	.101	.099	2.02%
1/7	1/13	.134	.132	1.52%
1/7	8/13	.090	.088	2.27%
1/7	1	.073	.071	2.82%
1/10	1/13	.095	.093	2.15%
1/10	8/13	.063	.062	1.61%
1/10	1	.051	.050	2.00%

otherwise uniformly biased device. Problems that have more than one gap can be solved provided that the voltages on the plates are all the same. Equation (3.35) can be translated and superimposed with the original equation to simulate the effects of multiple gaps in an otherwise uniform structure. It should be noted that this doesn't yield an exact solution and that superpositions of Eq. (3.35) should not be made if the gaps are too close together. A serious error could result. It is recommended that gaps of width 2a should not be superimposed any closer than a distance of 3a.

Equation (3.35) is plotted in Figs. 10-14 for various values of $\frac{a}{d}$, namely, 1/2, 1/3, 1/5, 1/7 and 1/10. In these plots, d=1 and $E_s = 1$. Thus, the plots are normalized. These figures can be used as a quick reference for the potentials of various structures. The potentials for structures like those in Fig. 1a and Fig. 1c can be obtained from Figs. 10-14 provided that the appropriate scaling factor is used. The constraints on the types of structures for which Figs. 10-14 can be used are

1) The surface voltage of the structure must be uniform except for the perturbation caused by plate separation.

2) Either $a/d \leq 1/3$ or $\epsilon_2 << \epsilon_1$.

Given that these constraints are satisfied, Figs. 10-14 can be used to calculate the absolute potential deviation from the one-dimensional potential given by Eq. (2.1) at a particular point.

The appropriate scaling factor (SF) is

$$SF = \frac{-\epsilon_1 d}{\epsilon_1 + \epsilon_2} E_S \tag{3.39}$$

where $\epsilon_1 E_S$ is the unperturbed charge density on the plate located at y=0. If V_a is the unperturbed voltage at y=0 then using Eq. (2.5)

$$E_S = \frac{V_a - V_{sp}(0)}{d}. \tag{3.40}$$

Another way to find E_S is to integrate the space charge density from the channel minimum point to the surface. Let y_m denote the channel minimum point. Then

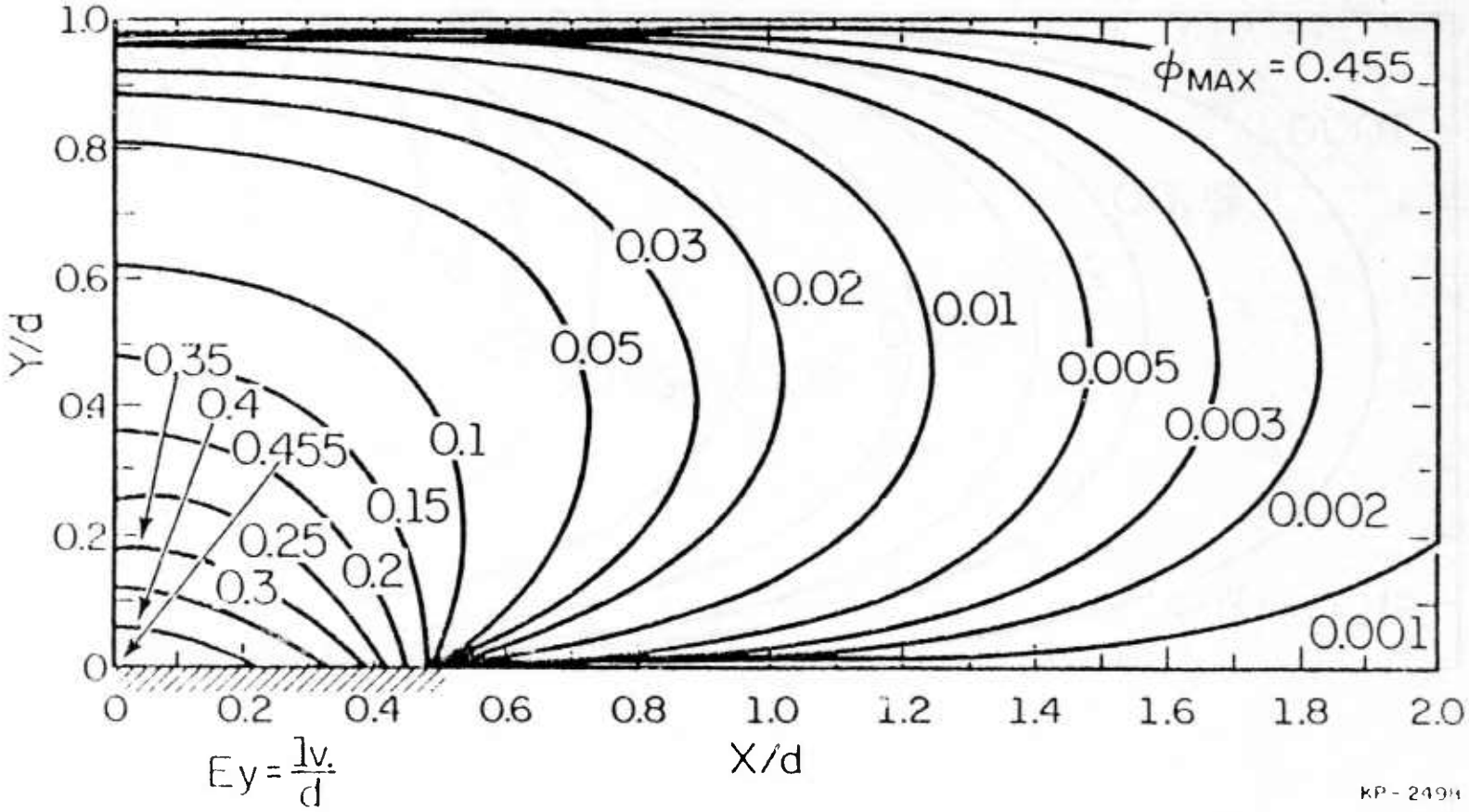

Fig. 10. Normalized potential deviation, for an isolated gap, $\left(\frac{a}{d} = 1/2\right)$.

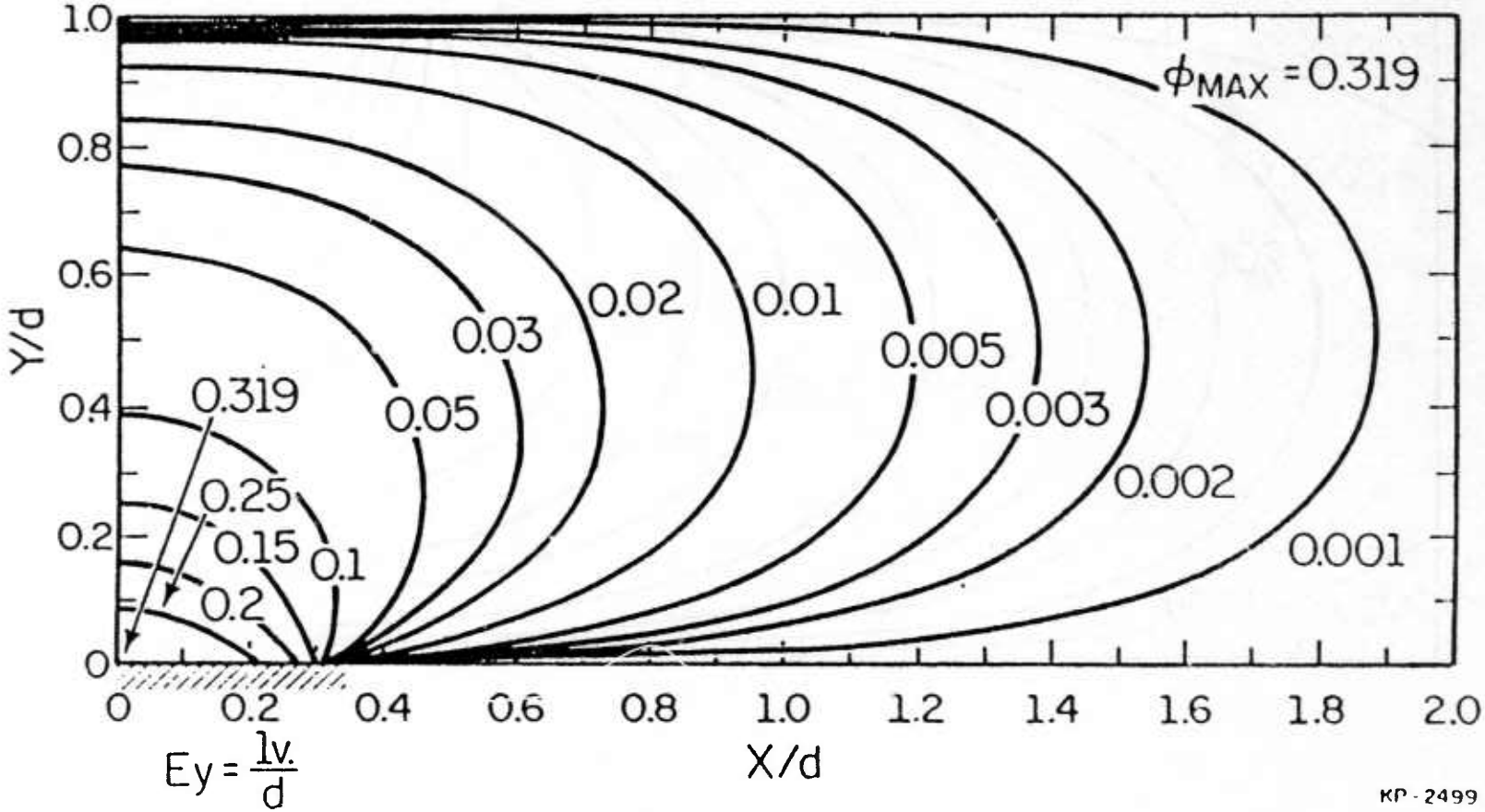

Fig. 11. Normalized potential deviation, for an isolated gap, $\left(\frac{a}{d} = 1/3\right)$.

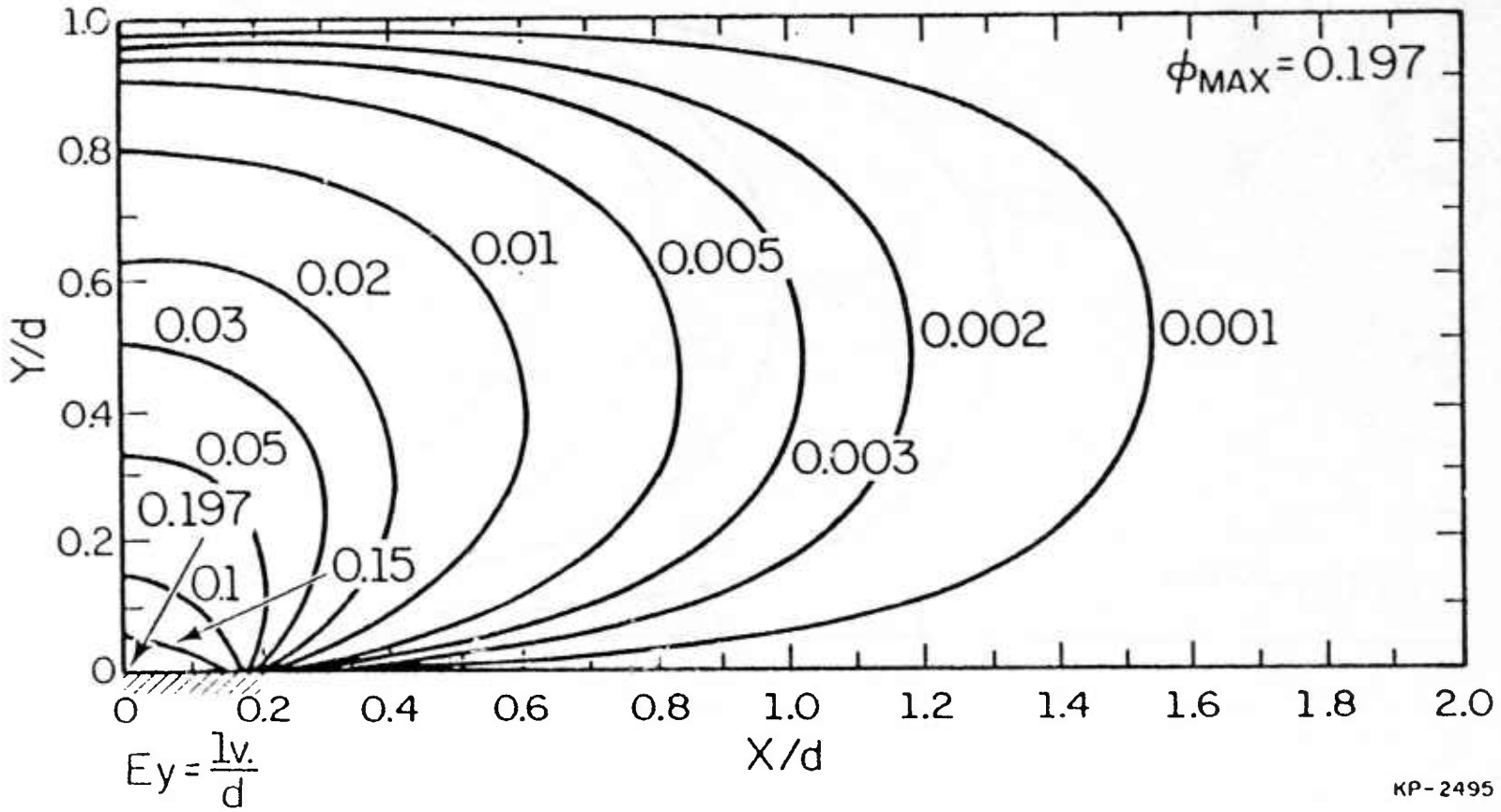

Fig. 12. Normalized potential deviation, for an isolated gap, $\left[\frac{a}{d} = 1/5\right]$.

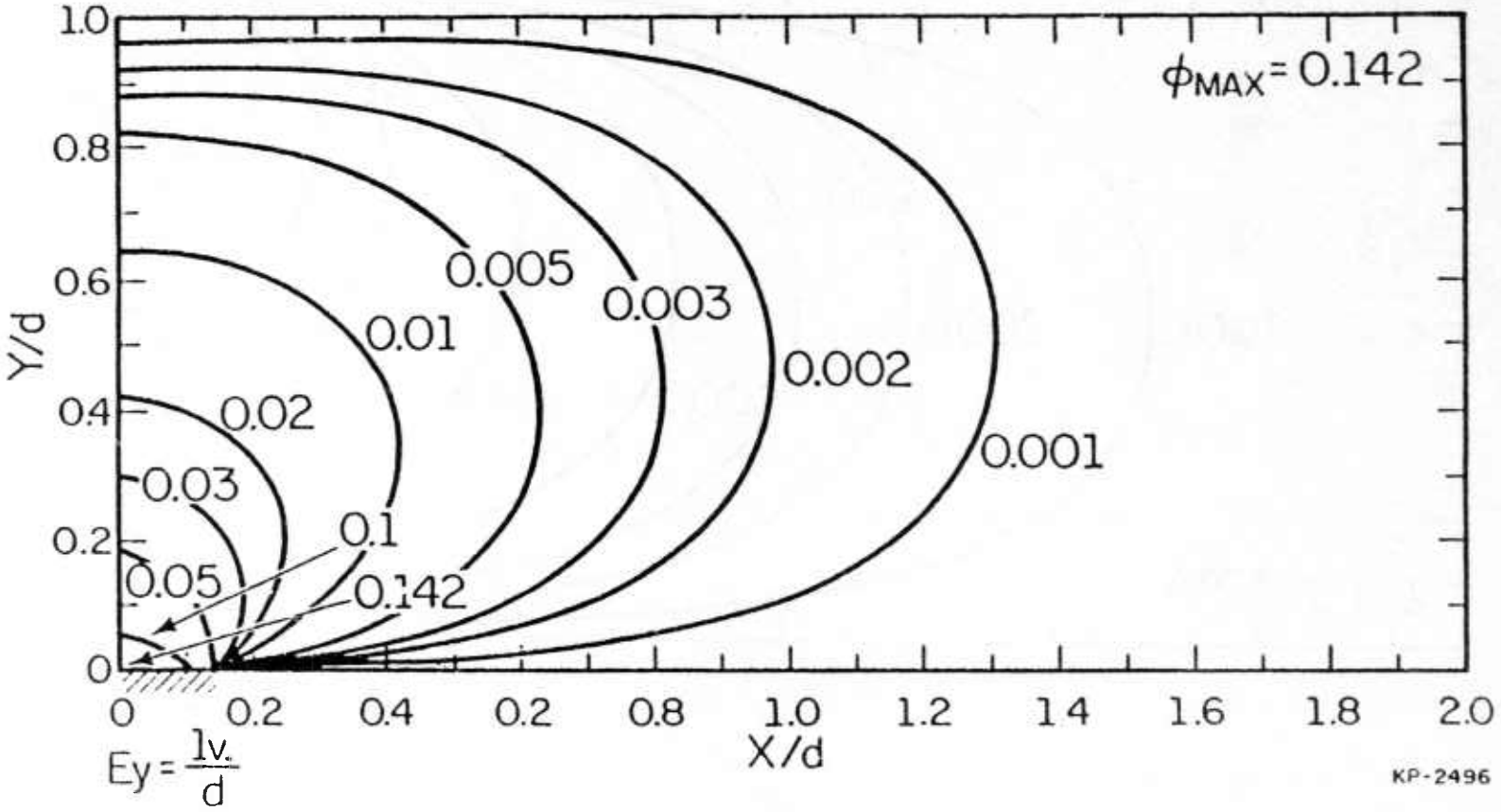

Fig. 13. Normalized potential deviation, for an isolated gap. $\left(\frac{a}{d} = 1/7\right)$.

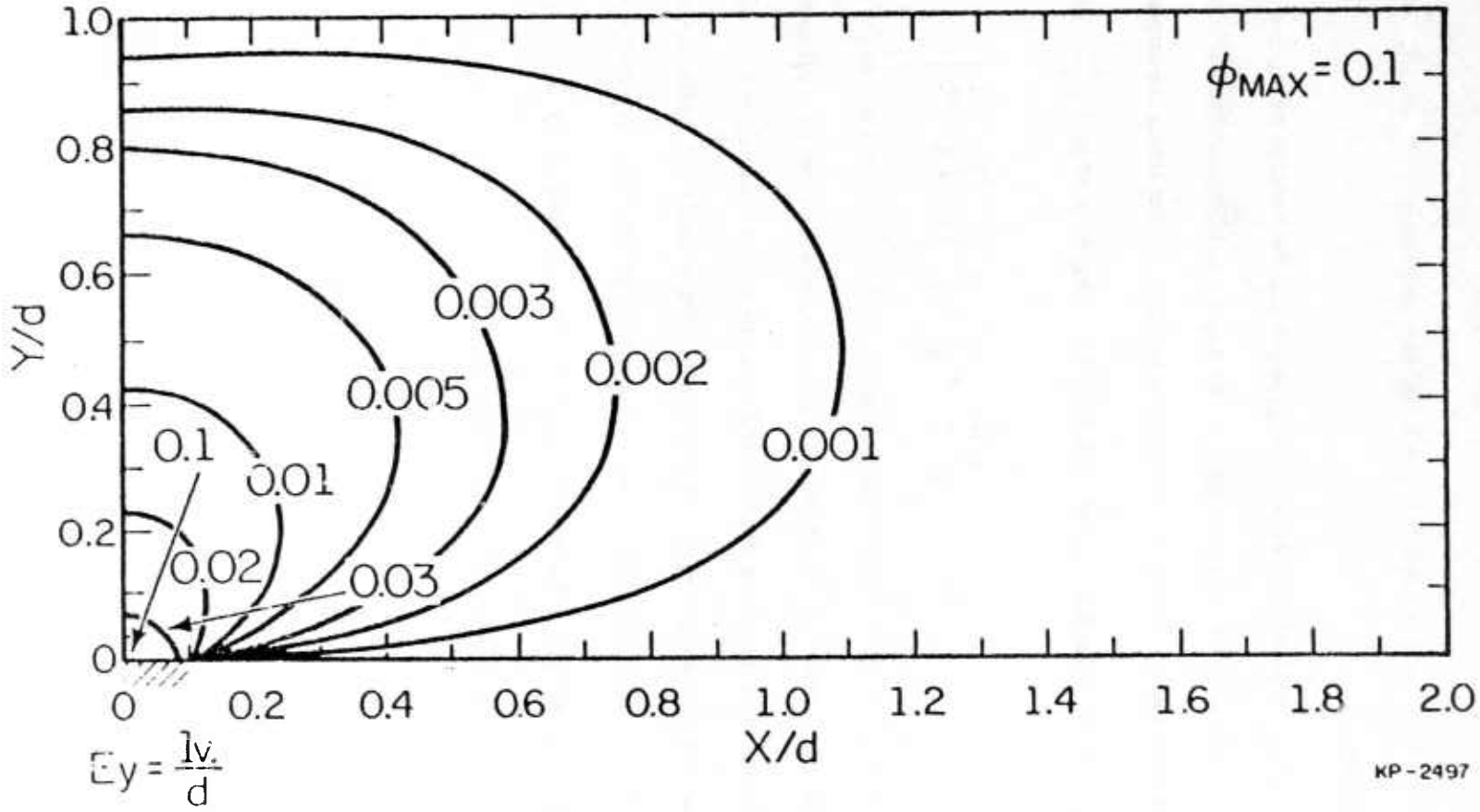

Fig. 14. Normalized potential deviation, for an isolated gap, $\left(\frac{a}{d} = 1/10\right)$.

$$E_S = \frac{1}{\epsilon_1} \int_0^{y_m} \rho(y)\, dy. \tag{3.41}$$

Hence, Figs. 10-14 can be used as a quick and easy reference for potentials caused by different device geometries.

A shallow implant of charge in the gaps can also be handled by adding a constant to the scaling factor. The constant will be equal to the electric field caused by the implanted charge. Let ρ_I equal the sheet charge density of the shallow implant. If one treats the implant as a delta function of charge at y = 0, then one can see from Eq. (3.41) that E_s is offset by $\frac{\rho_I}{\epsilon_1}$. Thus

$$E_s = \frac{V_a - V_{sp}(0)}{d} + \frac{\rho_I}{\epsilon_1} = \frac{1}{\epsilon_1} \left[\rho_I + \int_0^{y_m} \rho(y)\, dy \right]. \tag{3.42}$$

A note of caution is appropriate at this point. All of the expressions for potentials are derived under the assumption of full depletion; however, in a real device, full depletion may not occur depending on the bias on the channel and how the device was originally biased. In general, if the voltage at the surface in a region of plate separation exceeds the maximum voltage in the channel, then there is a high probability that the structure is not fully depleted and that the calculated potentials as given are not accurate. This situation is most likely to occur for a large $\frac{a}{d}$ ratio, hence, care should be taken when analyzing large gaps.

4. FOURIER SERIES METHOD

The previous section concentrated on the solution to Laplace's equation for isolated gap structures. It is possible to use the isolated gap case to simulate multiple gap structures; however, this may not always be a good approximation. Thus, a method for solving Laplace's equation with multiple gap structures is needed. Fourier analysis can be used for such a method.

Figure 15 shows a typical periodic structure which has three plates per period. Let the surface potential at y=0 be:

$$V(x,0) = a_o + \sum_{n=1}^{\infty} a_n \cos\frac{n\pi}{L}x + b_n \sin\frac{n\pi}{L}x$$

where L is the period of the structure. The boundary conditions that need to be satisfied are

$$V(x,d) = 0 \tag{4.1}$$

$$V(x,-\infty) = a_o \tag{4.2}$$

$$V(x,0) = V_i \text{ if } x\epsilon P_i \tag{4.3}$$

$$\epsilon_1\frac{\partial V_I}{\partial y}(x,0) = \epsilon_2\frac{\partial V_{II}}{\partial y} \text{ if } x\epsilon G \tag{4.4}$$

where P_i is the domain of points where the ith surface plate lies, V_i is the voltage on the ith plate, and G is the domain of points that fall in the gaps. Let R_I represent all points (x,y) between y=0 and y=d, and let the potential in this region be called $V_I(x,y)$. Also, let R_{II} represent all points such that $y<0$ and let the potential in this region be called $V_I(x,y)$. An expression for the potential in regions R_I and R_{II} can be found by applying the separation of variables to the Laplace equation. Fundamental solutions from this method are of the form sinh(ky)sin(kx), sinh(ky)cos(kx), cosh(ky)sin(kx) and cosh(ky)cos(kx). The values of k are restricted to $k = \frac{n\pi}{L}$, n = 1,2,...., by the periodicity requirement of the potential. Another fundamental solution of the Laplace equation is a linear potential of the form Ay + B. A linear combination of these fundamental solutions can be used to obtain an expression for the potential in regions R_I and R_{II}. The unknown coefficients must

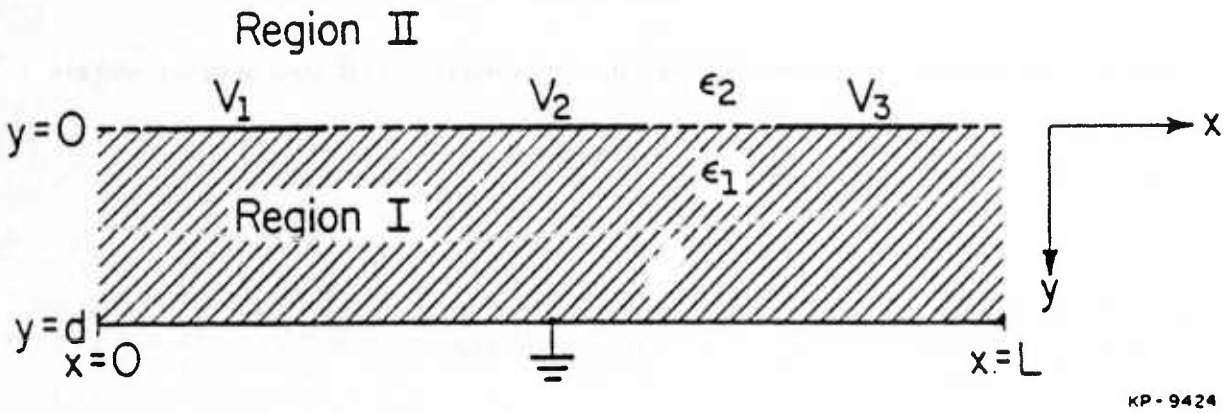

Fig. 15. Exemplary periodic structure.

then be evaluated to satisfy the boundary conditions. Solutions for the two regions that satisfy Eq. (4.1) and Eq. (4.2) are

$$V_I(x,y) = \frac{a_o(d-y)}{d} + \sum_n \frac{\sinh\left|\frac{n\pi}{L}(d-y)\right|}{\sinh\left|\frac{n\pi}{L}d\right|}\left|a_n \cos\frac{n\pi}{L}x + b_n \sin\frac{n\pi}{L}x\right|, \quad (x,y)\epsilon R_I$$

$$V_{II}(x,y) = a_o + \sum_n e^{-\frac{n\pi}{L}y}\left|a_n \cos\frac{n\pi}{L}x + b_n \sin\frac{n\pi}{L}x\right|, \quad (x,y)\epsilon R_{II} \; . \tag{4.5}$$

However, the boundary conditions of Eq. (4.3) and Eq. (4.4) are not satisfied. These two boundary conditions at y=0 are of two different types. Mixed boundary value problems like this are difficult to solve. In fact, there is no known deterministic way to solve for the Fourier coefficients, a_o, a_1,.... and b_1, b_2,..... Normal Fourier analysis can not be used as the surface potential is not known everywhere on the surface y=0. Thus, the best that can be done is to try to find a solution that is a best fit to the boundary conditions.

McKenna and Schryer have done a study of potentials for charge transfer devices [3]. In their analysis, they used a linear superposition of splines to represent the charge on the plates. Then, using a least-square optimization routine, they picked the combination of splines that minimized the error in Eq. (4.3) in a least-square manner. Also, in their analysis, Eq. (4.4) was automatically satisfied by the splines used. However, truncation of the Fourier series of the splines can lead to errors in Eq. (4.4). It is not expected that this error would be significant, however. There is little doubt that McKenna's and Schryer's method yields accurate results; however, the computation necessary is quite lengthy and involved. A method is to be presented that needs little computer memory and no special software, but yields very accurate results as compared with exact solutions known using conformal mapping techniques.

Expanding ρ_S at y=0 can, indeed, require many Fourier terms. However, expanding the potential at y=0 doesn't require nearly as many terms because the potential is continuous, but the charge density is not necessarily continuous. Unless the electric fields must be known exactly at the

surface, y=0, then directly expanding the potential at the surface in a Fourier series should yield suitably accurate results. Equation (4.5) shows that contributions of higher-order terms decay exponentially into the depth of the substrate. Hence, the error due to truncating the series decays exponentially into the depth of the substrate. Thus, there could be a seemingly large error in the potential or electric field at the surface while a small error exists in the potential or electric field at the depth at which the mobile charge resides.

The first step in obtaining the Fourier coefficients in Eq. (4.5) is to truncate the series. Thus,

$$V_I(x,y) \approx \frac{a_o(d-y)}{d} + \sum_{n=1}^{N} \frac{\sinh\left[\frac{n\pi}{L}(d-y)\right]}{\sinh\left[\frac{n\pi}{L}d\right]} \left[a_n \cos\frac{n\pi}{L}x + b_n \sin\frac{n\pi}{L}x\right], \quad (x,y)\epsilon R_I$$

$$V_{II}(x,y) \approx a_o + \sum_{n=1}^{N} e^{\frac{n\pi}{L}y}\left[a_n \cos\frac{n\pi}{L}x + b_n \sin\frac{n\pi}{L}x\right], \quad (x,y)\epsilon R_{II}. \tag{4.6}$$

The next step is to sample the surface of the periodic structure and determine the constraining equations for those points from Eq. (4.6). If a point, x_o, falls on the ith plate, the P_i domain, then the constraining equation is

$$V_i = a_o + \sum_{n=1}^{N} a_n \cos\frac{n\pi}{L}x_o + b_n \sin\frac{n\pi}{L}x_o. \tag{4.7}$$

If the point, x_o, falls in a gap, the G domain, the constraining equation at the point x_o is

$$\sum_{n=1}^{N} \frac{n\pi}{L}\left[\coth\left(\frac{n\pi}{L}d\right) + \frac{\epsilon_2}{\epsilon_1}\right]\left[a_n \cos\frac{n\pi}{L}x_o + b_n \sin\frac{n\pi}{L}x_o\right] = \frac{-a_o}{d}. \tag{4.8}$$

There are various ways to satisfy these constraining equations at the sampled points. One can choose to have more sample points than Fourier coefficients or one can choose to have the same number of sample points as Fourier coefficients. If more sample points than coefficients are used, then an optimization program must be used to minimize the error in the constraining equations. Linear programming would be a good way to achieve this. When using an optimization routine, there is a great deal of liberty in how the error can be defined. Thus, care must be taken in the

definition of the error to avoid erroneous results.

If, on the other hand, the number of sample points equals the number of coefficients, then one has N constraining equations with N unknowns which can be solved using Gaussian elimination. The programming complexity of solving N equations in N unknowns is far, far less than optimizing N unknowns at N+m points; however, the computer memory is not used in as an efficient manner as in an optimization routine. Thus, there is a trade-off between programming complexity and efficient hardware use.

For this thesis, N sample points were used to solve for N coefficients. It was found that computer memory space was not the limiting factor in our calculations but that numerical error was the limiting factor. If the sample points were picked too close together, the matrices used would become singular.

How one chooses the sample points is crucial. The solution can explode if the sample points are not chosen carefully. Instinct would lead us to sample more densely in the regions of most rapid variation. This should be avoided, however, as the solution that is assumed is band-limited, but the true solution is not. At the corners of the Schottky plates the potential varies very rapidly. This rapid variation cannot be simulated with a truncated series. Thus, a small zone should be left, near the corner of every Schottky plate, in which no sample points are chosen. The best results that were achieved were with uniform sampling over [0,L) except for very small zones near the edge of every Schottky plate, in which no sampling was done.

If an even structure is analyzed, then all of the sine terms are zero. In addition, sample points should be chosen over the interval $[0, \frac{L}{2}]$. Sampling over the full interval may result in degenerate equations.

Using the above procedure, it is possible to get accurate expressions for the potential. To check the accuracy of the Fourier series method, the potential for the structure of Fig. 7 was calculated using conformal mapping and the Fourier series method. Parameters used were d = 1 μm, E = 10^6 V/m and various ratios of a/d where a is the half-width of the gap and d is the distance

between the two planar boundaries. The maximum potential of the structure is used as a reference of comparison. Table 2 compares these values as calculated by the two methods. The table also gives the overshoot and ripple of the potentials as calculated by the Fourier series method. As one can see, the two methods agree within 2% of each other and the Fourier series solutions exhibit low overshoot and ripple. The error in Table 2 is defined as

$$\% \text{ Error} = \frac{\text{Fourier Series} - \text{Conformal}}{\text{Conformal}} \times 100.$$

It should be noted that if one desires the solution of the Poisson equation for structures like those in Fig. 1, then Eq. (2.4) must be added to the Fourier series solution, which is a solution to Laplace's equation, with the plate voltages offset by $V_{sp}(0)$ as described previously in Chapter 2.

Table 2

Table 2. Comparison of Fourier series method with conformal mapping solution for d=1, $\epsilon_2 = 0$ and $E_S = 1$.

a/d	Fourier Series	Overshoot	Ripple	Terms	Conformal Mapping	% Error
1/2	.462V.	.87%	<.1%	80	.455V.	1.54
1/5	.200	1.0%	<.1%	80	.197	1.52
1/10	.102	.98%	<.1%	80	.100	2.00

5. CONCLUSION

Two methods of calculating two-dimensional electrostatic potentials for various buried channel charge transfer device geometries were presented which emphasized the effects of plate separation but did not include the effects of mobile charge. One method used conformal mapping and provided a quick and accurate way to determine the potential for single-isolated gap problems. The other method used Fourier analysis for arbitrary surface structures. These two methods were compared and, generally, agreed within 2%. In addition, normalized data was presented for the important case of an isolated gap in a uniformly biased device. This data can be used as a quick and easy reference for the effects of plate separation on the electrostatic potential of buried channel charge transfer devices.

List of References

[1] J. McKenna and N.L. Schryer, "On the Accuracy of the Depletion Layer Approximation for Charge Coupled Devices," *The Bell System Technical Journal*, vol. 51, pp. 1471-1485, Sept. 1972.

[2] J. McKenna and N.L. Schryer, "The Potential in a Charge Coupled Device with No Mobile Minority Carriers and Zero Plate Separation," *The Bell System Technical Journal*, vol. 52, pp. 669-698, May-June 1973.

[3] J. McKenna and N.L. Schryer, "The Potential in a Charge-Coupled Device with No Mobile Minority Carriers," *The Bell System Technical Journal*, vol. 52, pp. 1765-1793, Dec. 1973.

[4] M.G. Collet and A.C. Vliegenthart, "Calculations on Potential and Charge Distributions in the Peristaltic Charge- Coupled Devices " *Philips Research Reports*, vol. 29, pp. 25-44, 1974.

[5] H.W. Hanneman and L.J.M. Esser, "Field and Potential Distributions in Charge-Transfer Devices," *Philips Research Reports*, vol. 30, pp. 56-72, 1975.

[6] Handi El-Sissi, "Potential and Fields in Buried-Channel CCD's: A Two-Dimensional Analysis and Design Study," *IEEE Transactions on Electron Devices*, vol. ED-22, pp. 77-91, March 1975.

[7] Ira Deyhimy, Richard C. Eden, James S. Harris, Jr., "GaAs and Related Heterojunction Charge-Coupled Devices," *IEEE Transactions on Electron Devices*, vol. ED-27, pp. 1172-1180, June 1980.

[8] Kristin M. DeMeyer and Gilbert J. Declerck, "A New Method for the Two-Dimensional Calculation of the Potential Distribution in a Buried-Channel Charge-Coupled Device: Theory and Experimental Verification," *IEEE Transactions on Electron Devices*, vol. ED-28, pp. 313-321, March 1981.

[9] John Yuan-Tai Chen and C.R. Viswanathan, "An Interactive Two-Dimensional Model for Designing VLSI CCD's," *IEEE Transactions on Electron Devices*, vol. ED-30, pp. 1135-1142, Sept. 1983.

[10] T.O. Lester and D.L. Pulfrey, "A New Method Based on the Superposition Principle for the Calculation of the Two-Dimensional Potential in a Buried-Channel Charge-Coupled Device," *IEEE Transactions on Electron Devices*, vol. ED-31, pp. 999-1001, July 1984.

APPENDIX D

Slowness Surface Measurements for Zero and Five Degree [100]-cut GaAs

by

W.D. Hunt, R.L. Miller,[+] and B.J. Hunsinger[++]

This work was supported by the United States Air Force under contract F30602-84-C-0132, the Joint Service Electronic Program under contract N00014-84-C-0149 and Electronic Decisions Incorporated as a subcontract under prime contract number F30602-85-C-0170 sponsored jointly by the Defense Advanced Research Projects Agency and the United States Air Force

+ Current address: Gould Research Center, Rolling Meadows, Illinois

++ Other affiliation: President, Electronic Decisions Inc., Urbana, Illinois

Abstract

A modification to accommodate anisotropic loss is made to a method developed by Murray and Ash for computing the SAW slowness surface of piezoelectric substrates. The resulting algorithm is used to determine the slowness surface for the leaky or pseudo-surface wave which propagates on [100]-cut GaAs and for a cut five degrees off from this. The data thus obtained are used in a diffraction theory computer program to predict the shape of beam profiles as they propagate in the substrate material and accurate predictions of beam shapes are obtained.

Introduction

In recent years there has been growing interest in the development of monolithic signal processors on GaAs substrates. An example of such a device is the Acoustic Charge Transport (ACT) device[1] which is very simply a charge-coupled device (CCD) for which the charge packets are carried by the potential propagating with a surface acoustic wave (SAW) rather than the potential imposed by clock pulses applied to surface electrodes. In order that better ACT devices may be developed, more knowledge about the SAW properties of GaAs is needed. Heretofore GaAs has not been of great interest as a substrate material for SAW devices because it is so weakly piezoelectric. Its electromechanical coupling constant is one-sixtieth of that for $LiNbO_3$ and one-half of that for ST-Quartz. Because of this, SAW devices with reasonable efficiency, bandwidth, and processing gain are not feasible on GaAs. However, since GaAs is both a piezoelectric crystal and a semiconductor it is an attractive substrate material for ACT devices.

Were the wave propagating in the [110] direction on [100]-cut GaAs a Rayleigh wave as it is for YZ $LiNbO_3$ and ST-Quartz one could use the rather large existing body of knowledge describing propagation in those materials. However, the wave of interest in GaAs is a leaky or pseudo-surface wave which is a Rayleigh wave coupled to a transverse bulk shear as shown in Figure 1. For propagation precisely along the [110] direction the transverse shear component vanishes but as the propagation vector deviates from this direction the amount of energy radiated into the bulk shear component increases dramatically. An important tool often used to describe acoustic propagation in crystalline materials is the slowness surface which by convention is the magnitude of $\vec{k}\omega$ (i.e. the reciprocal of the velocity vector) as a function of its direction. Towards an economy of words and because the same information is represented I herein use the term slowness surface to describe both the velocity and the attenuation as functions of propagation direction. Theoretical studies by Penunuri[2] and by Penunuri and Lakin,[3] utilizing the Christoffel equations, predicted the slowness surface for zero-degree GaAs as shown in Figures 2 and 3. Observe in Figure 3 how quickly the attenuation increases as the propagation wave vector points away from the [110] direction. In just

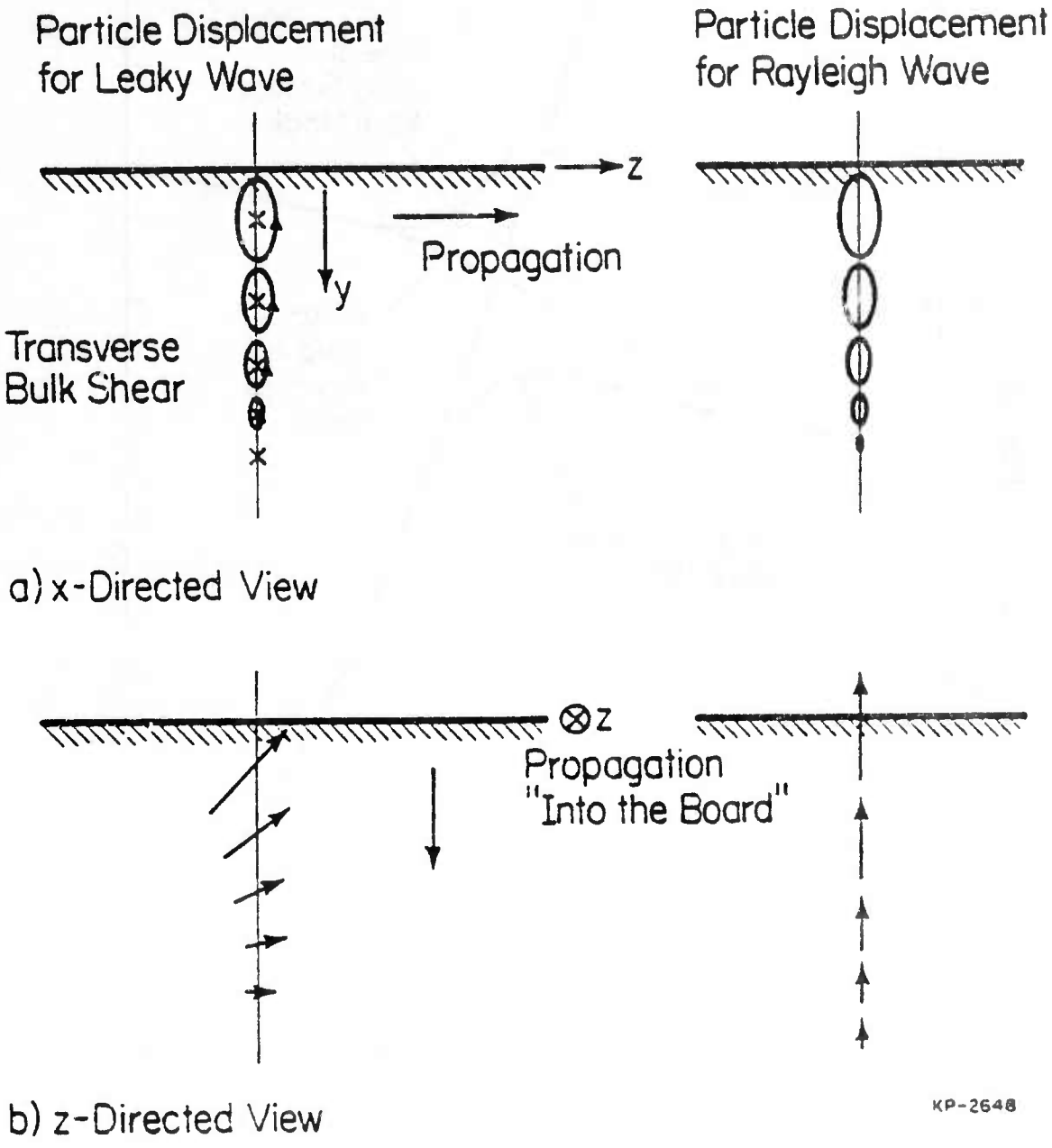

Figure 1. Pictorial representations of particle displacement for leaky wave.

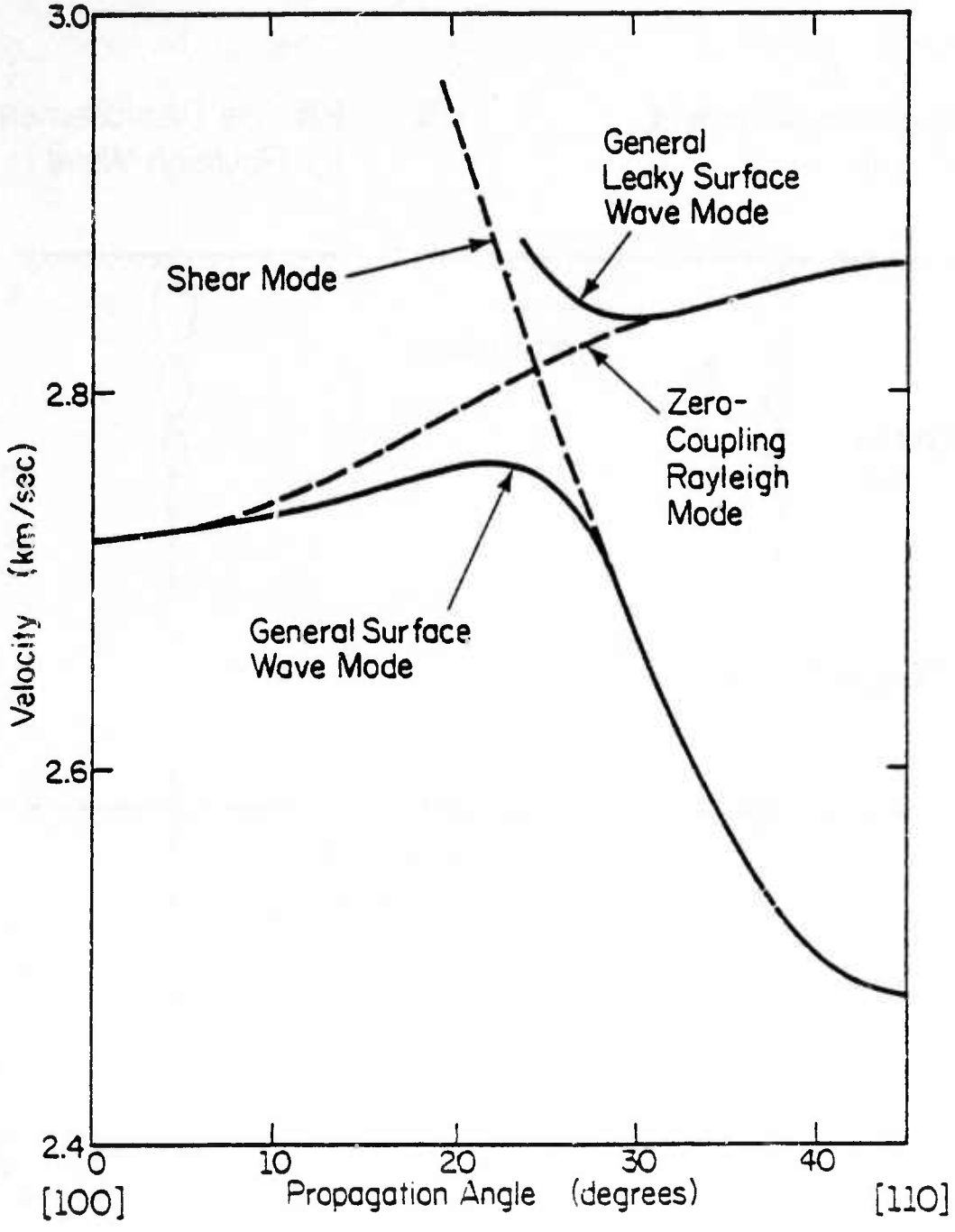

Figure 2. Surface wave velocity for [100]-cut GaAs.[2,3]

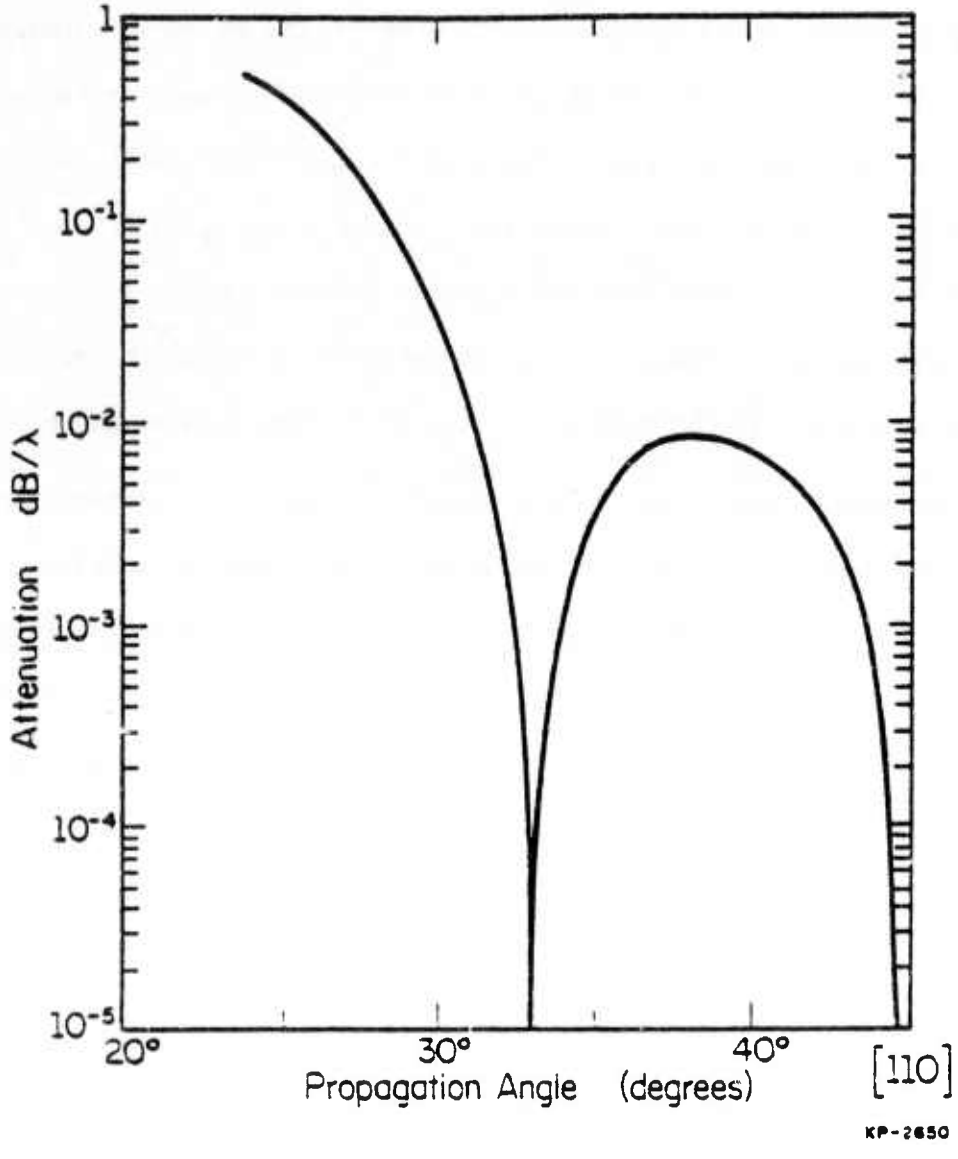

Figure 3. Attenuation of the leaky wave for [100]-cut GaAs.[2,3]

two degrees the attenuation due to the bulk shear has increased two orders of magnitude! Note, however, that this does not represent all of the attenuation. It represents only the acoustic power radiated into the bulk shear and does not include the normal viscous losses of the Rayleigh wave. One should keep in mind, though, that the attenuation shown in Figure 3 is a good indication of the increasing amplitude of the bulk shear as the wave vector deviates from the [110] direction. To the authors knowledge there has been no experimental evidence to verify or nullify the theoretically derived attenuation data and this paper represents the first publication of such data.

A key point, and one which motivated this study of zero and five-degree wafers, is that the substrate upon which epilayers are normally grown are not precisely [100]-cut but are instead two degrees off from that as shown in Figure 4. The reason for using the two-degree wafer is unclear. Some sources say that this is essential for the growth of high quality epitaxial layers[4] and others say that the evidence as to whether or not the surface normal being off by two degrees makes any difference is inconclusive. Regardless of this, the custom persists and epitaxial growth is typically performed on two degree wafers for GaAs and for other III-V compound semiconductors.

The method used to compute the slowness surface in this paper is the technique described by Murray and Ash[7] extended to deal with the anisotropic loss of the leaky wave on GaAs. The wave vector $k(\theta)$ is assumed to be complex and the resulting Helmholtz equation and subsequent Green's function can be used to derive the appropriate angular spectrum of plane waves formulation. Both the extended technique for computing the slowness surface and the diffraction theory used to propagate beam profiles result from this assertion that k be complex.

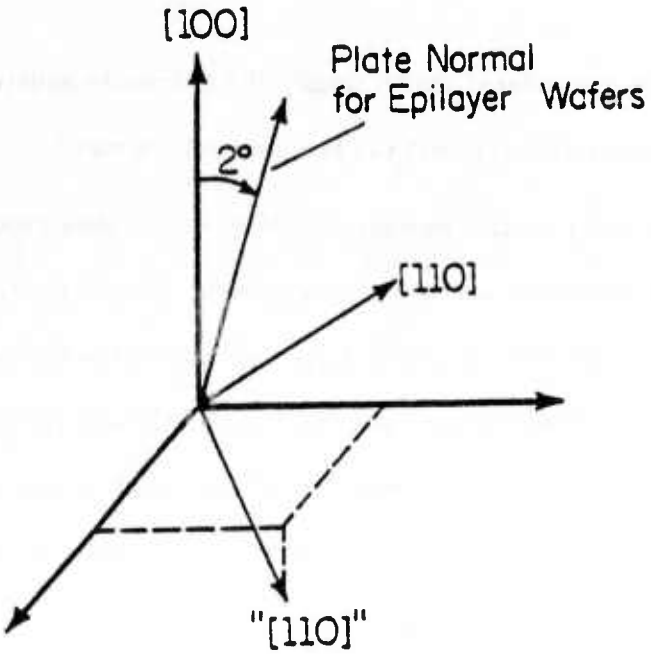

Figure 4. Crystal cut for conventional epilayer growth.

II. Methodology for Slowness Surface Determination

Murray and Ash[7] developed a method of computing the slowness surface for a SAW substrate from three laser probe scans made transverse to the direction of propagation as shown in Figure 5. The basis of this method is that the complex beam profile u can be represented by an angular spectrum of plane waves

$$u(x;z) = \frac{1}{2\pi} \int_{-\infty}^{\infty} U(k_x;z_o)\exp[i(k_x x + k_z(z - z_o))]dk_x \qquad (1)$$

where

$U(k_x;z_o)$ = Fourier transform of $u(x;z_o)$

$u(x;z_o)$ = complex wave amplitude of transverse scan taken at z_o

which derives from the requirement that u satisfy the Helmholtz equation. More details of the angular spectrum of plane waves approach can be found in Goodman.[8]

For the case of leaky waves it is important to note that the laser probe is only sensitive to the Rayleigh portion of the wave and not the transverse shear. As such the laser probe measurements, and indeed all of this formalism, describes the propagation of the Rayleigh portion of the wave which to first order is the portion of the wave which carries the electric potential. Thus, for example, the attenuation measured will be an indication of how much energy is lost from the Rayleigh wave - both through viscous losses and radiation into the bulk shear. In order to take into account the anisotropic loss we allow $k_z(\theta)$ to be complex, i.e.

$$k_z(\theta) = k_{zr}(\theta) + ik_{zi}(\theta) \qquad (2)$$

and this will give rise to an anisotropic exponential decay factor $e^{-k_{zi}(z-z_o)}$ in equation (1).

The relationship between the amplitudes in k-space of two subsequent transverse scans will be

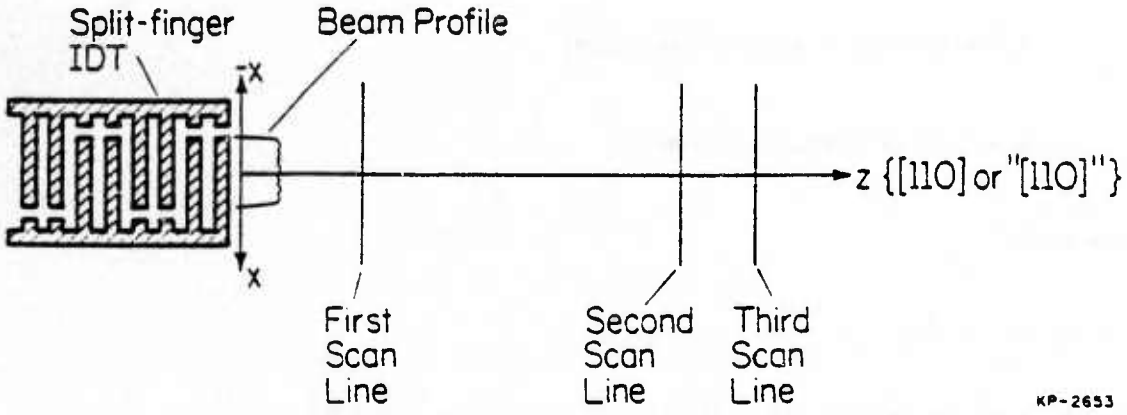

Figure 5. Transverse laser probe scans for slowness surface determination.

$$U_l(k_x;z_l) = U_m(k_x;z_m)e^{ik_z(z_l-z_m)} \tag{3}$$

i.e. the k-space representation or spectrum can be propagated in the z-direction by a complex phase factor due to the corresponding spectral component $k_z(k_x)$. If we write out the form of k_z we have

$$U_l(k_x;z_l) = U_m(k_x;z_m)e^{ik_{zr}(z_l-z_m)}\, e^{-k_{zi}(z_l-z_m)}. \tag{4}$$

Thus we see directly that since we can represent the spatial spectrum as

$$U_l(k_x;z_l) = A_l(k_x;z_l)e^{i\phi_l(k_x;z_l)} \tag{5}$$

where

A_l = magnitude of spectral component

ϕ_l = phase of spectral compone it

we can write

$$A_l(k_x;z_l) = A_m(k_x;z_m)e^{-k_{zi}(z_l-z_m)} \tag{6}$$

from which we can compute the imaginary portion of $k_z(k_x)$, namely

$$k_{zi} = \frac{1}{(z_m-z_l)}\, ln\left[\frac{A_l(k_x;z_l)}{A_m(k_x;z_m)}\right]. \tag{7}$$

To determine the real part of $k_z(\theta)$ we note

$$A_l(k_x;z_l)e^{i\phi_l} = A_m(k_x;z_m)e^{i\phi_m}e^{-k_{zi}(z_l-z_m)}\, e^{ik_zr(z_l-z_m)} \tag{8}$$

which using equation (6) can be reduced to

$$e^{i\phi_l} = e^{i\phi_m}e^{ik_{zr}(z_l-z_m)} \tag{9}$$

from which we will find

$$k_{zr} = \frac{1}{(z_l-z_m)}\left[\phi_l - \phi_m + 2\pi n(k_x)\right] \tag{10}$$

where

n_o = whole number of wavelengths between z_l and z_m along the z-direction

and where we have taken $(\phi_l - \phi_m)$ to be in the principal value range, $-\pi \leq (\phi_l - \phi_m) \leq \pi$. We have that $n'(k_x)$ is an integer incremented by $\pm$ 1 when $(\phi_l - \phi_m)$ crosses $\pm \pi$ and is zero when $k_x = 0$.

As can be seen from equation (10) an accurate procedure is needed to measure the velocity along the z-direction so that n_o can be obtained. The method used here, distinct from the one used by Murray and Ash,[7] is to make a longitudinal scan as shown in Figure 6 and to count from the phase response the number of cycles, n_o, between z_m and z_l. Clearly from the longitudinal scan one can also compute the wavelength and from the RF drive frequency obtain the velocity along the z-direction. Now that n_o is known k_{zr} can be computed according to equation (10).

To minimize computation time the Fourier transform specified in equation (1) is carried out using an FFT routine and as such the number of points in the FFT and the spacing between sample points in the transverse scan sets the spacing between sample points in k-space. This in turn sets the value of k_X associated with each point in the k-space representation of the scan and with each value of $k_{zr}(\theta)$ computed. We can now use trigonometry to compute the real part of the wave vector and the angle θ associated with each sample in k-space as

$$k(i) = \sqrt{k_x^2(i) + k_{zr}^2(i)} \tag{11}$$

$$\theta(i) = \tan^{-1}\left[\frac{k_x}{k_{zr}}\right] \tag{12}$$

where

i = k-space sample point index

We now have the wave vector and a relation between i and θ and so we can obtain the velocity

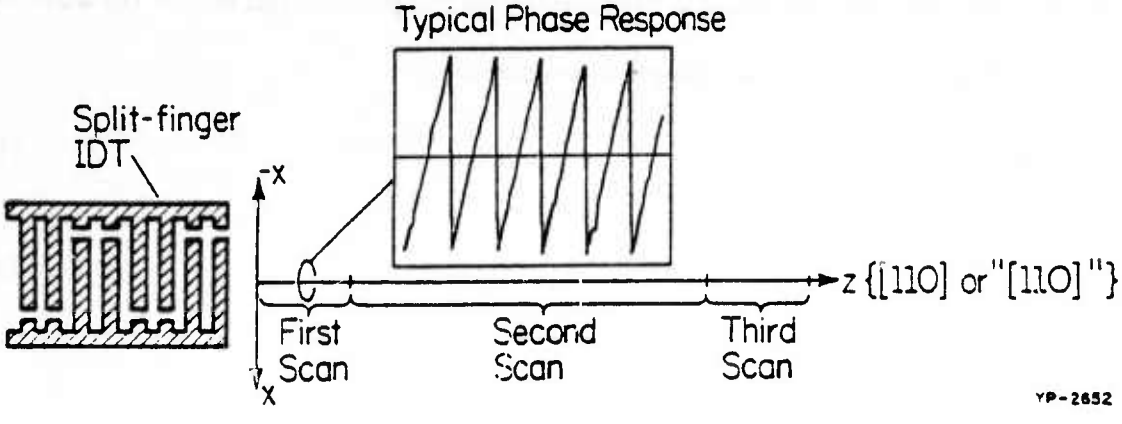

Figure 6. Longitudinal scans for determination of $v(\theta = 0)$

$v(\theta)$ as

$$v(\theta) = \frac{\omega}{k(\theta)}. \tag{13}$$

By using the third and first scans shown in Figure 5 one can again compute the slowness surface and average the results with those of the first and second scans to obtain smoother velocity and attenuation data.

III. Experimental Procedure

For these experiments split finger inter-digital transducers (IDT) were fabricated on zero and five-degree Cr-doped Horizontal Bridgman wafers using approximately 2000 Å of Al. The fingers and spacings of the IDT were 1 μm and hence the nominal operating frequency was 360 MHz. The transducers were 30 wavelengths wide and 100 wavelengths long.

The laser probe system used to make the longitudinal and transverse scans has been described in a concurrent publication[6] and will not be discussed here in detail. It is sufficient to say that the magnitude and phase of the surface displacement as a function of position is recorded and that typically signal-to-noise ratios of 50 to 60 dB are achieved. Also it should be noted that for the experiments described herein a 2 μm diameter laser spot was used.

The first step in the experiments was to establish a good estimate of the velocity along the [110] direction and this was done by the following procedure. Before the longitudinal scans shown in Figure 6 were made, the axes of the translation stage upon which the device is mounted are aligned under computer control so that the x-axis is parallel to the transverse features of the IDT within 0.01 degrees. A sequence of three scans are made along the z-direction. The first over a range of 100 μm in 0.1 μm steps, the second a much coarser scan over 4300 μm in 1 μm steps, followed by another fine increment scan over the final 100 μm of the propagation path at 0.1 μm increments. With the phase response of the fine increment scans one can establish a first order estimate of the wavelength and by counting the large number of wavelengths in the coarse middle scan one can refine this estimate further. Knowing the RF drive frequency one can then compute the velocity, $v(\theta=0)$ along the [110] direction.

Once the wavelength has been established transverse scans as shown in Figure 5 can be made and the data required for the slowness surface calculation described in Section II can be obtained. For the computations presented in this paper the spacing between sample points was 2 μm and the extent of the transverse scans went well beyond the beam profile to ensure that all of the propagating surface wave was sampled. If one uses the beam provided by the transducer to compute the

slowness surface one is, by classical diffraction theory, limited to an angular range given by

$$\theta_{max} = \text{half angle of beam spread} = \sin^{-1}(1/p) \tag{14}$$

where p = beam width in wavelengths

In order to extend the angular coverage of the beam and hence to provide a larger extent of data for the slowness surface, one can make a diffraction slit for the waves.[7] In the present study this was accomplished by depositing a one-to-one mixture of xylene and rubber cement in the manner shown in Figure 7. With the diffraction slit in place the three scans needed for computation of the slowness surface were made and were subsequently processed using a computer program which implements the method of Section II. Data thus obtained are presented in Section IV.

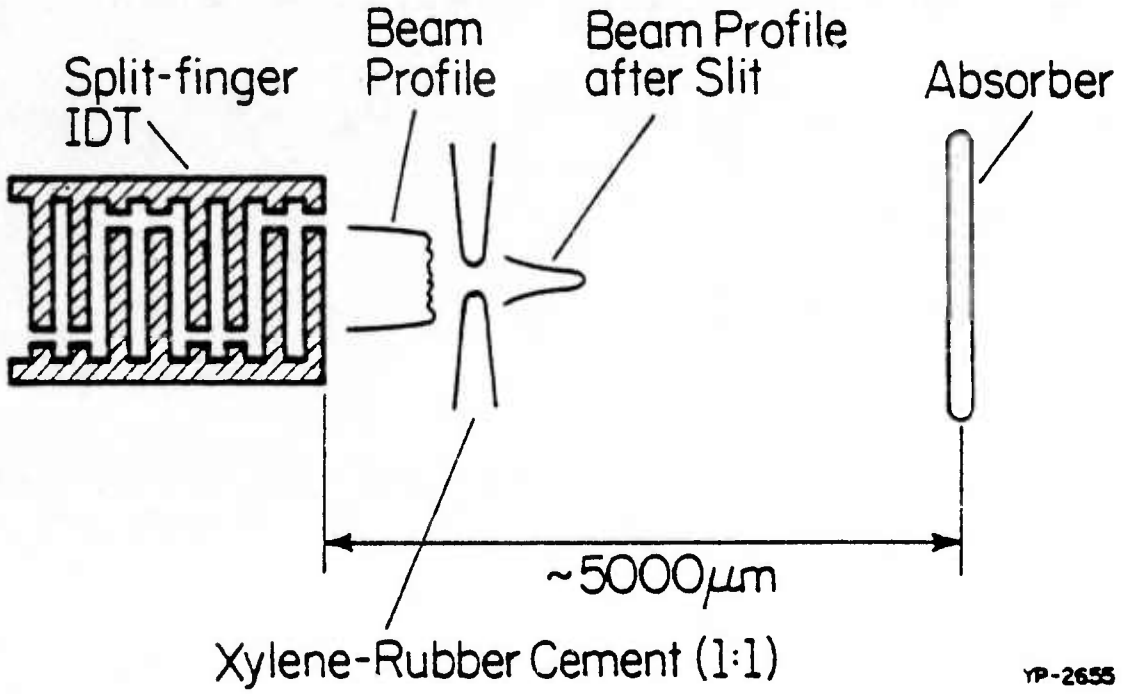

Figure 7. Devices and xylene-rubber cement slit.

IV. Results and Discussion

In Figure 8 we show the velocity curve from the zero-degree device together with that of the Deacon and Heighway experiments[9] and the theoretical data of Penunuri and Lakin.[3] The experimental results of Deacon and Heighway were obtained by fabricating IDT delay lines on GaAs at propagation angles from [100] to [110] in five-degree steps and monitoring the variation in propagation delay with angle. Note that the curve presented here lies between the theoretical prediction of Penunuri and Lakin and the experimental result of Deacon and Heighway and that the curvature of the results obtained herein is like that of Penunuri and Lakin at [110] and more like that of Deacon and Heighway at ten degrees off from this. Along the [110] direction we measure the velocity to be 2861.9 m/sec as compared with 2866 m/sec for Penunuri and Lakin and 2840 m/sec for Deacon and Heighway. This difference is not all that alarming as it is in tune with what has appeared in the literature previously. The velocity values reported have ranged from 2810 m/sec by Voltmer et al.[10] to 2865 m/sec by Campbell and Jones.[11] The reason for the variability is not clear as yet but may well be due to material variations or differences in the cut of crystal used.

The other component of the slowness surface is the attenuation and we have presented our results together with the predictions of Penunuri and Lakin in Figure 9. In processing the data, the scans were zero-filled to 4096 points and the two separate calculations of the slowness surface were made and then averaged as described in Section II. No further attempt has been made to smooth the data. It should be remembered at this point that the data of Penunuri and Lakin represents only the attenuation due to the leaky wave and does not include the normal viscous losses which are presumed to be relatively isotropic.

In the regions beyond two degrees from the [110] direction the experimental data follows the shape of the theoretical curve and is slightly larger, indicating that the observed attenuation is indeed due to a combination of the leaky wave loss and the viscous loss. At angles less than two degrees the viscous loss dominates yielding an on-axis loss of about 0.7 dB/μsec.

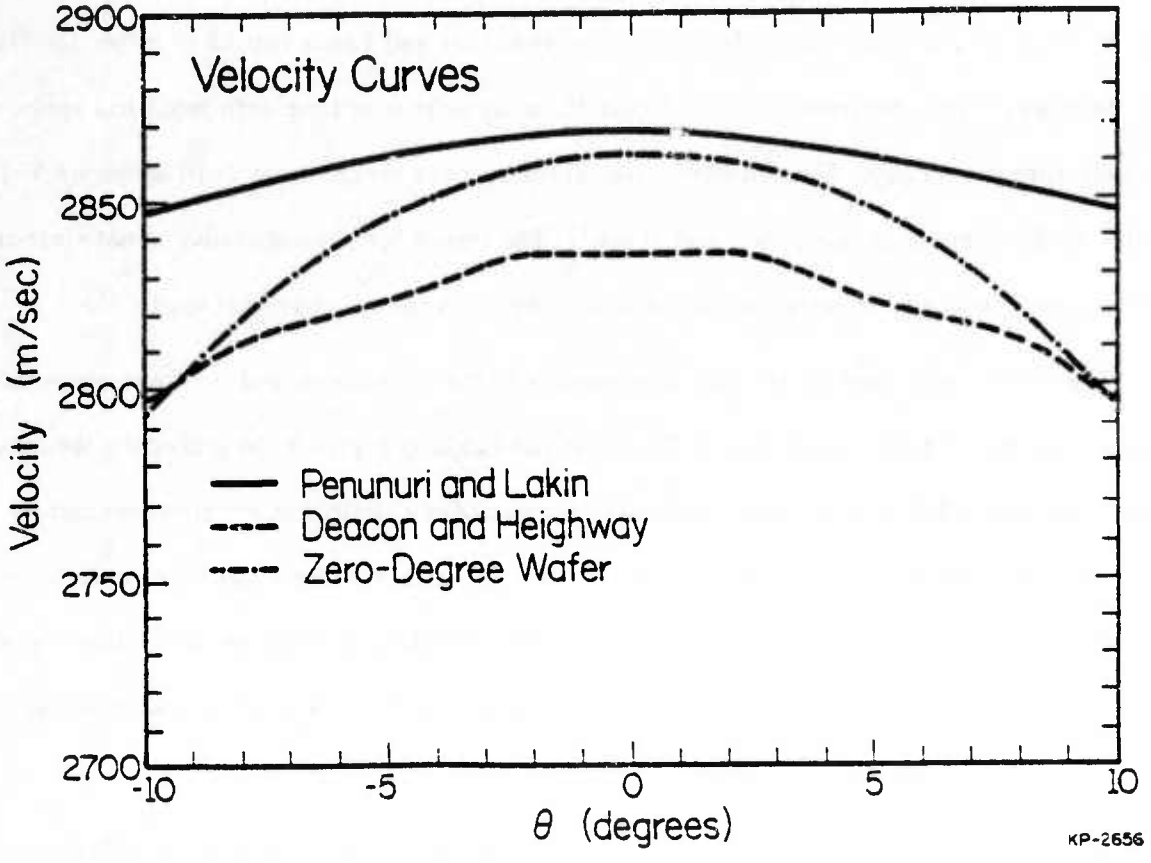

Figure 8. Velocity curves from: Penunuri and Lakin, Deacon and Heighway, and zero-degree wafer.

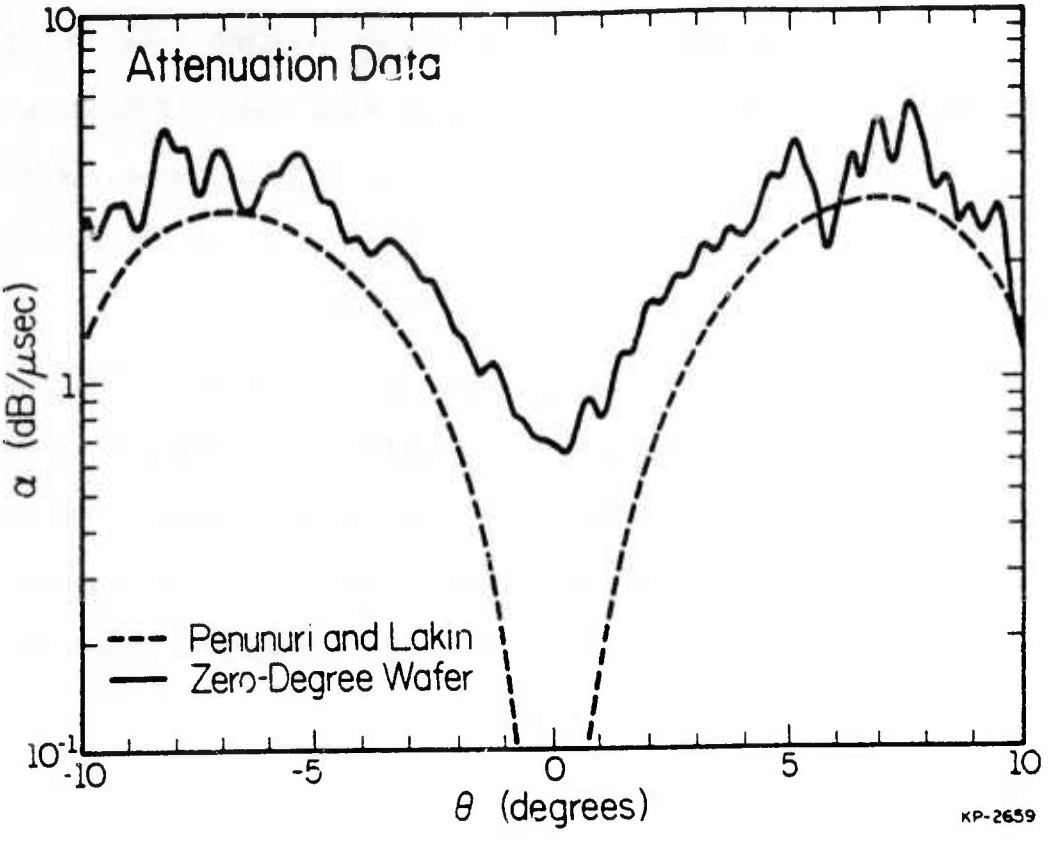

Figure 9. Attenuation data: Penunuri and Lakin, zero-degree wafer.

In Figure 10 we present the velocity curve for the five-degree wafer along with the data from the zero-degree wafer. Observe that along the [110] direction the velocity for the five-degree wafer is 2852.01 m/sec compared with 2861.9 m/sec measured for the zero-degree wafer. The asymmetry in the five-degree velocity curve is most probably due to a lack of SAW energy at the higher propagation angles. Because of the way the xylene-rubber cement slit is created there is not a great deal of control over its width and hence the amount of energy in the higher angles. The effect of this decreased energy content is also observed in the attenuation data shown in Figure 11 where at angles above five degrees the curve becomes noisy. If we assume that the z-directed velocity varies proportionally with the angle of the cut we would expect that the velocity for the two-degree wafers used for epitaxial growth would be approximately 2858 m/sec.

In Figure 11 we compare the attenuation data from the five-degree device with that of the zero-degree device. Up to about three degrees off from the [110] direction the two curves compare quite favorably but beyond that point the five-degree curve undergoes a steep increase before it becomes lost in the noise. This would give some indication that the leaky wave component is stronger for the five-degree cut than for the zero-degree cut but that along the [110] direction the viscous loss is much greater than the leaky wave loss for both.

The true test of the measured slowness surface is whether or not one can use it to accurately predict the propagation of a beam profile. Herein we have developed a computer program to propagate an acoustic beam a specified distance using the calculated slowness surface. The theoretical basis for this program is the angular spectrum of plane waves technique described in Section II. The procedure is to take transverse laser probe scans at positions 1 and 2 as shown in Figure 12 and to enter the scan at position 1 into the computer program which implements the diffraction theory. The user enters the distance in the z-direction between scan 1 and scan 2 and the program performs an FFT on scan 1 then propagates it the prescribed distance using the previously computed slowness surface and finally performs an inverse FFT to get back to the spatial domain. The computer propagated beam is then compared with the actual scan taken at position 2.

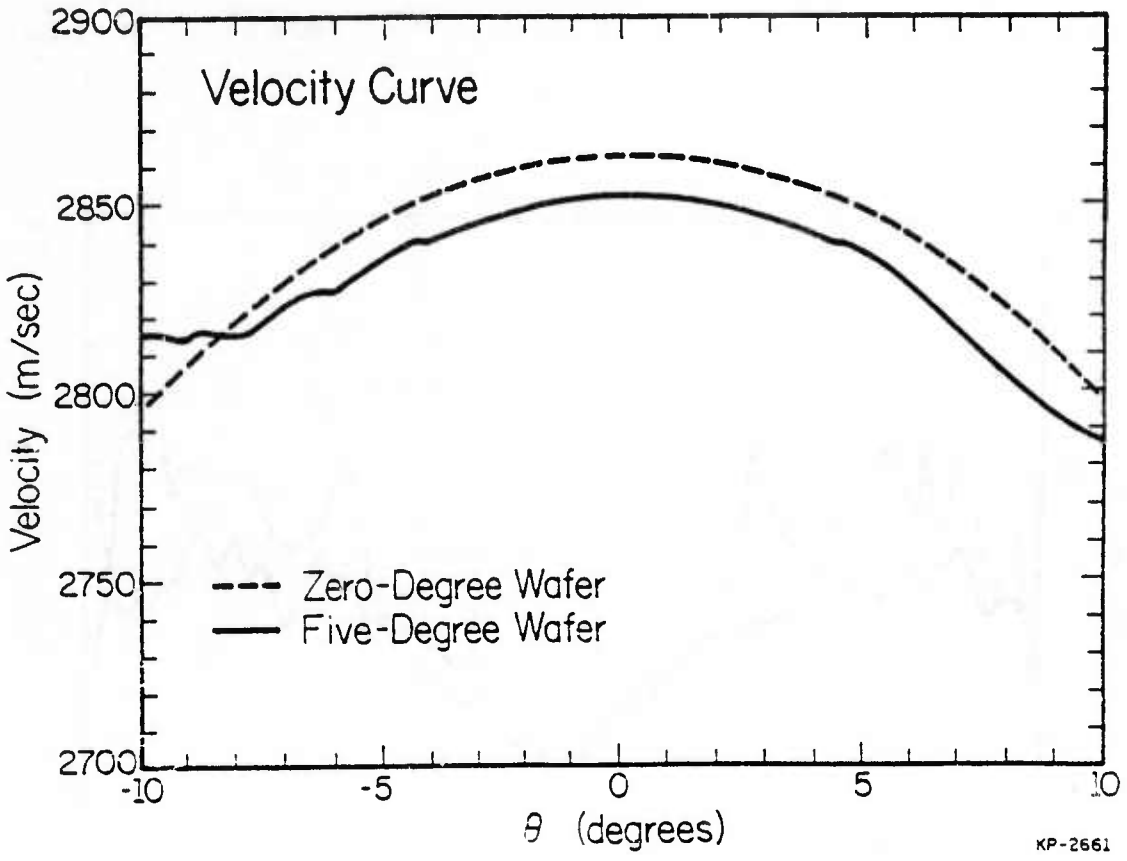

Figure 10. Velocity curve: zero-degree wafer and five-degree wafer.

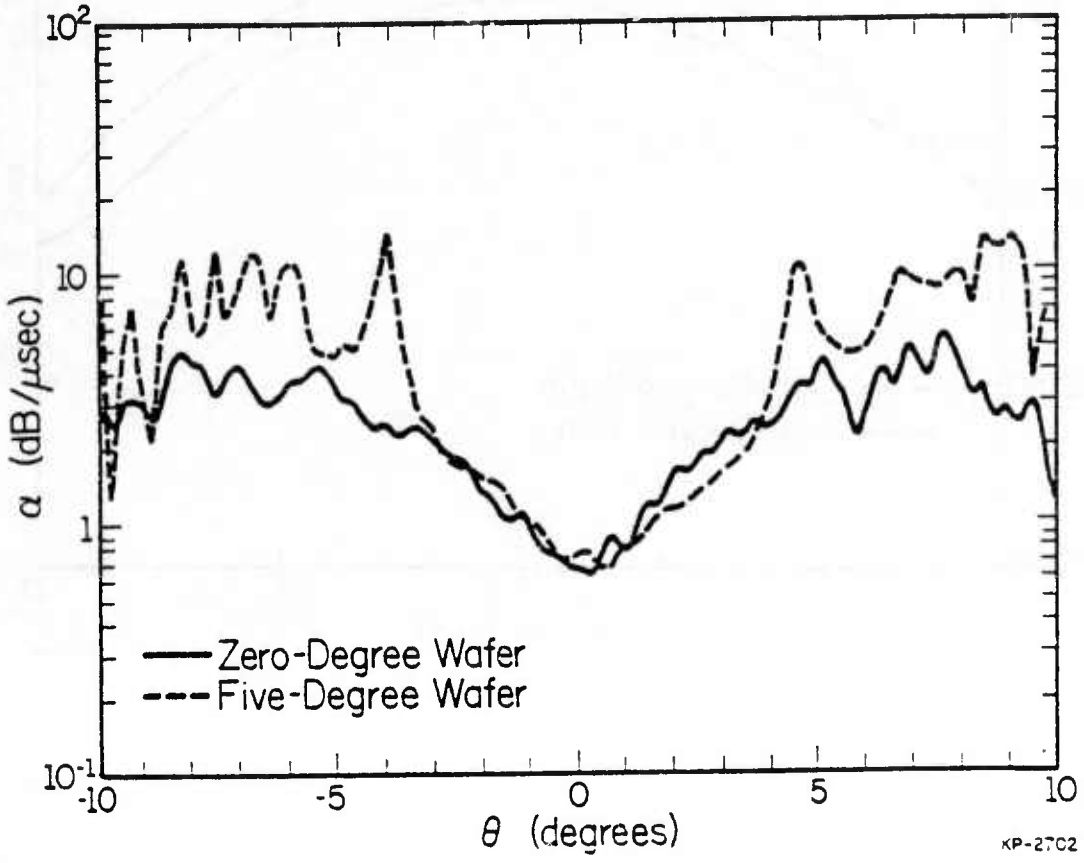

Figure 11. Attenuation curves: zero-degree wafer and five-degree wafer.

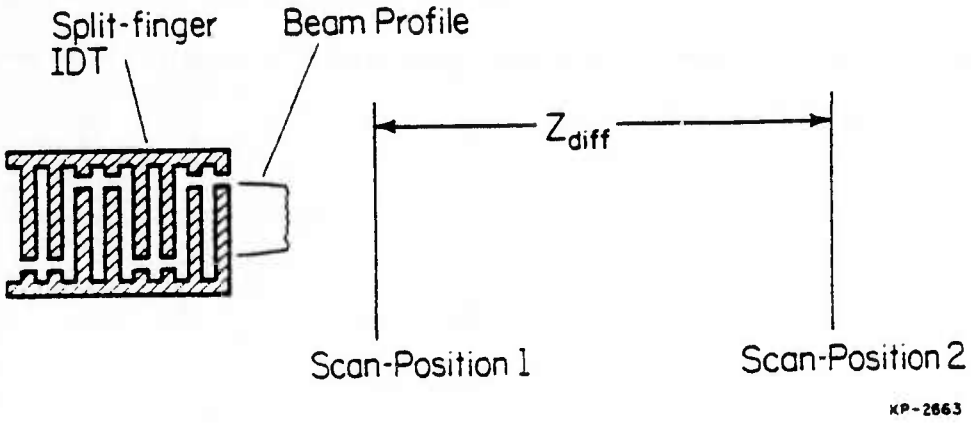

Figure 12. Scan positions for predicting beam profiles

$$z_{diff} = \begin{cases} 3536.2\ \mu m \text{ for zero—degree wafer} \\ 4484.4\ \mu m \text{ for five—degree wafer} \end{cases}$$

In Figure 13 we present for the zero-degree material the scan at position 1 along with the predicted and actual scan at position 2 which is a distance of 3536.2 μm away from position 1. Note the striking agreement between the predicted and actual scans. The magnitudes are nearly identical and the phase responses are close with the exception of a static offset of 50.2 degrees. If we assume the phase error is less than one wavelength the difference can be accounted for by either a velocity calculation error on the order of .03% or by errors in the translation stage on the order of 1 μm or a combination of the two. In Figure 14 we present the same scans for the five-degree material and again there is very good agreement between the predicted and measured magnitude responses and in this instance a difference of about 100 degrees in the phase response. The distance between scans 1 and 2 on the five-degree material was 4484.4 μm and hence the error of 100 degrees can be associated with a translation stage placement error of 2 μm or a velocity error on the order of .05% or a combination of the two.

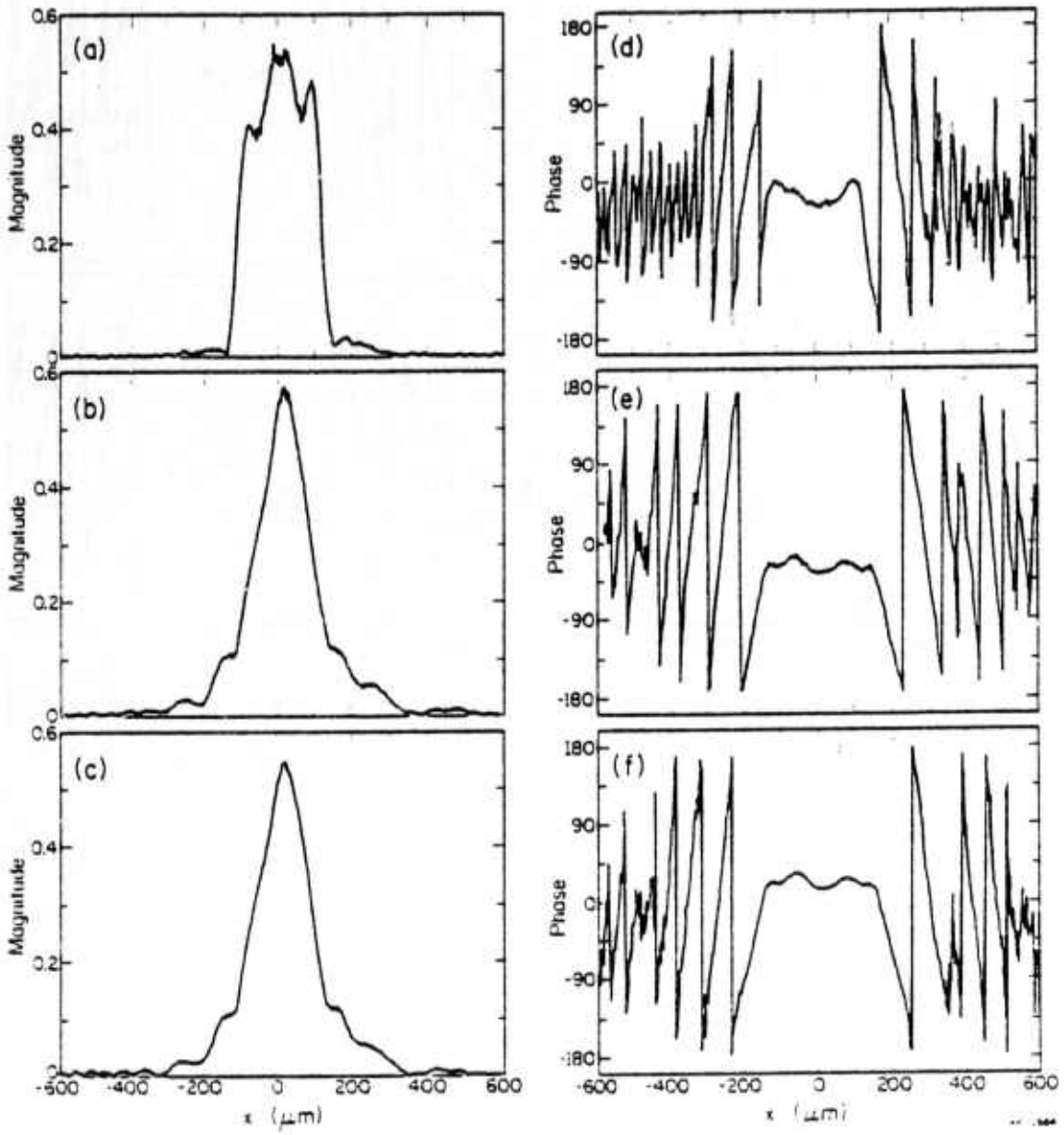

Figure 13. Zero-degree wafer: a) Magnitude of 1st scan. b) Magnitude of 2nd scan. c) Predicted magnitude of 2nd scan. d) Phase of 1st scan. e) Phase of 2nd scan. f) Predicted phase of 2nd scan.

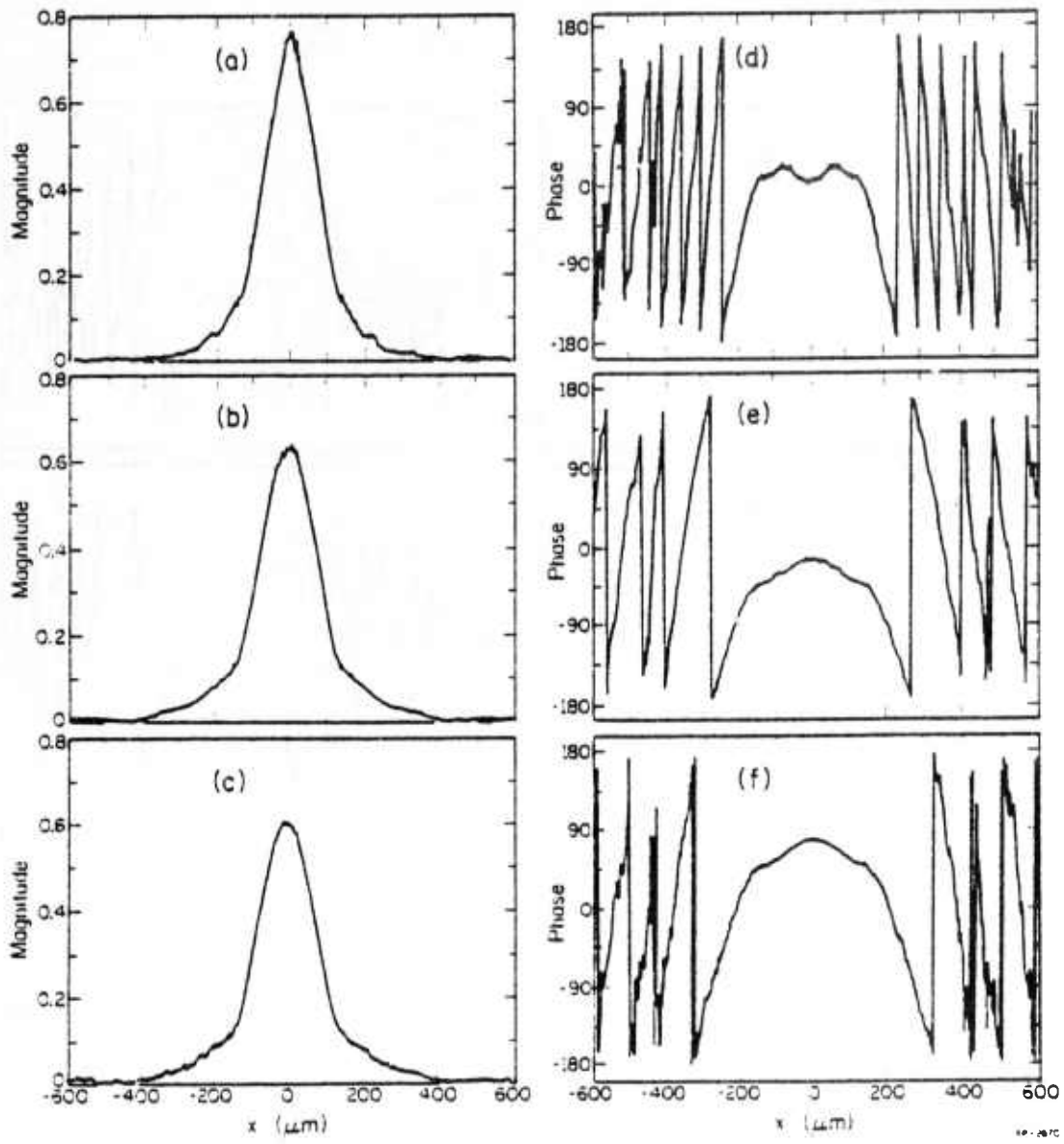

Figure 14. Five-degree wafer: a) Magnitude of 1st scan. b) Magnitude of 2nd scan. c) Predicted magnitude of 2nd scan. d) Phase of 1st scan. e) Phase of 2nd scan. f) Predicted phase of 2nd scan.

VI. Conclusion

In this paper we have presented an extension of the method of Murray and Ash from computing the slowness surface on materials exhibiting leaky wave propagation. The slowness surface obtained for the zero-degree Cr-doped Horizontal Bridgman compared well with the theoretical predictions of Penunuri and Lakin and with the experimental measurements of Deacon and Heighway. The true test of the slowness surface measurements is in their ability to predict the details of beam profile propagation and the slowness surfaces presented here yielded very good agreement between the predicted profile and the actual one. In addition it was found that along the [110] direction the attenuation is roughly the same for zero and five-degree cut GaAs wafers but that a few degrees off from this direction the attenuation curves diverge with the loss for the five-degree material becoming much greater. This would indicate the presence of a stronger bulk shear for the five-degree cut and would further imply that a similar, though somewhat reduced, situation may occur for the two-degree cut commonly used for epilayer growth.

References

1. M.J. Hoskins, Ph.D. Dissertation, University of Illinois, (Urbana, Illinois, 1983).

2. D. Penunuri, Ph.D. Dissertation, University of Southern California, (Los Angeles, California, 1976).

3. D. Penunuri and K.M. Lakin, 1975 *Ultrasonics Symposium Proceedings*, IEEE Cat. No. 75CH995-4SU (IEEE, New York, 1975) p. 478.

4. R.E. Williams, *Gallium Arsenide Processing Techniques* (Artech House, Dedham, Mass., 1984) p.43.

5. S.K. Ghandhi, *VLSI Fabrication Principles* (Wiley, New York, 1983) p. 251.

6. R.L. Miller, to be submitted to *Journal of Applied Physics*.

7. D. Murray and E.A. Ash, 1977 *Ultrasonics Symposium Proceedings*, IEEE Cat. no. 77CH1264-1SU (IEEE, New York, 1977) p. 823.

8. J.W. Goodman, *Introduction to Fourier Optics* (McGraw-Hill, New York, 1968) p. 48.

9. J.M. Deacon and J. Heighway, *Electronics Letters*, vol. 8, No. 1, 1972, p. 7.

10. F.W. Voltmer, E.P. Ippen, R.M. White, T.C. Lim, and G.W. Farnell, *Proceedings of the IEEE*, *56*, 1968, p. 1534.

11. J.J. Campbell and W.R. Jones, *Journal of Applied Physics*, *41*, 1970, pp. 2796-2801.

Figures

APPENDIX E

GALLIUM ARSENIDE SCHOTTKY BARRIER LEAKAGE CURRENTS

BY

JANICE MARIE PRYST

B. S., University of Illinois, 1984

THESIS

Submitted in partial fulfillment of the requirements
for the degree of Master of Science in Electrical Engineering
in the Graduate College of the
University of Illinois at Urbana-Champaign, 1986

Urbana, Illinois

ABSTRACT

The nonideal leakage currents of Schottky barrier diodes have been the focus of increased research activity in recent years. Solutions to this problem are desired since the Schottky barrier diode, a majority carrier device with virtually no minority carrier storage, is suitable for use in high-speed applications. A primary concern is that reverse biased Schottky barrier diodes exhibit much greater leakage currents than diffused p-n junctions. This thesis discusses three techniques for minimizing Schottky barrier reverse leakage current: utilizing a polyimide ring structure to reduce high electric fields at the diode periphery, using different Schottky metallizations, and annealing to modify the barrier height.

ACKNOWELDGEMENTS

I wish to thank Professor Bill J. Hunsinger for the support which made this research possible and extend warmest thanks to Dr. Michael J. Hoskins for providing the guidance and knowledge that helped me pursue my studies.

I am grateful to Ed Bogus and Jim Peterson for taking the time and effort to teach me the art of microfabrication, to Eric Creviston for assisting with the processing of the barrier height data, and to Vic Steel for generating the necessary mask artwork. The patient assistance of Julie Overholt during the preparation of this thesis is also greatly appreciated.

Finally, I wish to thank Tom for his loving support and thank my parents for providing encouragement when needed and always taking an interest in my work.

This work was supported by the United States Air Force under contract number F30602-84-C-0132.

I. INTRODUCTION

The Schottky barrier diode, with the attractive features of low turn-on voltage and negligible minority carrier injection, is desired for use in high-speed applications. However, reverse leakage currents must be minimized if practical diodes are to be obtained. Edge effects are the most obvious source of this leakage current. The Schottky barrier metal also determines the amount of leakage current since different metals display different characteristic leakage current values. A third factor that can determine the amount of leakage current is annealing, which is performed after fabrication is complete.

At the abrupt edge of the barrier metal, high electric fields develop [1]. Under reverse bias, these high electric fields lead to edge breakdown and therefore greater current flow. A p-type diffused guard ring can be used to reduce the edge effects, but this addition introduces minority-carrier injection from the guard ring at high-forward current levels, and thus a decrease in switching speed [2]. The use of a double diffused guard ring has also been studied; however, this structure requires more processing steps and may lead to process-induced leakage [3,4]. Presented in this thesis is another possible solution whereby a polyimide ring with sloping edges is formed so that the abrupt edge of the metal is eliminated. This configuration avoids the electric field peaking along the periphery, and hence, reduces leakage current.

After establishing the diode structure, a Schottky barrier metal with characteristically low leakage can be chosen. Chromium-copper/aluminum, aluminum, and titanium diodes are investigated. Chromium has good adhesion properties, while aluminum and titanium would be stable at the high temperatures encountered in IC fabrication. In order to study the effects of annealing on leakage current values, diodes with the three different Schottky metallizations are annealed at temperatures in the 125-275°C range.

II. THEORETICAL CONSIDERATIONS

According to the thermionic emission theory [5], diode current is described by the following equation

$$I = SA^{*} T^{2} \exp\left[\frac{-\phi_{bn}}{V_T}\right]\left\{\exp\left[\frac{V}{V_T}\right] - 1\right\} \tag{1}$$

where A^{*} is the effective Richardson constant, modified for the effective mass of an electron in GaAs to give a value of 8.1 $A/K^2 cm^2$ [6]. S, T, ϕ_{bn} (neglecting the effect of image-force barrier lowering), and V_T are the diode area, temperature, barrier height, and thermal voltage (25.9 mV at 300K), respectively. If the barrier height is sufficiently smaller than the bandgap so that the depletion-layer generation-recombination current is small in comparison with the Schottky emission current, and the $\exp(V/V_T)$ term is assumed to be negligible when reverse biased, then the reverse current will increase gradually with reverse bias according to

$$I_R = SA^{*} T^{2} \exp\left[\frac{-\phi_{bo}}{V_T}\right] \exp\left[\frac{\sqrt{qE/4\pi\epsilon_s}}{V_T}\right] \tag{2}$$

where ϕ_{bo} is the zero bias barrier height and

$$E = \sqrt{\frac{2qN_d}{\epsilon_S}\left[V_R + V_{bi} - V_T\right]}. \tag{3}$$

N_d is the donor concentration in the epitaxial layer, V_R is the applied reverse bias voltage, V_{bi} is the built-in potential, q is the fundamental electronic charge, and ϵ_s is the effective permittivity of GaAs.

Based upon Equation (1), an increase in barrier height or a decrease in the value of the Richardson constant will lead to a reduction in leakage current. Assuming that the Schottky barrier height is determined by the metal work function, ϕ_m, and is represented by

$$\phi_{bo} = \phi_m - \chi_s \tag{4}$$

where χ_s is the electron affinity of the semiconductor, the chromium-copper/aluminum diodes would form the highest barrier [7]. The aluminum diodes would form the lowest barrier, and the titanium Schottky barriers would have a value between the two. χ_s for gallium arsenide is 4.07 [8], and the work functions for chromium, titanium, and aluminum are 4.50, 4.33, and 4.28 eV, respectively [9].

Bardeen proposed that a potential barrier exists at the free surface of a semiconductor at thermal equilibrium [10]. This barrier can be pinned to its free surface value even after the metal-semiconductor contact is made if surface-state density is high enough. This pinning of the barrier causes it to be independent of the metal work function, ϕ_m. In Bardeen's theory, the barrier height is expressed as

$$\phi_{bo} = E_g - \phi_o \tag{5}$$

where E_g is the energy gap and ϕ_o is the energy level above the top of the valence band to which surface states are filled when the free surface is charge neutral [11]. A decrease in ϕ_o or an increase in E_g would increase the barrier height and therefore decrease leakage current. As reported in the literature, annealing of aluminum-gallium arsenide Schottky diodes at 250°C can increase the barrier height or decrease the value of the Richardson constant [12]. Heat treatment causes growth of an interfacial layer at the metal-semiconductor junction. This thin layer can lead to a reduction in the Richardson constant since majority carriers must now tunnel through the interfacial layer [13]. Based upon Equation (1), a decrease in A^* would cause a decrease in leakage current.

III. PROCESSING

A. Overview

Arrays of circular Schottky diodes of varying areas are fabricated on [100] cut, 2° rotated, n-type epitaxial, gallium arsenide substrates. The diode diameters used in this study are 550 μm, 700 μm, and 900 μm, resulting in areas of 0.238 mm^2, 0.385 mm^2, and 0.636 mm^2, respectively. Two different n-type doping levels, 0.4×10^{15} cm^{-3} and 1.8×10^{15} cm^{-3}, for the epitaxial layer are used to study leakage current variations with doping level.

The basic processing steps are the same for all diodes and are outlined below.

The ohmic layer (gold/germanium-nickel) is fabricated using standard photolithographic techniques:

1. *Photoresist application*. Type AZ 4110 positive photoresist is spun on at 4000 rpm for 30 seconds. A five-minute air dry is followed by a 25-minute softbake at 70°C.

2. *Exposure*. A Karl Suss contact mask aligner is used for exposure. The ultraviolet light has a wavelength of 300 nm and bulb intensity is 10.0 mW/cm^2. Since the mask is soda-lime and not the commonly used quartz, exposure takes slightly longer and is done for 45 seconds.

3. *Pattern development*. AZ 400K, diluted 1:4 with deionized water (DI), and cooled to a temperature of 22°C, is used for pattern development. Develop time is somewhat dependent on ambient temperature and relative humidity, which were not controlled variables in this investigation. For relative humidity in the 40-70% range and ambient temperature in the 69-88°F range, development takes roughly two minutes. A thorough DI rinse and nitrogen dry follow development.

4. *Metallization*. All evaporations except nickel and titanium are done by thermal evaporation in a diffusion oil pump vacuum system at a pressure of approximately 5×10^{-6} Torr. An electron beam is used for nickel and titanium evaporations.

5. *Liftoff*. A standard liftoff technique is used [14,15].

6. *Alloy*. The ohmic material is alloyed for five minutes in a tube furnace at 450°C with a hydrogen ambient.

With the exception of alloying, the Schottky layer is formed following the same procedure.

B. Modifications

1. Polyimide Rings

Use of polyimide rings requires an intervening process between the ohmic and Schottky metallizations (see Figure 1). In order to determine the effect of the polyimide rings and maintain a controlled experiment, half of the diodes on the wafer are fabricated with rings and half without. Assuming that the polyimide rings will minimize the electric field peaking at the periphery, the diodes with rings are expected to have leakage current values approaching those predicted by theory.

For the half of the wafer with rings, the polyimide processing is as follows. To avoid pinholing, two 0.5 μm thick layers of polyimide are spun on at 4000 rpm for 60 seconds. The polyimide, type PI 2555, is diluted 1:1 with T9035 thinner. Bake times and temperatures are optimized to produce ideal edge profiles. In this case, a 45° slope is desired. The first layer is baked at 150°C for 20 minutes, the second at 140°C for 30 minutes. A layer of AZ4110 positive photoresist is then spun on and baked at 90°C for 30 minutes. The wafer is exposed to ultraviolet light for 45 seconds, then developed in a 0.22N tetramethylammonium hydroxide (TMAH) solution that causes overcutting of the polyimide [16]. As mentioned previously, the polyimide bake times and temperatures determine the amount of overcutting.

The TMAH solution provides a one-step process for developing first the photoresist, then etching the polyimide. A spray rinse with acetone is used to remove the photoresist from the rings. High-temperature bakes (one hour at 180°C then two hours at 225°C) cure the polyimide and render it resistant to the effects of further processing.

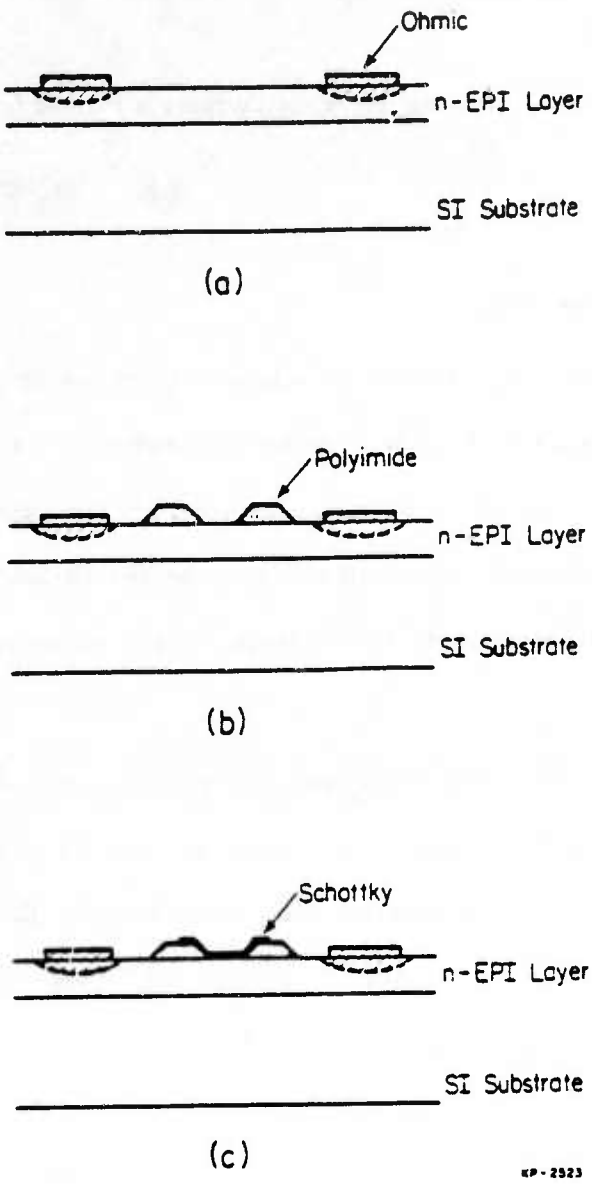

Figure 1. Fabrication sequence. (a) Ohmic metallization and alloy.

(b) Polyimide layer.

(c) Schottky metallization.

Since the Schottky metal overlaps the polyimide rings, the diode sizes are slightly decreased. Diameters become 360 μm, 510 μm, and 710 μm yielding areas of 0.1 mm^2, 0.2 mm^2, and 0.4 mm^2, respectively.

2. Different Metallizations

The three Schottky metallizations discussed in this thesis are chromium-copper/aluminum, aluminum, and titanium. The thermal stability of the first metal layer in contact with the gallium arsenide is of prime importance in high-power devices which operate at elevated temperatures (200-275°C) [17].

All three metallizations studied have been shown to display good thermal stability at high temperatures [18]. Chromium is less susceptible to oxidation and is stable up to about 400°C. However, gallium and/or arsenic outdiffusion is noticeable above this temperature [19]. Aluminum Schottky barriers have been found to be stable up to 345°C [20]. Above this temperature, outdiffusion of gallium and indiffusion of aluminum along with oxidation of aluminum are the main degradation mechanisms. Titanium is found to be stable with regard to both interdiffusion and oxidation up to 400°C [21]. All three metallizations are therefore good candidates for use in high-power gallium arsenide applications.

In this study, the chromium-copper/aluminum and aluminum diodes are filament-evaporated, while the titanium is deposited with a 10 kilovolt electron beam because of its high melting point (1800°C).

3. Annealing

As discussed earlier, low temperature (125-275°C) heat treatment can alter the Schottky barrier height and/or the Richardson constant. To determine if leakage current is affected, annealing of the Schottky diodes is performed after fabrication is complete. The annealing is carried out in a tube furnace with a nitrogen ambient. Reverse leakage current is measured before and after annealing and the values compared.

To eliminate nonuniformities between wafers, each of the wafers containing diodes with a particular metallization is sawed into four sections. Therefore, the diodes of each metallization have undergone the same processing. The sections contain samples of all three diode areas, and each section is annealed for 60 minutes at temperatures of 125, 175, 225, or 275°C.

IV. TESTING

A. Test Procedures

All leakage current measurements are made with an Alessi Industries wafer prober and a Tektronix 577 curve tracer. Since currents are in the nanoamp range, measurements must be made in the dark. Light shining on the sample will cause optical generation of carriers which will drastically increase the leakage current values.

In addition to measuring leakage currents, barrier height values are determined using current-voltage (I-V) measurements [22]. Current density (J_s) is plotted versus forward voltage in the linear region of operation, and an extrapolated value of J_s at zero volts is obtained. Barrier height is then calculated with the following equation:

$$\phi_{bo} = V_T \ln \left(\frac{A^* T^2}{J_s} \right) \tag{6}$$

B. Results and Interpretation

1. Polyimide Rings

As expected, the diodes with polyimide rings display much lower leakage current values than those without rings. Figures 2 and 3 show the increase of leakage current with area and the difference between leakage current values of the chromium-copper/aluminum diodes with and without polyimide rings. The measured leakage currents fall relatively close to the theoretical values, and since thermionic emission theory does not include edge effects, the data indicates that the polyimide rings effectively minimize excess leakage current at the diode periphery. The diodes without rings have higher leakage currents, and the current increases more rapidly at the outset but then starts to level off. If the plot were extrapolated out to infinite area, it appears that the two curves would meet since edge effects would be negligible.

Based upon a comparison between diodes with polyimide rings and diodes without, the leakage current can be separated into a bulk leakage plus generation-recombination current

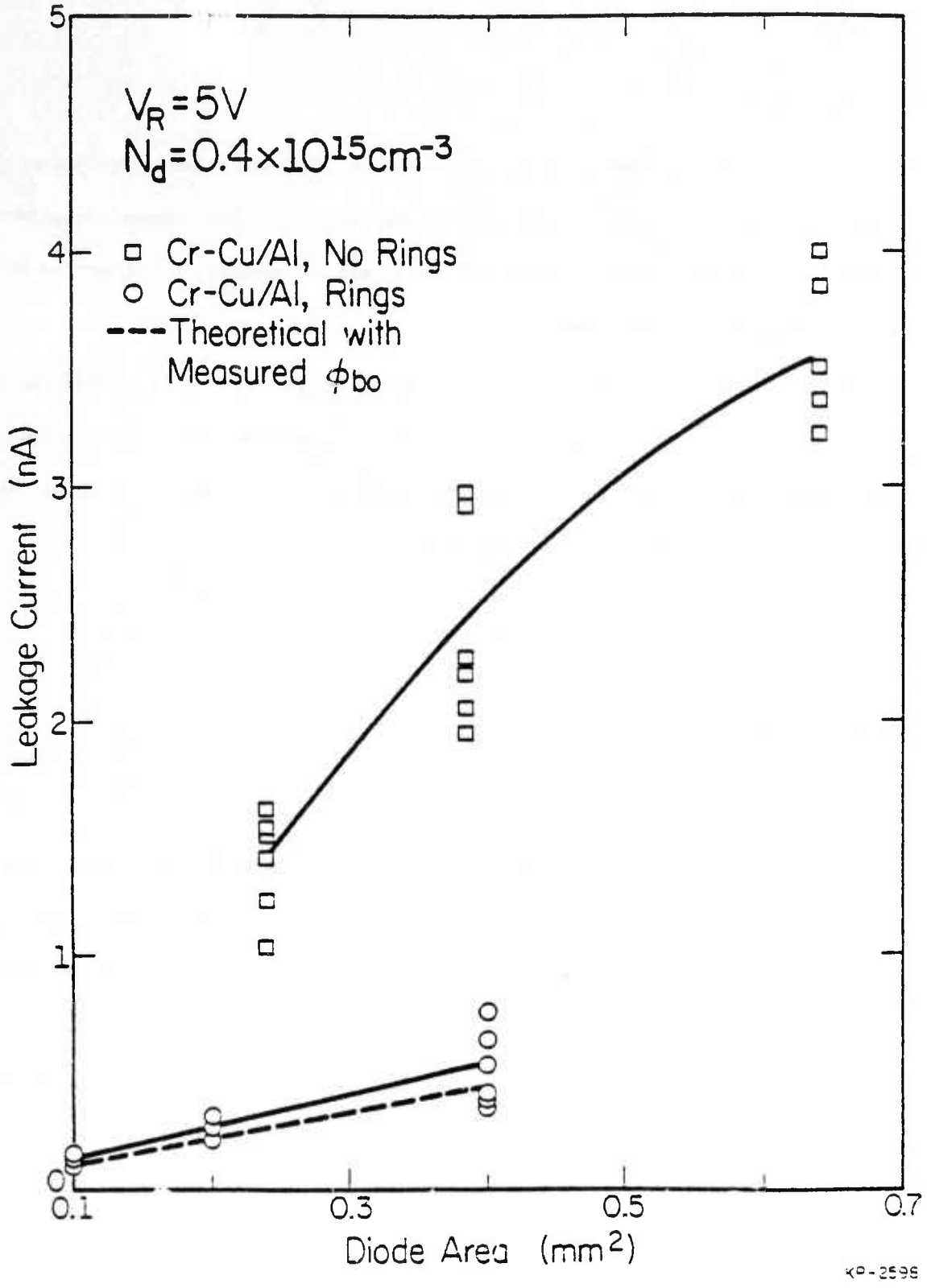

Figure 2. Leakage current versus diode area for the lower doped wafer.

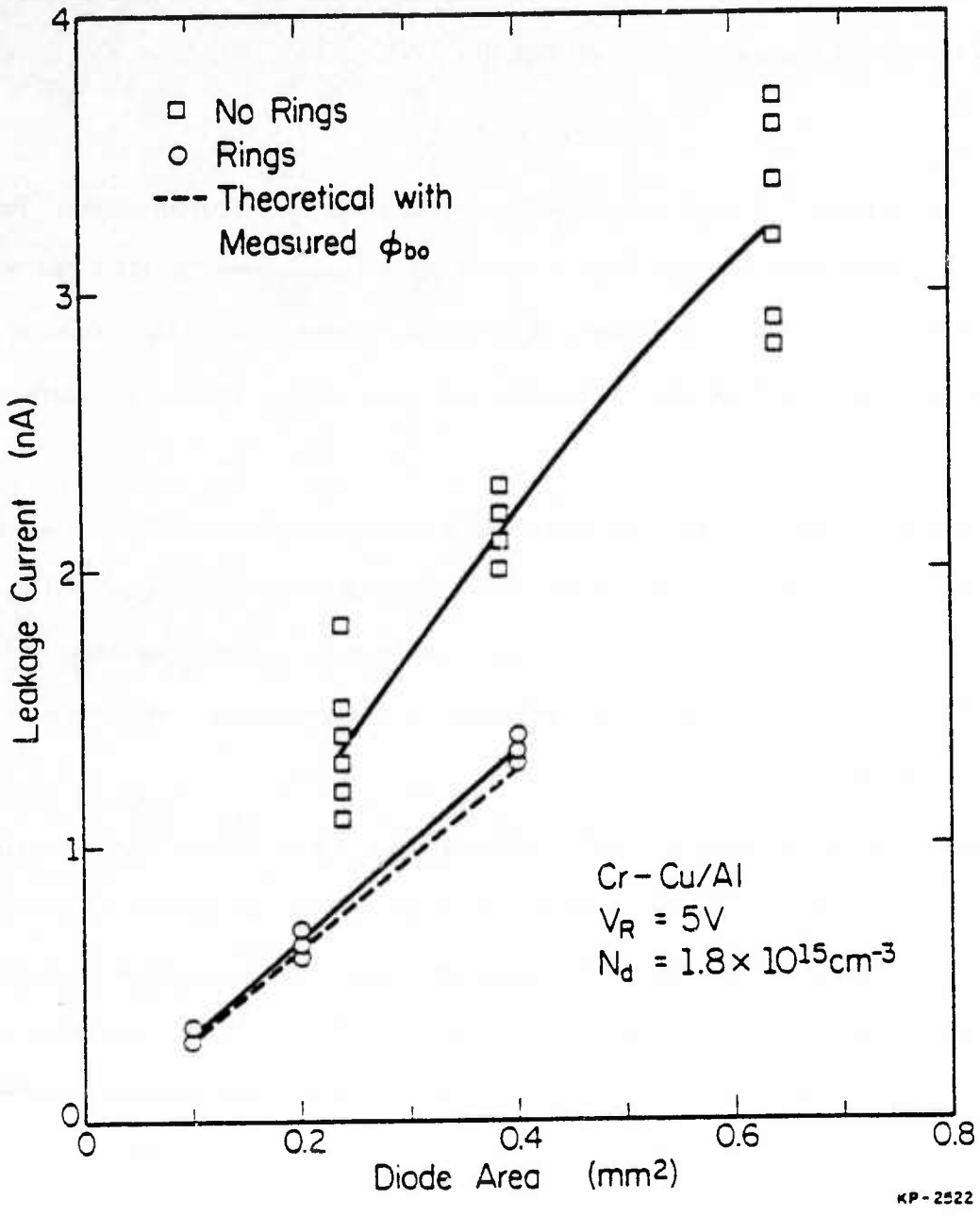

Figure 3. Leakage current versus diode area for the higher doped wafer.

component that scales with area and an edge leakage component that scales with circumference. An equation for the reverse leakage current might look like

$$I_r = (I_b + I_g) + I_e \tag{7}$$

where I_b is bulk leakage, I_e is edge leakage, and I_g is generation-recombination current. For the diodes with polyimide rings, the edge leakage term is approximately zero; therefore, the leakage current scales linearly with area. In addition, if the applied reverse voltage, V_R, is small enough, i.e., less than one volt, then the generation-recombination term is proportional to the square root of V_R.

Experimental results are higher than theoretical predictions in all cases. This is most likely due to generation-recombination current in the depletion region, which is neglected in theoretical calculations. Figure 4 supports the existence of depletion-layer generation-recombination current since the difference between theoretical and experimental leakage current values increases with increasing reverse bias.

The barrier heights, as determined by I-V measurements, remain constant with area, and the values are shown in Table 1. The measured barrier heights provide an accurate estimate of the magnitude of the leakage current for the polyimide ring diodes. The standard deviation for the chromium-copper/aluminum diodes without rings and the chromium-copper/aluminum diodes with rings on the lower doped wafer is 0.01 eV. For the chromium-copper/aluminum diodes with rings on the higher doped wafer, the standard deviation is negligible. A deviation in barrier height is responsible for scatter in the data points, since a 0.01 eV change in barrier height can alter the leakage current by as much as a factor of 1.5.

2. Different Metallizations

For both doping levels investigated (0.4×10^{15} cm^{-3} and 1.8×10^{15} cm^{-3}), the aluminum diodes have the largest leakage current values, and the chromium-copper/aluminum diodes have the lowest. This variance in leakage current values is displayed in Figure 5. Barrier height

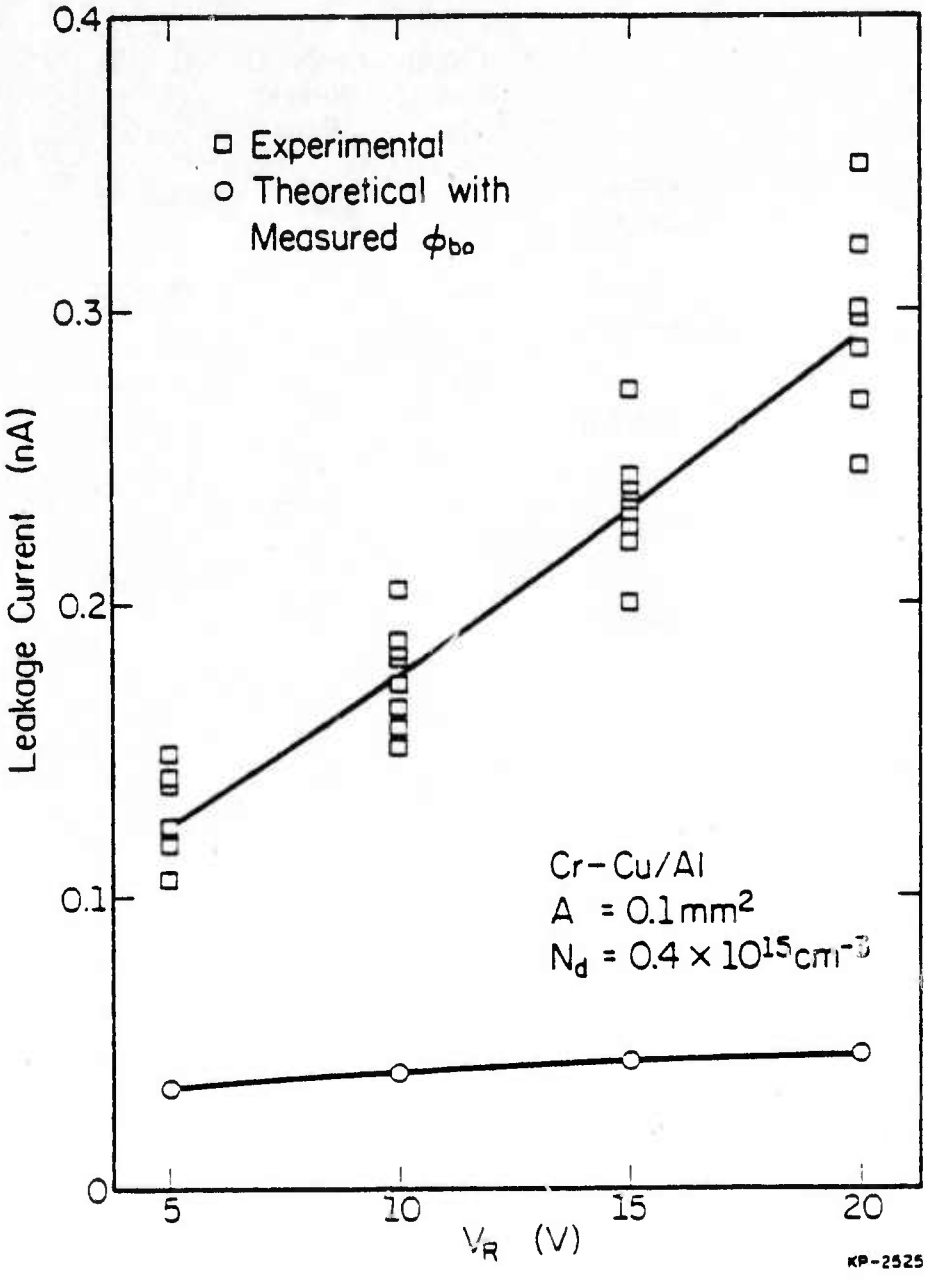

Figure 4. Leakage current versus applied reverse bias voltage for polyimide ring diodes on the lower doped wafer.

Table 1 Barrier height data for the three different metallizations and polyimide ring diodes on the higher doped wafer before and after annealing.

AVERAGE BARRIER HEIGHT (eV)

	Cr-Cu/Al With Rings	Cr-Cu/Al Without Rings	Al	Ti
BEFORE ANNEAL	.74	.76	.66	.81
125°C ANNEAL	.80	.79	.69	.87
175°C ANNEAL	.82	.82	.73	.87
225°C ANNEAL	____	____	.77	.89
275°C ANNEAL	____	____	.81	.89

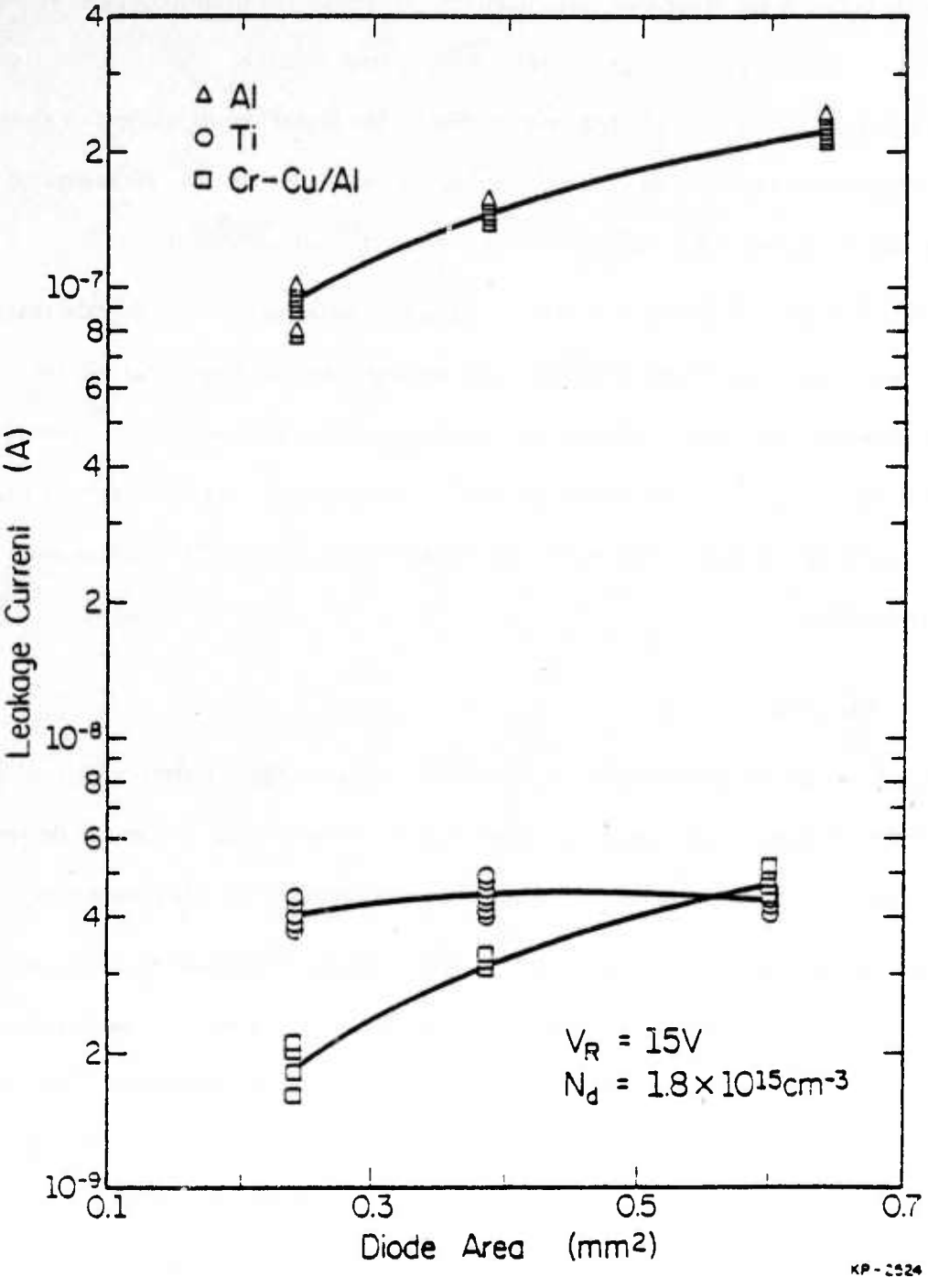

Figure 5. Leakage current versus diode area for the three different Schottky metallizations.

measurements correlate with the observed leakage currents. The titanium diodes exhibit leakage current values between the other two metallizations. However, the titanium diodes fabricated on the lower doped wafer display leakage currents closer to those observed with the aluminum diodes, whereas the leakage currents of the titanium diodes on the higher doped wafer fall closer to the chromium-copper/aluminum values. The discrepancy may be due to variations in surface preparation and/or slightly different conditions during the titanium evaporations.

The scatter in the data points and variance from one wafer to the next indicate that surface-state effects are a significant factor in determining leakage current. Auger analysis has revealed a correlation between high surface leakage and the presence of a surface gallium oxide layer [23]. The mechanisms proposed for the excess leakage are band bending due to charges in the surface oxide and conduction through a thin layer of arsenic located between the surface oxide and the gallium arsenide [24].

3. Annealing

Different trends are observed for each metallization as annealing temperature is increased. Leakage current decreases with increasing temperature for the aluminum diodes and decreases after reaching a certain temperature for the chromium-copper/aluminum and titanium diodes.

The polyimide ring structure with the chromium-copper/aluminum Schottky metallization yields less diodes suitable for controlled annealing experiments since half of the diodes have rings and half do not. Therefore, annealing of the chromium-copper/aluminum diodes is only performed at 125°C and 175°C. Although I-V measurements indicate an increase in barrier height, leakage current values are greater after annealing. Figure 6 shows this trend. Outdiffusion of the chromium or copper is a possible explanation for the increase in leakage current.

The aluminum diodes, on the contrary, show a marked decrease in leakage current after annealing at temperatures in the 125-275°C range, as can be seen in Figure 7. This decrease in leakage current, along with a corresponding increase in barrier height, agrees with the results of previous researchers [25,26]. Evidence exists that indicates that a thin $Al_xGa_{1-x}As$ region forms at

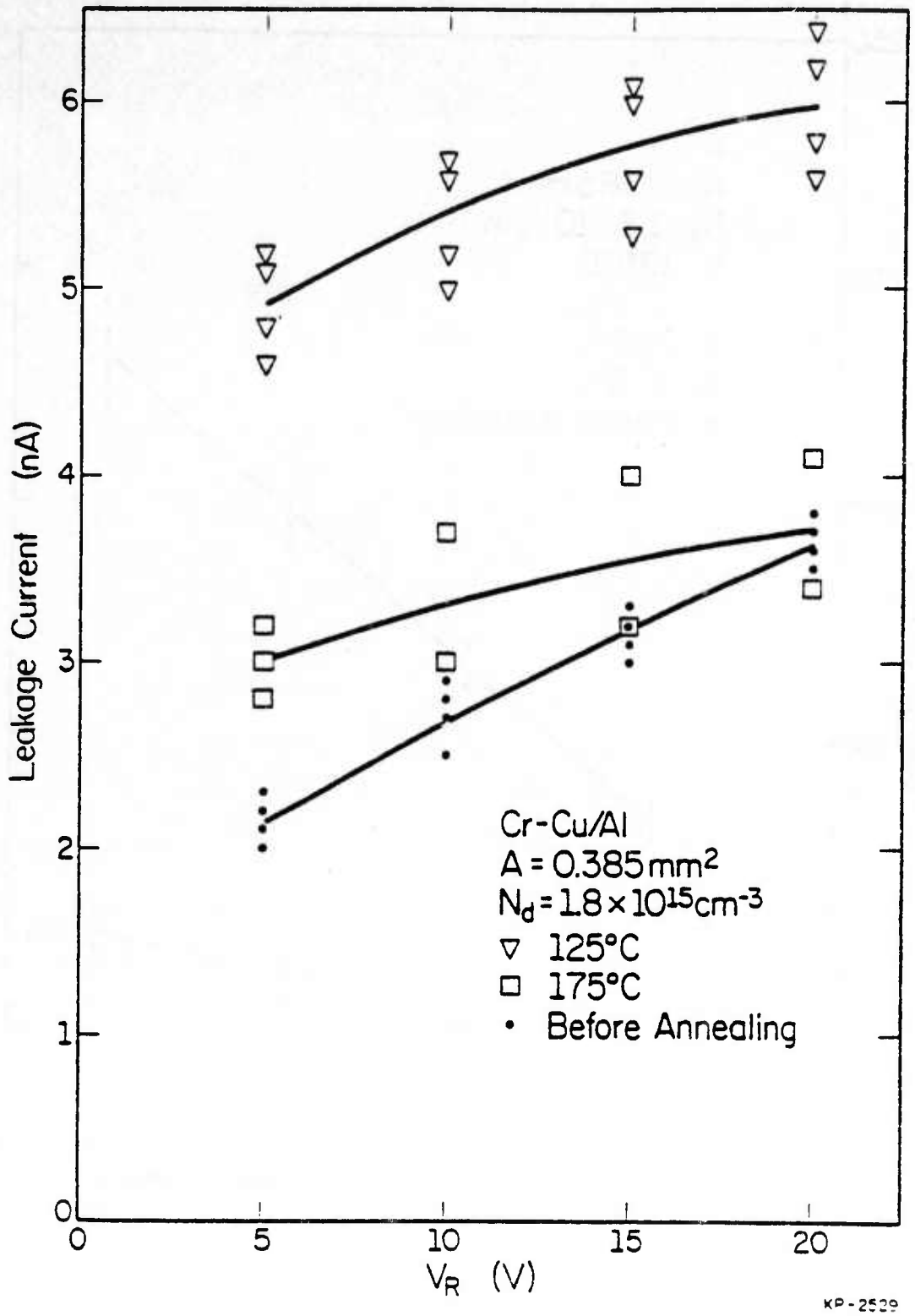

Figure 6. Leakage current versus applied reverse bias voltage for the chromium-copper/aluminum diodes.

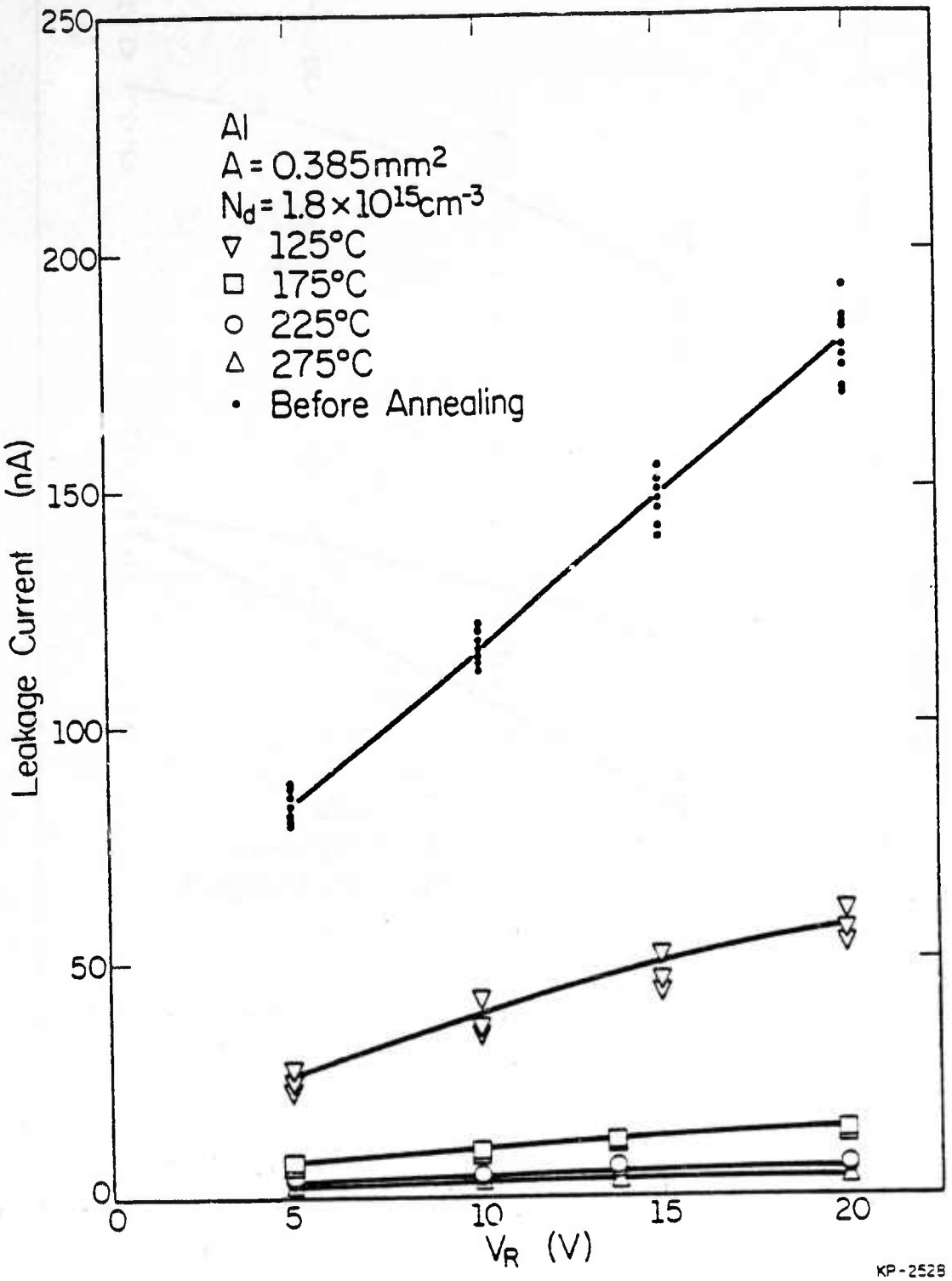

Figure 7. Leakage current versus applied reverse bias voltage for the aluminum diodes.

the metal-semiconductor interface [27]. The formation of this $Al_xGa_{1-x}As$ layer causes an increase in the band gap so the electrons see a higher barrier, resulting in lower leakage current.

As previously mentioned, the titanium diodes show an increase or decrease in leakage current, depending on the annealing temperature. Figure 8 displays the observed trends in leakage current values as annealing temperature is increased. Similar results are obtained on the higher doped wafer; however, there is more scatter in the data points. This may be due to a variance in surface-state density introduced during processing. It has been reported that resistivity measurements of gallium arsenide substrates show no difference in substrate resistivity , indicating that large leakage current variation is induced by processing rather than a change in resistivity [28].

A comparison of leakage current and barrier height trends for the three metallizations at the different annealing tempertaures is shown in Figure 9. At the lower annealing temperatures, leakage current in the chromium-copper/aluminum diodes increases with increasing annealing temperature, indicating that the outdiffusion of chromium and/or copper may be occurring. At higher temperatures, the increasing barrier height seems to be the overriding factor; hence, leakage current tends to decrease. For the aluminum diodes, barrier height is again increasing with temperature. However, outdiffusion is not a factor, so leakage current decreases as expected.

The titanium diodes exhibit characteristics similar to the chromium-copper/aluminum diodes. Although barrier height increases with temperature, leakage current increases at the lowest annealing temperature, then begins to decrease. Outdiffusion is predominant at the lower temperature, but becomes less of a factor as annealing temperature is increased and the barrier height continues to increase. The scatter in the data is due to deviation in the barrier height.

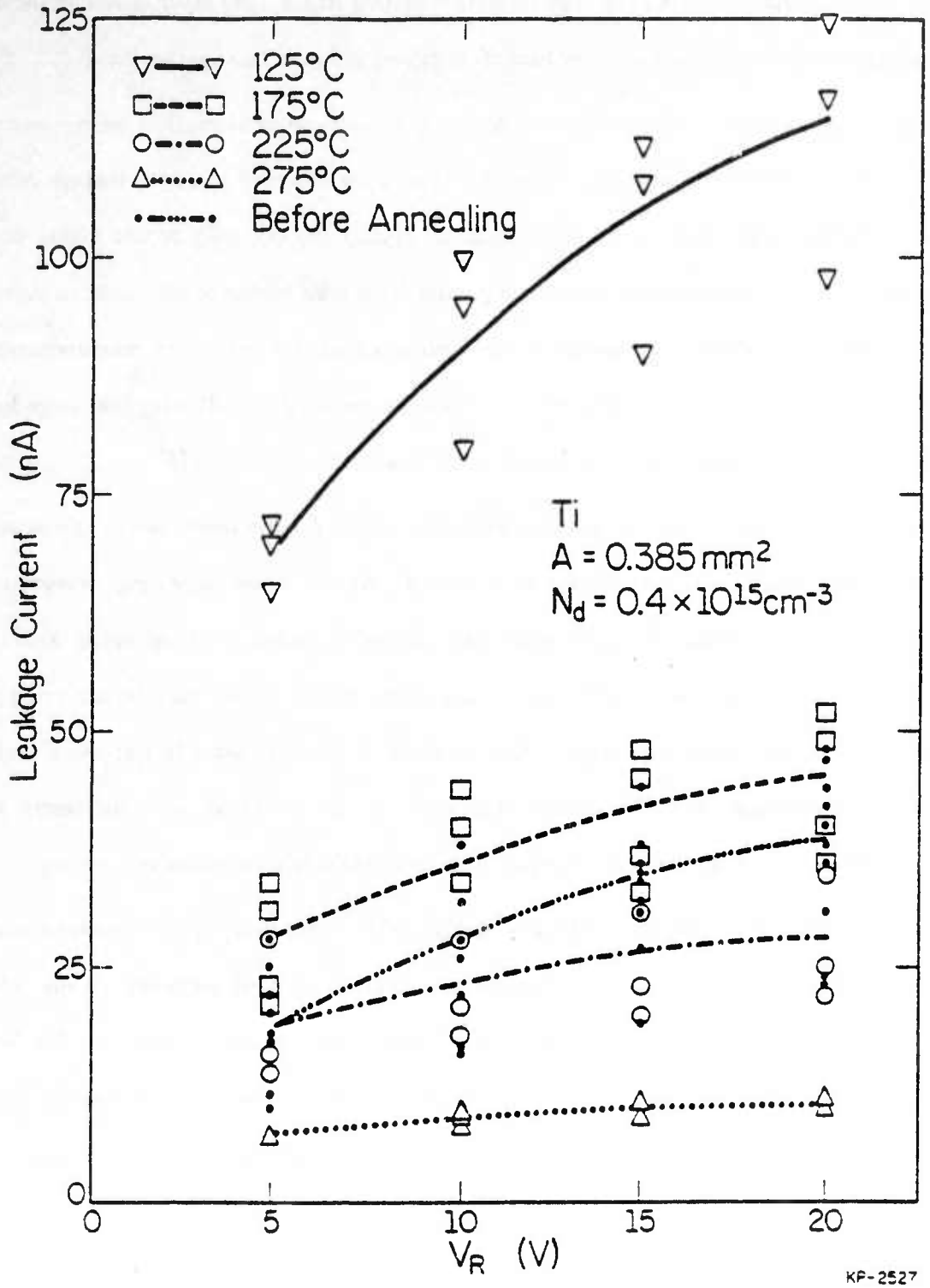

Figure 8. Leakage current versus applied reverse bias voltage for the titanium diodes.

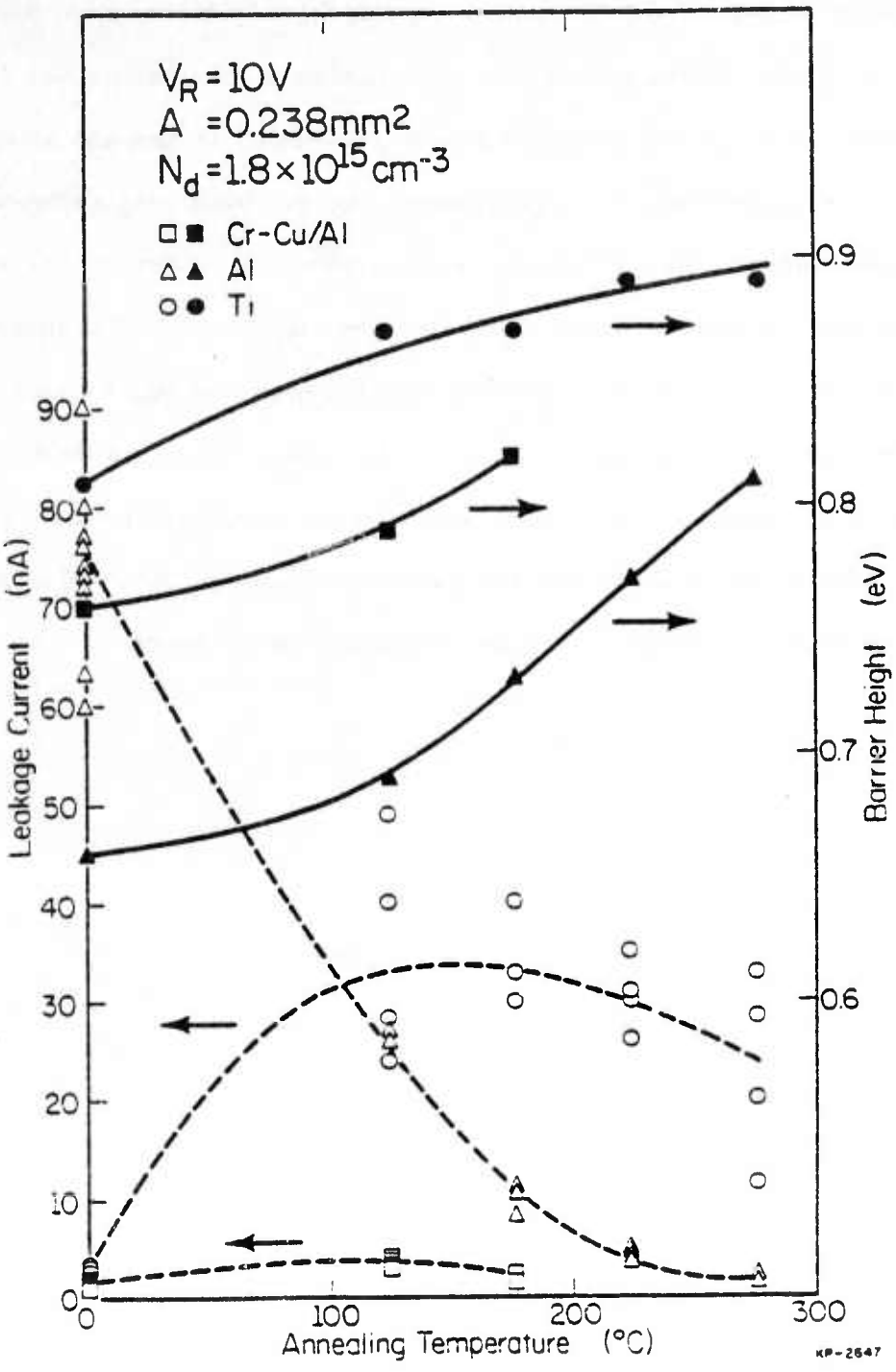

Figure 9. Leakage currents and barrier heights at different annealing temperatures for the three metallizations without polyimide rings.

V. CONCLUSION

In this thesis methods of reducing gallium arsenide Schottky barrier diode reverse leakage current are investigated. Reverse leakage current is described as the sum of a bulk leakage plus generation-recombination current component that is proportional to area and an edge leakage component that is proportional to circumference. The polyimide ring configuration, with chromium-copper/aluminum as the Schottky metal, achieves the lowest (0.1-1.4 nA) leakage current values since the edge component of leakage current is minimized. The aluminum diodes consistently have the largest amount of reverse leakage, but upon annealing, a drastic reduction in leakage current is observed. The titanium diodes display leakage currents in the nanoamp range; however, there is significant variation between wafers. Based upon this data, reducing edge effects will result in Schottky barrier diodes with the lowest reverse leakage current values and allows a correlation to be made between those values and the measured barrier height.

LIST OF REFERENCES

[1] C. Rhee, J. Saltich, and R. Zwernemann, "Moat-etched Schottky Barrier Diode Displaying Near Ideal I-V Characteristics," *Solid State Electronics*, Vol. 15, p. 1181, 1972.

[2] C. Rhee, p. 1181.

[3] J.L. Saltich and L.E. Clark, "Use of a Double-diffused Guard Ring to Obtain Near Ideal I-V Characteristics in Schottky Barrier Diodes," *Solid State Electronics*, Vol. 13, p. 857, 1970.

[4] P.A. Folkes, C.C. Chang, and E. Lane, "Process-induced Leakage Current in a Low Noise GaAs MESFET," *J. Electrochem. Soc.: Solid State Science and Technology*, Vol. 132, No. 6, p. 1417, June, 1985.

[5] S.M. Sze, *Physics of Semiconductor Devices*, New York: John Wiley and Sons, Inc., p. 258, 1981.

[6] N. Newman, "Annealing of Intimate Ag, Al, and Au-GaAs Schottky Barriers," *Med. Phys.*, Dec. 1984.

[7] B.L. Sharma, *Metal-semiconductor Schottky Barrier Junctions and Their Applications*, New York: Plenum Press, p. 4, 1984.

[8] S.M. Sze, p. 850.

[9] S.M. Sze, p. 204.

[10] J. Bardeen, "Surface States and Rectification at a Metal Semiconductor Contact," *Physical Review*, Vol. 71, No. 10, p. 717, May 15, 1947.

[11] J.L. Saltich, "Effects of Pre- and Post-annealing Treatments on Silicon Schottky Barrier Diodes," *Proc. of the IEEE*, Vol. 58, No. 3, p. 492, March, 1970.

[12] A.K. Srivastava and B.M. Arora, "Effect of Annealing on the Richardson Constant of Al-GaAs Schottky Diodes," *Solid State Electronics*, Vol. 24, No. 11, p. 1049, 1981.

[13] A.K. Srivastava, p. 1050.

[14] M. Hatzakis, B.J. Canavello, and J.M. Shaw, "Single-step Optical Lift-off Process," *IBM J. Res. Develop.*, Vol. 24, No. 4, p. 452, Jul, 1980.

[15] A. Fathimulla, "Single-step Lift-off Process Using Chlorobenzene Soak on AZ 4000 Resists," *J. Vac. Sci. Tech. B*, Vol. 3, No. 1, p. 25, Jan./Feb., 1985.

[16] F. Brunner, F. Frasch, and F. Schwerdt, "Etchant for Polyimides," *U.S. Patent 4,039,371*, Aug. 2, 1977.

[17] S.D. Mukherjee, C.J. Palmstron, and J.G. Smith, "The Thermal Stability of Thin Layer Transition and Refractory Metallizations of GaAs," *J. Vac. Sci. Tech.*, 17(5), p. 904, Sept./Oct. 1980.

[18] S.D. Mukherjee, "Reactions of Vacuum-deposited Thin Schottky Barrier Metallizations on Gallium Arsenide," *J. Vac. Sci. Tech.*, 16(2), p. 138, March/April, 1979.

[19] S.D. Mukherjee, p. 139.

[20] S.D. Mukherjee, p. 139.

[21] S.D. Mukherjee, p. 139.

[22] S.M. Sze, p. 280.

[23] P.A. Folkes, p. 1417.

[24] P.A. Folkes, p. 1417.

[25] A.K. Srivastava, p. 1049.

[26] N. Newman.

[27] N. Newman.

[28] P.A. Folkes, p. 1417.

DISTRIBUTION LIST

addresses	number of copies
Richard D. Hinman RADC/DCCD	20
RADC/DOL GRIFFISS AFB NY 13441	2
RADC/DAP GRIFFISS AFB NY 13441	2
ADMINISTRATOR DEF TECH INF CTR ATTN: DTIC-DDA CAMERON STA BG 5 ALEXANDRIA VA 22304-6145	12
DMAAC/STD 3200 South Second Street ST LOUIS MO 63118-3399	1
AFCSA/SAMI WASHINGTON DC 20330-5425	1
HQ USAF/SCTT WASHINGTON DC 20330	1

HQ USAF/RDSS
WASHINGTON DC 20330-5040 1

OASD (C3I), INFORMATION SYSTEMS
ROOM 3E187
WASHINGTON DC 20301-3040 2

HQ AFSC/DLAE
ANDREWS AFB DC 20334-5000 1

HQ AFSC/SDE
ANDREWS AFB DC 20334-5000 1

HQ AFSC/XRTD
ANDREWS AFB DC 20334 1

HQ AFSC/XRK
ANDREWS AFB MD 20334-500 1

HQ SAC/NRI (STINFO LIBRARY)
OFFUTT AFB NE 68113-5001 1

HQ SAC/SLPT
OFFUTT AFB NE 68113-5001 1

HQ ESC/DOOA
SAN ANTONIO TX 78243-5000 1

TAFIG/IIDD 1
ATTN: MR. ROBERTSON
LANGLEY AFB VA 23665-5000

HQ TAC/DOA (STINFO) 1
LANGLEY AFB VA 23665-5001

HQ TAC/DRCC 1
LANGLEY AFB VA 23665-5001

HQ TAC/DRCT 1
LANGLEY AFB VA 23665-5001

HQ TAC/DRCD 1
LANGLEY AFB VA 23665-5001

AFSC LIAISON OFFICE 1
LANGLEY RESEARCH CENTER (NASA)
LANGLEY AFB VA 23665-5000

HQ TAC/DOFR 1
LANGLEY AFB VA 23665

AFWL/NTATT (C E BAUM) 1
KIRTLAND AFB NM 87117-6008

HQ AFOTEC (OAWD) 1
Attn: Capt. Novack)
KIRTLAND AFB NM 87117-7001

ASD/ENEGA 1
WRIGHT-PATTERSON AFB OH 45433

ASD/AFALC/AXAE 1
WRIGHT-PATTERSON AFB OH 45433

ASD/ENAMA 1
WRIGHT-PATTERSON AFB OH 45430

ASD/XRS 1
WRIGHT-PATTERSON AFB OH 45433

AFIT/LDEE - TECHNICAL LIBRARY 1
BUILDING 640, AREA B
WRIGHT-PATTERSON AFB OH 45433-6583

AFWAL/MLPO 1
ATTN: DR. G. E. KUHL
WRIGHT-PATTERSON AFB OH 45433-6533

AFWAL/MLPO 1
WRIGHT-PATTERSON AFB OH 45433-6533

AFWAL/MLTE 1
WRIGHT-PATTERSON AFB OH 45433

AFWAL/FIES/SURVIAC 1
WRIGHT-PATTERSON AFB OH 45433

AFAMRL/HE
WRIGHT-PATTERSON AFB OH 45433-6573 1

AFHRL/LRS-TDC
WRIGHT-PATTERSON AFB OH 45433-6503 1

Area A Technical Library
2750 ABW/SSLT
Bldg 266, Rm 207, Post 203II
Wright-Patterson AFB OH 454433 1

1843EIG/EIEXM
WHEELER AFB HI 96854 1

AUL/LSE 67-342
MAXWELL AFB AL 36112-5564 1

HQ SPACECOM/XPYX
ATTN: DR. WILLIAM R. MATOUSH
PETERSON AFB CO 80914-5001 1

HQ ATC/TTQI
RANDOLPH AFB TX 78148 1

HQ ATC/TTQE
RANDOLPH AFB TX 78148 1

CODE H396RL TECHNICAL LIBRARY 1
DEFENSE COMMUNICATIONS
ENGINEERING CENTER
1860 WIEHLE AVENUE
RESTON VA 22090

COMMAND CONTROL AND COMMUNICATIONS DIV 1
DEVELOPMENT CENTER
MARINE CORPS DEVELOPMENT & EDUCATION COMMAND
ATTN: CODE DIOA
QUANTICO VA 22134

COMMANDER 1
BALLISTIC MISSILE DEFENSE SYSTEMS COMMAND
ATTN: DASD-H-MPL
PO BOX 1500
HUNTSVILLE AL 35807-3801

CHIEF OF NAVAL OPERATIONS 1
ATTN: OP-941F
WASHINGTON DC 20350-2000

COMMANDING OFFICER 1
NAVAL AVIONICS CENTER
LIBRARY - D/765
INDIANAPOLIS IN 46218

COMMANDING OFFICER 1
NAVAL TRAINING EQUIPMENT CENTER
TECHNICAL INFORMATION CENTER
BUILDING 2068
ORLANDO FL 32813-7100

COMMANDER 1
NAVAL OCEAN SYSTEMS CENTER
ATTM: TECHNICAL LIBRARY, CODE 9642
SAN DIEGO CA 92152-5000

US NAVAL WEAPONS CENTER, CODE 343 1
ATTN: TECHNICAL LIBRARY
CHINA LAKE CA 93555

SUPERINTENDENT (CODE 1424) 1
NAVAL POSTGRADUATE SCHOOL
MONTEREY CA 93943-5100

COMMANDING OFFICER 1
NAVAL RESEARCH LABORATORY
CODE 2627
WASHINGTON DC 20375

NAVELEXSYCOM 1
PDE-110-33
WASHINGTON DC 20363

REDSTONE SCIENTIFIC INFORMATION CENTER 2
US ARMY MISSILE COMMAND
REDSTONE SCIENTIFIC INFORMATION CENTER
ATTN: DRSMI-RPRD
REDSTONE ARSENAL AL 35898-5241

Advisory Group on Electron Devices 2
Attn: Security Office
201 Varick Street, 11th Floor
New York NY 10014

FRANK J SEILER RESEARCH LAB 1
FJSRL/NHL
ATTN: MAJOR TERRENCE F. DEATON
US AIR FORCE ACADEMY
COLORADO SPRINGS CO 80840-6528

LOS ALAMOS SCIENTIFIC LABORATORY 1
ATTN: REPORT LIBRARY
MAIL STATION 5000
LOS ALAMOS NM 87545

AIR FORCE ELEMENT (AFELM) 1
THE RAND CORP
1700 MAIN STREET
SANTA MONICA CA 90406

Commander 1

HQ, Fort Huachuca
TECH REF DIV
ATTN: BESSIE BRADFORD
Ft. Huachuca AZ 85613-6000

AF TACOM TEST TEAM/TEO 1
Attn: LT JAMES GRAVES
FT HUACHUCA AZ 85635

AEDC LIBRARY (TECH REPORTS FILE) 1
MS-100
ARNOLD AFS TN 37389-9998

U.S. DEPARTMENT OF TRANSPORTATION LIBRARY 1
FOB-10A SECTION, M-493.2, Room 930
800 INDEPENDENCE AVE. S.W.
WASH DC 20591

1839 EIG/EIET (KENNETH W. IRBY) 1
KEESLER AFB MS 39534-6348

1839 EIG/EIEE 1
KEESLER AFB MS 39534-6348

JTFPMO 1
Attn: Technical Director
1500 Planning Research Drive
McLean VA 22102

HQ AFCC/DAPL 1
BLDG P-40 NORTH, RM 9
SCOTT AFB IL 62225-6001

AWS TECHNICAL LIBRARY 1
FL4414
SCOTT AFB IL 62225-5438

AFEWC/ESRI 1
SAN ANTONIO TX 78243-5000

485 EIG/EIER (DMO) 2
GRIFFISS AFB NY 13441-6348

HQ ESD/XRX 1
HANSCOM AFB MA 01731

ESD/ICP 1
HANSCOM AFB MA 01731-5000

ESD/XRC (AFSC) 1
HANSCOM AFB MA 01731-5000

ESD/XRSE 1
HANSCOM AFB MA 01731-5000

ESD/SCS-2 1
HANSCOM AFB MA 01731-5000

ESD/TCS-2B 1
ATTN: MAJOR JOSEPH H. SCHMOLL
HANSCOM AFB MA 01731-5000

The Software Engineering Institute 1
Attn: Major Dan Burton, USAF
580 South Aiken Avenue
Pittsburch PA 15232-1502

DIRECTOR 1
NSA/CSS
ATTN: T5112 /TDL (MARJORIE E. MILLER
FORT GEORGE G MEADE MD 20755-6000

DIRECTOR 1
NSA/CSS
ATTN: W161
FORT GEORGE G MEADE MD 20755-6000

DIRECTOR 1
NSA/CSS
ATTN: R-8314 (MR. ALLEY)
FORT GEORGE G MEADE MD 20755-6000

DIRECTOR 1
NSA/CSS
ATTN: R24
FORT GEORGE G MEADE MD 20755-6000

DIRECTOR 1
NSA/CSS
ATTN: R21
FORT GEORGE G MEADE MD 20755-6000

DIRECTOR 1
NSA/CSS
ATTN: DEFSMAC (JAMES E. HILLMAN)
FORT GEORGE G MEADE MD 20755-6000

DIRECTOR 1
NSA/CSS
ATTN: R06
FORT GEORGE G MEADE MD 20755-6000

DIRECTOR
NSA/CSS
ATTN: R1
FORT GEORGE G MEADE MD 20755-6000 1

DIRECTOR
NSA/CSS
ATTN: R31
FORT GEORGE G MEADE MD 20755-6000 1

DIRECTOR
NSA/CSS
ATTN: R4
FORT GEORGE G MEADE MD 20755-6000 1

DIRECTOR
NSA/CSS
ATTN: R5
FORT GEORGE G MEADE MD 20755-6000 1

DIRECTOR
NSA/CSS
ATTN: R8
FORT GEORGE G MEADE MD 20755-6000 1

DIRECTOR
NSA/CSS
ATTN: R9
FORT GEORGE G MEADE MD 20755-6000 1

DIRECTOR
NSA/CSS
ATTN: S031
FORT GEORGE G MEADE MD 20755-6000 1

DIRECTOR
NSA/CSS
ATTN: S21
FORT GEORGE G MEADE MD 20755-6000 1

1

DIRECTOR
NSA/CSS
ATTN: V307
FORT GEORGE G MEADE MD 20755-6000

1

DIRECTOR
NSA/CSS
ATTN: W07
FORT GEORGE G MEADE MD 20755-6000

1

DIRECTOR
NSA/CSS
ATTN: W314 (MRS. JACKSON)
FORT GEORGE G MEADE MD 20755-6000

1

DIRECTOR
NSA/CSS
ATTN: R521
FORT GEORGE G MEADE MD 20755-6000

1

DIRECTOR
NSA/CSS
ATTN: R522
FORT GEORGE G MEADE MD 20755-6000

1

DIRECTOR
NSA/CSS
ATTN: R523
FORT GEORGE G MEADE MD 20755-6000

1

DIRECTOR
NSA/CSS
ATTN: R53 (JOHN C. DAVIS)
9800 SAVAGE ROAD
FORT GEORGE G MEADE MD 20755-6000

Electronic Decisions Inc — 5
1776 East Washington Street
attn: Dr Kansy
Urbana, IL 61801

RCA-Aerospace + Defense — 1
attn: Wayne D. Moyers
ATL Bld
Rt 38
Moorestown, NJ 08057

MICRILOR — 1
attn: J. Cafarella
9 Lakeside Office Park
North Ave
Wakefield, MA 01888

System Planning Corporation — 1
attn: S. Dereska
1500 Wilson Blvd
Arlington, VA 22209

DARPA/PMO — 1
attn: Ms Carolyn Chewning
1400 Wilson Blvd
Arlington, VA 22209-2308

DARPA/TTO — 3
attn: Mr John Entzminger
1400 Wilson Blvd
Arlington, VA 22209

Gould Inc — 1
NAVCOM Systems Division
attn: Dr. Hardy
4323 Arden Drive
El Monte, CA 91731

Gould Inc — 1
Advanced Systems Development Division
attn: Glynn Ramasy
6730 Baymeadow Drive
Glen Burnie, Maryland 21061

BMO/MYEP
attn: Lt John Conrad
Norton AFB CA 92409-6468 1

United Technology Research Center
attn: Tom Grudkowski
Mail Stop 31
Silver Lane
East Hartford, Conneticut 06108 2

AWFAL/AAWW-2
attn: Lt Cook
Wright Patterson AFB OH 45433 1

AWFAL/AADE
attn: Lutz Micheel
Wright Patterson AFB OH 45433 1

DARPA/STO
1400 Wilson Blvd
Arlington, VA 22209-2308 1

MITRE
Strategic Communications
attn: E. Ferrari
Bedford MA 01730 1

MITRE Corporation
attn: Harry Cronson/MS R350
Burlington Rd
Bedford MA 01730 1

RADC/ESEE
attn: Jerry Silverman
Hanscom AFB MA 01731 1

RADC/ESEE 1
attn: Paul Pellegrini
Hanscom AFB MA 01731

RADC/EEAC 1
attn: Rick Webster
Hanscom AFB MA 01731

AFATL/DLMT 1
attn: Mr Boudreaux
Eglin AFB FL 32542-5320

Naval Research Labs 1
attn: Ed Koos/ Code 5730
4555 Overlook Ave, SW
Washington DC 20375-5000

AFWAL/AADE-2 1
attn: Gordon Rabanus
Wright Patterson AFB OH 45433

CIA/ORD 1
(Attn: Dr. Robert Braunstein)
Washington DC 20505

SAIC 1
Attn: Kenneth L. Jordan
1710 Goodridge Dr.
McLean, VA 22102

Coordinated Science Lab 5

University of Illinois
1101 W. Springfield Ave,
Urbana, IL 61801

SD/DAAX
Attn: Capt Poterba
P.O. Box 92960
WPC
Los Angeles, CA 90009 1

SD/DAAX
(Attn: Scott B Eckert)
P.O. Box 92960
WPC
Los Angeles, CA 90009 1

Aerospace Corp
(Attn: Dr. J. R. La Frieda, ML-211)
P.O. Box 92957
Los Angeles, CA 90009 1

SCPE, Inc.
(Attn: Dr. Seymour Stein)
56 Great Meadow Rd.
Newton Centre, MA 02159 1

RADC/IRAA
attn: Emily A. Krzysiak
Bldg 240
Griffiss AFB NY 13441 2

Harry Diamond Labs
(Attn: John Pellegrino)
SLCHD-RT-RB
2800 Powder Mill Rd
Adelphi, MD 20783 1

Harry Diamond labs
(Attn: Mike Patterson)
SLCHD-RT-RB
2800 Powder Mill Rd
Adlphi, MD 20783 1

JPL 264-801
Attn: Ed Posner
4800 Oak Grove Drive
Pasadena, CA 91109 1

Director 1
USA Signal Warfare Center
attn: AMSEL-SW-EA, D.A. Harkleroad
Vint Hill Farms Station
Warrenton, VA 22186

AFWAL/AAAI-2 1
Attn: 1Lt G. Mikulanicz)
Wright-Patterson AFB OH 45433

Signal Science Inc. 1
(Attn: John P. King)
7223 Parkway Dr.
Suite 105
Hanover, MD 21076

MIT Lincoln laboratory 1
(Attn: Irvin G. Stiglitz)
P.O. Box 73
Lexington, MA 02175

Birch Associates Inc. 1
(Attn: J. N. Birch)
1001 Spring St.
Suite 206
Silver Spring, MD 20910

Pollard Road Inc. 1
(Attn: V. L. Lynn)
Suite 708
2361 Jefferson-Davis Hwy
Arlington, VA 22202

IDA/CRD 1
(ATTN: L. A. LIPORACE)
Thanet Rd.
Princeton, NJ 08540

DARPA/STO 1
(Attn: Dr. Ken Ando)
1400 Wilson Blvd
Arlington VA 22209-2308

DARPA/DSO
(Attn: Dr. Richard Reynolds)
1400 Wilson Blvd
Arlington, VA 22209-2308 1

Arthur Cohen
Department of Defense
9800 Savage Rd
Ft Meade, MD 20755-6000
Attn: R-8 1

Robert Bode
Department of Defense
9800 Savage Rd
Ft Meade, MD 20755-6000
Attn: R-522 1

F. W. Bishop
Department of Defense
9800 Savage Rd
Ft Meade, MD 20755-6000
Attn: R-55 1

David Kisak
Department of Defense
9800 Savage Rd.
Ft Meade, MD 20755-6000
Attn: R-744 1

Paul Boudreaux
Department of Defense
9800 Savage Rd
Ft Meade, MD 20755-6000
Attn: R-54 1

Ken Caster
Department of Defense
9800 Savage Rd
Ft Meade, MD 20755-6000
Attn: W322 1

Richard Fray
Department of Defense
9800 Savage Rd
Ft Mead, MD 20755-6000
Attn: W-311 1

Wayne E. Smith 1
Department of Defense
9800 Savage Rd
Ft Meade, MD 20755-6000
Attn: G-43

Bret R. Schneider 1
Department of Defense
9800 Savage Rd
Ft Meade, MD 20755-6000
Attn: R-744

Capt Roger Colvin 1
Department of Defense
9800 Savage Rd
Ft Meade, MD 20755-6000
Attn: W-233

Dr. Milo Hruby 1
Department of Defense
9800 Savage Rd
Ft Meade, MD 20755-6000
Attn: R-5

James Piersall 1
Department of Defense
9800 Savage Rd
Ft Meade, MD 20755-6000
Attn: R-741

Mr. William Edwards 1
Air Force Wright Aeronautical Laboratory
(Attn: AFWL/AAD)
Wright-Patterson AFB OH 45433

Dr. Krueger 1
Air Force Wright Aeronautical Laboratory
Attn: AFWL/AS
Wright-Patterson AFB OH 45433

Dr. Carter Morris 1
Central Intelligence Agency
Attn: ORD
Washington, DC 20505

Dr. George Simons 1
Harry Diamond Labs
2800 Powder Mill Rd
(Attn: DELHD-RT-RB)
Adelphi, MD 20783

US Army Night Vision and 1
Electro-Optical laboratory
Attn: DELNV-AC Mr. Terry Jones
Advanced Concepts Division
Ft Belvoir, VA 22060-5677

Mr. Walter Gelnovatch 1
Diector, US Army Electronics Tech.
and Devices Laboratory (ERADCOM)
Attn: DELET-M
Fort Monmouth, NJ 07703

Dr. Edwin T. Hunter 1
Director, US Army Electronics Tech.
and Devices Laboratory (ERADCOM)
attn: DELET-I
Fort Monmouth, NJ 07703

Mr. Harper Whitehouse 1
Naval Ocean Systems Center
Attn: Code 741
271 Catalina Boulevard
San Diego, CA 92152

Dr. Timothy [illegible]fee 1
Director of Research
Naval Research Laboratory
4555 Overlook Drive, SW
Washington, DC 20375-5000

Mr. Robert Evans 1
Naval Research Laboratory
4555 Overlook Drive, SW
Attn: Code 5752
Washington, DC 20375-5000

Mr. Nelson Head 1
Naval Research Laboratory

4555 Overlook Drive, SW
Attn: Code 7570
Washington, DC 20375-5000

Dr. J. M. Killiany 1
Naval Research Laboratory
4555 Overlook Drive, SW
Attn: Code 6810
Washington, DC 20375-50000

Dr. Merril Skolnik 1
Naval Research Laboratory
4555 Overlook Drive, SW
Attn: Code 5300
Washington, DC 20375-5000

Mr. William Waters 1
Naval Research Laboratory
4555 Overlook Drive, SW
Attn: Code 5330
Washington, DC 20375-5000

Mr. James Queen 1
Naval Surface Weapons Center
Attn: Code F05
Dahlgren, VA 22448

Dr. Kenneth L. Davis 1
Office of Naval Research
800 N. Quincy Street
Attn: Code 414
Arlington, VA 22217-5000

Commander Paul Girard 1
Office of Naval Research
800 N. Quincy Street
Attn: Code 411
Arlington, VA 22217-5000

Theodore A. Kircher 1
Department of Defense
9800 Savage Rd
Ft Meade, MD 20755-6000
Attn: R-744

Mr. Jack Tehan 1
Air Force Wright Aeronautical Laboratory
CAttn: AFWL/A-AW
Wright-Patterson AFB OH 45433

Mr. J. P. Letellier 1
Office of Naval Technology
800 N. Quincy Street
Arlington, VA 22217-5000

Dr. William Novick 1
US Army Electronic Warfare Laboratory
Attn: DELEW-C
Fort Monmouth, NJ 07703-5303

Dr.David Jaskowiak, Director 1
US Army Signal Warfare Laboratory
Attn: DELSW-CC
Vinthill Farms Station
Warrenton, VA 22186-5100

Mr. Benjamin M. Elder 1
The John Hopkins University
Applied Physics Laboratory
John Hopkins Road
Laurel, MD 20707

Mr. Monty Frost 1
ARGO Systems
884 Hermosa Court
Sunnyvale, CA 94986

Dr. George E. Smith 1
AT&T Bell Laboratories
600 Mountain Ave
Room 2A-323
Murray Hill, NJ 07974

Dr. Stanley Robinson 1
Environmental Institute of Michigan
P.O. Box 8618
Ann Arbor, MI 48107

Mr. James R. Willhite 1
Gould Inc.
Gould Research Center
40 Gould Center
Rolling Meadows, IL 60008

Hazeltine Corp 1
attn: J. Murphy
Hill Rd
Greenlawn, NY 11740

Mr. Richard Benz 1
Honeywell Information Systems
7900 West Park Drive
Attn: Mail Stop 410
McLean, VA 22102

Dr James Chan 1
Magnavox
Advanced Products & Systems Company
2829 Maricopa Street
Torrance, CA 90503

Dr. J. A. Higgins 1
Rockwell International Corporation
1049 Camino Dos Rios
P.O. Box 1085
Thousand Oaks, CA 91360

Dr. Lew Claiborne 1
Texas Instruments, Incorporated
P.O. Box 660246
Mail Stop 409
Dallas, TX 75266

Dr. Carl Panasik 1
Texas Instruments, Incorporated
Mail Stop 255
P.O. Box 660246
Dallas, TX 75266

Mr. Nick Willis 1
Technology Service Corporation
Information Systems Division
1945 Gallows Road, Suite 404
Vienna, VA 22180

Mr. Bob Graziano 1
Technology Service Corporation
Information Systems Division
1945 Gallows Road, Suite 404
Vienna, VA 22180

Dr. Soong Hak Lee 1
Westinghouse Defense Electronics
P.O. Box 746
Mail Stop 1112
Baltimore, MD 21203

Dr. Harry Salvo 1
Westinghouse Defense Electronics
P.O. Box 746
Mail Stop 1112
Baltimore, MD 21203

Mr. Louis Lome 1
Central Intelligence Agency
Attn: ORD
Washington, DC 20505

DIRECTOR 1
NSA/CSS
ATTN: L-222
FORT GEORGE G MEAD MD 20755-6000

General Dynamics 1
attn: Dr Mathis, MS-7202-H
P.O. Box 85310
San Diego, CA 92138

DARPA/NTO 1
attn: Dr Al Ellenthorpe
1400 Wilson Blvd
Arlington, VA 22209-2308

DARPA/DSO 1
attn: Mr Sven Roosild
1400 Wilson Blvd
Arlington, VA 22209-2308

General Electric Company 1
attn: Stephen Wanuga
Electronics Lab, Rm 244
Electronics Park
Syracuse, NY 13221

Hughes 1
Industrial Electronics Group
attn: Preston Campbell
P.O. Box 2940
Torrance CA 90509-2940

Lockheed 1
attn: Robert Ward
3251 Hanover St.
Palo Alto, CA 94304

Teledyne MMIC 1
att: Lynwood Cosby
1501 Wilson Blvd
Arlington, VA 22209-2550

Rensselaer Polytech Institute 1
attn: Pankaj Das
Troy, NY 12181

DBA Systems 1
attn: William Druyun
11781 Jackson Memorial Highway
Fairfax, VA 22033-3360

Hughes 1
Ground Systems Group
attn: David Effinger
P.O. Box 3310
Fullerton, CA 92634-3310

Grumman Electronics Systems 1
attn: Howard Engleson
Bethpage, NY 11714-3585

System Engineering And Development Corp 1
attn: Terry Turpin
9150 Rumsey Rd
Columbia, MD 21045

GT-Tech Inc 1
attn: Ed German
5 Meadow Mist Court
Reislertown, MD 21136

Science Applications Int Corp 1
attn: Jurgen Gobien
1710 Goodridge Drive
McLean, VA 22102

Motorola 1
attn: Ray Hammond
Government Electronics Group
82011 McDowell Rd, P.O. Box 1417
Scottsdale, AZ 85252

Raytheon 1
attn: William Hillyard
1215 Jefferson Davis HWY
Suite 1500
Arlington, VA 22202

DBA Systems Inc 1
attn: Manfred Hirt
11781 Jackson Memorial Hwy
Fairfax, VA 22033-3360

ITT, Defense Communications Div 1
attn: James Irvine
492 River Rd
Nutley, NJ 07110

Rockwell Int, Avionics Group 1
attn: Stefan Koczo
400 Collins Rd NE
Cedar Rapids, IA 52498

Syracuse University
attn: Philipp Kornreich
103 Redwood Drive
Syracuse, NY 13201 1

Hughes, Microwave Products Div
attn: Chia Chuan Lee
P.O. Box 2940
Torrance, CA 90509-2940 1

GTE, Advanced Components Technology Center
attn: Harry Lockwood
40 Sylvan Rd
Waltham, MA 02254 1

Sperry
attn: Ken Matysik
Sperry Park, P.O. Box 64525
St. Paul, MN 55164-0525 1

Northrop, Defense Systems Div
atttn: Fred McKean
600 Hicks Rd
Rollig Meadows, IL 60008-1098 1

Westinghouse, Defense Group
attn: D. Mergerian
Frriendship Site, box 1693
Baltimore, MD 21203 1

Lockheed- Georgia Co
attn: R. W. Milling
Marietta, GA 30063 1

Raytheon, research Div
attn: Gary Montress
131 Spring St
Lexington, MA 02173 1

Scope Inc
attn: Richard Mosehauer
1860 Michael Faraday Drive
Reston, VA 22090 1

Sanders Associates
attn: George Norris
Daniel Webste Hwy
South, C.S. 2041
Nashua, NH 03061-2041 1

Sensis Corp
attn: James Perry
The Market Place, Route 92
Manlius, NY 13104 1

System Technologies
attn: Michael Price
9525 Worrell Ave
Lanham/Seabrook, MD 20706 1

Ford Aerospace
attn: Arlyn Asch
Aeronutronic Div
Ford Rd
Newport Beach, CA 92658 1

Rockwell, Science Center
attn: Rajeshwar Sahai
1049 Camino Dos Rios, P.O. Box 1085
Thousand Oaks, CA 91360 1

Martin Marietta
attn: Tsi-shung Sun
1450 So Rolling Road
Baltimore, MD 21227-3898 1

Eaton Corp, AIL Div
attn: Jesse Taub
Commack Road
Deer Park, NY 11729 1

Varian Associates 1
attn: Michael Wright
611 Hansen Way
Mail Stop K-103
Palo Alto, CA 94303-0883

Texas Instruments 1
attn: Claude Tew
13500 North Central Expressway
P.O. Box 225936
Dallas, TX 75265

Adams-Russel Electronics Co 1
attn: Thomas Zeltwanger
Communications Program Div
1370 Main St
Waltham, MA 02154

RCA AT Labs 1
attn: Wolf Altman
Moorestown Corporate Center
Route 38
Moorestown, NJ 08057

Draper Lab 1
attn: Paul VanBroekhoven
555 Technology Square
Cambridge, MA 02139

Fairchild 1
attn: Thomas Brown
Space and Electronics Comppany
Germantown, MD 20874

Decision-Science Applications 1
attn: Arthur BruckHeim
1901 North Moore St
Suite 1000
Arlington, VA 22209

MISSION
of
Rome Air Development Center

RADC plans and executes research, development, test and selected acquisition programs in support of Command, Control Communications and Intelligence (C^3I) activities. Technical and engineering support within areas of technical competence is provided to ESD Program Offices (POs) and other ESD elements. The principal technical mission areas are communications, electromagnetic guidance and control, surveillance of ground and aerospace objects, intelligence data collection and handling, information system technology, ionospheric propagation, solid state sciences, microwave physics and electronic reliability, maintainability and compatibility.